THE EVOLUTION OF DEEP-WATER SALT-TECTONIC STRUCTURES, NUMERICAL MODELING STUDIES APPLIED TO THE NORTHWESTERN GULF OF MEXICO

by

Sofie Gradmann

Submitted in partial fulfillment of the
requirements for the degree of
Doctor of Philosophy

at

Dalhousie University
Halifax, Nova Scotia
September 2012

DALHOUSIE UNIVERSITY

DEPARTMENT OF EARTH SCIENCES

The undersigned hereby certify that they have read and recommend to the Faculty of Graduate Studies for acceptance a thesis entitled "THE EVOLUTION OF DEEP-WATER SALT-TECTONIC STRUCTURES, NUMERICAL MODELING STUDIES APPLIED TO THE NORTHWESTERN GULF OF MEXICO" by Sofie Gradmann in partial fulfillment of the requirements for the degree of Doctor of Philosophy.

Dated: September 11., 2012

External Examiner: _____
Dr. Hemin Koyi

Research Supervisor: _____
Dr. Christopher Beaumont

Examining Committee: _____
Dr. Djordje Grujic

_____
Dr. Mark Deptuck

Departmental Representative: _____
Dr. Rebecca Jamieson

DALHOUSIE UNIVERSITY

DATE: September 11., 2012

AUTHOR: Sofie Gradmann

TITLE: THE EVOLUTION OF DEEP-WATER SALT-TECTONIC STRUCTURES, NUMERICAL MODELING STUDIES APPLIED TO THE NORTHWESTERN GULF OF MEXICO

DEPARTMENT OR SCHOOL: Department of Earth Sciences

DEGREE: Ph.D. CONVOCATION: May YEAR: 2013

Signature of Author

Table of Contents

List of Tables

List of Figures

Abstract

Salt tectonics is a key player in the evolution of many worldwide sedimentary basins on rifted continental margins. For more than a century, the evolving structures have been studied; but focus remained primarily on the onshore and shallow-water regions. The evolution of the poorly studied deep-water salt-tectonic structures is the focus of this thesis. Investigations are performed using 2D numerical models that comprise a viscous salt layer overlain by a frictional-plastic passive margin sedimentary sequence from shelf to deep water.

This thesis addresses multiple salt-tectonic processes (gravity spreading, evolution of fold belts and salt canopies, diapirism) in a general context but with special focus on the structural evolution of the northwestern Gulf of Mexico (GoM). Here, multiple phases of gravity-spreading induced salt mobilization and thin-skinned deformation occurred throughout the Cenozoic. During the latest, late Oligocene-Miocene phase, the Perdido Fold Belt (PFB) formed from a 4.5 km thick pre-kinematic section as a prominent salt-cored deep-water structure above the pinch-out of the autochthonous salt. It is here demonstrated with analytical as well as numerical calculations that the folding of the PFB can have formed by gravity spreading alone without basement tectonics. A requirement for this deformation is very high pore-fluid pressure in the sediments, which effectively reduces the sediments' mechanical strength. These values are refined using numerical models that couple compaction-induced fluid pressure to mechanical deformation. It is shown that very high fluid pressure is only necessary at the landward base of the deforming system; fluid pressure in other regions may remain moderate. This study shows, for the first time, the regional and dynamic evolution of pore-fluid pressure in a continental margin sedimentary system above salt. Additionally, the contribution of 'lateral compaction' during fold-belt evolution is addressed.

Landward of the PFB, a large-scale canopy developed during the Eocene. Its evolution is studied by investigating three different concepts of canopy evolution that have been proposed in the scientific literature. A canopy evolving via the mechanism of squeezed diapirs is most similar to the Eocene canopy of the northwestern GoM. A canopy evolving via the mechanism of breached anticlines is similar to that observed above the landward end of the PFB. Dynamic diapir growth is addressed in a neutral stress regime under uneven sedimentation employing a new mechanism of diapir initiation and evolution.

Acknowledgements

First and foremost I'd like to thank Chris Beaumont for supervising my work, for always finding time to discuss the models, and for always being willing to tackle the problems I was running into.

I'd like to thank all the members of the Dalhousie Geodynamics Group and my supervisory committee, but especially Steven Ings and Markus Albertz for contributing with valuable discussions, useful ideas, and for important help with decision makings.

I'd like to thank all the graduate students of the Earth Science department for making my stay at Dalhousie University so enjoyable. This also includes many long days and evenings in the office. I am especially grateful to Dawn Kellett, Konstanze Stübner, Neil Davies, and Sakalima Sikaneta for entertaining me even in these long hours I had to sit and work in my office.

I am grateful to all those people that walked passed my office with smiles on their faces, greeting me: Guang Yang, Anne Gold, John Newgard, John Gosse, Annina Margreth, and Jose-Luis Antinao.

And I'd like to thank all the people that supported me during my time in Norway when I eventually finished the PhD. I thank Jörg Ebbing for his patience and understanding when I spent more time than I should have working on the thesis. And huge gratitude goes to Laura Marello, Aziz Nasuti, and Claudia Haase, who were in similar pre-PostDoc situations as me, and who provided me with tremendous moral support.

Oh Sopale!

(after and inspired by Georg Kreisler's "Mütterlein")

I sit in my office as night closes in,
    but wont turn the PC off yet.
I think of the years that have passed in a spin
    and ponder with joy and regret:

To whom am I grateful for what I achieved?
    Dalhousie? Chris Beaumont? My fate?
(No,) my gratitude goes to a software alone,
    (that) I like and adore and I hate.

Oh Sopale! Oh Sopale! What a dear friend you have been,
    foldbelts, diapirs and canopies
conjured you onto the screen.

Oh Sopale! Oh Sopale! Oh how dear you are to me!
    One could almost say that without you
I would lack my PhD.

When I tried to model foldbelts
    you made both the grids mismatch
the Lagrangian and Eulerian -
    took me half a year to patch.

You turned buckling into kinking,
    - never did I find out why.
I tried hard to control fold lengths,
    and another year went by.

You provide for sed'mentation:

margins prograde, flat and steep,
fill and spill and sinusoidal -
never mind the color creep.

Supra-lithostatic pressure
(and) decompaction are your pref-
ferred way to annoy me when I
use you as SOPALE-ff.

Oh Sopale! Oh Sopale! Many nights you spent with me,
in the bunker of the LSC.
I enjoyed your company.

You caused me much trouble and made me concede.
You did have a mind of your own.
We fought and we quarreled, but now I succeed.
And meanwhile, close friends we have grown.

Oh Sopale! Oh Sopale! How I'll miss you from here on.
You have taught me 'bout the mod'ling world.
You have taught me to move on.

Oh my friends, oh my friends, listen what I say to you:
If you contemplate to do field work,
please don't do it, it's where hazards lurk.
Gath'ring seismic data from the sea?
Just refrain from it and leave it be.
Working in the lab has no avail:
dang'rous acids and fumes to inhale.
If you plan to use a microscope,
then your eyes go bad, there is no hope.
But if you plan to use SOPALE, do it without further ado!

Chapter 1

Introduction

1.1 Motivation

Salt-tectonic structures and salt-tectonic deformation have been the subject of scientific research for more than a century. Combined with appropriate stratigraphic units, these structures often function as hydrocarbon traps and are therefore of enormous economic significance. Whereas shallow-buried on- and offshore structures have been intensely studied, the understanding of the structures of the deep-water areas is still limited - despite growing activity of deep-water exploration.

The understanding of salt-tectonic processes changed fundamentally in the early 1990s, when it was realized that the very different rheologies of salt and its sedimentary overburden (viscous and frictional-plastic, respectively) as well as laterally varying stress induced, for example, by differential loading often played a more significant role for structural evolution than the density contrast between the two materials. Large-scale gravity gliding above weak salt was observed on several continental margins, generating domains of upslope extension and downslope shortening. It became clear that the concepts of local evolution of structures were no longer sufficient, but that the regional (margin-scale) salt-tectonic deformation and associated stress regimes also needed to be considered, which especially holds true for the deep-water structures. Definitions of the salt-tectonic terminology used in this thesis are given in Appendix A.

The Gulf of Mexico (GoM) comprises one of the most extensive salt basins in the world and possesses a large number of different salt structures such as diapirs, canopies and salt-cored fold belts. The hydrocarbon abundance of this sedimentary basin has supported more than a century of exploration and salt-tectonic research. This thoroughly mapped salt basin is therefore well suited to investigate the evolution of deep-water salt structures in context with the much better investigated shallow-water structures upslope.

Methods of salt-tectonic investigations range from geological mapping and extensive geophysical surveys to laboratory experiments on rock salt and analogue and numerical models. Modeling methods make it possible to quantitatively investigate the processes that shaped the currently observed structures; numerical approaches permit to test a wide range of parameter values involved in these processes. Numerical modeling of salt-tectonic deformation is still a relatively young field of research, albeit one that has advanced rapidly during the last decade.

In this thesis, I investigate the yet poorly explored structures of the deep-water GoM (which have recently become of economic interest), by employing the modern concepts of margin-scale, gravity-driven deformation above a weak salt layer, and using the new and powerful technique of geodynamic numerical modeling to salt tectonics.

1.2 Background I: Developments in Salt-Tectonic Research

Salt tectonics came into the focus of geological research a century ago when it was recognized that hydrocarbon discoveries were closely related to salt structures (*Jackson*, 1995). Early investigations centered around the salt diapirs of the North German Basin and the US Gulf Coast (*Jackson*, 1995). With increasing exploitation of the onshore areas and technological development, hydrocarbon exploration and related salt-tectonic research extended to the offshore areas, again primarily taking place in the Gulf Coast region. Exploration of the deep-water areas (water depths >500 m) only started during the early 1990s, mainly in the GoM, West Africa and Brazil (*Pettingill and Weimer*, 2002). Today, an increasing number of giant discoveries are made in deep-water regions (*Pettingill and Weimer*, 2002). Nevertheless, the processes and structures that are relevant to the deep-water areas, as well as the interaction of regional salt-tectonic deformation and local structural evolution are still poorly understood.

The term 'salt' is often used interchangeably with 'halite' (rock salt), but also to describe the thick evaporitic sequences in sedimentary basins (although these comprise other minerals such as anhydrite, gypsum, or calcite, and even detrital clastics). Halite is the most abundant mineral in an evaporitic sequence. Its physical properties differ strongly from those of most other sedimentary rocks and account for the

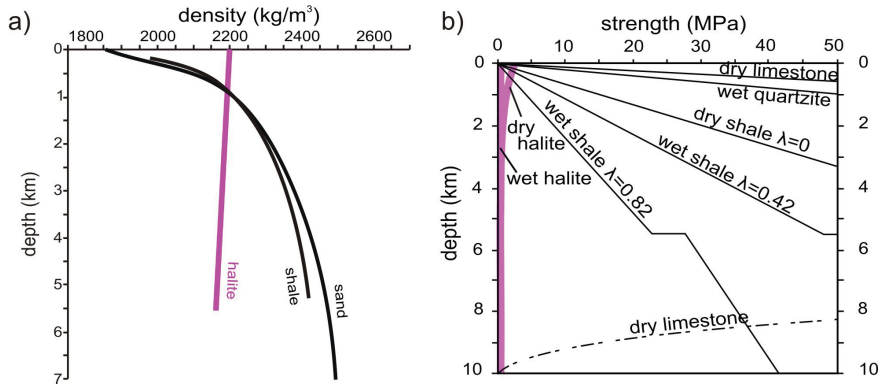

Figure 1.1: Salt and sediment density (a) and strength (b). After *Jackson and Talbot* (1986) and *Jackson and Vendeville* (1994)

distinctive characteristics of salt tectonics. Halite is already fully compacted at depth of 50 m (*Casas and Lowenstein*, 1989) and maintains a near-constant density below this depth with slightly decreasing values owing to temperature effects (Figure 1.1a) (*Talbot*, 1979). As a result, halite is less dense than most clastic sediments at depths greater than approximately one kilometer. The second important characteristic of halite is its extremely low yield strength (Figure 1.1b), which is generally exceeded by geological stresses. At geological timescales, halite therefore behaves as a viscous fluid (*Urai et al.*, 1986; *van Keken et al.*, 1993), which responds immediately to tectonic stresses and can serve as detachment surfaces and localize deformation.

The comparatively low density of salt strongly guided the early salt-tectonic research, which was primarily based on the concepts of vertical salt movement and buoyancy-driven diapirism (e.g. *Trusheim*, 1957, 1960). These concepts were able to explain most of the observed diapir shapes and structures found around diapirs but failed to account for the brittle deformation observed above them (keystone grabens, listric faults, etc.), because both salt and overburden were considered to be viscous materials.

The understanding of salt-tectonic processes changed drastically during the early 1990s. It had already been suggested several decades before that the mechanical strength of clastic sediments commonly exceeds the buoyancy force of underlying salt and thus that density contrasts alone generally cannot initiate salt diapirs (*Nettleton and Elkins*, 1947). Only recently did it receive widespread attention (*Vendeville and Jackson*, 1992; *Poliakov et al.*, 1993a; *Schultz-Ela et al.*, 1993). It was concluded

that early stages of diapirism must therefore be accompanied by an additional tensile or compressive deviatoric stress (*Vendeville and Jackson*, 1992). It was furthermore recognized that differential sediment loading above a developing diapir can largely control to its growth. The diapir evolution may nevertheless still be strongly driven by the density difference between salt and overburden (*Schultz-Ela et al.*, 1993).

The different rheologies of salt and sediments not only hamper diapir initiation, they can also facilitate horizontal movements of the viscous salt as well as of its brittle overburden, and thereby become a key driver of salt tectonics. A weak salt layer can decouple basement and overburden deformation and result in so-called thin-skinned tectonics, which affects only the cover rocks and leaves the basement undeformed. *Cobbold et al.* (1989) demonstrated, by means of analogue experiments, that a weak salt layer can sustain sliding of the sedimentary overburden on the scale of an entire continental margin.

Large-scale gravitational deformation of sedimentary overburden above mobilized salt can generally be separated into two different processes. 'Gravity gliding' (Figure 1.2a) occurs when the sedimentary overburden is destabilized by a regional seaward tilt of the system. The overburden then translates without significant internal deformation (*Schultz-Ela*, 2001). 'Gravity spreading' (Figure 1.2b) occurs if the differential stresses in the unevenly thick sedimentary overburden become large enough to bring it to failure, which can be assisted by channel (Poiseuille) flow of the salt as it is mobilized by the differential loading (*Gemmer et al.*, 2004, 2005) and induces an additional basal drag force on the overburden. The sedimentary wedge will then extend or spread laterally and thin vertically if a weak detachment layer (such as salt) is present. Many linked systems of extension and shortening show a combination of these two mechanisms (*Schultz-Ela*, 2001) (Figure 1.2c, 1.3).

The insight into linking of upslope extension and downslope shortening has proven crucial in the investigation and understanding of the deep-water structures (*Jackson*, 1995; *Peel et al.*, 1995; *Mohriak et al.*, 1995). Local salt-sediment interaction plays a major role on a smaller scale, where the sediment loads influence the evolution of salt-tectonic structures such as diapirs, canopies, salt nappes or fold belts. These can in turn influence the local sediment distribution and enable feedback mechanisms that are still poorly understood.

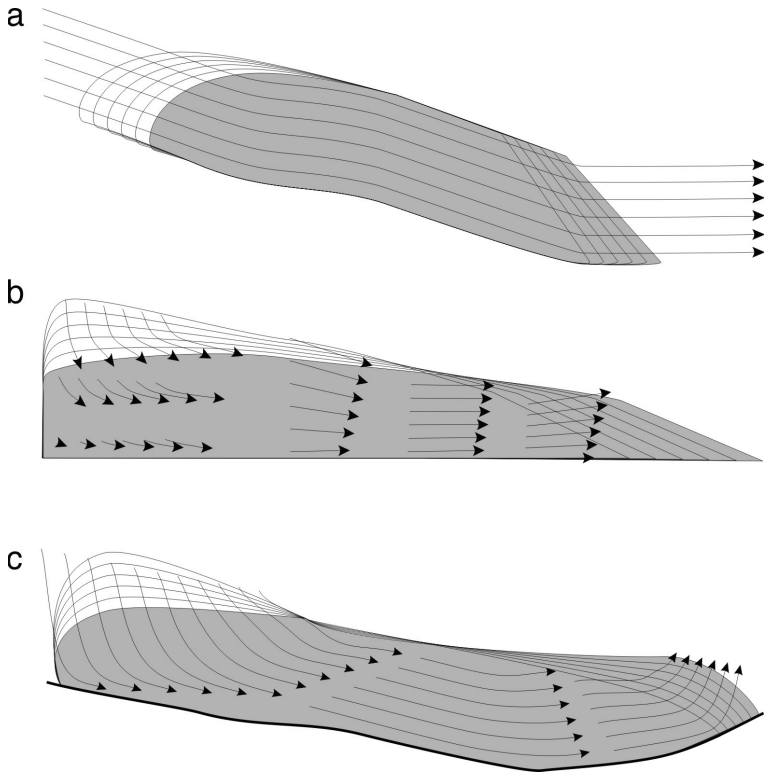

Figure 1.2: Modes of gravity-driven deformation. (a) Gravity gliding of rigid block, no internal deformation. (b) Gravity spreading, rock mass deforms internally. (c) Combined gravity-driven deformation. From *Rowan et al.* (2004).

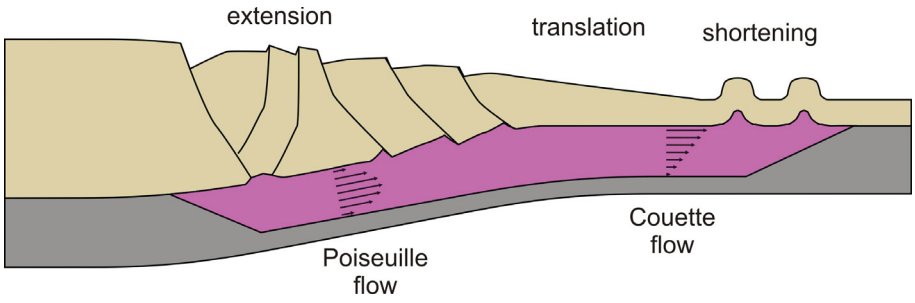

Figure 1.3: Schematic of gravity spreading showing domains of extension, translation and shortening as well as dominant viscous flow in the salt layer. After *Letouzey et al.* (1995).

1.3 Background II: Salt Tectonics and the Northwestern Gulf of Mexico

The Gulf of Mexico(GoM), together with the adjacent coastal domains, has an exceptionally long history of salt-tectonic research. The salt basin comprises a variety of structures such as diapirs, canopies, salt nappes, salt tongues, and deep-water fold belts, which formed during multiple phases of extensive gravity spreading (*Peel et al.*, 1995).

The Gulf of Mexico salt basin extends almost 500 km along the northern margin of the gulf and reaches widths of nearly 300 km (Figure 1.4). The syn- to post-rift Louann Salt is commonly interpreted to have been deposited as a continuous layer during the Late Jurassic (*Diegel et al.*, 1995; *Peel et al.*, 1995). It is overlain by a thick unit of Cretaceous deep-water carbonates and shales (*Fiduk et al.*, 1999; *Trudgill et al.*, 1999). Subsequent Cenozoic shelf progradation and siliciclastic sediment deposition led to multiple phases of salt mobilization, which created the structures of diapirs, canopies, and fold belts observed today (*Diegel et al.*, 1995, Figure 1.5).

The northwestern Gulf of Mexico has experienced at least four phases of gravity spreading (*Peel et al.*, 1995; *Radovich et al.*, 2007): The landward domain is dominated by extensional faults of different age (Late Cretaceous to Miocene) soling out at the allochthonous salt level. In the Eocene, large-scale folds developed landward of the future Perdido Fold Belt (*Peel et al.*, 1995) and a vast canopy formed, whose evolution is investigated in Chapter 5). This allochthonous salt layer served as a décollement layer during the Oligocene. At the deep-water end of the salt basin is the Perdido Fold Belt, a 4.5 km thick, salt-cored structural domain that formed during the youngest (late Oligo-Miocene) gravity-spreading phase. The circumstances that led to its gravitationally-driven formation are addressed in Chapters 2, 3 and 4.

Mirroring advances in salt-tectonic concepts and drilling technology, exploration and research first focussed on the evolution of onshore diapirs and their surrounding structures (*Jackson*, 1995), then expanded to similar structures in the shallow offshore domains. During the 1970s and 1980s the GoM became the world's frontier in deep-water exploration with targets mainly located within Miocene structures (minibasins, diapirs) (*Whaley*, 2006). The hydrocarbon potential of thick sedimentary sequences in the ultra-deep water regions of the outer continental shelf was only recognized in the late 1990s, and first successful petroleum discoveries were made in the Atwater fold

belt of the eastern GoM (*Hall*, 2002). It was then discovered that the Eocene Lower Wilcox Formation, which also constitutes the host rocks to most onshore petroleum discoveries in the western Gulf Coast region, extended more than 400 km offshore as an extensive basin-floor fan system containing massive sand-rich turbidite sections. The first successful discovery from the deep-water Wilcox Formation took place in 2001 in an anticline of the Perdido Fold Belt (*Meyer et al.*, 2005). Continued exploration of the deep-water fold belts of the GoM ensued, accompanied by new insights in the salt-tectonic and sedimentary evolution of this enormous salt basin.

The phase of exploration of the deep-water fold belts of the northwestern GoM partly occurred coevally with the research of the PhD study presented here. The new data and insights obtained by the hydrocarbon industry are mostly not publicly available and could therefore only to a limited degree be incorporated into this research. Nevertheless, new insights gathered from recent publications and at conferences were integrated in our research projects, expanding the knowledge about salt structures at the outer limit of salt basins and current hydrocarbon exploration. In this thesis, I investigate the salt-tectonic evolution of the northwestern Gulf of Mexico beginning with the youngest, best-known structures and going back in time to the older, less well-known structures.

1.4 Background III: Numerical Modeling in Salt Tectonics

Research in salt tectonics has employed a growing number of methods, starting with geological mapping, later incorporating among others drilling results, seismic mapping and gravity modeling. The first analogue experiments in salt tectonics investigated diapir evolution by modeling salt and sediments as two fluids of different densities (*Nettleton*, 1934). Analogue modeling has since played a key role in understanding of salt tectonics and experiments advanced to elaborate 3-dimensional models using silicon putty and sand to represent viscous salt and brittle overburden, respectively (e.g. *Vendeville and Jackson*, 1992; *Weijermars et al.*, 1993; *Ge et al.*, 1997; *Costa and Vendeville*, 2002; *Krezsek et al.*, 2007).

The early applications of numerical methods in salt-tectonic research also focussed on the evolution of diapirs through Rayleigh-Taylor instabilities between two viscous fluids of different densities (*Schmeling*, 1987; *Zaleski and Julien*, 1992; *Poliakov et al.*,

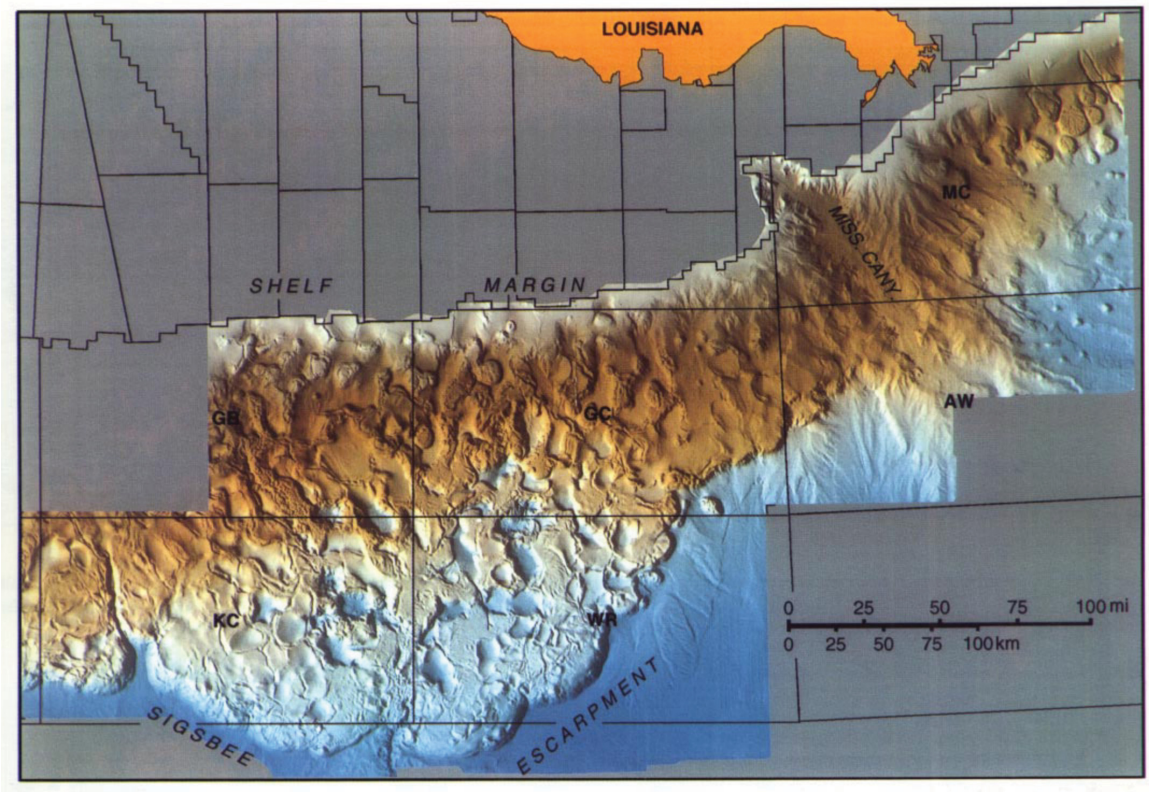

Figure 1.4: Bathymetry of the northern Gulf of Mexico illustrating the extent of allochthonous salt and its superposed sedimentary structures. Data are from the NOAA multibeam bathymetric survey. KC = Keathley Canyon, GB = Garden Banks, GC = Green Canyon, WR = Walker Ridge, MC = Mississippi Canyon, and AW = Atwater. From *Diegel et al.* (1995)

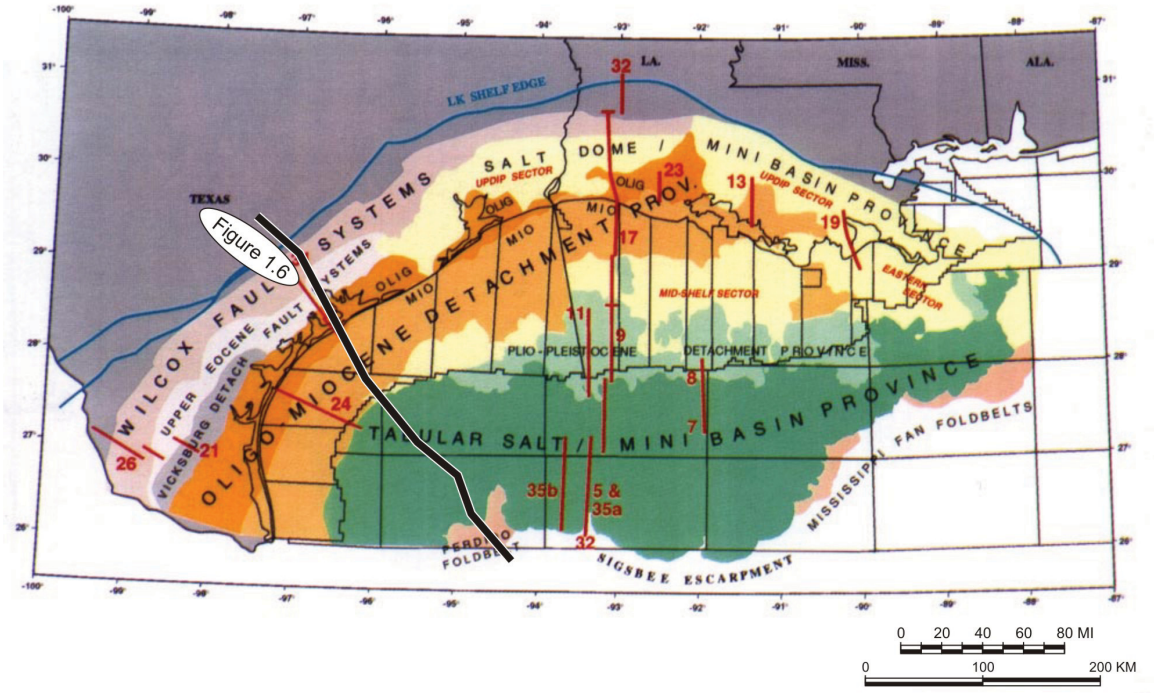

Figure 1.5: Tectono-stratigraphic provinces of the northern Gulf of Mexico Basin. From *Diegel et al.* (1995)

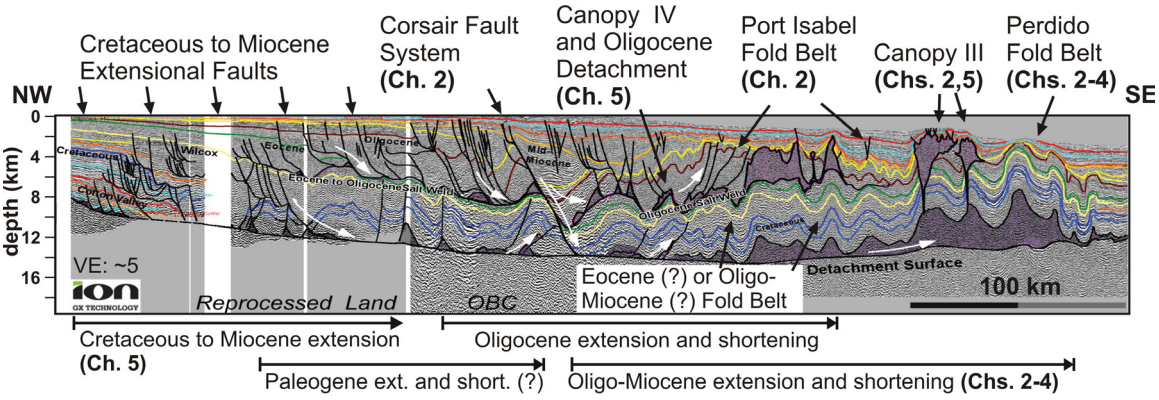

Figure 1.6: Regional NW-SE trending seismic profile from the northwestern Gulf of Mexico extending from onshore into deep water (from *Radovich et al.*, 2007). Large-scale gravity-spreading structures (extensional faults, allochthonous salt, fold belts) are indicated as well as the thesis chapters addressing their evolution. Location is shown in Figure 1.5. More detailed figure descriptions can be found in the original publication and Figure 5.2.

1993b). Following the paradigm shift in salt tectonics of the early 1990s, when the importance of the salt's low strength and high mobility, and the effect of lateral differential pressure was recognized, numerical models were used to quantitatively address the effects of brittle overburden on diapirism (*Schultz-Ela et al.*, 1993; *Poliakov et al.*, 1993a; *Daudre and Cloetingh*, 1994; *Poliakov et al.*, 1996). The insight that extension provides a favorable mechanism for diapir initiation was first demonstrated by analogue models and subsequently confirmed with numerical modeling approaches (*Poliakov et al.*, 1993a; *Daudre and Cloetingh*, 1994). With the advance of computational technology, numerical models progressed towards studies of more complex structures (e.g. *Chemia et al.*, 2008) or regional salt-tectonic evolution (e.g. *Gemmer et al.*, 2004, 2005).

Numerical modeling provides an excellent tool for investigating the evolution of salt-tectonic structures, because it encompasses the entire evolution of the structures and is subject to very few restrictions regarding parameter values and scales, though it is commonly limited to 2D studies. Geological and geophysical studies only capture a snapshot of the current situation which evolved under a certain set of circumstances. Such studies are nevertheless essential for constraining any modeling experiment.

Analogue models can capture the three-dimensional evolution of salt-tectonic structures but are more restricted to a certain range of parameter values than numerical models. It is furthermore difficult to include processes like water loading, compaction or pore-fluid pressure effects, but new methods are being developed in these fields (*Mourgues and Cobbold*, 2003). For the two-dimensional numerical models presented here, it is important that the investigated, first-order, large-scale processes and structures of a continental margin do not vary significantly along strike, because out-of-plane salt flow and deformation cannot be captured.

1.4.1 Geodynamic Modeling with SOPALE

In this section I briefly explain the concepts and approaches of the modeling method used in this thesis. A more thorough and mathematical description is given in Chapters 2 and 3, and more details can be found in *Fullsack* (1995) and *Morency et al.* (2007).

In geodynamic modeling, we are interested in the bulk behavior of a material, rather than in the individual behavior of microscopic structures (grains, minerals, molecules). This is achieved through the concepts of continuum mechanics by describing the materials as homogenous solids or fluids. The corresponding governing equations accurately capture the overall behavior as long as the length and time scales involved are sufficiently large. The governing equations describe the conservation of mass, momentum and energy and additionally include constitutive equations. The latter describe the material-dependent response to external forces, such as the rheological behavior during mechanical deformation.

For geodynamic deformation, which is characterized by low velocities and high viscosities, a simplified equation of motion can be derived from the conservation laws: Inertial forces are negligibly small compared to the viscous forces (low Reynolds number), and the general equation for fluid flow (Navier-Stokes) can be reduced to that of creeping flow (Stokes flow). Allowing for incompressibility further simplifies the equation of motion, which together with the equation for conservation of mass, represents the fundamental equations in geodynamic modeling.

The material's rheology is described as the relation of stress to strain. This relation is linear in the most basic case, which is here used to describe the rheology of viscous salt. Frictional-plastic behavior is approximated by introducing a Drucker-Prager yield criterion. Deformation then occurs only when deviatoric stresses reach the yield stress, which depends on the mean stress, the effective internal angle of friction, and cohesion.

The governing partial differential equations need to be solved for a number of different materials in an often complex and deforming model domain. In the finite element technique, the model domain is subdivided into numerous components of simple geometries and uniform properties, for each of which a solution for the complex partial differential equations can be approximated. The resulting large set of simplified, interdependent equations is then solved simultaneously for all elements. Boundary conditions are given as the behavior of velocities and stresses at the edges of the model domain and are necessary to constrain the solution.

The software SOPALE used in this thesis solves the governing equations for the displacement velocities for a given timestep (*Fullsack*, 1995). These velocities are

applied to update the position of the model material before the calculations of the next timestep are performed. The model uses an Arbitrary Lagrangian-Eulerian (ALE) formulation, in which computations are made on an Eulerian grid that adapts vertically to respond to the evolving model geometry. The material properties are tracked and updated using a set of moving Lagrangian particles. This approach allows calculations to be made for very large deformation (*Fullsack*, 1995).

In Chapters 3 and 4, the calculations are expanded to include compaction-induced fluid-pressure generation (Figure 1.7, *Morency et al.*, 2007). The principle of effective stress is employed (*Terzaghi*, 1936, 1943), which states that pore fluids bear a part of the load of the overlying sediment column and the remaining pressure is carried by the sediment matrix. This implies that porous sediments are effectively weakened by pore-fluid pressure.

Modeled sediment compaction includes the effects of both mechanical and viscous compaction, which change the bulk volume of the porous sediment. The volumetric strain rate in turn controls the fluid flow in porous media, here approximated as Darcy fluid flow.

The equations for compaction and fluid flow are coupled to the equations of purely mechanical deformation through the displacement velocities as well as the effective pressure, which controls mechanical failure and sediment compaction. Iterative solving is required to obtain consistent values for the velocity and pressure fields (*Morency et al.*, 2007). The porosity is updated after the iterations converge.

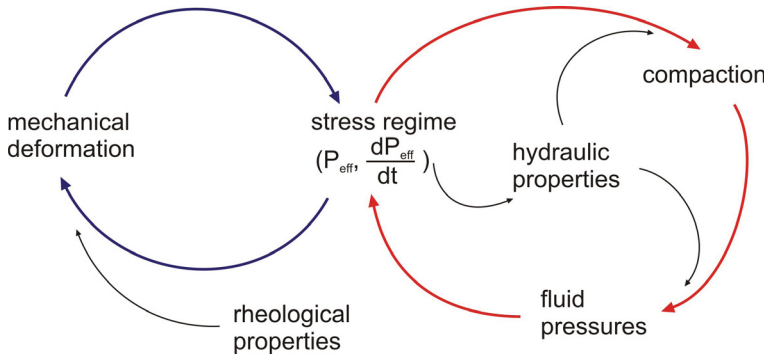

Figure 1.7: Schematic illustrating the coupling of mechanical deformation to compaction-driven pore-fluid generation via the effective stress.

1.5 Organization and Contributions

This thesis comprises four paper-style chapters as well as three appendices describing the salt-tectonic vocabulary used in this thesis as well as additional analytical and numerical work. Chapter 2, *Factors Controlling the Evolution of the Perdido Fold Belt, Northwestern Gulf of Mexico, Determined from Numerical Models*, has been published in the Journal of Tectonics (*Gradmann et al.*, 2009). Additional analytical and numerical calculations that were not included in the chapter are given in Appendix B. Chapter 3 and 4, *Coupled Fluid Flow and Sediment Deformation in Margin-Scale Salt-Tectonic Systems: 1. Development and Application of Simple, Single-Lithology Models* and *Coupled Fluid Flow and Sediment Deformation in Margin-Scale Salt-Tectonic Systems: 2. Layered Sediment Models and Application to the Northwestern Gulf of Mexico* are two companion papers that have been published in the Journal of Tectonics this year (*Gradmann et al.*, 2012; *Gradmann and Beaumont*, 2012). In Appendix C, software modifications that have been tested and in parts included in the models of Chapters 3 and 4 are discussed. Chapter 5, *Numerical Modeling Study of Mechanisms of Salt Canopy Evolution and their Application to the Northwestern Gulf of Mexico*, is currently in preparation to be submitted to a peer-reviewed journal. The final chapter summarizes and discusses the thesis results with respect to the key salt-tectonic issues addressed in this thesis: (1) initiation of gravity spreading above salt on continental margins, (2) development of salt tectonic structures (fold belts, canopies, diapirs), and (3) the salt-tectonic evolution of the northwestern Gulf of Mexico.

1.5.1 Chapter 2: *Factors Controlling the Evolution of the Perdido Fold Belt, Northwestern Gulf of Mexico, Determined from Numerical Models*

In the second chapter, the evolution of the Perdido Fold Belt, a large-scale, deep-water structure located at the distal end of the large salt basin in the northwestern GoM is examined. An analytical calculation of the stability conditions of a salt-bearing continental margin is presented, and its implications applied to the northwestern Gulf of Mexico. Subsequently, 2-D finite element numerical models are employed to study the evolution of the Perdido Fold Belt as a gravity-driven fold belt, both

in a local context and in the context of the larger-scale passive margin influenced by adjacent allochthonous salt structures. The sensitivity of fold-belt evolution to different factors such as sediment strength, salt thickness and viscosity, and sub-salt basement geometry are investigated. The results have been published in the Journal of Tectonics with Chris Beaumont and Markus Albertz as second and third author, respectively (*Gradmann et al.*, 2009).

The stability analysis is based on the work of *Gemmer et al.* (2005). S. Gradmann extended their theory to include local isostatic balancing of the continental-margin system, which becomes important as the load of a prograding sediment wedge induces a landward tilt of the base of the basin and thereby enhances the stability of the system. The software for the 2-D numerical models was developed by *Fullsack* (1995) and subsequently extended and improved by the Dalhousie Geodynamics Group. S. Gradmann was primarily responsible for the design, computation and analysis of the numerical models of the northwestern Gulf of Mexico, as well as for the writing of the corresponding manuscript. C. Beaumont contributed to all these aspects with frequent and long discussions and many helpful ideas. M. Albertz was involved in the design and discussion of the first set of models.

1.5.2 Chapters 3 and 4: *Coupled Fluid Flow and Sediment Deformation in Margin-Scale Salt-Tectonic Systems: 1. Development and Application of Simple, Single-Lithology Models* and *Coupled Fluid Flow and Sediment Deformation in Margin-Scale Salt-Tectonic Systems: 2. Layered Sediment Models and Application to the Northwestern Gulf of Mexico*

Chapters 3 and 4 are two companion papers that investigate the effects of compaction-generated fluid-pressure on sediment strength and the associated gravity-driven deformation in a continental-margin salt-tectonic system. A new finite element software is used that expands on the earlier version (*Fullsack*, 1995) by including dynamic calculations of compaction-driven pore-fluid pressure generation (*Morency et al.*, 2007).

Chapter 3 explores the overpressuring behavior of sandstone-type and shale-type material undergoing both viscous and mechanical compaction and the associated effects on sediment strength and margin stability. In Chapter 4, the cases of sedimentary sequences comprising layers of both sandstone-type and shale-type lithologies

are investigated and these more realistic scenarios are applied to the setting of the northwestern Gulf of Mexico, thus expanding on the stability criteria developed in Chapter 2 (*Gradmann et al.*, 2009). Furthermore, an improved formulation of viscous compaction is developed, which allows for stronger porosity and temperature dependence of this process. Both papers have been published in the Journal of Tectonics. C. Beaumont and S. Ings are second and third author of the first paper, respectively (*Gradmann et al.*, 2012), the second paper is a collaboration of S. Gradmann and C. Beaumont (*Gradmann and Beaumont*, 2012).

S. Gradmann prepared and conducted all model experiments. This included the identification of a suitable parameter space for modeling compaction and overpressuring of different sedimentary material (salt- and shale-type) as well as modifications of the software to allow for amendments of the compaction process. The compilation and interpretation of the model results was to a large extent performed by S. Gradmann. The manuscripts of both papers were written by S. Gradmann, aided by C. Beaumont. C. Beaumont contributed significantly to the discussion and interpretation of the model results, as well as to the design of numerous model experiments. S. Ings was involved in the design and execution of the first model experiments (Chapter 3) and contributed through many discussions to their scientific interpretation and analysis.

1.5.3 Chapter 5: *Numerical Modeling Study of Mechanisms of Salt Canopy Evolution and their Application to the Northwestern Gulf of Mexico*

The focus of the sixth chapter lies again on the evolution of salt-tectonic structures in the northwestern Gulf of Mexico. Three mechanisms are investigated that may lead to salt-canopy formation; and their respective implications for the canopy's structural evolution and style are compared to the Eocene salt canopy in the northwestern Gulf of Mexico. This structure evolved in the central part of the salt basin, landward of the Perdido Fold Belt. In addition to canopy formation, this chapter also addresses the development of diapirs that evolve in the absence of regional tectonic stresses and may serve as precursory structures for canopy development. A new diapir mechanism driven by uneven sedimentation is introduced, preliminary numerical tests are performed, and a quantitative analytical treatment of the mechanism is provided.

The regional models of canopy evolution were designed, discussed and analyzed by S. Gradmann and C. Beaumont. The diapir models were primarily developed by S. Gradmann who also conducted all model experiments. The quantitative analysis of sedimentation-induced diapirism was performed by S. Gradmann. The manuscript preparation was the work of S. Gradmann with the help of C. Beaumont and others.

1.5.4 Appendix A: *Glossary of Salt-Tectonic Terminology*

This appendix comprises a lists of brief definitions of the salt-tectonic terminology used in this thesis.

1.5.5 Appendix B: *Stability Analysis of Continental Margin System over Viscous Substratum*

This appendix expands and completes the analytical calculations of margin stability presented in Chapter 2 (*Gradmann et al.*, 2009). The effects of isostatic balancing of a salt-sediment system are discussed and analytical and numerical results are compared.

S. Gradmann performed the analytical calculations and designed, computed and analyzed the numerical models. C. Beaumont contributed with frequent discussions and helpful ideas.

1.5.6 Appendix C: *Addendum to Chapters 3 and 4*

In this appendix, I explain several modifications of the software used in Chapters 3 and 4, which couples compaction-induced fluid pressure generation to mechanical deformation. These modifications address the controlling and limiting decompaction and ultra-high pore-fluid pressure (through a mechanism mimicking fault valving).

Chapter 2

Factors Controlling the Evolution of the Perdido Fold Belt, Northwestern Gulf of Mexico, Determined from Numerical Models

This chapter has been published as "*Gradmann, S., C. Beaumont, and M. Albertz (2009), Factors controlling the evolution of the Perdido Fold Belt, northwestern Gulf of Mexico, determined from numerical models, Tectonics, 28(2).*" Reproduced by permission of American Geophysical Union. Minor editorial corrections have been applied.

2.0 Abstract

The Perdido Fold Belt (PFB) is a prominent salt-cored deep-water structure in the northwestern Gulf of Mexico. It is characterized by symmetric, kink-banded folds of a ca. 4.5 km thick pre-kinematic layer and its vicinity to the extensive Sigsbee Salt Canopy. We use 2D finite element numerical models to study the evolution of the PFB as a gravity-driven fold belt both in a local context and in the context of the larger-scale passive margin, influenced by adjacent allochthonous salt structures. We show that parameters such as overburden strength, salt geometry or salt viscosity determine timing, extent and location of the modeled fold belt. Simplified models of the Gulf of Mexico show that toe-of-slope folding is a viable mechanism to develop diapirs in the deep salt basin, and to delay folding of the distal overburden. In this scenario, the PFB likely represents the terminal folding of a much larger, diachronously formed fold belt system.

2.1 Introduction

The Perdido Fold Belt (PFB) in the northwestern Gulf of Mexico (Figures 2.1-2.3) is a deep-water salt-tectonic contractional structure that has recently become a focus

of intensive hydrocarbon-related studies, but still remains insufficiently understood. It is one of several deep-water fold-and/or-thrust belts that are known from several continental margins worldwide including the Gulf of Mexico (Atwater (or Mississippi Fan) Fold Belt, Perdido Fold Belt, Mexican Ridges, Port Isabel Fold Belt) (*Weimer and Buffler*, 1992; *Peel et al.*, 1995; *Fiduk et al.*, 1999; *Trudgill et al.*, 1999; *Rowan et al.*, 2000; *Wu and Bally*, 2000; *Marton et al.*, 2000; *Hall*, 2002; *Rowan et al.*, 2004), offshore Brazil (*Demercian et al.*, 1993; *Cobbold et al.*, 1995; *Mohriak et al.*, 1995; *Davison*, 2007), offshore Africa (*Morley and Guerin*, 1996; *Spathopoulos*, 1996; *Cramez and Jackson*, 2000; *Marton et al.*, 2000; *Rowan et al.*, 2004; *Fort et al.*, 2004; *Hudec and Jackson*, 2004) and several others (*Rowan et al.*, 2004, and references therein). These fold-and-thrust belts are generally interpreted to be the result of gravity spreading and/or gliding of sedimentary overburden above a weak substratum of salt (strictly evaporites) or overpressured shale, which produces linked proximal extensional and distal contractional domains. The fold-and-thrust belts vary in structural style (fault-bend folds, concentric folds, kink-banded folds, symmetric vs. asymmetric folds, imbricate thrusts), overburden thickness, overburden composition, and the location and timing of the deformation relative to other processes that affect the large scale evolution of the margin (*Rowan et al.*, 2004). Fold belts are one of a range of deep-water contractional salt-tectonic structures (including e.g. salt tongues, canopies and inflated salt massifs) that develop at the distal end of a gravity-driven spreading system (*Tari et al.*, 2003). Currently, it is not known which conditions favor the evolution of one versus another structure.

In addition to their significance for hydrocarbon exploration, rifted margin deep-water fold-and-thrust belts are of scientific interest, in particular in regard to the features and processes that control their initiation and evolution. These features and processes, which may encompass large parts of the margin, include a number of factors such as the geometry of the extended basement, the regional dip owing to thermal and isostatic subsidence, the evolving distribution of sediments, their bulk strength and density, and the viscosity and density of the salt. An improved understanding of the role of these factors can help to constrain conditions that lead to failure of the system and help predict the associated spreading velocity, the way in which the linked extensional/contractional domains propagate diachronously seaward through

the system, and the related development of smaller-scale structures such as folds, diapirs and canopies. The PFB is among the best studied salt-cored deep-water fold belts and is the one with the most published work and publicly available data.

The PFB is located at the seaward limit of the autochthonous Middle Jurassic Louann Salt (Figure 2.1) and comprises highly symmetric, salt-cored folds over a region of ca. 80 by 100 km (Figures 2.2-2.3). Only one major phase of shortening and folding of less than 10 Ma duration occurred during late Oligocene-early Miocene in the PFB region, which resulted in relatively simple structures with very little syn-deformational sedimentation. Several unique features distinguish it from many other deep-water fold belts including the large thickness (4.5 km) of the pre-kinematic Late Jurassic to Miocene section together with the absence of earlier folding, the highly symmetric kink-banded folds, the seaward tilt of the entire fold belt, the almost synchronous evolution of its folds, and its vicinity of the large allochthonous salt structure of the Sigsbee Canopy (*Trudgill et al.*, 1999; *Rowan et al.*, 2000) (Figures 2.2 and 2.3). Despite the relative simplicity of the PFB, its relationship to the older, more landward depositional regimes and the evolution of allochthonous salt is complex and remains subject to discussion.

The goal of this paper is to explain the first-order structures of the PFB in a dynamical context by comparing its presently understood evolution with those of a series of finite element model experiments. We address the following questions that are fundamental to the evolution of the PFB.

1. What horizontal forces and overburden strengths were necessary in order to fold such a thick (ca 4.5km) sediment layer by gravity spreading alone?

2. What determined the almost synchronous evolution of the PFB within <10 Ma?

3. Did salt geometry, specifically thickness, taper and possible sub-salt basement steps, influence the formation of the PFB?

4. When and how did the inflation of the underlying salt and tilting of the PFB take place?

5. How may salt have been expelled into the Sigsbee Canopy and similar precursory structures and what role did this allochthonous salt play in the PFB evolution?

The intent of the research reported here is an assessment of the factors that controlled the formation of the Perdido Fold Belt specifically, plus an initial evaluation of the contraction and folding hypothesis for the precursor regional development of the northwestern Gulf of Mexico. The evolution of the western Gulf of Mexico is complex and involved several superimposed phases of deformation landward of the PFB, and there are a range of interpretations of the observations concerning these phases which is discussed in section 2.2. The level of uncertainty therefore increases as time recedes. This makes modeling in the form of a complete forward simulation of the evolution of the system unattractive because initial conditions and early evolution cannot be established with certainty. Instead, we choose to work backwards and start with a limit analysis (section 2.3) and a simplified experiment designed only to investigate the formation of the PFB (section 2.5). We then vary these models to test some of the possible conditions that may have existed prior to folding of the PFB (section 2.6) and then consider the regional precursor phase (section 2.7).

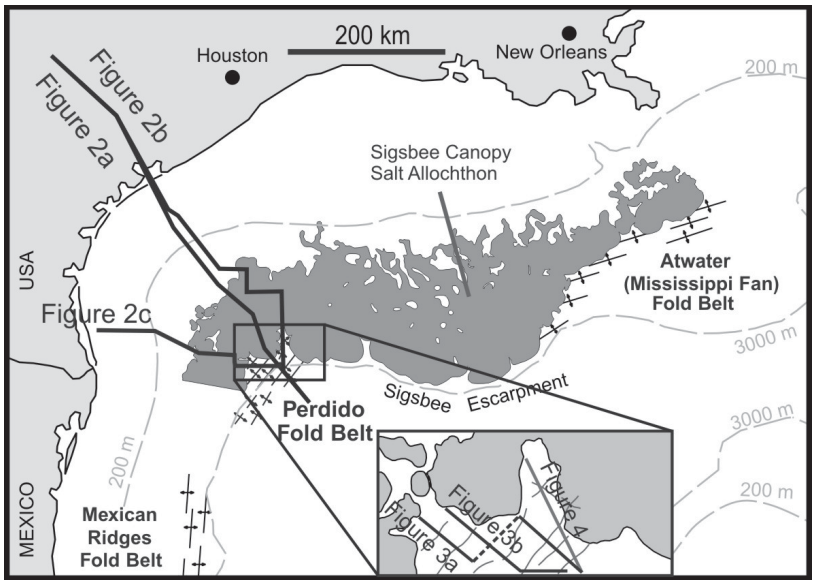

Figure 2.1: Regional map of northern Gulf of Mexico showing the Cenozoic fold belts and the extent of allochthonous salt after *Fiduk et al.* (1999), salt outline is from *Simmons* (1992). The locations of the cross sections shown in Figures 2.2, 2.3 and 2.4 are indicated.

2.2 The Perdido Fold Belt

2.2.1 Description of the Perdido Fold Belt

The PFB is situated in the northwestern Gulf of Mexico in water depths of 2-3 km (Figure 2.1). It occupies the 60-70 km wide region between the limit of the autochthonous Middle Jurassic Louann Salt and the allochthonous Sigsbee Salt Canopy, beneath which it continues for another 20-30 km (*Peel et al.*, 1995; *Hall*, 2002; *Rowan et al.*, 2004) (Figures 2.2 and 2.3). *Radovich et al.* (2007a) interprets another 100 km wide landward continuation of the fold belt. The northern section of the PFB, which is located in US waters, is well studied with multiple geophysical surveys (*Weimer and Buffler*, 1992; *Trudgill et al.*, 1999; *Camerlo and Benson*, 2006; *Meyer et al.*, 2007; *Radovich et al.*, 2007a). The southern section, located in Mexican waters, is rarely referred to in the public literature. Several wells have been drilled into the Perdido folds in the last decade (*Meyer et al.*, 2007). None of them penetrated to the depth of the autochthonous Louann Salt but several were successful discoveries of hydrocarbon reserves.

In cross section, the PFB comprises a band of angular folds with wavelengths of ca. 10 km (Figure 2.3) and a seaward dipping fold envelope of ca. 5°. This dip tilts the entire fold belt and is a result of the seaward tapering of the underlying salt wedge; the fold amplitude decreases only marginally. The tilt of the fold belt decreases to 1-2° in the distal 15-20 km, leading to a bend in the fold envelope (Figure 2.3b). It should be noted that the seismic cross section shown in Figure 2.3b does not run perpendicular to the fold axis in the distal part and therefore displays larger apparent wavelengths. Furthermore, eight individual folds have been identified in the recent work of *Camerlo and Benson* (2006), whereas previous studies identified fewer folds (*Trudgill et al.*, 1999; *Fiduk et al.*, 1999; *Rowan et al.*, 2000)(inset of Figure 2.1).

The folds are highly symmetric, occasionally leaning landward or seaward. The folds are separated by narrow zones of deformation, which were shown to be kink bands by *Camerlo and Benson* (2006). This supersedes the earlier interpretation of fault-bound detachment folds (e.g. *Weimer and Buffler*, 1992; *Peel et al.*, 1995; *Trudgill et al.*, 1999).

The stratigraphic column can be divided into pre-, syn- and post-kinematic sections. The pre-kinematic section remains at ca. 4.5 km thickness throughout the fold belt. It consists of shallow and deep marine carbonates and marls (∼2.1 km), chalks and marls (∼0.5 km), and deep marine muds and sands, e.g. turbidites (∼2.0 km) (*Rowan et al.*, 2000). Deep marine sediments also form the thin, syn-kinematic layer present in the synclinal regions (<0.4 km) as well as the post-kinematic, Neogene sequence (∼2.0 km). Other estimates of the total thickness of the pre-kinematic layer can be obtained from pre-stack depth migrated seismic sections (*Meyer et al.*, 2005; *Camerlo and Benson*, 2006; *Waller*, 2007; *Radovich et al.*, 2007a) and give values ranging between 4.3 km and 5.4 km. Indicators for salt acting as a very weak detachment are the high symmetry of folds as well as their magnitude, indicating flow of the substrate from beneath synclines into anticlines (*Rowan et al.*, 2000). Out-of-plane salt flow has probably not played a significant role since the fold structures, including the salt thickness, are to first order similar along strike.

2.2.2 Evolution of the Northwest Gulf of Mexico Margin and its Relationship to the Perdido Fold Belt

The Gulf of Mexico opened as a rift basin in the Late Triassic-Early Jurassic. The autochthonous Louann salt was deposited in Middle Jurassic above a synrift sedimentary sequence. The Cretaceous was dominated by carbonate deposition, clastic sediments followed. During the Cenozoic the shelf edge of the continental margin prograded by more than 200 km to its present location (*Fiduk et al.*, 1999; *Galloway et al.*, 2000). Shelf progradation rates were on average 0.4 cm/a but locally reached values of ca. 1.0 cm/a during episodes of enhanced sediment input in the middle Eocene, Oligocene and middle Miocene (*Galloway et al.*, 2000). Sediment input came from the Hudson and Rio Grande embayment located to the north and west of the PFB region, respectively. In the middle Miocene, sediment input ultimately shifted farther east toward the Louisiana shelf leaving the northwestern Gulf of Mexico with pelagic to hemipelagic sedimentation (*Fiduk et al.*, 1999).

As a result of the deposition of prograding shelf and slope sediments onto the autochthonous salt basin, the sedimentary overburden failed and gravity spreading set in, leading to landward extension and seaward shortening (Figure 2.2). Multiple

Figure 2.2: Regional cross sections from the northwestern Gulf of Mexico showing large scale gravity spreading structures (extensional faults, allochthonous salt, fold belts). Locations are shown in Figure 2.1. (a) NW-SE trending seismic profile extending from onshore into deep water from *Radovich et al.* (2007b) (published with permission of ION/GXT and SEI). The approximate sediment thickness at the end of Oligocene of ca. 10 km is marked. More detailed figure descriptions can be found in the original publication and Figure 5.2. (b) NW-SE trending profile extending from onshore into deep water (F. Peel, personal communication, 2007, after *Peel et al.*, 1995). (c) W-E trending profile across the offshore region of the continental margin from *Rowan et al.* (2004).

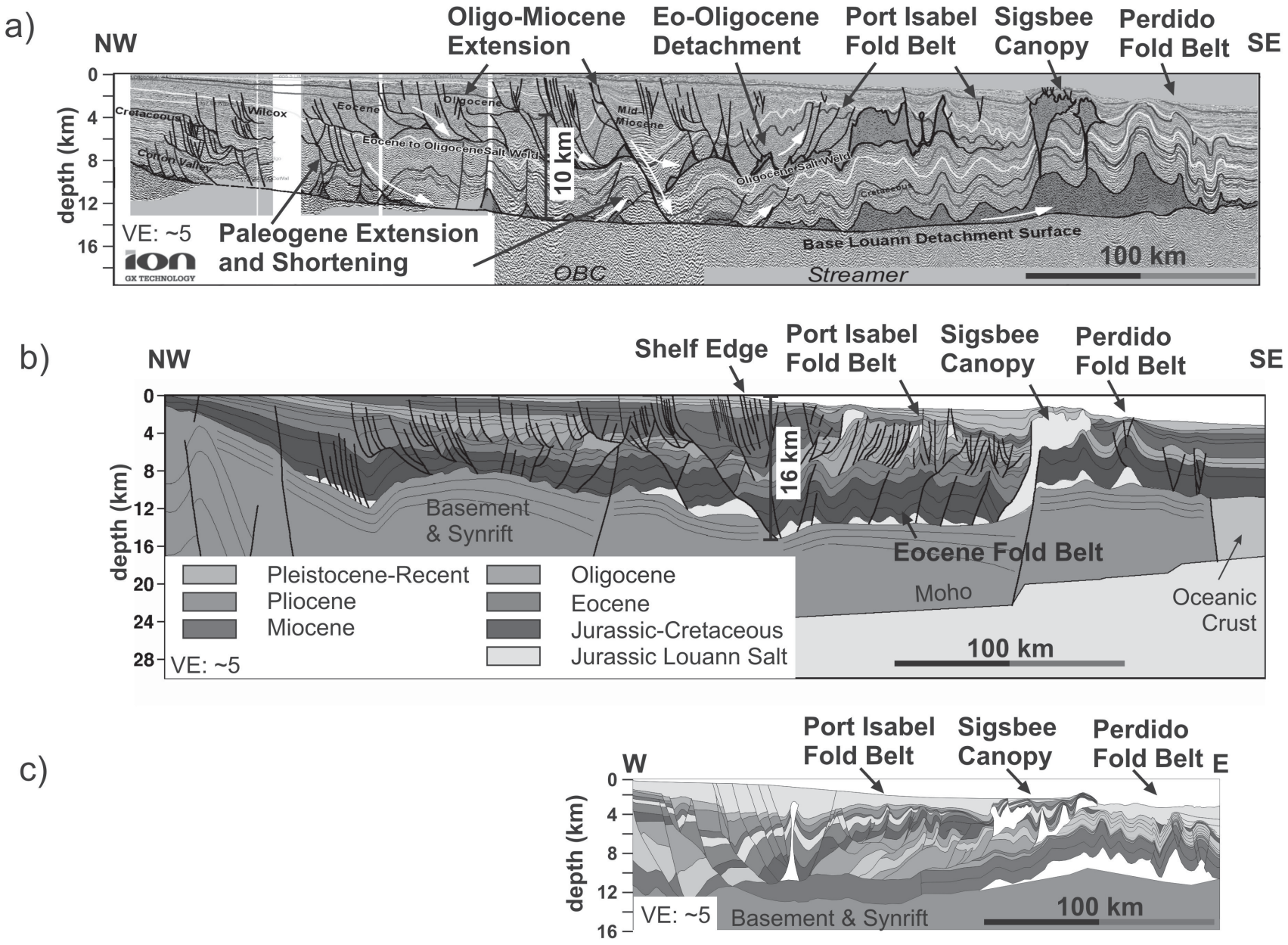
a)
NW
SE
Oligo-Miocene Extension
Eo-Oligocene Detachment
Port Isabel Fold Belt
Sigsbee Canopy
Perdido Fold Belt
depth (km)
0
4
8
12
16
Cretaceous
Wilcox
Clifton Valley
Eocene
Oligocene
Mid-Miocene
Eocene to Oligocene Salt Weld
10 km
Oligocene Salt Weld
Cretaceous
Base Louann Detachment Surface
VE: ~5
Paleogene Extension and Shortening
OBC
Streamer
100 km
b)
NW
SE
Shelf Edge
Port Isabel Fold Belt
Sigsbee Canopy
Perdido Fold Belt
depth (km)
0
4
8
12
16
20
24
28
16 km
Basement & Synrift
Eocene Fold Belt
Moho
Oceanic Crust
Pleistocene-Recent
Pliocene
Miocene
Oligocene
Eocene
Jurassic-Cretaceous
Jurassic Louann Salt
VE: ~5
100 km
c)
W
E
Port Isabel Fold Belt
Sigsbee Canopy
Perdido Fold Belt
depth (km)
0
4
8
12
16
VE: ~5
Basement & Synrift
100 km

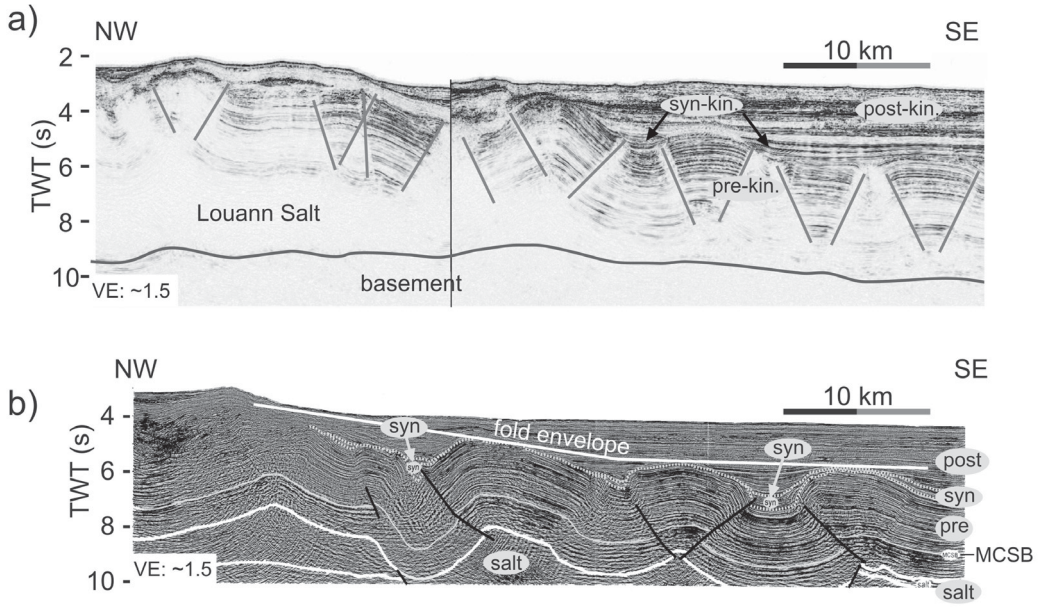

Figure 2.3: Interpreted seismic lines across the PFB. See Figure 2.1 for locations. (a) Seismic line across the entire extent of PFB from *Camerlo and Benson* (2006). (b) Seismic line across the PFB from *Rowan et al.* (2000). Horizons shown are the Mid Cretaceous Sequence Boundary (MCSB, now interpreted to be top Cretaceous; *Winker*, 2004) and those that bound major tectonostratigraphic units.

extensional fault systems in the Mesozoic to Cenozoic sediments have been interpreted as evidence of several separate phases of gravity spreading (*Diegel et al.*, 1995; *Peel et al.*, 1995; *Trudgill et al.*, 1999; *Radovich et al.*, 2007a). *Peel et al.* (1995) identified a Paleocene-early Eocene, a middle-late Eocene, an early Oligocene-early Miocene and a late Oligocene-middle Miocene extensional phase, each occurring seaward of the previous one. The total upslope extension of the northwestern Gulf of Mexico continental margin is estimated to be about 80 km (*Peel et al.*, 1995). Only two compressional settings have been unambiguously identified: the distal PFB itself and the Port Isabel Fold Belt, located above an allochthonous salt detachment (Figure 2.2). Recent studies (*Rowan et al.*, 2005; *Radovich et al.*, 2007a) link the Port Isabel Fold Belt to Oligocene-early Miocene extension, the PFB to late Oligocene-mid Miocene extension. The extension during the earlier phases of shelf failure must have been accommodated in some manner further landward; the PFB only accounts for 5-10 km of shortening (*Peel et al.*, 1995; *Trudgill et al.*, 1999), and pre-Oligocene

deformation is absent in the distal sediments. *Peel et al.* (1995) describes an earlier, very gently folded contractional belt that extends more than 100 km landward of the Sigsbee Canopy in the Jurassic to Eocene unit (Figure 2.2b). They note, however, that this fold belt could not have accommodated all of the extension on the upper slope. More evidence for Cretaceous folding in the deeper part of the northern Gulf of Mexico basin has recently been given by *Philippe et al.* (2005), *Philippe and Guerin* (2006), *Guerin et al.* (2006), and *Radovich et al.* (2007a). Early shortening may have been overprinted by later extension, which makes it difficult to identify such structures. *Radovich et al.* (2007a) describes an almost 400 km wide fold belt at the autochthonous salt level that reaches from the present-day onshore region to the seaward pinch-out of the salt (Figure 2.2a). Here, the PFB appears to be only the distal end of this extensive fold belt that accommodated extension throughout the Cenozoic.

Interpretations by other authors (e.g. *Rowan et al.*, 2005) do not show the strong Cenozoic folding in the entire northwestern Gulf of Mexico. A salt canopy developed above this putative fold belt in late Eocene and later acted as a detachment surface for the Port Isabel Fold Belt. In addition to the allochthonous salt, Eocene shales were also involved in the evolution of this fold belt (*Diegel et al.*, 1995; *Peel et al.*, 1995; *Camerlo et al.*, 2004; *Rowan et al.*, 2004). While gravity spreading took place at the shallow allochthonous detachment in the late Oligocene-early Miocene, it must also have stepped back down onto the autochthonous salt level to create the PFB (*Rowan et al.*, 2005; *Radovich et al.*, 2007a).

The evolution of the two allochthonous salt bodies in the northwestern Gulf of Mexico in late Eocene and Oligo-Miocene times is discussed in section 2.7. The late Eocene paleocanopy served as a detachment for the Port Isabel Fold Belt and now extends for ca. 100 km. The allochthonous salt above and adjacent to the PFB is part of the extensive Sigsbee Salt Canopy that covers several thousand square kilometers in the northern Gulf of Mexico (Figure 2.1) but is reduced to a few coalesced or isolated salt tongues in the western section (*Fiduk et al.*, 1996, 1999) (inset of Figure 2.1). This salt body (for simplicity, here also called Sigsbee Canopy) seems to have moved very little distance from its feeder in the northwestern part (Figures 2.2a and 2.2b), whereas further to the south and east it migrated for 50-100 km (*Peel et al.*, 1995;

Decalf et al., 2004) (Figure 2.2c).

2.2.3 Folding Episodes and Timing of the Formation of the Perdido Fold Belt

Most of the published data do not show seismic markers at high enough resolution to constrain the timing of the folding of the PFB unambiguously and well data are also limited. Dates for the onset of the main folding phase range from early Oligocene (*Diegel et al.*, 1995; *Peel et al.*, 1995) to end of Oligocene (*Rowan et al.*, 2005; *Radovich et al.*, 2007a), the duration of folding ranges between 6 Ma (*Peel et al.*, 1995) and 15 Ma (*Fuqua*, 1990; *Diegel et al.*, 1995; *Peel et al.*, 1995), depending on the consideration of different phases of folding. Recent interpretations of modern seismic data put the folding activity in late Oligocene-mid Miocene time (*Rowan et al.*, 2005; *Radovich et al.*, 2007a). A detailed fold growth study by *Waller* (2007) identifies a more complex evolution of the PFB: The most landward anticline started to develop slowly in early Oligocene, followed by its seaward adjacent anticline. In the late Oligocene to early Miocene, deformation rapidly increased and created folds throughout the rest of the PFB area. A reactivation phase occurred during the Pliocene.

We use the most recent interpretation of *Waller* (2007) with a main phase of deformation lasting approximately 10 Ma in late Oligocene-early Miocene. The changes in interpreted time of deformation reflect the availability of more recent data. There is no fundamental disagreement about current interpretations (F. Peel, personal communication, 2008).

The late folding compared to the early onset of extension (Paleocene-Eocene) has been discussed extensively. *Peel et al.* (1995) identifies the early Eocene folding landward of the PFB (Figure 2.2b). *Trudgill et al.* (1999) explain the delay between early upslope extension and late downslope shortening by invoking the Sigsbee Salt Canopy as a buffer. A diapir-canopy system may have contributed to compensating the early landward extension by narrowing the feeder diapir, expelling salt onto the seafloor, and overthrusting the sediment layer. Later, once the feeders had been depleted and pinched off, the stress could be transferred farther seaward, beyond the region of the Sigsbee Canopy, and fold the undeformed sediments to form the PFB.

Another process that can accommodate some amount of early shortening is lateral compaction.

2.2.4 Inflation of the Perdido Fold Belt

Given that the pre-kinematic section of the PFB is tilted but of uniform thickness, the tilting accompanied by the inflation of the underlying salt must have occurred after deposition of these sedimentary layers and after or during their deformation (*Trudgill et al.*, 1999). The timing and cause of inflation of the salt detachment layer, however, are disputed. *Trudgill et al.* (1999) suggest a post-shortening, early Pliocene salt inflation generated by the load of the seaward extruding Sigsbee Canopy. *Rowan et al.* (2000) argue that the inflation of the Louann Salt occurred with, or immediately after, the main folding phase of the PFB. *Waller* (2007) points out that a significant amount of salt inflation could result from salt being squeezed out of the narrowing anticlines and from beneath the sinking synclines. The distal synclines are below their regional datum even after restoration (*Rowan et al.*, 2000; *Waller*, 2007). This implies a net deflation of salt occurred underneath the distal end of the fold belt.

2.2.5 Initial Salt Geometry

The initial salt thickness and subsalt basement geometry may have had significant influence on the style, location and timing of the folds (*Rowan et al.*, 2000). NE-SW trending basement steps, corresponding to faults in the extended continental crust, have been inferred from gravity and high resolution seismic data (*Trudgill et al.*, 1999). It has also been suggested that a major basement step localized the formation of the Sigsbee diapir (*Peel et al.*, 1995) (Figure 2.2b). The initial thickness of the salt underlying the PFB has been reconstructed by *Trudgill et al.* (1999) to be 2.5-3 km at the northwestern end of the restored section (50-60 km landward of the salt pinch-out) thinning to zero at the southeastern end (Figure 2.4). This corresponds to an initial landward tilt of the base of the salt of approximately 2.5°. The wedge-shaped sediment sequence deposited after inflation exerted a larger load on the distal end, and isostatically tilted the salt base to what is currently an almost horizontal attitude (*Trudgill et al.*, 1999). *Diegel et al.* (1995) estimate the average initial salt thickness of the central Gulf of Mexico basin to be 2.4 km.

The current landward extent of the autochthonous salt can be taken from Figures 2.2b and 2.2c to be at least 250 km from the distal pinch-out. Another 100 km landward, extensional faulting can be found, that soles onto the top of the basement (Figures 2.2a and 2.2b) suggesting that the weak detachment layer extended this far. The absence of salt in the present-day configuration indicates that salt was efficiently evacuated, or that it was originally very thin and below seismic data resolution.

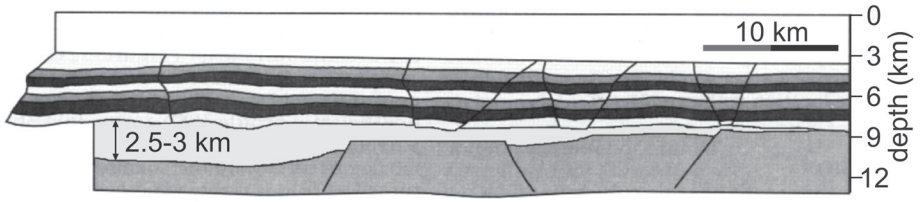

Figure 2.4: Two-dimensional restoration of a NNW-SSE trending seismic profile across the PFB from *Trudgill et al.* (1999). Location is shown in Figure 2.1. Salt is colored light grey, sedimentary overburden is marked by banded units. Shortening across the 60 km wide domain is estimated to be 5-10 %.

2.3 Limit Analysis for Margin Stability

In order for gravitational spreading to occur, the differential load across the margin must be sufficient to cause failure of the landward and seaward sections of the overburden. Following failure, a larger differential load causes the margin to become more unstable, leading to faster gravity-spreading-related deformation. A quantitative stability assessment of the northwestern Oligocene Gulf of Mexico can reveal the conditions under which the PFB can have formed due to gravity spreading alone or under which crustal tectonics were required. The knowledge about failure of a system is also crucial for the design of numerical models.

Gemmer et al. (2004, 2005) developed a quantitative limit analysis to determine the conditions for gravitational failure of a salt-bearing continental margin system. The force balance yields a relationship between margin geometry (salt and sedimentary overburden thickness) and sediment strength that describes the system at the onset of gravitational spreading. The limit analysis presented here extends the analysis of *Gemmer et al.* (2005) by including the isostatic response to sediment loading

and a description of pore-fluid pressure that is related to the mean (dynamical) stress instead of the lithostatic stress (weight of the overburden).

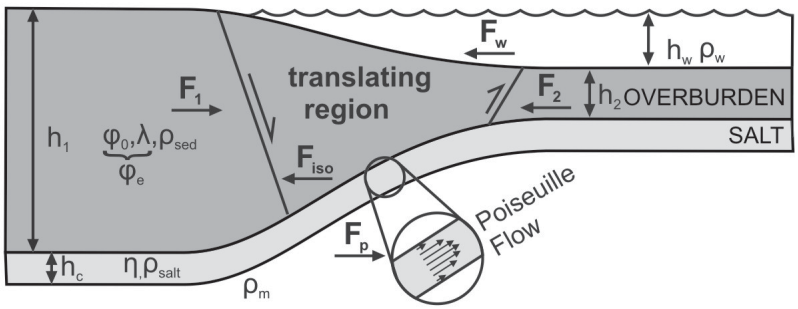

Figure 2.5: Conceptual model of a salt-bearing continental margin with the horizontally acting forces that are used for the limit analysis. See section 2.3 and Table 2.3 for description of parameters. Diagram is not to scale.

Figure 2.5 shows a schematic continental margin, where a salt layer of constant thickness is overlain by a seaward thinning frictional sedimentary overburden. The entire system is locally isostatically balanced assuming a substratum of uniform density. The horizontal forces acting on the system at failure are:

F_1 - limiting tensile failure strength of the landward sediment overburden,

F_2 - limiting compressive failure strength of the seaward sediment overburden,

F_{iso} - downslope (gliding) force owing to landward tilt of base that results from isostatic adjustment,

F_p - drag force exerted on the base of the overburden by Poiseuille flow in the viscous layer,

F_w - water loading force, acting as a buttress to seaward movement.

If the seaward-directed forces exceed the landward-directed forces the system becomes unstable and the overburden fails and translates seaward. The state of incipient failure is described by balancing all forces

$$F_1 + F_2 + F_p + F_w + F_{iso} = 0. \tag{2.1}$$

These forces can be estimated in terms of the system parameters (see Appendix 2.10). Substitution of these equations for individual forces into the equation above leads to the following force balance:

$$h_1^{*2}\, k_a - h_2^{*2}\, k_p + T\,(h_1^* - h_2^*) + (T-1)\,(h_1^{*2} - h_2^{*2}) = 0 \qquad (2.2)$$

with h_1^*=h_1/h_c, h_2^*=h_2/h_c , k_a=$1/k_p$=$(1-\sin\varphi_e)/(1+\sin\varphi_e)$, $\sin\varphi_e$=$(1-\lambda)\,\sin\varphi_0$ and T=$(1-\frac{\rho_w}{\rho_s})\frac{\rho_m-\rho_s}{\rho_m-\rho_w}$. h_1 and h_2 are the landward and seaward sediment thicknesses, h_c is the salt thickness. T includes ρ_w, ρ_{sed}, and ρ_m, (the density of the water, sediment, and mantle) and describes the effects of isostatic compensation. k_a and k_p describe the tensile and compressive sediment strength using φ_e, the effective angle of friction of the overburden, which in turn is a function of φ_0, the internal angle of friction, and λ=p_f/p, the ratio of pore-fluid pressure to mean stress. This equation for the condition for incipient failure of a continental margin system is independent of the salt viscosity and salt density.

In the case of the PFB, the geometry of the Oligocene Gulf of Mexico is relatively well known and densities of the sediments and mantle can be estimated. Equation 2.2 then yields a value for the sediment strength of the PFB at incipient failure. Figure 2.6 shows the sediment thickness required for margin failure plotted against effective strength of overburden (displayed as effective angle of friction φ_e or pore-fluid pressure ratio λ) for different salt thicknesses. h_2 is chosen to be 4.5 km, ρ_w=1000 kg/m^3, ρ_s=2300 kg/m^3 and ρ_m=3300 kg/m^3. The region below each curve (small h_1 and large φ_e) represents stable systems; the region above each curve marks settings where sediment thickness h_1 is high enough and overburden strength low enough to destabilize the continental margin system.

If the Oligocene shelf thickness is estimated to be 10±1 km (Figure 2.2a) at the time of failure and the initial salt thickness was between 2 and 3.5 km, the corresponding sediment strength is given by effective angles of friction of φ_e=5-6.4°. This range represents the maximum strength for which folding of a 4.5 km thick overburden was possible with the assumed geometrical configuration. The values of φ_e=5-6.4° correspond to pore-fluid pressure ratios of 0.73-0.79 for sand (φ_0=25°). These values are significantly higher than hydrostatic pore-fluid pressures ($\lambda\approx$0.43) but are generally not unusual for large sedimentary basins (*Huffman and Bowers*, 2002). Also,

effective angles of friction for shales rich in low-friction clay minerals are often 10° or lower. The values of φ_e=5-6.4° resulting from the limit analysis are regarded as a mean value for the entire section averaging over different lithologies and pore-fluid pressure regimes.

The limit analysis describes a simplified salt-bearing continental margin system and omits the influence of several properties that are likely to have at least minor effects on the stability. For example, the calculations do not take into account thermally induced tilt of the margin, finite extent of the salt basin, variable salt thickness or lateral and vertical variations of sediment properties (e.g. composition, compaction, or variations in pore-fluid pressures). The thermal tilt of the margin, which adds a downslope gliding term to the force balance, is considered to be negligible for the current application because the limit analysis is applied to the distal, seaward, part, of the margin (Figure 2.2) in the vicinity of the PFB, a region that will have undergone mainly uniform thermal subsidence.

The limit analysis only describes the state of failure but does not apply to the subsequent phases of gravity spreading and deformation. The immediate post-failure velocity of the sliding overburden can, however, be estimated by including the traction force F_c exerted by the salt on the base of the translating overburden. After failure, any excess seaward force of the previously described forces (equation 2.1) will be balanced by this traction force. F_c can be calculated assuming a simple Couette (shear) flow in the salt layer of uniform thickness (*Gemmer et al.*, 2004, 2005):

$$F_c = -\eta \frac{v_c}{h_c} L \qquad \text{and} \qquad v_c = -\frac{F_c\, h_c}{\eta\, L}, \tag{2.3}$$

where v_c and L are the velocity and length of the translating overburden. This equation shows that overburden translation and associated deformation occur in general faster over unstable regions that are narrow (small L) with thicker or less viscous (large h_c or small η) salt.

The outcome of the limit analysis shows that gravity spreading alone can be responsible for the formation of the PFB. If overburden sediments were sufficiently weak, no crustal tectonics (*Wilson*, 2003) need be involved to fold the 4.5 km thick overburden. In the next section, we apply the constraints on the material properties derived above and investigate the evolution of Perdido-type fold belts using finite

element models.

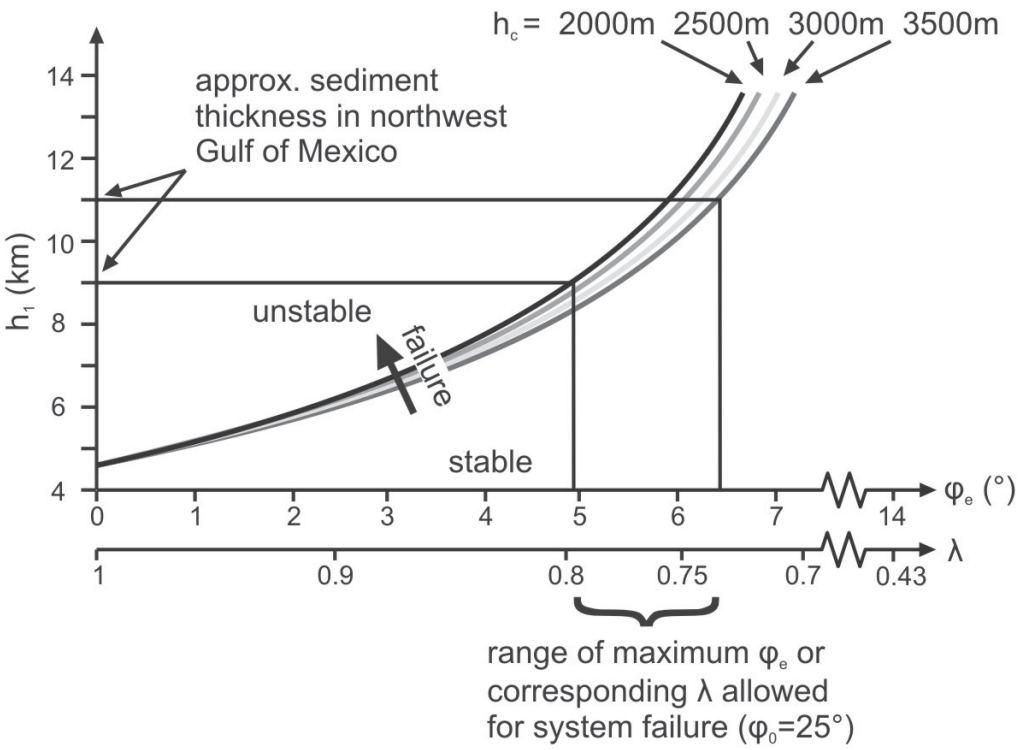

Figure 2.6: Results of limit analysis for margin stability applied to Oligocene-type setting in the northwestern Gulf of Mexico. Sediment thickness required for margin failure is plotted against effective strength of overburden (displayed as effective angle of friction φ_e or pore-fluid pressure ratio λ) for different salt thicknesses. The internal angle of friction of a dry sediment overburden is set to φ_0=25°. Additional parameters that enter the equation for margin stability are h_2=4500 m, ρ_m=3300 kg/m^3, ρ_s=2300 kg/m^3, and ρ_w=1000 kg/m^3. For a given landward sediment thickness of 10 ± 1 km at incipient failure, the overburden strength needs to be reduced by moderate to high pore fluid pressures ($0.73 < \lambda < 0.8$) to effective strengths of ($5° < \varphi_e < 6.4°$).

2.4 Finite Element Numerical Modeling

We use 2D mechanical finite element models to investigate the evolution of salt-cored fold belts on a passive continental margin. The models describe plane-strain, incompressible, viscous-plastic fluid flow (*Fullsack*, 1995; *Willett*, 1999). Deformation is governed by the equation of motion (conservation of momentum, no inertial forces) and the equation for conservation of mass, which, for incompressible flow, can be written as the divergence of the velocities.

$$\frac{\partial p}{\partial x_j} + \frac{\partial \sigma_{ij}}{\partial x_i} + \rho\, g_j = 0 \qquad i,j = 1,2 \tag{2.4}$$

$$\frac{\partial v_i}{\partial x_i} = 0 \tag{2.5}$$

where summation is implied over repeated indices, p is the mean stress, x_1 and x_2 are the spatial dimensions, ρ is the density, and g is the gravitational acceleration acting in the $j = 2$ direction. σ_{ij} is the stress tensor that relates to strain rates by the constitutive law for viscous deformation

$$\sigma_{ij} = p\,\delta_{ij} + 2\,\eta_e\,\dot{\varepsilon}_{ij} \tag{2.6}$$

where δ_{ij} is the Kronecker delta, η_e is the effective viscosity, and $\dot{\varepsilon}_{ij}$ is the strain rate tensor defined by

$$\dot{\varepsilon}_{ij} = \frac{1}{2}\left(\frac{\partial v_i}{\partial x_j} + \frac{\partial v_j}{\partial x_i}\right). \tag{2.7}$$

η_e is constant for linear viscous materials and stress-dependent for non-linear viscous materials. The velocity-based equations (2.4) and (2.5) are then solved using finite element techniques (*Fullsack*, 1995). Behavior of frictional-plastic material is characterized by a threshold value of stress below which no deformation occurs and at which plastic deformation sets in. This yield stress is approximated for brittle material (such as sedimentary rocks) by the Drucker-Prager yield criterion, which is equivalent to the Coulomb criterion for incompressible, plane-strain deformation

$$\sqrt{J_2'} = p\,(1-\lambda)\,\sin\varphi_0 + C\,\cos\varphi_0 \tag{2.8}$$

where $J_2' = \frac{1}{2}\sigma_{ij}'\,\sigma_{ij}'$ is the second invariant of the deviatoric stress ($\sqrt{J_2'}$ is the yield stress), λ is the pore-fluid pressure ratio, φ_0 is the internal angle of friction and C is the cohesion. The effects of pore-fluid pressure can be considered to be included in an effective angle of friction $\sin\varphi_e = (1-\lambda)\sin\varphi_0$. The plastic flow at yield can again be described by equations (2.4) to (2.7) with a stress-dependent effective viscosity

$$\eta_e = \frac{1}{2}\sqrt{\frac{J_2'}{\dot{I}_2'}} \tag{2.9}$$

where $\dot{I}_2' = \frac{1}{2}\dot{\varepsilon}_{ij}'\,\dot{\varepsilon}_{ij}'$ is the second invariant of the deviatoric strain rate (*Willett*, 1999).

The calculations use an Arbitrary Lagrangian-Eulerian (ALE) method in which computations are made on an Eulerian grid that stretches vertically to adapt to the evolving model geometry. The material properties are tracked and updated using a set of moving Lagrangian particles. This approach allows calculations to be made for very large deformation.

Material density can be constant (as used for salt) or burial-dependent (as used for compacting sediments). For compacting material, a new density is calculated each time step for each element depending on its burial depth z (*Korvin*, 1984).

$$\rho_{sed} = \rho_g - (\rho_g - \rho_w)\,\Phi_0\,e^{-c\,z} \tag{2.10}$$

where ρ_{sed}, ρ_g, and ρ_w are the densities of the sediment, the grain matrix, and the pore fluid, respectively, Φ_0 is the initial surface porosity and c is the compaction coefficient. Densities increase with burial but do not decrease during exhumation. In order to account for mass loss as fluid is expelled, the volume of each element decreases kinematically by vertical contraction as the density increases. It is assumed that expelled fluids are lost from the system. Horizontal compaction likely also occurs in the natural systems, but it is not taken into account. Effects of compaction on sediment strength or coupling with pore-fluid pressures are not included.

The numerical models presented here are applied to a continental margin setting in which a layer of salt is overlain by pre-existing and prograding sediments. The entire system is submerged under water. The weight of the water column is calculated as a force acting normal to the seafloor, thereby increasing the solid and fluid pressures of the model materials. Isostatic adjustment is calculated by assuming a flexural elastic beam at the base of the model and an underlying inviscid fluid with density ρ_m.

The model bathymetry z_0 (the profile of the continental margin) is given by a half-Gaussian shape defined by the total increase in water depth across the margin h_w, the width of the slope region w, and the location x_0 of the edge of the shelf.

$$z_0(x) = \begin{cases} 0 & x \le x_0 \\ h_w\,exp\,(-(\frac{x-x_0}{w})^2) & x > x_0 \end{cases} \tag{2.11}$$

Sedimentation is treated kinematically by progradation of this slope profile with a prescribed velocity v_{prog} and corresponding filling of accommodation space below the profile with sediments.

2.5 Reference Model

2.5.1 Design of Reference Model

A reference model (model R-0) was designed to represent a simplified, prototype version of the Oligocene northwestern Gulf of Mexico continental margin in which gravity spreading leads to the formation of a fold belt at the end of the autochthonous salt basin. Modifications of the reference model are then used to test the sensitivity of the fold belt evolution to variations in different parameters (overburden strength, salt viscosity, initial salt geometry, etc.). The starting configuration of the reference model is shown in Figure 2.7.

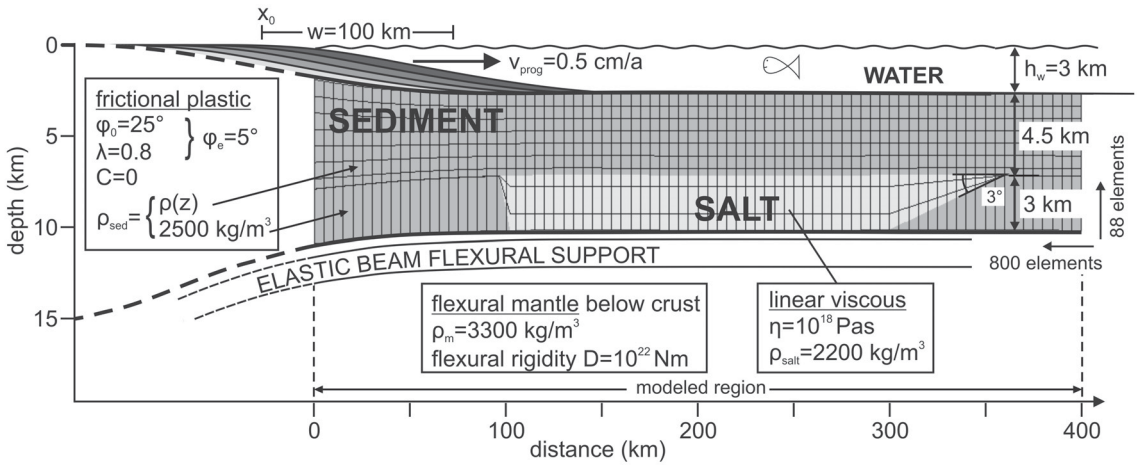

Figure 2.7: Design of reference model R-0. Frictional-plastic sediments overlie a 200 km-wide, 3 km-thick salt basin. The model includes prograding sedimentation, sediment compaction, parametric effects of pore-fluid pressures, isostatic adjustment, and the loading effects of the water column. For a full list of model parameters and their discussion see section 2.5 and Table 2.1.

A list of all relevant model parameters is given in Table 2.1. The salt basin width of 260 km is regarded as a conservative estimate of the actual extent of the autochthonous salt and here represents the residual width of the autochthonous Louann Salt remaining at the time when the PFB formed. The initial salt thickness is set to

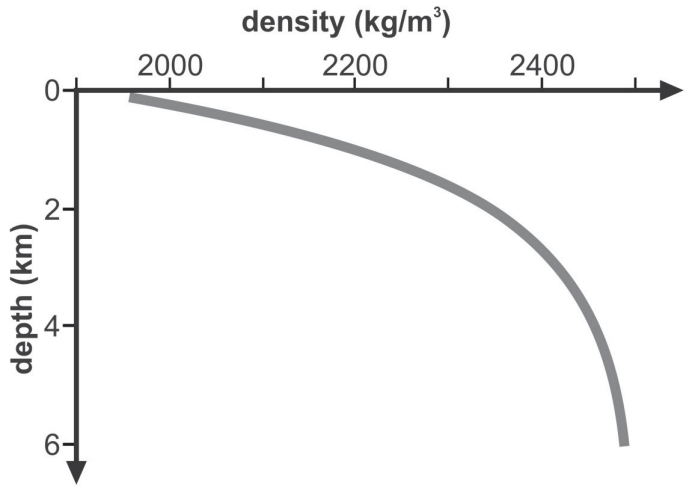

Figure 2.8: Average compaction trend for sediments in the Gulf of Mexico used in the numerical models. Curve simplified from *Jackson and Talbot* (1986) with sediment density defined as $\rho_{sed}=\rho_g - (\rho_g - \rho_w)\,\Phi_0\,exp(-cz)$, where grain density ρ_g=2500 kg/m^3, pore fluid density ρ_w=1000 kg/m^3, initial porosity Φ_0=0.4 and compaction coefficient c=0.0007 m^{-1}. z is burial depth.

3 km with tapering at approximately 2.5° in the distal end, according to reconstructions by *Trudgill et al.* (1999) (section 2.2 and Figure 2.4). These reconstructions involving highly mobile salt are difficult and often inaccurate, but in absence of better constraints we use these values for the starting configuration. In the strict sense, the material underlying the sediments represents interlayered evaporites, not necessarily only halite. We model halite with a linear viscous rheology, which is a good approximation for deformation under low strain rates (*Urai et al.*, 1986). Its effective viscosity is known from lab experiments to lie between 10^{16} and 10^{19} Pa s (*van Keken et al.*, 1993; *Ter Heege et al.*, 2005) where lower values represent weaker (wetter) salt. We use an intermediate value of 10^{18} Pa s. Salt density is 2200 kg/m^3 (*Jackson and Talbot*, 1986).

An initial sediment cover of 4.5 km (thickness of pre-kinematic, Jurassic-Oligocene section of the PFB) across the entire salt basin is considered to result from earlier (aggradational) deposition. Sedimentation during the model evolution is prescribed by the seaward prograding half-Gaussian profile (equation 2.11) with a slope width of w=100 km and a maximum water depth of just below 3 km. This value is intermediate between present-day water depths of 2-3 km and water depths at the end of the Cretaceous estimated to be 4-5 km in the deep Gulf of Mexico (*Winker and*

Buffler, 1988). The slope profile is located outside the model domain in the starting configuration and progrades onto the salt basin at a rate of 0.5 cm/a, slightly higher than the Cenozoic average of 0.4 cm/a (*Galloway et al.*, 2000). With this choice of parameters the maximum sediment thickness in the numerical models matches the observed maximum thickness of 16 km in the Gulf of Mexico (Figure 2.2b).

Sediment strength is based on the results of the limit analysis of section 2.4. An effective angle of friction of φ_e=5° (φ_0=25°, λ=0.8) predicts gravity spreading to occur. Cohesion is considered negligible by comparison with the frictionally sustained stresses. Material laterally enclosing the salt basin does not compact. It represents either synrift sediments, that are already fully compacted, or crustal basement, which does not compact. Its density is set to 2500 kg/m^3. The 4.5 km thick overburden as well as the sediments deposited during the model evolution compact, following a depth-dependent density curve which was obtained from several well data sets from the Gulf of Mexico (Figure 2.8) (*Jackson and Talbot*, 1986). The resulting average compacted densities of a 4.5 and a 16 km thick section are 2320 and 2450 kg/m^3, respectively.

Lithosphere below the salt basin only influences the isostatic compensation. The flexural rigidity of D=10^{22} Nm represents relatively stiff lithosphere corresponding to values estimated from old, passive continental margins (*Watts*, 2001). For simplicity, lateral variations in crustal thickness (or equivalent variations in flexural rigidity) are not accounted for. The effect of a thinner, extended crust, as expected in the distal area of the passive margin, would be a slightly larger water depth.

2.5.2 Evolution of the Reference Model

Figure 2.9 shows three key stages in the development of the reference model R-0. The entire model evolution can be seen in the supporting electronic material (modelR0.mp4)[1]. During the first 24 Ma sediments simply prograde, building up a continental slope and differential load across the margin. Once the sediment thickness reaches approximately 10 km, overburden failure and translation of the central part of the sedimentary unit are observed (Figure 2.9a). An extensional growth fault basin evolves landward while the seaward region develops gentle sinusoidal detachment

[1]Supplementary material is provided as electronic attachments and is described in Appendix D.

Table 2.1: Input parameters for numerical models. Values given are those used in reference model R-0.

Parameter	Symbol	Value
Sediment		
initial (distal) thickness	h_2	4.5 m
maximum thickness above initial salt level	h_1	13 km
sediment density (non-compacting)	ρ_{sed}	2500 kg/m^3
sediment density (compacting)	ρ_{sed}	$\rho_g - (\rho_g - \rho_w)\,\Phi_0\, exp(-cz)$
sediment grain density	ρ_g	2500 kg/m^3
pore-fluid and water density	ρ_w	1000 kg/m^3
initial porosity	Φ_0	0.4
compaction coefficient	c	0.0007 m^{-1}
burial depth	z	
internal angle of friction	φ_0	25°
pore-fluid pressure ratio	λ	0.8
effective angle of friction	φ_e	5°
Salt		
initial width of salt layer	w_{salt}	200 km + 60 km taper
initial thickness	h_c	3 km
initial taper angle	α	3°
density	ρ_{salt}	2200 kg/m^3
viscosity	η	10^{18} Pa s
Lithosphere		
density	ρ_m	3300 kg/m^3
flexural rigidity	D	10^{22} Nm
Progradation Profile		
width	w	100 km
max. height	h_w	3 km
progradation velocity	v_{prog}	0.5 cm/a
Finite Element Grid		
width		400 km
number of elements (horizontal)		800 (each 500 m wide)
number of elements (vertical)		88
basement		2
salt		20
sedimentary overburden		66

folds (Figures 2.9b and 2.10a). As these folds shorten, fold limbs steepen and shear (Figure 2.10b). The detailed nature of these narrow zones of deformation in between individual folds cannot be determined with the current model resolution. They might represent kink bands, shear bands or a continuum mechanics approximation of thrust faults, but will here be referred to as kink bands because they resemble the narrow deformation zones of the PFB (*Camerlo and Benson*, 2006). (Figures 2.10b and 2.10c, section 2.5.3). Ongoing shortening is ultimately absorbed in a single thrust fault at the pinch-out of the salt (Figure 2.9c). The rolling hinge in this model evolves without large-scale faulting, as in the similar laboratory model (*Ge et al.*, 1997) but would result in extensive fracturing of the pre-kinematic layer.

2.5.3 Comparison of Reference Model to the PFB

Figure 2.10 shows a comparison of two seismic sections from the PFB with an equivalent section from the reference model R-0. Both show very similar fold belts but differ in the timing of folding and amplitude of the folds.

Shape and Wavelength of Folds

The wavelengths of the early detachment folds of the model vary laterally across the salt taper region, and decrease from 20 to 12 km (Figure 2.10a). The later stage of the model evolution (Figure 2.10b) as well as the seismic cross section of the PFB show triangular to trapezoidal folds bounded by narrow, kink band-like deformation zones. The width of the triangular plugs between two conjugate kink bands is larger in the model fold belt than in the PFB, and is partly related to different dip angles of the kink bands. Deformation in the model sediments always localizes at angles of 45° to the principal stresses owing to their incompressibility. They will therefore dip close to 45° assuming horizontal and vertical principal axes, whereas the kink bands of the PFB dip at approximately 55-60°. Despite these differences, the average wavelength that includes the folded and the relatively undeformed sections in between individual pairs of kink bands is similar. Again, it should be noted that the seismic line of Figure 2.10c is slightly oblique to the fold axis of the PFB (section 2.2.1).

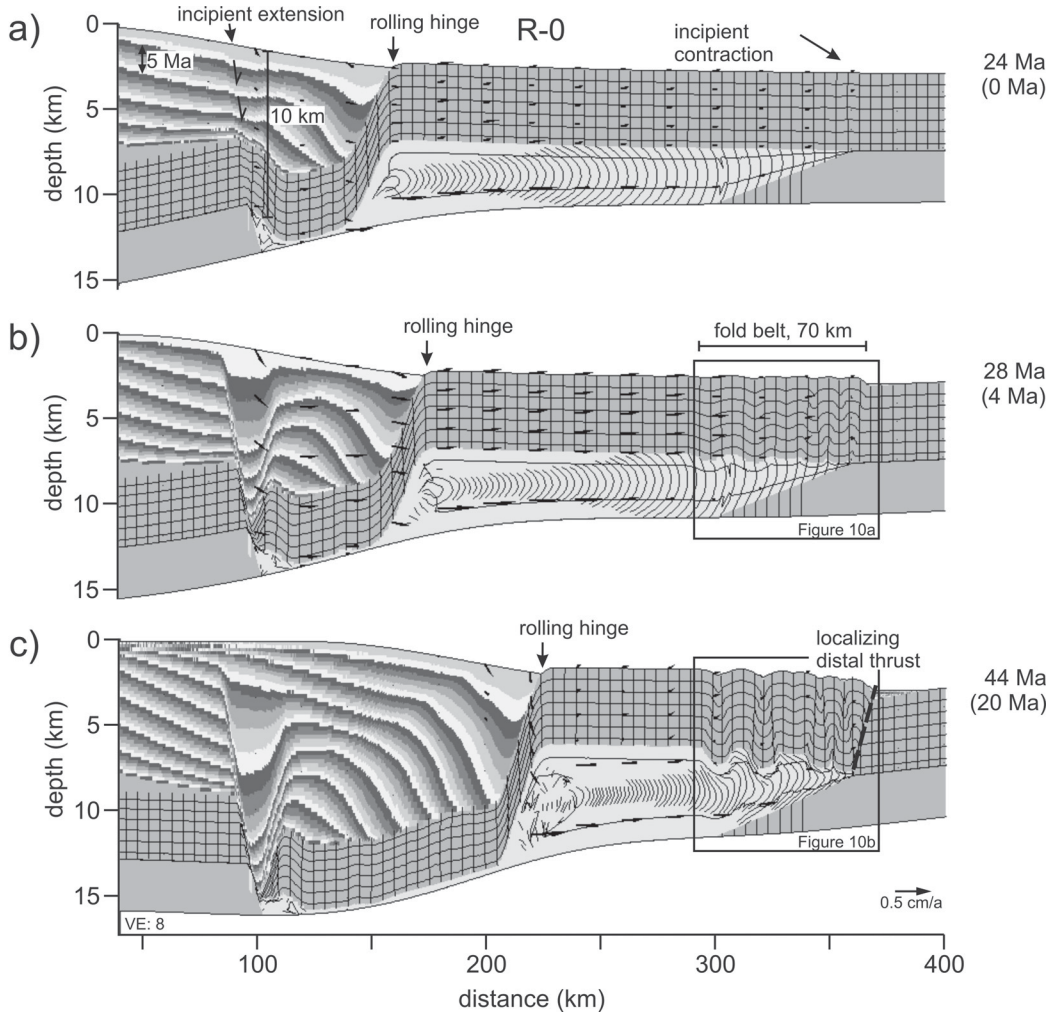

Figure 2.9: Evolution of reference model R-0 at different stages of gravity spreading showing the formation of a 70 km wide fold belt. Ages denote model run time, ages in brackets denote time since onset of gravity spreading. (See also animation modelR0.mp4 of auxiliary material.) VE denotes vertical exaggeration. The grayscale (colorscale for animation) shows the chronostratigraphy in 5 Ma major bands, each divided into 1 Ma sub-bands. Same coding is used in later figures. Labels in marked details refer to Figures 2.10a,b.

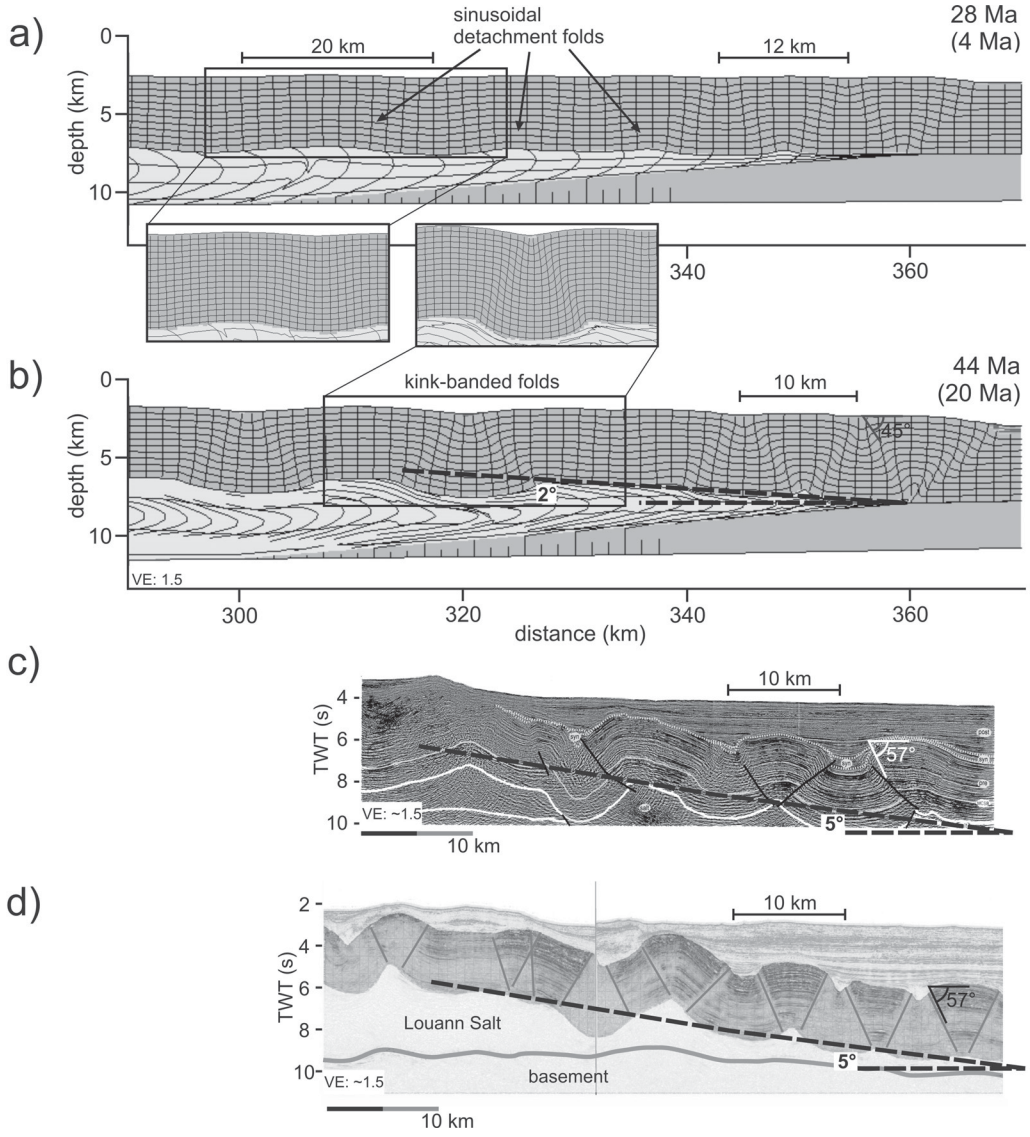

Figure 2.10: (a) Early evolution of the fold belt of model R-0 (reference model) with sinusoidal detachment folds. (b) Fully developed model fold belt with kink-banded folds and comparison to (c,d), seismic sections of PFB from *Rowan et al.* (2000) and *Camerlo and Benson* (2006). See text for further discussion. Ages denote model run time, ages in brackets denote time since onset of gravity spreading.

Inflation and Taper Angle

In both the PFB and model R-0 the underlying salt layer inflates during the evolution of the fold belt (Figures 2.9c and 2.10b). Both taper angles are about 5°. Model R-0 started with an initial taper angle of 3° (Figure 2.7), hence the inflation only amounts to 2°. A similar evolution has been suggested for the PFB (Figure 2.4) (*Trudgill et al.*, 1999), where an initial taper of the salt of 2.5° was present prior to folding. The present horizontal position of the salt base was attributed to the isostatic effect of the post-kinematic sediment wedge.

Amount and Rate of Shortening, Timing

Deformation in the model fold belt starts as folding at the seaward salt pinch-out. It spreads within 3-4 Ma to its maximum width, forming a 70 km wide fold belt (Figures 2.9b and 2.10a). This length correlates roughly with the width of the salt taper region and may result because the thinning layer reduces the salt flow and exerts additional traction on the overburden. However, as is shown in the following section, the fold belt is generally not restricted to the salt taper width.

The early fold belt consists of low-amplitude, sinusoidal detachment folds (Figure 2.10a). Kink band formation along the fold limbs starts approximately 6 Ma after onset of deformation. Folds continue to grow for another 14 Ma after which all shortening localizes in the single distal thrust (Figure 2.9c). The modeled fold belt develops in about twice the time as the natural system (20 Ma vs. ∼10 Ma). The amount of shortening accommodated in the model fold belt is approximately 11 km. This corresponds to 16% shortening across the 70 km wide fold belt and is similar to the 5-10 km shortening stated for the PFB. Although the total shortening is similar, the amplitude of the folds is only 0.5-1.5 km compared to the 2.5 km in the natural system. This indicates that a significant amount of shortening is accommodated in the model by pure-shear thickening. The modeled fold amplitudes at the top of the deformed section are approximately three times smaller than at its base (0.5 km vs. 1.5 km). This disparity can be attributed to the different density contrasts along the fold interfaces, which either counteract or enhance fold uplift, and also indicates pure-shear deformation.

2.6 Variations of Reference Model

Despite discrepancies in fold amplitude and timing, the numerical models proved to be capable of developing a Perdido-type fold belt and in this section we will investigate which parameters determine the style and timing of this fold belt.

The sensitivity of the model R-0 to parameter variations was tested in order to understand the effects that these parameters have on the deformation and evolving structures. These sensitivity tests can be used to better constrain aspects of the original setting of the northwestern Gulf of Mexico.

2.6.1 Sediment Strength

The effective sediment strength of the reference model (φ_e=5°) is a parameter derived from the limit analysis and can be interpreted to represent sand (φ_0=25°) under moderately high pore-fluid pressures (λ=0.8). The limit analysis only provides a guide to system behavior and cannot be applied to the numerical models accurately. Nevertheless, the effects of variations in overburden strength, which are predicted by the analytic calculations to result in stable or highly unstable conditions, can also be observed in the numerical models.

Figure 2.11 shows three models with different effective sediment strengths. An effective sediment strength noticeably higher than in the reference model, achieved by reducing λ, (e.g. model R-S1, λ=0.7, φ_0=25°, φ_e=7°), leads to a stable system (Figure 2.11a). The models exhibits no landward failure and no gravity spreading. The compacting overburden, which is denser than the salt, still sinks into the substratum, displacing the salt and thereby inflating the distal part of the basin. But no horizontal movement of the overburden takes place. When the effective sediment strength is only slightly larger than in the reference model (e.g. model R-S2, λ=0.75, φ_e=6°, Figure 2.11b), failure again occurs but the gravity spreading velocity is lower (<0.1 cm/a vs. 0.3 cm/a). In this case, for the same period of time less shortening occurs than in the reference model and the lateral extent of the fold belt is much narrower, about 30 km across, comprising only 2 anticlines. Models with lower effective sediment strengths than in the reference model (e.g. model R-S3, λ=0.9, φ_e=2.5°, Figure 2.11c) fail and start to deform at a lower landward sediment thickness and

develop with higher spreading velocity (0.5 cm/a vs. 0.3 cm/a) than in the reference case. This leads to a wider fold belt with higher amplitude folding. Also, individual synclines detach from the surrounding folds and sink into the underlying, less dense salt creating 'pop-down' structures. Given these results, a model with $\lambda \sim 0.85$ will provide the best match to the geometry and duration of folding observed for the PFB.

2.6.2 Slope Width

The width of the prograding slope of the continental margin and the corresponding steepness of the continental slope at Oligo-Miocene times are poorly constrained from the seismic cross-section of the Gulf of Mexico (Figure 2.2). A sensitivity analysis was used to determine how the progradation width w (the continental slope width) influences the model evolution and in order to assist the reconstruction of the conditions during formation of the PFB.

A model with a wider (and less steep) slope than in the reference model (model R-W1, w=150 km, Figure 2.12a) deforms significantly slower (<0.1 cm/a vs. 0.3 cm/a) and develops a much shorter fold belt. The full extent of the fold belt is reached >10 Ma after onset of deformation. A margin that is half as wide and therefore steeper than in the reference case (model R-W2, w=50 km, Figure 2.12b) develops higher spreading velocities (0.5 cm/a vs. 0.3 cm/a) and is more unstable than model R-0. Already, only 2 Ma after onset of deformation the fold belt width has reached its full extent, which is almost twice as large as the extent of the fold belt in the reference model.

2.6.3 Salt Viscosity

Salt viscosity is not a tightly constrained parameter. It may vary by orders of magnitude among autochthonous, allochthonous, wet and dry salt (*van Keken et al.*, 1993; *Ter Heege et al.*, 2005). Figure 2.13 shows a panel of model R-V1 with a salt viscosity of 10^{19} Pa s, ten times higher than the reference model's salt viscosity. Here, a fold belt forms at the toe of the slope in the central part of the salt basin and gradually propagates seaward. As the limit analysis (section 2.4) shows, the criteria for gravity spreading of a continental margin system is independent of the salt viscosity.

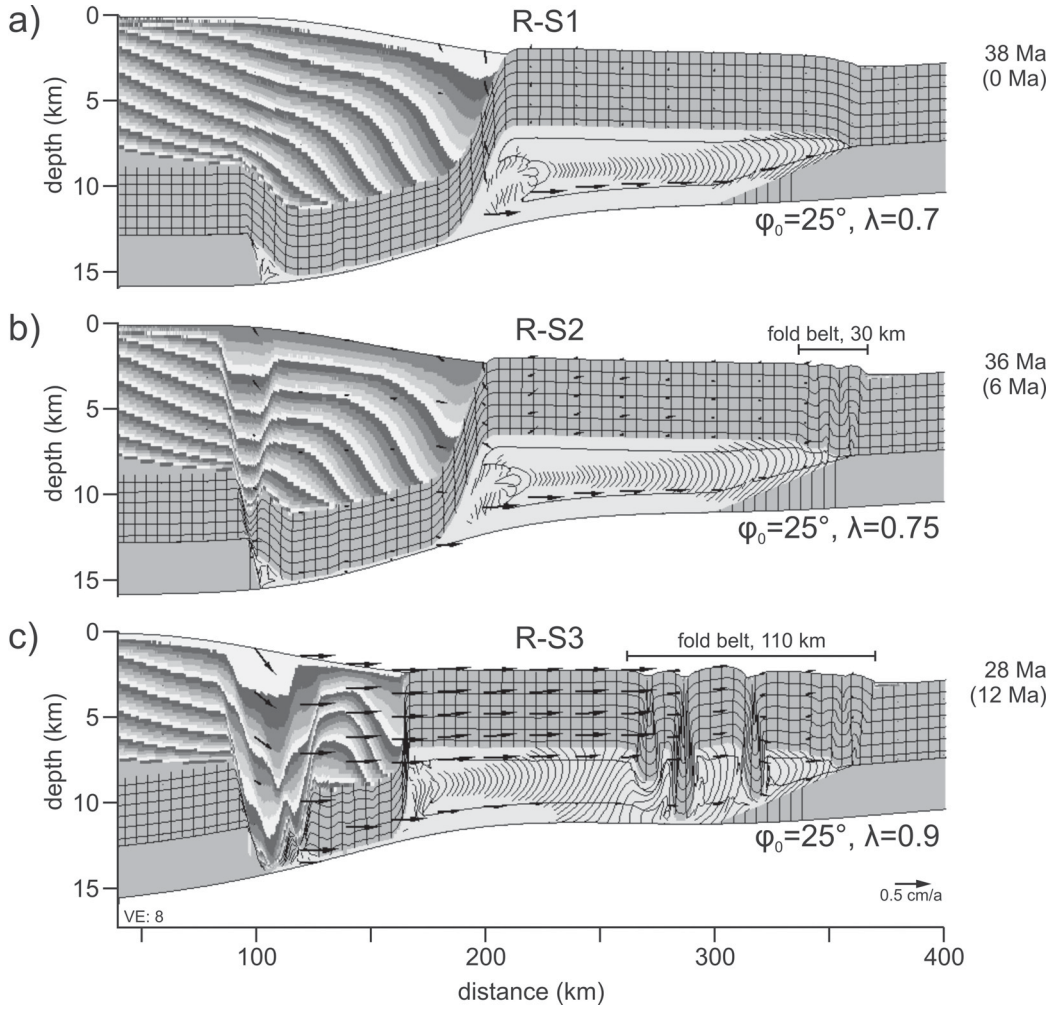

Figure 2.11: Results from numerical models R-S1, R-S2, R-S3 with varying pore-fluid pressure ratios λ. Ages denote model run time, ages in brackets denote time since onset of gravity spreading. (a) Model R-S1 with moderate pore-fluid pressures (high sediment strength) develops no gravity spreading. (b) Model R-S2 with slightly higher pore-fluid pressures than model R-0 develops gravitational spreading, deformation occurs more slowly and over a narrower contractional region than in the reference case. (c) Model R-S3 with higher pore-fluid pressures (weaker sediments) shows earlier and faster deformation over a wider contractional region than in model R-0.

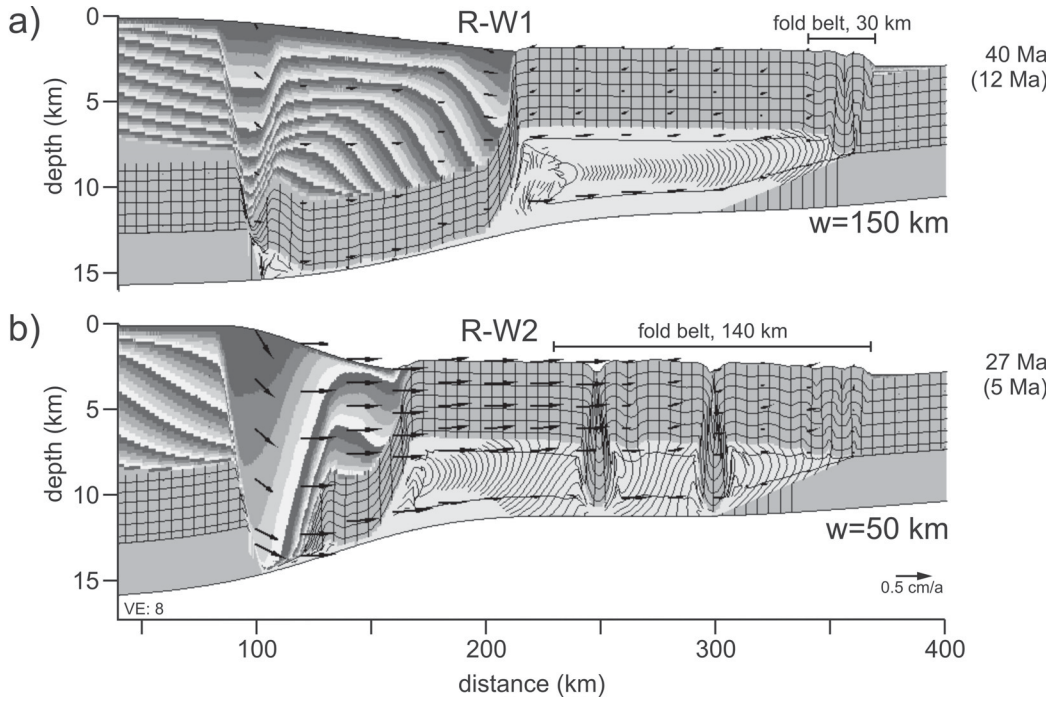

Figure 2.12: Results from models R-W1 and R-W2 with varying width of the slope region of the margin. Ages denote model run time, ages in brackets denote time since onset of gravity spreading. (a) Model R-W1 with a 50% wider slope than in the reference model shows slower deformation and a narrower fold belt. (b) Model R-W2 with a half as wide slope as in the reference model develops faster deformation of the overburden and a wider fold belt.

However, it directly controls the post-failure velocity and length scale with which the overburden translates seaward owing to the basal traction force exerted by the Couette flow (equation 2.3).

The Couette drag force $F_c = \eta\, v_c\, L/h_c$ is theoretically the same in both models R-0 and R-V1 since it must equal the sum of the forces described in equation (2.1), which depends only on the system parameters that are the same in both models. The larger viscosity η of model R-V1 must therefore be compensated by a smaller translational velocity v_c and a smaller length scale L (with h_c being constant). This is observed in the model evolution (Figure 2.13), where only the landward part of the overburden is translated and deformed. In addition to slowing down the horizontal salt movement, the vertical salt movement is also restricted by higher salt viscosity. Pop-down structures are less prone to sink into the higher viscosity underlying salt layer than into the less viscous material in the reference model, and allochthonous salt structures will also be less likely to evolve.

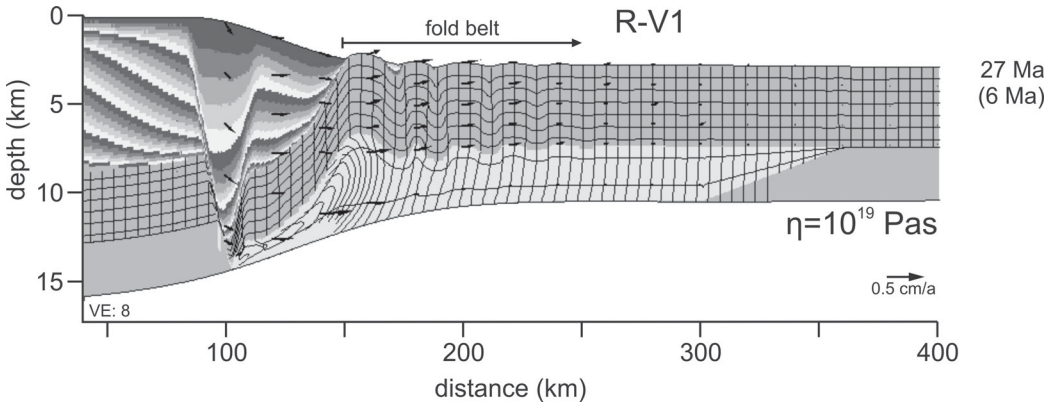

Figure 2.13: Results from model R-V1 with ten times higher salt viscosity than in the reference model R-0. Ages denote model run time, ages in brackets denote time since onset of gravity spreading. Folding initiates at the toe of the slope and propagates seaward across the entire salt basin, whereas deformation in the reference model starts and remains close to the salt pinch-out.

2.6.4 Salt Geometry and Thickness

The orientations of basement steps parallel to the trend of the fold hinges of the PFB suggest that the geometry of the salt basin may have had a significant influence on fold belt evolution (*Trudgill et al.*, 1999). In order to test the effects of basement

steps on timing and style of fold belt formation, the geometry of the distal end of the salt basin is varied (gradual and steep tapers, basement steps). We illustrate the effects using model R-G1 (Figure 2.14). Here, the salt abruptly thins over a basement step from the nominal 3 km thickness to 500 m, 60 km landward of the salt pinch-out.

Folding first localizes where the salt layer thins, then rapidly propagates seaward above the thin salt layer within ca. 1 Ma. Fold wavelengths are similar throughout the fold belt since both salt and overburden thickness are constant in this region. As this model evolves, the originally sinusoidal folds continue to shorten and fold limbs again steepen to form kink bands. The fold amplitude is restricted by the salt thickness. Once synclines ground, fold growth ceases. Continued sediment progradation squeezes the salt basinward. Salt flow is, however, restricted by the basement step and thinned salt layer and inflates only the landward part of the distal section (Figure 2.14c). As a result, the landward region of the fold belt is more strongly uplifted and tilted than the remaining seaward region. Accordingly, a bend develops in the fold belt. Models with thinner distal salt layers (not shown here) develop a steeper tilt of the landward fold belt section, leading to a stronger bend of the fold belt. The bend in the fold envelope observed in seismic data from the PFB (Figure 2.3b) may therefore be explained by the presence of very thin salt beneath the fold belt at the time of salt inflation.

In summary, basement steps that abruptly decrease the salt thickness do not delay the folding of the sediments above the distal end of the salt basin but localize the deformation above this region. Thin salt inhibits fold growth and salt inflation.

2.6.5 Sediment and Salt Density

The compaction of sediments, which is included in all models presented here, assists in pushing the margin toward failure and additionally results in increased deformation rates relative to cases of non-compacting sediments. For a given difference in thickness between shelf and deep-water sediments, the differential load of compacting sediments becomes larger than in a non-compacting system. This in turn also means that the shelf sediment thickness required to cause margin failure will be reduced to a value smaller than the values obtained from the limit analysis (section 2.4) for which sediments of uniform density were assumed.

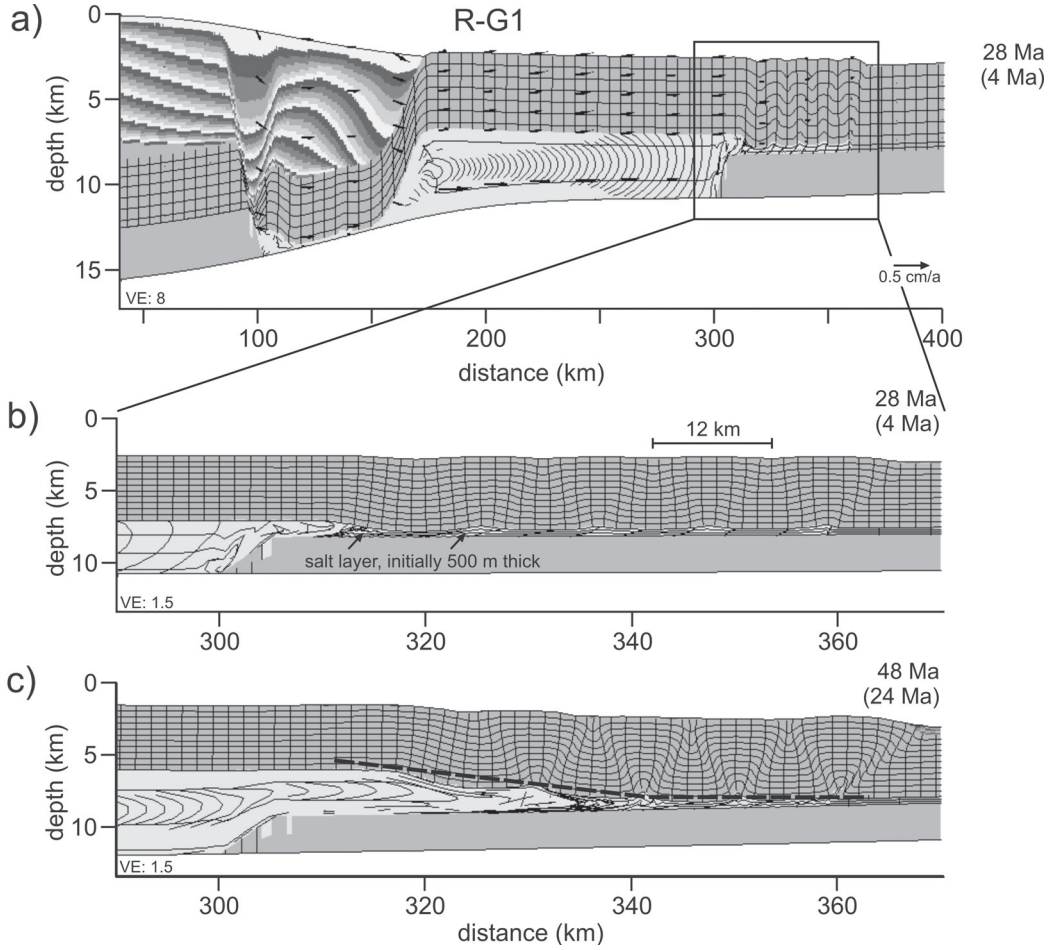

Figure 2.14: Results from model R-G1 with single basement step thinning the salt from 3 to 0.5 km for the distal 60 km. Ages denote model run time, ages in brackets denote time since onset of gravity spreading. Folding localizes at the basement step and folds develop synchronously in the sediments above the thinner salt section. Symmetric folds of equal wavelength evolve, turning into kink-banded folds. Salt inflation is strongly inhibited by the basement step and abrupt thinning of the salt layer and is restricted to the vicinity of this step, leading to a strong bend in the fold belt.

The density of salt may also vary and takes values closer to 2150 kg/m^3 with increasing temperatures at greater depths (*Jackson and Talbot*, 1986). Although these variations in absolute salt density may only be minor and will not affect the system in regard to lateral translation, the density relative to the overlying sediments determines the buoyancy force which can play a crucial role for vertical salt movement. From model experiments with varying salt densities (not shown here), it was observed that the different density contrasts had almost no effect on the lateral movement of the overburden, the fold amplitudes and the fold belt extent during the early phases of gravity spreading. An increased density contrast did, however, enhance sinking of the pop-down structures, thereby increasing the overall shortening rate slightly. As discussed in section 2.7, increased shortening together with enhanced buoyancy force can lead to expulsion of salt from the autochthonous level. Development of allochthonous salt structures also occurs in the reference model (with lower density contrast) but at a much later stage when the overburden has undergone much greater shortening (see movie_modelR0 in the auxiliary material). The density contrast between compacting sediment and salt appears to be key to the development of allochthonous salt structures in this type of setting.

2.6.6 Effect of the Landward Canopy

The models described so far only address the problem of mobilization of autochthonous salt beneath a thick overburden during sediment progradation. However, the conditions landward of the PFB are more complex and the data (Figure 2.2) have been interpreted to include an allochthonous salt (or possibly mixed salt/shale) canopy which facilitated gravity spreading at a second, higher level, resulting in the formation of the Port Isabel fold belt.

The behavior of this multilayer system is clearly more complicated than our simple models. We address in section 2.7 one mechanism that may have been responsible for the development of the salt canopy. Here, we are concerned with the effect of the canopy on the horizontal force balance and gravity spreading system during folding of the PFB. We simplify the emplacement of the canopy by representing it as a pre-existing salt layer above the main overburden layer (Figure 2.15) and investigate

the evolution of this system during the same sediment progradation as in the reference model. The specific question is whether the modified system requires higher or lower levels of pore fluid pressure to develop a Perdido-type fold belt than the simple systems. Three different models were run with pore-fluid pressure ratios of 0.7, 0.8, and 0.9. Similar to the sensitivity analysis presented in section 2.6.1, the model with lowest pore-fluid pressure ratio λ is stable, the model with intermediate λ is unstable like the reference model, and the model with λ of 0.9 deforms very rapidly.

Figure 2.15 (model R-C1) shows the evolution of a model with a 500 m thick secondary (allochthonous) salt layer and λ=0.8. Gravity spreading starts with the earliest deposition of the prograding sediment wedge along the upper detachment level and continues for 24 Ma (Figure 2.15 a and 2.15 b). The salt of the autochthonous level is squeezed seaward due to the load of the prograding sediment pile, creating a sag of the upper detachment level. The growing differential thickness of the overburden eventually leads to failure with respect to the lower salt detachment, initiating gravity spreading of the full overburden column. The upper detachment then ceases to be active. Figure 15 c and 15 d show the model 4 Ma after onset of the second gravity spreading, displaying again extension at the landward end of the autochthonous salt basin and folding at the seaward end. This evolution is similar to that of the reference model (Figure 2.9b), yet some differences occur. The shallow detachment level allowed the sediment wedge to extend further basinward (by sliding), which resulted in a more gradual transition from depleted to non-depleted salt. Accordingly the amount of salt displaced is higher, leading to stronger seaward inflation, which in turn facilitates the sinking of individual synclines (Figure 2.15c). The presence of the allochthonous salt layer, a proxy for the canopy, profoundly modifies the stratigraphy and structure of the model (compare Figures 2.9b and 2.15c). This change results in a geometry that is similar to that shown in Figure 2.2 in which sediments in the region of the upper level dip landward towards extensional faults, not mainly seaward as in the expulsion rollovers of earlier models.

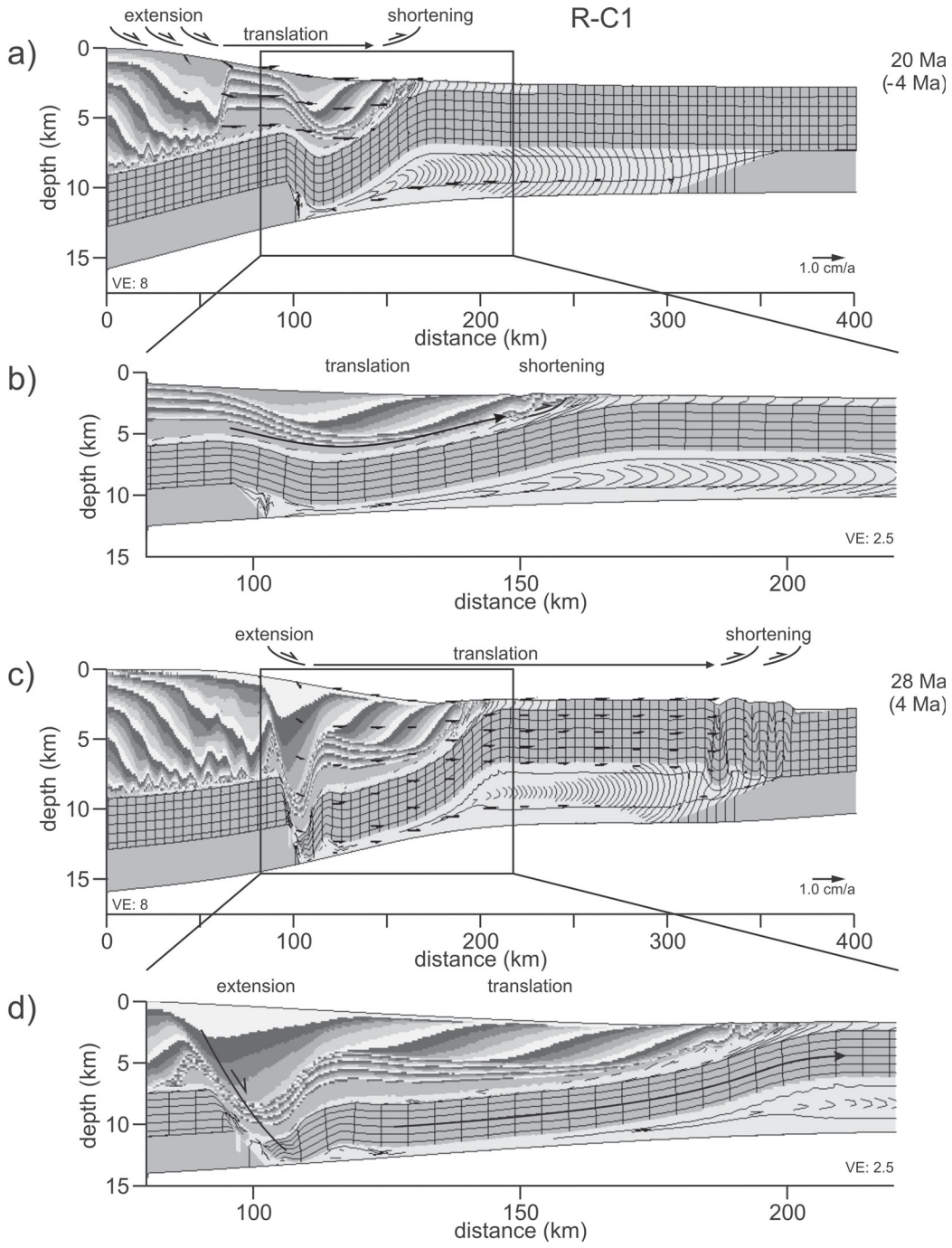

Figure 2.15: Results from model R-C1 with a second salt sheet of 500 m thickness emplaced before model start and extending from 0 to 230 km. Ages denote model run time, ages in brackets denote time since onset of gravity spreading at lower salt level. (a) Model evolution at time of gravity spreading along upper detachment. (b) Close-up of Figure 2.15a showing domains of translation and shortening. (c) Model evolution at time of gravity spreading along lower detachment. (d) Close-up of Figure 2.15c showing domains of extension and translation. See text for further discussion.

2.7 Evolution of the PFB in a Regional Context

2.7.1 Motivation

The evolution of the PFB has likely been affected by the landward-located allochthonous salt structures (Figure 2.2). In addition, the fold belt's evolution may be related to the folding of the Jurassic to Cretaceous sediment carapace that extends for more than 100 km landward of the Sigsbee Canopy. In this section, we investigate the way in which the system may have evolved to produce both this wide-spread folding and associated salt diapirs and canopies.

Three main concepts are used to explain the evolution of salt canopies. The most common involves a set of diapirs that are squeezed and expel their salt onto the seafloor. This concept may require early extension to form diapirs and requires subsequent shortening. A second concept does not involve any extension or shortening of the sedimentary section. It simply consists of a large salt body that is squeezed by an expulsion rollover protruding into the salt (*Ge et al.*, 1997; *Rowan and Inman*, 2005). Again, the squeezed salt escapes to the seafloor. The third concept involves a purely contractional setting and, if necessary, erosion (*Coward and Stewart*, 1995). As detachment folds above the salt layer are progressively shortened and tightened, high local stresses develop along the fold hinges and allow the buoyant salt to breach the anticlines and extrude to the sea floor. Examples of such contractional deep-water diapirs have been reported from the Gulf of Lion (*Vendeville and Gaullier*, 2005) and the Gulf of Mexico (*Hall*, 2002; *Philippe et al.*, 2005). A wide domain of shortening occupying most of the northwestern Gulf of Mexico salt basin has been interpreted by *Philippe et al.* (2005), *Guerin et al.* (2006), as well as *Radovich et al.* (2007a). We will focus on testing the third, fully contractional concept.

Three regional models RM-1 to RM-3 (Figure 2.16) were designed to investigate the widespread folding in the deep-water Gulf of Mexico as well as the development of diapirs and canopies in this compressional setting. They test three end-member cases of a range of model conditions that cover a broad domain in parameter space, indicated by the triangle of Figure 2.16. The variable parameters include the location of toe-of-slope folding and associating diapirism (varying slope and salt basin width), the amount of salt available (varying salt thickness and viscosity) and the presence

of basement steps. The parameter choices may not completely bracket the conditions of the natural system but they can help to predict the behavior of systems extending in different directions of the parameter space.

2.7.2 Design of Models RM-1 to RM-3

Shortening and associated diapirism may have occurred in two places, the Sigsbee Canopy, approximately 80 km landward of the salt pinch-out, and the Eocene paleo-canopy, approximately 150-200 km landward of the pinch-out. To obtain shortening in a more landward part of the salt basin than in the reference model we utilize toe-of-slope folding as it developed in model R-V1 of section 2.6.3 (Figure 2.13). The viscosity of 10^{19} Pa s used in model R-V1 has a high value, especially when considering allochthonous salt, which commonly consists mostly of halite. To achieve the same high basal traction required for toe-of-slope folding we reduce the thickness of the salt layer (equation 2.3).

In addition to varying salt viscosity and salt layer thickness, the models include a range of salt geometries of the autochthonous salt basin, differing widths of the progradation profiles, and a slightly lower salt density (2150 vs. 2200 kg/m^3) than in the earlier models (see section 2.6.5).

Model RM-1 (Figure 2.17) has a 260 km wide salt basin, which is 1 km thick over 200 km, and tapers seaward over the last 60 km. Salt viscosity (η=10^{18} Pa s) and width of the slope profile (w=100 km) are as in the reference model R-0. The progradation rate of the sedimentation profile (v_{prog}=0.4 cm/a) is 20% less than in the reference model. This velocity was chosen to ensure that sediment progradation is slow enough to evacuate the salt underneath the shelf relatively efficiently. Lower progradation rates cause the system to evolve more slowly and only marginally enhance the amount of salt available for allochthonous salt structures.

Models RM-2 and RM-3 both have a salt basin of 360 km total width. This value was chosen to agree with the corresponding estimated restored width of the detachment level of the Cretaceous system (Figures 2.2a and 2.2b and section 2.2). The width of the slope profile is set to w=50 km to allow toe-of-slope folding and associated diapirism to occur in the landward half of the salt basin. Sediment progradation velocity is v_{prog}=0.5 cm/a. Model RM-2 has a salt basin that is 2 km thick over 240 km

and tapers over the remaining 120 km. Salt viscosity is higher than in model RM-1 (η=5×10^{18} Pa s) to ensure toe-of-slope folding. Model RM-3 has two basement steps, one thinning the salt from 2 km to 1 km after 150 km, the second one thinning the salt to 200 m after 300 km, leaving the distal 60 km with a thin salt layer of uniform 200 m thickness. This configuration was chosen to investigate whether basement steps can initiate or facilitate diapirism. The salt viscosity (η=3×10^{18} Pa s) is intermediate to those of models RM-1 and RM-2.

The time of margin failure and onset of deformation in models RM-1 to RM-3 now either represents late Oligocene (when the formation of the Sigsbee Canopy is considered) or early Paleogene (when formation of the late Eocene paleocanopy is considered). The latter choice agrees with the Cretaceous timing of initial shortening suggested by *Philippe et al.* (2005) and (*Guerin et al.*, 2006) (Mesozoic-Paleogene) and *Radovich et al.* (2007a) (early Paleogene).

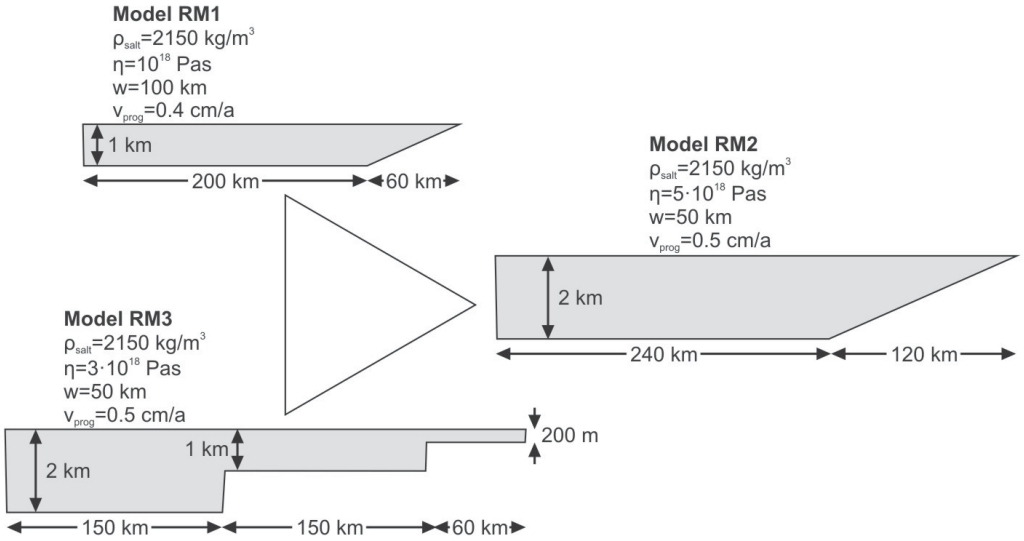

Figure 2.16: Setup for models RM-1 to RM-3, designed to show the evolution of allochthonous salt structures and basin-wide, propagating fold belts. The triangle indicates that the models are covering a broad domain in parameter space, investigating the location of toe-of-slope folding and associating diapirism (varying slope and salt basin width), the amount of salt available (varying salt thickness and viscosity) and the presence of basement steps.

2.7.3 Evolution of Regional Models RM-1 to RM-3

All three models RM-1 to RM-3 undergo similar stages of deformation, but the order in which these stages evolve varies somewhat (Figures 2.17-2.19). These stages are salt evacuation from beneath the prograding slope and associated inflation farther seaward, overburden failure and onset of gravity spreading causing toe-of-slope folding, propagation of folds with eventual folding of the distal section (sinusoidal folding followed by kinking), diapirism, and extrusion of salt into an allochthonous sheet. These stages and their respective timings are summarized in Table 2.2. The main differences between the models are the location of the allochthonous salt and its evolution relative to fold belt propagation. In model RM-1, folding reached the end of the salt basin before a diapir develops whereas in models RM-2 and RM-3 diapirs form before the outermost 4.5 km of sediments are folded.

Toe-of-slope Folding

All three models develop toe-of-slope fold belts like model R-V1 (Figure 2.13), confirming that a range of salt thicknesses, viscosities and strain rates can collectively produce the critical basal traction required to cause failure of the overburden at the toe of the slope. Coeval extensional structures develop landward of the fold belt where the autochthonous salt is efficiently evacuated.

In model RM-1 (Figure 2.17 and modelRM1.mp4 of the auxiliary material) the folding that initiates at the toe of the slope propagates laterally toward the end of the salt basin within 5 Ma forming a 120 km wide fold belt. The sinusoidal detachment folds tighten and develop kink bands after another 20 Ma (Figure 2.17b).

In model RM-2 (Figure 2.18 and modelRM2.mp4 of the auxiliary material) the folds propagate continuously for 17 Ma to the salt pinch-out, forming a >250 km wide fold belt. Ongoing shortening narrows the folds and forms first conjugate kink bands, and later seaward leaning folds and thrusts (the latter shown in auxiliary material).

In model RM-3 (Figure 2.19) the deformation front does not propagate as continuously as in models RM-1 and RM-2 but quickly jumps to the basement steps from where it spreads seaward. A >200 km wide fold belt forms within 21 Ma. With continuing shortening of the sinusoidal detachment folds, the distal overburden above

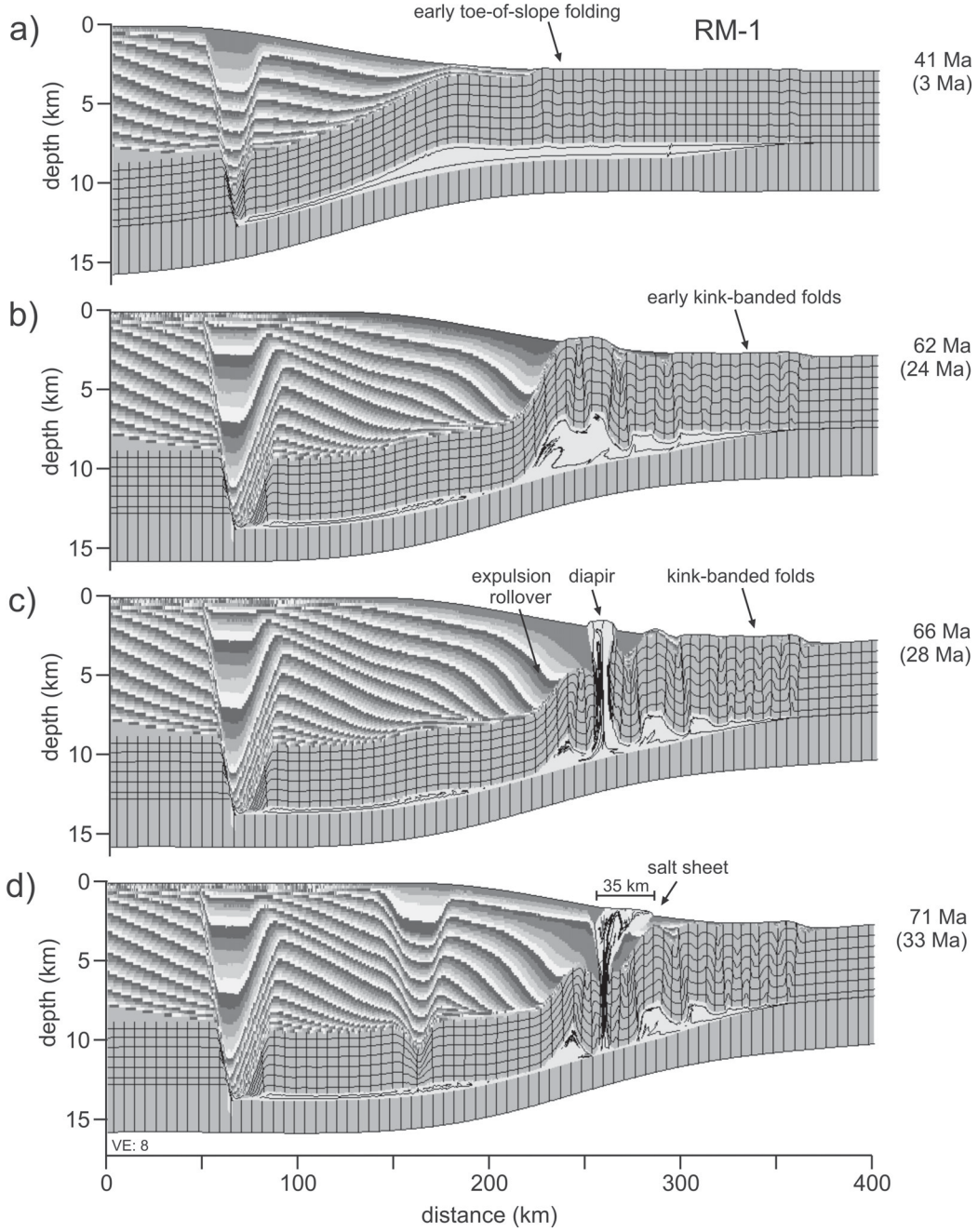

Figure 2.17: Results from model RM-1 (thin salt basin). Ages denote model run time, ages in brackets denote time since onset of gravity spreading. (See also animation modelRM1.mp4 of auxiliary material.) (a) Model evolution at time of early toe-of-slope folding. (b) Model evolution at time when entire distal section experiences kinking. (c) Model evolution at time when diapir extrudes 100 km landward of salt pinch-out. (d) Model evolution before folds become asymmetric.

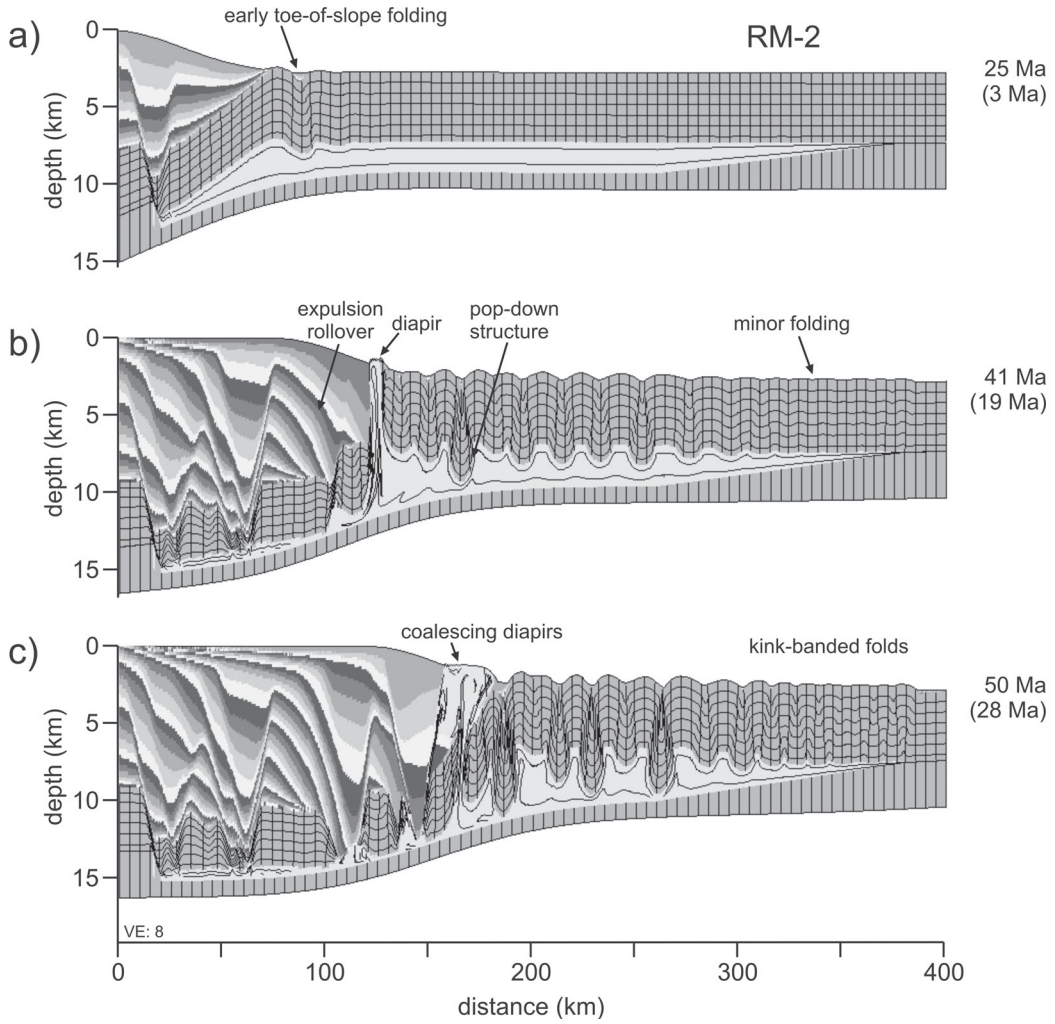

Figure 2.18: Results from model RM-2 (wide salt basin, narrow margin width). Ages denote model run time, ages in brackets denote time since onset of gravity spreading. (See also animation modelRM2.mp4 of auxiliary material.) (a) Model evolution at time of early toe-of-slope folding. (b) Model evolution at time when diapir extrudes 200 km from salt pinch-out. The distal section is basically undeformed at this stage. (c) Model evolution at time when distal section shows kink folding, and when the first diapir coalesces with a second one.

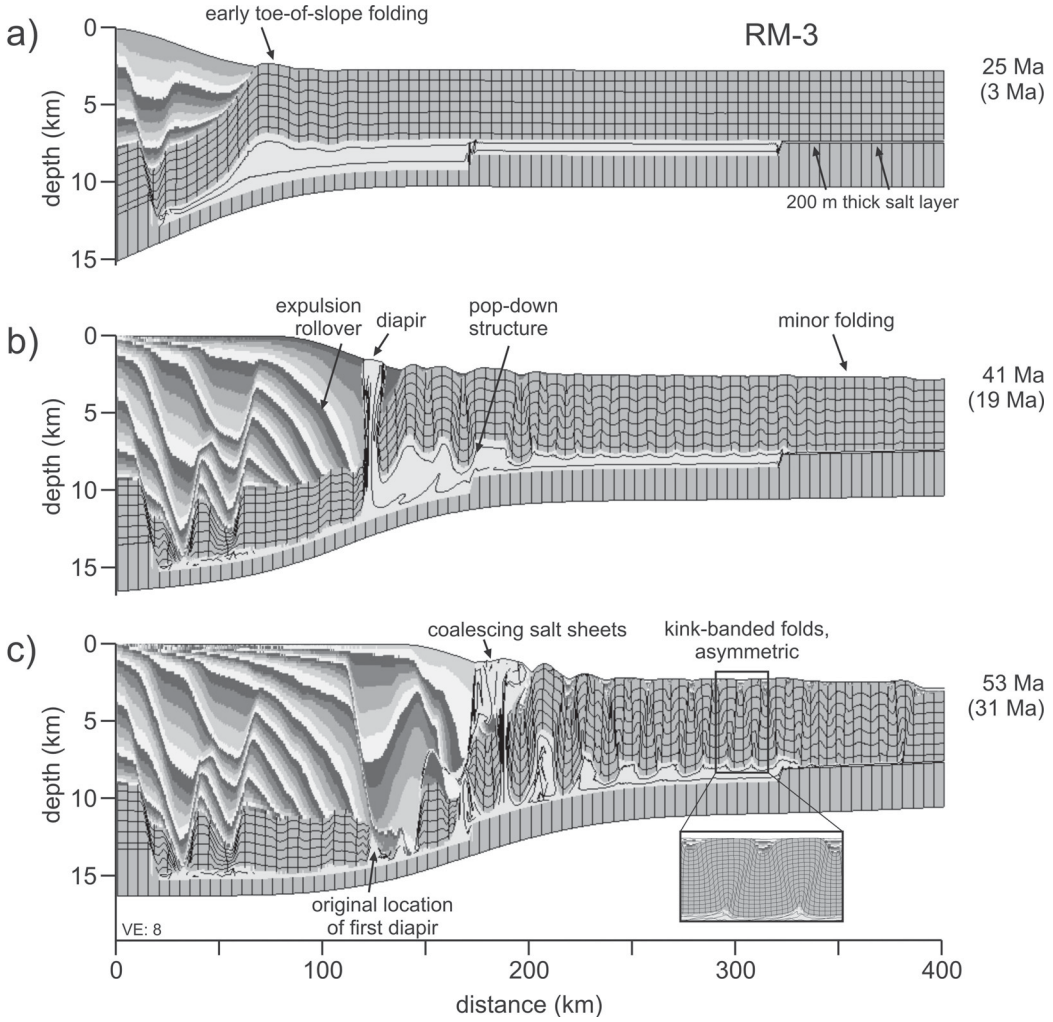

Figure 2.19: Results from model RM-3 (wide salt basin, two basement steps, narrow margin width). Ages denote model run time, ages in brackets denote time since onset of gravity spreading. (a) Model evolution at time of early toe-of-slope folding. (b) Model evolution at time when diapir extrudes 250 km from salt pinch-out. The distal section is basically undeformed at this stage. (c) Model evolution at time when distal section shows folding, and when the first diapir coalesces with a second one. Note that the canopy located above the basement step originated about 50 km further landward.

the 200 m thick salt layer develops seaward vergent kink bands and thrusts, omitting the stage of symmetric kink-banded folds.

Position and Timing of Diapirs

All three models develop localized diapirs through the mechanism of breaching anticlines described in the beginning of this section. Quickly, within <2 Ma, they pierce through the 4.5 km thick overburden to the sea floor where they form allochthonous salt sheets.

In model RM-1, with a narrower salt basin (260 km) and wider continental slope (w=100 km), a diapir forms adjacent to a 100 km wide toe-of-salt fold belt, which at this time already extends to the salt pinch-out (Figure 2.17c). The narrowing of the diapir and salt extrusion through its feeder buffers shortening in the distal fold belt for a period of 7 Ma (Figures 2.17c and 2.17d). The salt sheet extends for about 35 km over the fold belt (Figure 2.17d) before the distal, kink-banded folds become asymmetric. After this point we consider the amount of shortening in the system too high to compare it properly to the northwestern Gulf of Mexico.

In models RM-2 and RM-3 with a wider salt basin (360 km) and narrower continental slope (w=50 km), the first diapir forms approximately 250 km landward of the salt pinch-out (Figures 2.18b and 2.19b). At this stage, almost no deformation has occurred above the distal end of the salt but sets in within a couple of million years after the diapir formation. The evolving salt sheets of model RM-2 and RM-3 spread seaward and coalesce with a second diapir that forms 7 or 12 Ma later, respectively, and farther seaward (Figures 2.18c and 2.19c). In both models RM-2 and RM-3 folding is not interrupted during the formation of diapirs or canopies.

Diapirs commonly coincide with basement steps. However, as model RM-3 shows (Figure 2.19b), the localization of the initial diapir is not directly related to the position of the basement step. Instead, the thinner salt seaward of the basement step together with sinking synclines block the salt flow and cause anticlines to be breached. Furthermore, once formed, diapirs undergo significant lateral translation (Figures 2.19b and 2.19c) so that a diapir currently positioned close to a step does not necessarily imply that the step created it.

2.7.4 Discussion of Regional Models

Models RM-1 to RM-3 are only simplified dynamical evaluations of the folding and breached anticline concept for the development of allochthonous salt. Nevertheless, the results match the interpretation that a wide region of the carapace of Jurassic and Cretaceous sediments landward of the PFB underwent diachronous folding in the early Paleogene and that this folding propagated to the toe-of-salt region and created the PFB, probably in the late Oligocene to Miocene (section 2.2.2 (*Peel et al.*, 1995; *Philippe et al.*, 2005; *Radovich et al.*, 2007a). The model results also demonstrate that toe-of-slope folding and associated breaching of anticlines can create salt sheets and canopies. The delay in deformation of the distal sediment cover relative to the onset of gravity spreading (5, 15 and 21 Ma, respectively in these models) mainly results from the time required to propagate the fold belt from the toe of the slope to the end of the salt basin. But the results also show that squeezing of diapirs and evacuation of salt can buffer seaward deformation (by 7 Ma in model RM-1) and may have delayed folding of the PFB as proposed by *Trudgill et al.* (1999). Given several diachronously evolving diapirs and varying sedimentation rates, the delay may have been significantly longer than a few million years.

From a local perspective, model RM-1 very well reproduces a Sigsbee Canopy-type evolution implied by the interpretations of *Peel et al.* (1995) and *Radovich et al.* (2007a) (Figure 2.2a and 2.2b), in which the feeder of the salt sheet is located near the distal end of the salt basin and the sheet spreads only approximately 30 km seaward to overlie the fold belt. The diapir in model RM-1 reproduces the interpretation of *Radovich et al.* (2007a) (Figure 2.2a), where salt directly extrudes from the underlying anticlines.

From a more regional perspective, Models RM-2 and RM-3 demonstrate canopies that develop in the salt basin's center and spread for several tens of kilometers. However, these models do not reproduce canopies that spread for >100 km or involve large volumes of salt as observed in the northern and northeastern Gulf of Mexico (*Diegel et al.*, 1995).

Other limitations of the current regional models are: the short delay (ca. 2 Ma) between the diapirism and the terminal folding, instead of 10-15 Ma as observed; the perhaps excessive folding required to breach an anticline, and; the requirement

for weak sediments, implying high pore fluid pressures, which may be difficult to sustain throughout folding. Despite these limitations it is possible that an Eocene paleocanopy, on which the Port Isabel fold belt formed (*Peel et al.*, 1995; *Radovich et al.*, 2007a) (Figure 2.2a and 2.2b), may have evolved in a setting comparable to RM-2 (wide salt basin, landward-located toe-of-slope folding). The Sigsbee Canopy now overlying the PFB may represent a later-stage second cycle of the same process when sediments had prograded farther into the system (Figure 2.20). In summary, folding and subsequent breaching of anticlines may be a viable mechanism for the development of allochthonous salt sheets. However, this does not prove this mechanism operated in the landward part of western Gulf of Mexico, and the remaining two concepts (section 2.7.1) must also be tested.

Table 2.2: Stages and timing of evolution of regional models RM-1 to RM-3. All times are given relative to onset of gravity spreading.

Model Stage	RM-1	RM-2	RM-3
shelf build-up, salt evacuation and inflation	-38-0 Ma	-22-0 Ma	-22-0 Ma
margin failure, onset of toe-of slope folding	0 Ma	0 Ma	0 Ma
deformation of distal section			
sinusoidal detachment folding	5-11 Ma	17-26 Ma	21-26 Ma
kink band formation	11-28 Ma	26-38 Ma	none
asymmetric folding, thrusting	36 Ma and after	38 Ma and after	26 Ma and after
diapirism	28 Ma	19 Ma	19 Ma

2.8 Summary and Conclusions

The results reported here are intended to be an assessment of the factors that controlled the formation of the PFB specifically, plus an initial evaluation of the contraction and folding hypothesis for the precursor regional development of the northwestern Gulf of Mexico. Because the evolution of the western Gulf of Mexico is complex, involving several phases, of which the earlier ones have interpretational uncertainties, we chose to work backwards through time. We started with a series of simplified experiments designed only to investigate the formation of the PFB. We then varied these models to test some of the possible conditions that may have existed prior to folding of the PFB and finally considered the regional precursor phase to the PFB folding.

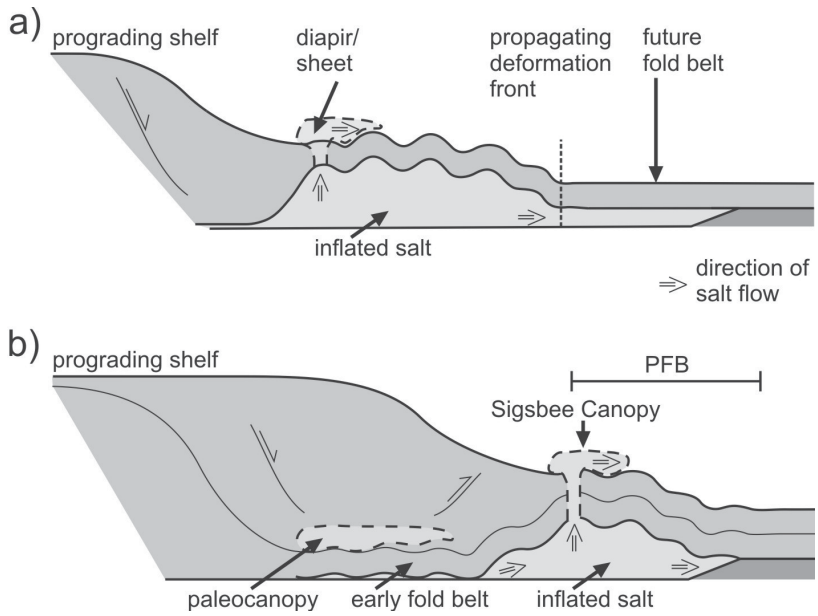

Figure 2.20: Conceptual model of possible evolution of fold belts and allochthonous salt structures in the northwestern Gulf of Mexico. (a) After formation of an early fold belt, salt extrudes through shortened anticlines. (b) Toe-of-slope folding has propagated, formed a later, second fold belt and a second generation of allochthonous salt develops seaward of the earlier one. The final scenario resembles the Miocene Gulf of Mexico with the Port Isabel Fold Belt having formed above the Eocene paleocanopy and the Sigsbee Salt extruding from the just forming Oligo-Miocene PFB (Figure 2.2).

In sections 2.3 and 2.5 we addressed the requirements for failure and gravitational spreading of a simplified representation of the Gulf of Mexico system in the vicinity of the PFB. The limit analysis indicates that a system with an overall geometry similar to the restored system, including a very thick (4.5 km) pre-kinematic overburden, can fail under gravity if the overburden sediments are weak, with effective angles of friction of ca. 5°-6.4°. This is interpreted as sediment weakened by moderate to high pore-fluid pressures, depending on its internal, dry strength. Pore-fluid pressure ratios λ would have to be as high as 0.73-0.8 for sand (internal angle of friction of 25°). The result is independent of salt viscosity and relatively insensitive to variations in salt thickness between 2 and 3.5 km.

The need for weak sediments, likely owing to high pore fluid pressures, is corroborated by the results obtained from the finite element reference model R-0 and its variations (section 2.5 and 2.6). Based on these results regarding failure conditions, geometry and amount of shortening of the fold belt, as well as the duration of its evolution, we estimate that the natural conditions are best matched when λ=0.85. Episodic loss of fluid pressure may have occurred on short (e.g. seismicity) timescales during deformation, through fault valving and other mechanisms, but this would not prevent continued deformation if high pressures were restored on similarly short timescales.

We also investigated (section 2.6) the consequences of different widths of the prograding sediment wedge, the effect of different possible salt basin geometries, the effect of variations in salt viscosity, and salt and sediment density. By comparison with the reference model, narrower prograding continental slopes are more unstable, leading to faster translation of the overburden and shorter folding events; higher viscosity salt, (10^{19} Pa s vs. 10^{18} Pa s) causes folding at the toe-of-slope region instead of the toe-of-salt region; the folding and fold belt geometry are somewhat sensitive to the geometry of the distal salt basin, but less so than conceptual models suggest. Similarly, anticipated natural variations of salt and overburden density and of the resulting buoyancy force barely influence the fold belt development, except with regard to the more efficient sinking of pop-down structures into a less denser substratum and the breaching of anticlines.

The simple models investigated in section 2.6 produce expulsion rollover geometries (e.g. Figure 2.9) that are unlike the sedimentary geometry of the Gulf of Mexico observed in the Oligo-Miocene strata (Figure 2.2). We showed (section 2.6.6) that more realistic model geometries result when an additional upper salt layer is added that mimics the inferred canopy that existed beneath this region. Model R-C1 undergoes early detachment involving the upper-level system but later detachment and deformation step down to the lower level resulting in the formation of a distal fold belt. This behavior is similar to that inferred for this region of the Gulf of Mexico and demonstrates how precursor phases of extension can have been partially buffered by upper level shortening as seen in the Port Isabel Fold Belt. An important result is that for gravitationally-driven failure to occur in R-C1-type models, the sediments must be equally weak as those required in the earlier, simplified models. This means that the existence of the upper level canopy does not modify the overall mechanics of the system in regard to folding of the lower level.

The models of section 2.7 demonstrate that folding and subsequent breaching of anticlines may be a viable mechanism for the development of allochthonous salt sheets, such as the Sigsbee Canopy above the PFB. We also tested the concept of an earlier phase of folding and breaching of anticlines (as seen in model RM-2) as the source of the paleocanopy on which the Port Isabel Fold Belt formed (Figure 2.2). This would represent an earlier cycle, similar to that occurring more recently in the Sigsbee Canopy (Figure 2.20). This earlier cycle links back to model R-C1 in that it provides a mechanism for the development and emplacement of the second salt layer used in that model. However, the encouraging results of models RM-1 to RM-3 do not prove that the mechanism of folding and breached anticlines operated in the landward part of the northwestern Gulf of Mexico, and we need to evaluate the two competing concepts (section 2.7.1). If the folding is shown to be more widespread, as suggested by *Radovich et al.* (2007a), it implies that the development of the PFB is only the last phase in the diachronous evolution of a giant submarine fold belt.

Limitations and successes of the model experiments and results also need to be discussed. The limit analysis used here does not include an overall seaward tilt of the system, which would occur if there was significant differential thermal contraction across the region of interest. We have applied the limit analysis to the PFB and

its adjacent region, which is at the outer limit of the rifted margin, where thermal subsidence is likely to be relatively uniform and therefore would not induce a gliding component. Application of the limit analysis to more landward parts of the system should include a seaward tilt of the system but estimating its value will require reconstruction of the margin geometry corrected for the isostatic effects of sediment loading.

All of the models assume uniform progradation rates for margin sedimentation that are close to the observed average progradation rate of the edge of the shelf during the Cenozoic until the end of PFB folding. However, it is known that there were episodes of faster and slower progradation lasting millions of years (*Galloway et al.*, 2000). The progradation rate was waning during the initial PFB folding (late Oligocene), reaching a relatively constant value, ca. 0.5 cm/a, in Miocene. Therefore the results of the models used here for PFB folding are valid. However, early episodicity will modify the salt tectonics and should be included in models of the complete evolution of the margin. These major, long-term changes in sedimentation rates will likely influence the development of allochthonous salt sheets by enhancing salt expulsion during faster progradation and enhancing surface salt flow when the progradation rate was slow.

The models include the effect of vertical sediment compaction on density and volume. Horizontal compaction may be significant both before and during folding and may account for part of the deficit in the shortening observed in the linked extension-contraction systems. The partitioning of compaction between horizontal and vertical cannot be investigated using the current model formulation.

Lastly, we answer the questions raised in section 2.1.

1. The analytic limit analysis discussed in section 2.3 demonstrates that a 4.5 km thick fold belt can form by gravity spreading alone, provided that the sediments have an averaged effective angle of friction of 5°-6.4°, implying that moderately high pore-fluid pressures ratios of ca. 0.8 developed and were maintained during deformation.

2. The numerical model experiments demonstrate that a Perdido-type fold belt can form in a relatively short time interval (∼10 Ma) if the system is relatively unstable with translation velocities of ∼0.4 cm/a. Such velocities are consistent

with weak sediments with pore-fluid pressure ratios of ∼0.85. These velocities are also favored by moderate salt viscosity salt (10^{18} Pa s) and a narrow continental slope.

3. The initial salt viscosity and geometry can have various effects on the evolution of a Perdido-type fold belt. Thin or high viscosity salt causes folding to localize at the toe of the continental slope as opposed to the toe of salt (model R-V1). A tapering salt layer slows the flow of salt and leads to a more diachronous evolution of folds than in the case of a uniform thickness salt layer (model R-0 vs. R-G1). Also, salt tapering decreases the wavelength of early sinusoidal folds above the thinning salt. Moderate basement steps localize folding but do not directly initiate diapirism in the models.

4. Salt inflation in the distal region occurs mostly during or after folding. The loads of the prograding sedimentary overburden and of an extruding salt sheet both squeeze the autochthonous salt seaward. Distal inflation is partly inhibited if the salt is initially thin. This leads to slower propagation of the inflated section and to a steeper angle of the tilted overburden.

5. Folding and extrusion of salt through breached anticlines appears to be a viable mechanism for the expulsion of salt into allochthonous sheets and canopies and is interpreted to have occurred at least locally below the Sigsbee Canopy. If this mechanism was also responsible for the development of earlier, more landward, allochthonous salt sheets, folding of the main overburden layer must have developed diachronously at a regional scale, implying the system evolved by toe-of-slope folding as in model RM-2. If correct, this means the PFB is only the last phase in the development of a giant submarine fold belt.

2.9 Acknowledgements

Funding for this project was provided by an Atlantic Innovation Fund contract to Dalhousie University, a Killam Scholarship and a Government of Canada Award to SG, an IBM SUR grant and the Canada Research Chair in Geodynamics to CB. We also like to thank Shell International Exploration and Production, Inc. for their kind

support and ION/GXT for permission to show their data. Numerical computations were made with the software SOPALE, developed by Philippe Fullsack and augmented by Bonny Lee. We wish to thank Frank Peel for his helpful and constructive reviews and advice and an anonymous reviewer for his detailed review. Glen Stockmal is acknowledged for his critical reading of the manuscript, and Steve Ings and Mark Rowan for fruitful discussions.

2.10 Appendix: Limit Analysis for Margin Stability

The limit analysis introduced in section 2.3 is derived and explained here. As shown by *Gemmer et al.* (2004, 2005), the state of failure of the continental margin can be captured by a balance of the horizontal forces acting on the system where these forces take their maximum limiting values (Figure 2.5). The parameters used in the following calculations to describe the continental margin setting are listed in Table 2.3 and depicted in Figure 2.21.

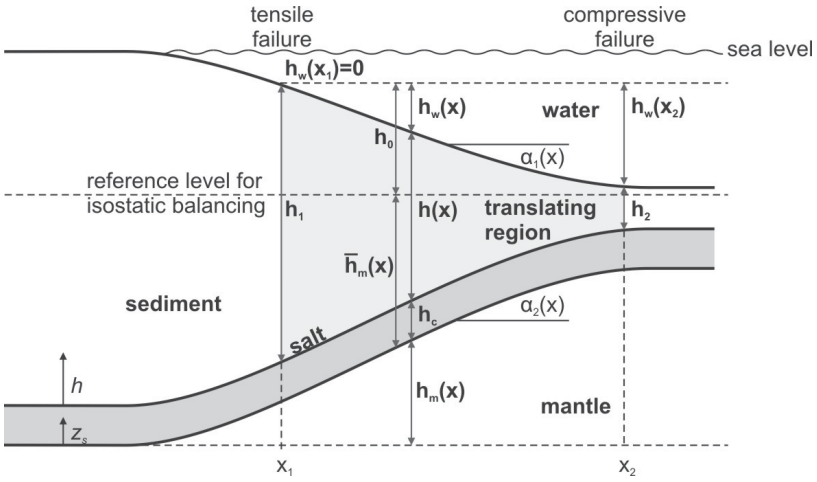

Figure 2.21: Geometry of schematic continental margin system underlain by a layer of salt as used in limit analysis (see section 2.3 and Appendix 2.10). The terminology is described in Table 2.3. Diagram is not to scale.

2.10.1 F_1 and F_2: Tensile and Compressive Forces

The Mohr-Coulomb yield criterion for non-cohesive, frictional-plastic behavior of the overburden is used to calculate the limiting tensile and compressive stresses in a 2D

Table 2.3: Parameters used in limit analysis for margin stability.

Symbol	Parameter
Forces, Stresses and Pressures	
F_1	limiting tensile failure strength of the landward sediment overburden
F_2	limiting compressive failure strength of the seaward sediment overburden
F_{iso}	downslope (gliding) force owing to tilt of base that results from isostatic adjustment
F_p	drag force exerted by Poiseuille flow in viscous layer
F_w	water loading force, acting as buttress to seaward movement
F_c	drag force exerted by Couette flow in viscous layer
σ_1, σ_3	maximum and minimum principal stress
σ_e	effective stress, modified by effects of pore-fluid pressure
σ'	stress reduced by weight of overlying water column
σ_{xx}, σ_{zz}	horizontal and vertical stress (i.e. weight of the overburden)
p_f	pore-fluid pressure
p	mean stress
p'_f	pore-fluid pressure reduced by weight of overlying water column
p'	mean stress reduced by weight of overlying water column
p_w	pressure exerted by overlying water column
Geometry	
$h(x)$	thickness of overburden
x_1, x_2	location of tensile and compressive failure
h_1=$h(x_1)$	thickness of overburden at location of tensile failure
h_2=$h(x_2)$	thickness of overburden at location of compressive failure
$h_w(x)$	height of the water column relative to height at x_1
h_c	thickness of salt layer
$h_m(x)$	thickness of lithospheric mantle relative to lowest point of sedimentary system
$\overline{h}_m(x)$	thickness of mantle material expelled by overburden during isostatic adjustment
$\alpha_1(x)$	slope of seafloor
$\alpha_2(x)$	slope of base of the system
Material Properties	
φ_0	internal angle of friction
φ_e	effective angle of friction, modified by pore-fluid pressure
λ	pore-fluid pressure ratio
η	viscosity
ρ_w	density of water
ρ_s	density of salt and sediment
ρ_m	density of mantle
Others	
g	acceleration due to gravity
k_a, k_p	factors describing the tensile and compressive sediment strength
R	ratio of water and sediment density relative to mantle density
T	factor including the material densities and effects of isostatic compensation
v_c	Couette flow velocity

vertical section of frictional material overlying a viscous substratum.

$$\sigma_{e1} - \sigma_{e3} = (\sigma_{e1} + \sigma_{e3}) \sin\varphi_0, \tag{2.12}$$

where σ_e is the effective stress, (the stress reduced by the pore-fluid pressure p_f, σ_e=$\sigma - p_f$). The pore-fluid pressure is parameterized by its ratio to the mean stress. For a sub-aqueous system, this definition is expanded and values relative to the pressure of the overlying water column, p_w, are used (*Davis et al.*, 1983):

$$\lambda = \frac{p'_f}{p'} = \frac{p_f - p_w}{p - p_w} = \frac{p_f - p_w}{\frac{\sigma_1+\sigma_3}{2} - p_w} \tag{2.13}$$

By using

$$\sin\varphi_e = (1-\lambda)\sin\varphi_0 \quad \text{and} \tag{2.14}$$

$$\sigma' = \sigma - p_w \tag{2.15}$$

equation (2.12) can then be rewritten as

$$\sigma_1 - \sigma_3 = (\sigma'_1 + \sigma'_3) \sin\varphi_e. \tag{2.16}$$

We assume that the maximum principal stress in the tensile setting is the vertical stress σ_{zz}, and the minimum stress is the horizontal stress σ_{xx}. In the compressive setting, minimum and maximum stresses are oriented in the opposite way. By combining equations (2.15) and (2.16) we then obtain:

$$\sigma'_{zz} - \sigma'_{xx} = (\sigma'_{zz} + \sigma'_{xx}) \sin\varphi_e \tag{2.17}$$

$$\sigma_{xx} = k_a\, \sigma'_{zz} + p_w, \quad \text{with} \tag{2.18}$$

$$k_a = \frac{1 - \sin\varphi_e}{1 + \sin\varphi_e}, \tag{2.19}$$

$$\sigma'_{zz} = \rho_s\, g\, h(x) \quad \text{and} \tag{2.20}$$

$$p_w = \rho_w\, g\, h_w(x). \tag{2.21}$$

The water depth at the location of compressive failure can be calculated using the Airy model of isostasy and a simple geometric calculation

$$(h(x) + h_c)\,\rho_s + h_w(x)\,\rho_w = \overline{h}_m(x)\,\rho_m \tag{2.22}$$

$$h_w(x) + h(x) + h_c = h_0 + \overline{h}_m(x). \tag{2.23}$$

Given that a uniform layer of water exerts the same pressure on the landward and seaward end of the system, it does not influence the horizontal force balance. The effect of water reduces to the difference in depth $h_w(x_1)$-$h_w(x_2)$. Therefore, by taking $h_w(x_1)$=0, $h_w(x_2)$ becomes the increase in water depth relative to the water depth at x_1. It follows:

$$h_0 = (h_1 + h_c)\,\frac{\rho_m - \rho_s}{\rho_m} \quad \text{and} \tag{2.24}$$

$$h_w(x) = R\,(h_1 - h(x)) \quad \text{with} \tag{2.25}$$

$$R = \frac{\rho_m - \rho_s}{\rho_m - \rho_w}. \tag{2.26}$$

$$h_w(x_2) = R\,(h_1 - h_2), \tag{2.27}$$

$$\frac{d\,h_w(x)}{d\,x} = -R\,\frac{d\,h(x)}{d\,x}. \tag{2.28}$$

To calculate the total horizontal force in the overburden at failure, we need to integrate the horizontal stresses vertically throughout the overburden:

$$F_1 = \int_0^{h_1} \sigma_{xx,\,extension}\,dh = \int_0^{h_1} k_a\,\sigma'_{zz} + p_w(x_1)\;dh = \frac{1}{2}\,\rho_s\,g\,k_a\,h_1^2, \tag{2.29}$$

with $p_w(x_1) = 0$. Similar calculations for the compressive region yield:

$$\sigma'_{xx} - \sigma'_{zz} = (\sigma'_{zz} + \sigma'_{xx})\,\sin\varphi_e \quad \text{and} \tag{2.30}$$

$$F_2 = -\frac{1}{2}\,\rho_s\,g\,k_p\,h_2^2 - \rho_w\,g\,h_w(x_2)\,h_2 \quad \text{where} \tag{2.31}$$

$$k_p = \frac{1}{k_a} = \frac{1 + \sin\varphi_e}{1 - \sin\varphi_e}. \tag{2.32}$$

2.10.2 F_p: Poiseuille-Flow Force

A Poiseuille flow is induced in a viscous layer by the pressure gradient exerted by the overburden and by the slope of the viscous layer itself. The shear stress exerted on the upper boundary of the viscous layer integrated over the whole failing section gives the total horizontal force. The shear stress τ_p is a product of the viscosity η and the velocity gradient:

$$F_p = -\int_{x_1}^{x_2} \tau_p \, dx = -\int_{x_1}^{x_2} \eta \, \frac{\partial v_x}{\partial z_s}\Big|_{z_s=h_c} dx \tag{2.33}$$

where z_s is the vertical coordinate in the salt layer, and v_x is the horizontal flow velocity of the salt. Assuming that the pressure changes gradually along the layer, a thin-sheet approximation for the velocity distribution in a horizontal salt layer (*Lobkovsky and Kerchman*, 1991) can be applied:

$$v_x = -\frac{1}{2\,\eta}\,\frac{d\,p}{d\,x}\,z_s\,(h_c - z_s). \tag{2.34}$$

The pressure gradient $d\,p/d\,x$ is written in terms of the lateral change in water and overburden load and the local slope of the salt layer.

$$\frac{d\,p}{d\,x} = \frac{d\,(\rho_s\,g\,h(x) + \rho_w\,g\,h_w(x))}{d\,x} + \rho_s\,g\,\frac{d\,h_m(x)}{d\,x} \qquad \text{with} \tag{2.35}$$

$$\frac{d\,h_m(x)}{d\,x} = -\frac{d\,(h_w(x) + h(x))}{d\,x} = -(1-R)\frac{d\,h(x)}{d\,x}. \tag{2.36}$$

Combining equation (2.33), (2.34) and (2.35) using equation (2.28), the total Poiseuille flow force is then:

$$F_p = \frac{1}{2}\,g\,R\,(\rho_s - \rho_w)\,h_c\,(h_1 - h_2). \tag{2.37}$$

2.10.3 F_{iso}: Downslope (Gliding) Force Owing to Isostasy

The landward tilt of the base of the system adds an extra gravity-induced downslope (gliding) force to the system. This force is simply calculated by

$$F_{iso} = \int_{x_1}^{x_2} F_G \, \sin \alpha_2(x) \, dx \tag{2.38}$$

where

$$\begin{aligned} F_G &= \rho_s \, g \, h(x) + \rho_w \, g \, h_w(x) \text{ and} && (2.39) \\ \sin \alpha_2 &\approx \tan \alpha_2 = \frac{d \, h_m(x)}{d \, x} = -(1 - R) \frac{d \, h(x)}{d \, x}. && (2.40) \end{aligned}$$

It follows that

$$F_{iso} = -\frac{1}{2} \, \rho_s \, g \, (1 - R) \, (h_1^2 - h_2^2) - \frac{1}{2} \, \rho_w \, g \, R \, (1 - R) \, (h_1 - h_2)^2. \tag{2.41}$$

2.10.4 F_w: Force due to Water Load

The water exerts a buttress force against the seaward movement of the overburden. This force is the integrated pressure of the water column that acts on the overburden.

$$\begin{aligned} F_w &= \int_{h_w(x_1)}^{h_w(x_2)} \rho_w \, g \, h_w(x) \, dh_w(x), \qquad \text{and with equation (2.25)} \\ F_w &= -\frac{1}{2} \, \rho_w \, g \; R^2 (h_1 - h_2)^2. && (2.42) \end{aligned}$$

2.10.5 Force Balance

At the point of failure the horizontal forces balance.

$$
\begin{aligned}
0 &= F_1 + F_2 + F_p + F_{iso} + F_w && (2.43)\\
0 &= \frac{1}{2}\,\rho_s\,g\,k_a\,h_1^2 \\
&\quad -\frac{1}{2}\,\rho_s\,g\,k_p\,h_2^2 - \rho_w\,g\,R\,(h_1-h_2)\,h_2 \\
&\quad +\frac{1}{2}\,g\,R\,(\rho_s-\rho_w)\,h_c\,(h_1-h_2) \\
&\quad -\frac{1}{2}\,\rho_s\,g\,(1-R)\,(h_1^2-h_2^2) - \frac{1}{2}\,\rho_w\,g\,R\,(1-R)\,(h_1-h_2)^2 \\
&\quad -\frac{1}{2}\,\rho_w\,g\;R^2(h_1-h_2)^2 && (2.44)
\end{aligned}
$$

To non-dimensionalize the equation we divide by $\frac{1}{2}\,\rho_s\,g\,h_c^2$, introduce $h_1^*{=}h_1/h_c$, $h_2^*{=}h_2/h_c$ and obtain

$$
\begin{aligned}
0 &= h_1^{*2}\,k_a - h_2^{*2}\,k_p + (h_1^*-h_2^*)\,(1-\frac{\rho_w}{\rho_s})\,R \\
&\quad -(1-R)\,(h_1^{*2}-h_2^{*2}) \\
&\quad -\frac{\rho_w}{\rho_s}\,R\left(2\,(h_1^*-h_2^*)\,h_2^* + (1-R)\,(h_1^*-h_2^*)^2 + R(h_1^*-h_2^*)^2\right) \\
&= h_1^{*2}\,k_a - h_2^{*2}\,k_p + (h_1^*-h_2^*)\,(1-\frac{\rho_w}{\rho_s})\,R \\
&\quad -(1-R+\frac{\rho_w}{\rho_s}\,R)\,(h_1^{*2}-h_2^{*2}) \\
&= h_1^{*2}\,k_a - h_2^{*2}\,k_p + T\,(h_1^*-h_2^*) + (T-1)\,(h_1^{*2}-h_2^{*2}) \quad \text{with} && (2.45)\\
&\quad T = (1-\frac{\rho_w}{\rho_s})\,R.
\end{aligned}
$$

Solution of equation (2.45) for a given choice of density and geometrical parameters gives the values of k_a, k_p and associated φ_e values that place the system at the verge of failure.

Bibliography

Camerlo, R., D. Meyer, and R. Meltz (2004), Shale tectonism in the northern Port Isabel Fold Belt, in *Salt Sediment Interactions and Hydrocarbon Prospectivity: Concepts, Applications, and Case Studies for the 21st Century. GCSSEPM Conference Proceedings*, pp. 817–839.

Camerlo, R. H., and E. F. Benson (2006), Geometric and seismic interpretation of the Perdido fold belt: Northwestern deep-water Gulf of Mexico, *AAPG Bulletin*, *90*(3), 363–386.

Cobbold, P. R., P. Szamarti, L. S. Demercian, D. Coelho, and E. A. Rossello (1995), Seismic and experimental evidence for thin-skinned horizontal shortening by convergent radial gliding on evaporites, deep-water Santos Basin, Brazil, in *Salt Tectonics, A Global Perspective*, *AAPG Memoir*, vol. 65, edited by M. P. A. Jackson, D. G. Roberts, and S. Snelson, pp. 305–321, AAPG, Tulsa, Oklahoma.

Coward, M., and S. Stewart (1995), Salt-influenced structures in the Mesozoic-Tertiary cover of the southern North Sea, U.K, in *Salt Tectonics, A Global Perspective*, *AAPG Memoir*, vol. 65, edited by M. P. A. Jackson, D. G. Roberts, and S. Snelson, pp. 229–250, AAPG, Tulsa, Oklahoma.

Cramez, C., and M. P. A. Jackson (2000), Superposed deformation straddling the continental-oceanic transition in deep-water Angola, *Marine and Petroleum Geology*, *17*(10), 1095–1109.

Davis, D., J. Suppe, and F. A. Dahlen (1983), Mechanics of fold-and-thrust belts and accretionary wedges, *Journal of Geophysical Research*, *88*(B2), 1153–1172.

Davison, I. (2007), Geology and tectonics of the South Atlantic Brazilian salt basins, in *Deformation of the continental crust; the legacy of Mike Coward*, *Geological Society Special Publications*, vol. 272, edited by A. Ries, R. Butler, and R. Graham, pp. 345–359, Geological Society of London.

Decalf, C., S. Lock-Williams, N. Weber, M. Cubanski, C. Yough, M. Etemadi, and L. Liro (2004), Emplacement and evolution of salt in the Alaminos Canyon protraction area, Gulf of Mexico, in *Salt Sediment Interactions and Hydrocarbon Prospectivity: Concepts, Applications, and Case Studies for the 21st Century. GCSSEPM Conference Proceedings*, pp. 636–651.

Demercian, S., P. Szatmari, and P. R. Cobbold (1993), Style and pattern of salt diapirs due to thin-skinned gravitational gliding, Campos and Santos basins, offshore Brazil, *Tectonophysics*, *228*(3-4), 393–433.

Diegel, F. A., J. F. Karlo, D. C. Schuster, R. C. Shoup, and P. R. Tauvers (1995), Cenozoic structural evolution and tectono-stratigraphic framework of the northern Gulf Coast continental margin, in *Salt Tectonics, A Global Perspective*, *AAPG Memoir*, vol. 65, edited by M. P. A. Jackson, D. G. Roberts, and S. Snelson, pp. 109–151, AAPG, Tulsa, Oklahoma.

Fiduk, J. C., B. D. Trudgill, M. G. Rowan, P. Weimer, P. E. Gale, B. E. Korn, R. L. Phair, W. T. Gafford, G. R. Roberts, S. W. Dobbs, and C. K. Guu (1996), Allochthonous salt surrounding Alaminos Canyon, northwestern deep Gulf of Mexico, *Transactions - Gulf Coast Association of Geological Societies*, *46*, 27–38.

Fiduk, J. C., P. Weimer, B. D. Trudgill, M. G. Rowan, P. E. Gale, R. L. Phair, B. E. Korn, G. R. Roberts, W. T. Gafford, R. S. Lowe, and T. A. Queffelec (1999), The Perdido fold belt, Northwestern deep Gulf of Mexico, Part 2; Seismic stratigraphy and petroleum systems, *AAPG Bulletin*, *83*(4), 578–612.

Fort, X., J. P. Brun, and F. Chauvel (2004), Contraction induced by block rotation above salt (Angolan margin), *Marine and Petroleum Geology*, *21*(10), 1281–1294.

Fullsack, P. (1995), An arbitrary Lagrangian-Eulerian formulation for creeping flows and its applications in tectonic models, *Geophysical Journal International*, *120*(1), 1–23.

Fuqua, D. A. (1990), Seismic structural analysis of the Perdido fold belt, Alaminos Canyon area, northwestern Gulf of Mexico, Master's thesis.

Galloway, W. E., P. E. Ganey-Curry, X. Li, and R. Buffler (2000), Cenozoic depositional history of the Gulf of Mexico basin, *AAPG Bulletin*, *84*(11), 1743–1774.

Ge, H., M. P. A. Jackson, and B. C. Vendeville (1997), Kinematics and dynamics of salt tectonics driven by progradation, *AAPG Bulletin*, *81*, 398–423.

Gemmer, L., S. J. Ings, S. Medvedev, and C. Beaumont (2004), Salt tectonics driven by differential sediment loading: Stability analysis and finite element experiments, *Basin Research*, *16*, 199–219.

Gemmer, L., C. Beaumont, and S. J. Ings (2005), Dynamic modeling of passive margin salt tectonics: Effects of water loading, sediment properties, and sedimentation patterns, *Basin Research*, *17*, 383–402.

Guerin, G., Y. Philippe, and J.-A. Dal (2006), Impact of amount of gravity-driven compression and intermediate décollement levels on the Sigsbee Salt Canopy formation, Gulf of Mexico, *Abstracts, CD-ROM, AAPG Annual Convention*.

Hall, S. H. (2002), The role of autochthonous salt inflation and deflation in the northern Gulf of Mexico, *Marine and Petroleum Geology*, *19*(6), 649–682.

Hudec, M. R., and M. P. A. Jackson (2004), Regional restoration across the Kwanza Basin, Angola; salt tectonics triggered by repeated uplift of a metastable passive margin, *AAPG Bulletin*, *88*(7), 971–990.

Huffman, A. R., and G. L. Bowers (Eds.) (2002), *Pressure regimes in sedimentary basins and their prediction*, *AAPG Memoir*, vol. 76, AAPG, Tulsa, Oklahoma.

Jackson, M. P. A., and C. J. Talbot (1986), External shapes, strain rates, and dynamics of salt structures, *GSA Bulletin*, *97*(3), 305–323.

Korvin, G. (1984), Shale compaction and statistical physics, *Geophysical Journal of the Royal Astronomical Society*, *78*, 35–50.

Lobkovsky, L., and V. Kerchman (1991), A two-level concept of plate tectonics; application to geodynamics, *Tectonophysics*, *199*(2-4), 343–374.

Marton, L. G., G. C. Tari, and C. T. Lehmann (2000), Evolution of the Angolan passive margin, West Africa, with emphasis on post-salt structural styles, in *Atlantic Rifts and Continental Margins*, *Geophysical Monograph*, vol. 115, edited by W. Mohriak and M. Talwani, pp. 129–149, AGU, Washington, D.C.

Meyer, D., L. Zarra, D. Rains, B. Meltz, and T. Hall (2005), Emergence of the Lower Tertiary Wilcox trend in the deepwater Gulf of Mexico, *WorldOil Magazine*, *226*(5).

Meyer, D., L. Zarra, and J. Yun (2007), From BAHA to Jack, evolution of the Lower Tertiary Wilcox trend in the deepwater Gulf of Mexico, *The Sedimentary Record*, *5*(3), 4–9.

Mohriak, W. U., J. M. Macedo, R. T. Castellani, H. D. Rangel, A. Z. N. Barros, M. A. L. Latgé, A. M. P. Mizusaki, P. Szamarti, L. S. Demercian, J. G. Rizzo, and J. R. Aires (1995), Salt tectonics and structural styles in the deep-water province of the Cabo Frio region, Rio de Janeiro, Brazil, in *Salt Tectonics, A Global Perspective*, *AAPG Memoir*, vol. 65, edited by M. P. A. Jackson, D. G. Roberts, and S. Snelson, pp. 273–304, AAPG, Tulsa, Oklahoma.

Morley, C. K., and G. Guerin (1996), Comparison of gravity-driven deformation styles and behavior associated with mobile shales and salt, *Tectonics*, *15*(6), 1154–1170.

Peel, F. J., C. J. Travis, and J. R. Hossack (1995), Genetic structural provinces and salt tectonics of the Cenozoic offshore U.S. Gulf of Mexico: A preliminary analysis, in *Salt Tectonics, A Global Perspective*, *AAPG Memoir*, vol. 65, edited by M. P. A. Jackson, D. G. Roberts, and S. Snelson, pp. 153–175, AAPG, Tulsa, Oklahoma.

Philippe, Y., and G. Guerin (2006), Development of turtle-back anticlines in gravity-driven compressional domains: Evidences from the deepwater Gulf of Mexico, *Abstracts, CD-ROM, AAPG Annual Convention*.

Philippe, Y., D. Wittoesch, and G. Guerin (2005), Importance of gravity-driven compressional tectonics in northern offshore and deep-offshore Gulf of Mexico: New observations and implications for subsalt interpretation, *Abstracts, CD-ROM, AAPG Annual Convention*.

Radovich, B., C. Connors, and J. Moon (2007a), Deep imaging of the Paleogene, Miocene structure and stratigraphy of the western Gulf of Mexico using 2D prestack depth migration of mega-regional onshore to deep water, long-offset seismic data, in *The Paleogene of the Gulf of Mexico and Caribbean Basins: Processes, Events, and Petroleum Systems. GCSSEPM Conference Proceedings*, pp. 307–322, (CD Rom).

Radovich, B., J. Moon, C. Connors, and D. Bird (2007b), Insights into structure and stratigraphy of the northern Gulf of Mexico from 2D pre-stack depth migration imaging of mega-regional onshore to deep water, long-offset seismic data, *Transactions - Gulf Coast Association of Geological Societies*, *57*, 633–637.

Rowan, M. G., and K. F. Inman (2005), Counterregional-style deformation in the deep shelf of the northern Gulf of Mexico, *Transactions - Gulf Coast Association of Geological Societies*, *55*, 716–724.

Rowan, M. G., B. D. Trudgill, and J. C. Fiduk (2000), Deep-water, salt-cored foldbelts: Lessons from the Mississippi Fan and Perdido Foldbelts, northern Gulf of Mexico, in *Atlantic Rifts and Continental Margins*, *Geophysical Monograph*, vol. 115, edited by W. Mohriak and M. Talwani, pp. 173–191, AGU, Washington, D.C.

Rowan, M. G., F. J. Peel, and B. C. Vendeville (2004), Gravity-driven fold belts on passive margins, in *Thrust tectonics and hydrocarbon systems*, *AAPG Memoir*, vol. 82, edited by K. R. McClay, pp. 157–182, AAPG, Tulsa, Oklahoma.

Rowan, M. G., K. F. Inman, and J. C. Fiduk (2005), Oligo-Miocene extension at the Louann level in the northern Gulf of Mexico: Kinematic models and examples, *Transactions - Gulf Coast Association of Geological Societies*, *55*, 725–732.

Simmons, G. R. (1992), The regional distribution of salt in the northwestern Gulf of Mexico; styles of emplacement and implications for early tectonic history, *Bulletin - Houston Geological Society*, *35*(4), 7.

Spathopoulos, F. (1996), An insight on salt tectonics in the Angola Basin, South Atlantic, in *Salt tectonics*, *Geological Society Special Publications*, vol. 100, edited by G. Alsop, D. Blundell, and I. Davison, pp. 153–174, Geological Society of London.

Tari, G., J. Molnar, and P. Ashton (2003), Examples of salt tectonics from West Africa: a comparative approach, in *Petroleum Geology of Africa: New Themes and Developing Technologies*, *Geological Society of London Special Publication*, vol. 207, edited by T. J. Arthur, D. S. MacGregor, and N. R. Cameron, pp. 85–104, Geological Society of London, London,UK.

Ter Heege, J. H., J. H. P. de Bresser, and C. J. Spiers (2005), Rheological behaviour of synthetic rocksalt; the interplay between water, dynamic recrystallization and deformation mechanisms, *Journal of Structural Geology*, *27*(6), 948–963.

Trudgill, B. D., M. G. Rowan, J. C. Fiduk, P. Weimer, P. E. Gale, B. E. Korn, R. L. Phair, W. T. Gafford, G. R. Roberts, and S. W. Dobbs (1999), The Perdido fold belt, northwestern deep Gulf of Mexico: Part 1, Structural geometry, evolution and regional implications, *AAPG Bulletin*, *83*(1), 88–113.

Urai, J. L., C. J. Spiers, H. J. Zwart, and G. S. Lister (1986), Weakening of rock salt by water during long-term creep, *Nature*, *324*, 554–557.

van Keken, P. E., C. J. Spiers, A. P. van den Berg, and E. J. Muyzert (1993), The effective viscosity of rocksalt: Implementation of steady-state creep laws in numerical models of salt diapirism, *Tectonophysics*, *225*(4), 457–476.

Vendeville, B., and V. Gaullier (2005), Salt diapirism generated by shortening and buckle folding, *Abstracts, CDROM, AAPG Annual Convention*.

Waller, T. D. (2007), Structural Analysis of the Perdido Fold Belt: Timing, Evolution and Structural Cycle, Master's thesis, Texas A&M University.

Watts, A. B. (2001), *Isostasy and flexure of the lithosphere*, University of Cambridge, Cambridge, United Kingdom.

Weimer, P., and R. T. Buffler (1992), Structural geology and evolution of the Mississippi Fan fold belt, deep Gulf of Mexico, *AAPG Bulletin*, *76*(2), 225–251.

Willett, S. D. (1999), Rheological dependence of extension in wedge models of convergent orogens, *Tectonophysics*, *305*(4), 419–435.

Wilson, H. H. (2003), Extensional evolution of the Gulf of Mexico Basin and the deposition of Tertiary evaporites, *Journal of Petroleum Geology*, *26*, 403–428.

Winker, C. D. (2004), Stratigraphy and structural timing of the Perdido Foldbelt, an emerging toe-of-slope play in the northwestern deep-water Gulf of Mexico, *Transactions - Gulf Coast Association of Geological Societies*, *54*, 765.

Winker, C. D., and R. Buffler (1988), Paleogeographic evolution of early deep-water Gulf of Mexico and margins, Jurassic to Middle Cretaceous (Comanchean), *AAPG Bulletin*, *72*(3), 318–346.

Wu, S., and A. W. Bally (2000), Slope tectonics; comparisons and contrasts of structural styles of salt and shale tectonics of the northern Gulf of Mexico with shale tectonics of offshore Nigeria in Gulf of Guinea, in *Atlantic Rifts and Continental Margins*, *Geophysical Monograph*, vol. 115, edited by W. Mohriak and M. Talwani, pp. 151–172, AGU, Washington, D.C.

Chapter 3

Coupled Fluid Flow and Sediment Deformation in Margin-Scale Salt-Tectonic Systems: 1. Development and Application of Simple, Single-Lithology Models

This chapter has been published as "*Gradmann, S., C. Beaumont, and S. Ings (2012), Coupled fluid flow and sediment deformation in margin-scale salt-tectonic systems: 1. Development and application of simple, single-lithology models, Tectonics, doi:10.1029/2011TC003033.*" Reproduced by permission of American Geophysical Union. Minor editorial corrections have been applied.

3.0 Abstract

A methodology is presented to model coupled fluid flow and deformation in rifted continental margin composite salt and siliciclastic tectonic systems; and we investigate their compaction and overpressuring behavior associated with continental margin-scale gravitational spreading. Compaction-driven Darcy fluid flow in clastic sediments is coupled through the effective pressure to their frictional-plastic yielding and mechanical deformation. Viscous flow of underlying salt is independent of fluid pressure. Numerical models are adapted to the Oligo-Miocene phase of large-scale gravitational failure in the northwestern Gulf of Mexico, and represent the first study of this system that includes dynamically evolving fluid pressures. Here we present the methodology and prototype models with single uniform sediment lithologies and simple parameterizations of their properties. The models serve to illustrate the interactions among compaction, generation of fluid overpressure, and gravitational failure and spreading. Mechanical and viscous compaction behavior of sandstone-type and shale-type sediments are investigated. Results demonstrate that mechanical compaction can generate moderate overpressures in thick shale-type material, whereas

high overpressures require viscous compaction. In sandstone-type material, only viscous compaction can generate significant overpressures, though this requires tens of millions of years. Changes in the stress regime during gravitationally driven deformation enhance compaction and overpressure. Although illustrative of the methodology and basic processes, none of the prototype single-lithology models satisfactorily reproduces Oligo-Miocene fluid pressure and deformational regimes of the Gulf of Mexico. Numerical models of layered sediments together with an improved formulation of viscous compaction, presented in *Gradmann and Beaumont* (2012, Chapter 4), are more successful.

3.1 Introduction

Fluid pressures play an important role in many geological processes. In particular, they are inextricably linked to compaction in sedimentary basins and to the associated reduction of rock strength leading, for example, to gravity-driven tectonics on continental margins, the subject of this paper. The interaction among fluid pressures, local stress regime, mechanical failure, and deformation has long been recognized and quantified (e.g. *Terzaghi*, 1936, 1943; *Biot*, 1941). However, it has only recently been applied to large-scale tectonic problems (e.g. *Mourgues et al.*, 2009; *Ings and Beaumont*, 2010).

We investigate the role of pore-fluid pressure in the problem of large-scale, gravity-driven salt tectonics on rifted continental margins, in which overpressured siliciclastic sediments overlie viscous salt. Gravity spreading above salt layers has been observed on many continental margins worldwide (*Weimer and Buffler*, 1992; *Peel et al.*, 1995; *Demercian et al.*, 1993; *Jackson*, 1995) and has also been studied in analogue (*Ge et al.*, 1997; *Fort et al.*, 2004; *Vendeville*, 2005; *Krezsek et al.*, 2007) and numerical experiments (*Gemmer et al.*, 2004, 2005; *Gradmann et al.*, 2009; *Maxwell*, 2009). Earlier modeling of coupled fluid-mechanical systems applied to sedimentary basins has focussed on fluid pressures in purely siliciclastic sedimentary systems (*Mourgues and Cobbold*, 2003; *Morency et al.*, 2007; *Ings and Beaumont*, 2010).

Our motivation is to improve on our earlier salt-tectonic research concerning formation of continental margin salt-cored fold and thrust belts. *Gradmann et al.* (2009) developed numerical models of the formation of the Oligo-Miocene Perdido Fold Belt

in the northwestern Gulf of Mexico (Figure 3.1), in which constant pore-fluid pressure ratios were specified *a priori*. It was demonstrated that a constant pore-fluid pressure ratio of approximately λ=0.8 would have been necessary for vigorous Oligocene gravity spreading. However, pore-fluid pressure ratios that are both high and constant, i.e. spatially uniform, are not realistic and no consideration was given to the origin and spatial or temporal development of the high fluid pressures.

We here investigate the development of pore-fluid pressures during sediment compaction, and the circumstances under which the associated reduction in sediment strength leads to failure and gravitational spreading of the system. Furthermore, the changes in stress that accompany deformation provide a feedback effect on compaction and pore-fluid pressure generation. The Oligocene northwestern Gulf of Mexico is chosen as our study area (Figure 3.1) because large-scale gravity spreading above salt in this region was used in our earlier study (*Gradmann et al.*, 2009) and because a significant amount of previously published work is available for this system.

Gravity spreading of a continental margin-scale sedimentary wedge above a salt substrate occurs when increasing differential stress in the sedimentary wedge causes it to fail. This process is different from gravity gliding, which is activated by a slope in the substratum, not by the differential load of the overburden. The detachment surface of the deformation that occurred during the Oligo-Miocene in the northwestern Gulf of Mexico is currently dipping landward (Figure 3.1a) and likely dipped this way at the time of deformation. If this is true, the system deformed by gravity spreading, not gliding. However, in both cases, deformation resulted in the formation of an upslope (landward) domain of extension, a central domain of translation and a downslope (seaward) domain of shortening (e.g. *Letouzey et al.*, 1995; *Rowan et al.*, 2004; *Vendeville*, 2005). A weak substrate such as salt or shale can reduce the basal friction and therefore act as a potential décollement. The décollement of a salt-based system will be governed by viscous flow as opposed to frictional detachment in highly overpressured shale (*Ings and Beaumont*, 2010). In the case of gravity spreading, channel (Poiseuille) flow of the salt also assists the failure by applying a basal drag on the overburden as the salt is squeezed and mobilized by the differential loading (*Gemmer et al.*, 2004, 2005). Yielding depends on the strength of the overburden and therefore on the second component of the problem, the fluid pressure regime

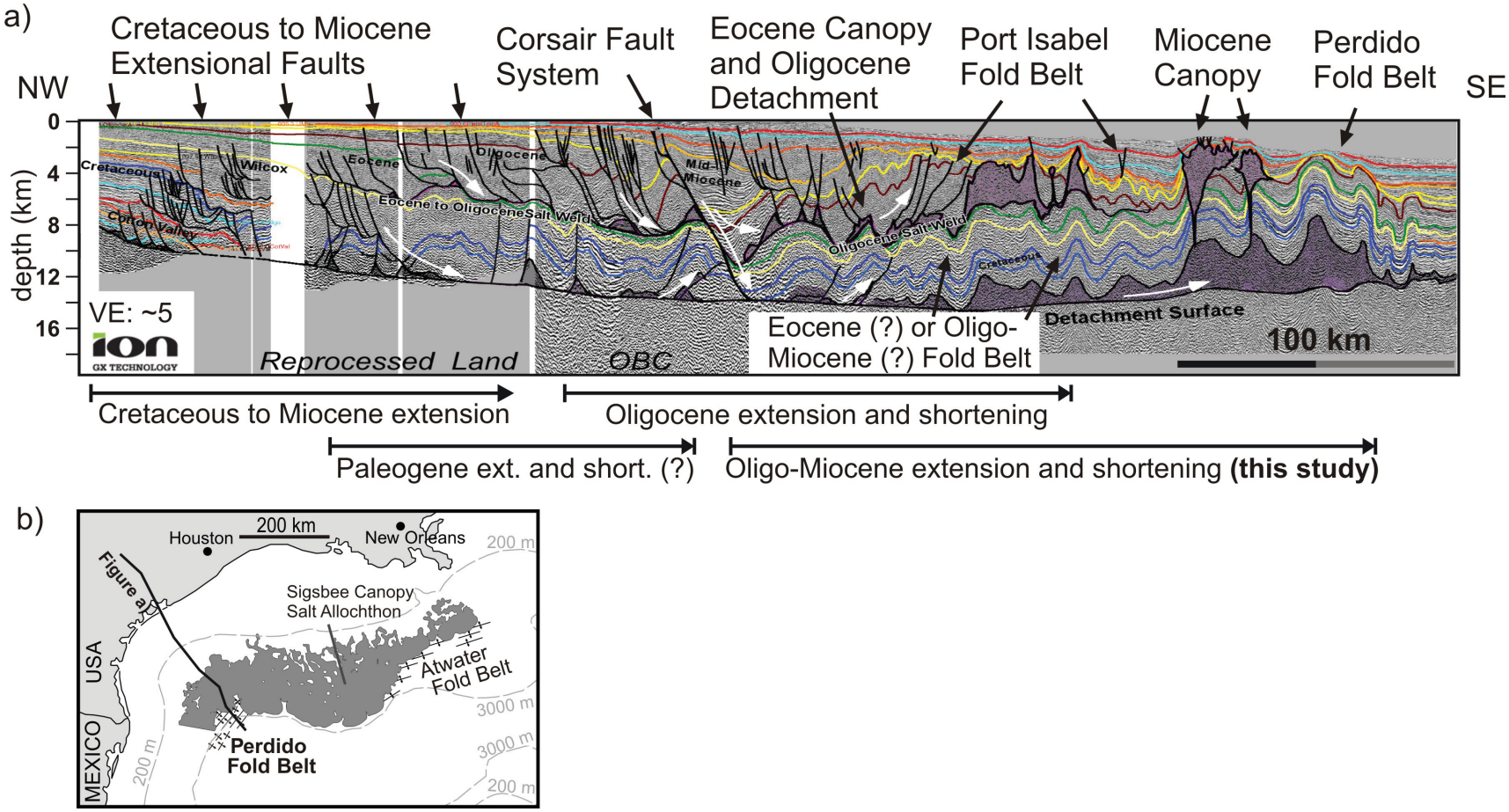

Figure 3.1: (a) Regional NW-SE trending seismic profile from the northwestern Gulf of Mexico extending from onshore into deep water (after *Radovich et al.* (2007), published with permission of ION/GXT and SEI). Large-scale gravity spreading domains and structures (extensional faults, allochthonous salt, fold belts) are indicated. More detailed figure descriptions can be found in the original publication and Figure 5.2. (b) Regional map of northern Gulf of Mexico showing the location of the allochthonous salt and the Cenozoic fold belts after *Fiduk et al.* (1999), salt outline is from *Simmons* (1992).

(*Gemmer et al.*, 2005; *Morency et al.*, 2007; *Gradmann et al.*, 2009). This sensitivity to fluid pressures makes salt-based gravity spreading systems well-suited as natural examples to study the feedback relations between overpressuring and deformation.

Pore-fluid pressure will be hydrostatic in saturated porous and permeable sediments when the system is 'well drained'. In 'poorly drained' sediments fluid pressure may exceed hydrostatic values and the system is termed 'overpressured'. Several mechanisms cause the development of overpressure, including sediment compaction, hydrocarbon generation, and mineral transformations such as the smectite-illite transition (*Luo and Vasseur*, 1996; *Osborne and Swarbrick*, 1997; *Colten-Bradley*, 1987; *Freed and Peacor*, 1989). The first process is regarded as the most widespread and best understood (*Swarbrick and Osborne*, 1998), and is investigated in this study. In particular, we consider both mechanical and viscous compaction which respectively contribute to pore-space reduction and the development of overpressure by rearrangement of grains to a closer packed state and by pressure solution and re-precipitation (*Schneider et al.*, 1996; *Fowler and Yang*, 1999).

In most instances mathematical formulations of this coupled system and their applications explore only the one-dimensional problem in which sediment compacts vertically under its own weight in response to spatially uniform deposition of sediments (*Gordon and Flemings*, 1998; *Suetnova and Vasseur*, 2000). The mechanics of the grain matrix are not included, nor is the tectonic deformation of the overall system considered. It has, however, been recognized that vertical compaction alone is not sufficient to describe fluid pressure regimes in tectonic systems (*Berry*, 1973; *Yassir and Bell*, 1996; *van Ruth et al.*, 2003), where sediments may also compact laterally. Regions subject to gravity spreading are good candidates for the study of lateral (horizontal) compaction because the difference between extension and shortening in the bounding zones allows the lateral compaction to be estimated directly (*Butler and Patron*, 2010).

Morency et al. (2007) expanded the 2D finite element code `SOPALE` (*Fullsack*, 1995) to include calculations of compaction and pore-fluid pressure coupled with the mechanical deformation of the grain matrix. Equations for Darcy flow describe the pore-fluid flow in fully saturated, porous media, and mechanical and viscous compaction of the pore space provide the source/sink terms. The compaction-driven

fluid flow is coupled to the deformation of the grain matrix via the effective stress. This formulation not only takes into account that fluid overpressures weaken sediments and can facilitate deformation, but also that the mechanical deformation feeds back on the stress regime and therefore on compaction and evolving fluid pressure.

The model of *Morency et al.* (2007) is used here to investigate the effects of coupled fluid-mechanical behavior of a salt-tectonic gravity-spreading system. We first describe the physical basis and methods used in this study (section 3.2) and put them in the context of earlier and related research. The models, described in section 3.3, use sediments with a single lithology and demonstrate contrasting behaviors of well-drained (sandstone-type) and poorly-drained (shale-type) sediments. Results of the different models are presented and discussed in section 3.4. In *Gradmann and Beaumont* (2012, Chapter 4), we present numerical models which consider lithologically layered sediments as well as an improved formulation of viscous compaction.

3.2 Finite Element Numerical Modeling

Calculations for fluid flow and for mechanical deformation are combined by expanding a velocity-based plane-strain, viscous-plastic finite element numerical model (*Fullsack*, 1995; *Willett*, 1999) to include sediment compaction and pressure effects of fluid flow in porous media (*Morency et al.*, 2007). The models are designed for large-scale deformation (creeping flow) including self-consistent pore-fluid pressure.

We first provide an overview of the physics and mathematics of fluid flow and compaction, then introduce the formulation of mechanical creeping flow and lastly comment on their coupling as it is implemented in the models of *Morency et al.* (2007) and *Ings and Beaumont* (2010). The description only includes the most important aspects, for additional information we refer readers to *Morency et al.* (2007).

3.2.1 Background

Pore-fluid pressure in the context of sediment compaction and fluid flow in porous media has been investigated for more than a century (see, e.g., references in *Bjørlykke*, 1997). Hydromechanics advanced fundamentally through the work of *Terzaghi* (1936, 1943). He introduced the principle of effective stress/effective pressure (P_{eff}), which holds that for saturated sediments, pore fluids (P_f) bear a part of the load of the

overlying sediments (P) and the remaining pressure (P_{eff}) is carried by the sediment matrix. (P_{eff}=$P - P_f$). Correspondingly, because the strength of a material is directly related to the effective stress it experiences, material strength decreases as pore pressure increases and effective pressure decreases.

Fluid pressure generation by compaction in sediments has been mathematically formulated by coupling the compaction and associated loss of pore volume to the pressure-driven flow of the expelled fluid through the porous and permeable sediment. Formulations have considered poro-elastic media (*Biot*, 1941) and the role of effective pressure in mechanical compaction (e.g. *Bredehoeft and Hanshaw*, 1968; *Smith*, 1971; *Audet and Fowler*, 1992; *Revil et al.*, 2002). Empirical compaction relations were described by *Athy* (1930). Pressure solution has been described mathematically as volumetric viscous compaction under effective pressure (e.g. *Angevine and Turcotte*, 1983; *Birchwood and Turcotte*, 1994; *Revil*, 2001). Combined mechanical and viscous compaction were, for example, studied by *Schneider et al.* (1996), *Suetnova and Vasseur* (2000), and *Connolly and Podladchikov* (2000). Most of these studies focussed on the one-dimensional case where changes in the stress regime are primarily induced by sediment loading.

3.2.2 Fluid Flow in Porous Sediments

Darcy Fluid Flow

Flow of fluid through a saturated, permeable sedimentary rock is described to first order by Darcy flow. The Darcy velocity is the velocity of the fluid relative to the solid such that the flux $\boldsymbol{q}_D$, the volumetric flow rate per unit surface area, is:

$$\boldsymbol{q}_D = n\,(\boldsymbol{v}_f - \boldsymbol{v}_s), \tag{3.1}$$

where n is the porosity, and $\boldsymbol{v}_f$ and $\boldsymbol{v}_s$ are the fluid and solid flow velocities, respectively. The choice of n as the symbol for porosity was made to avoid confusion with φ, the symbol of the internal angle of friction used in this manuscript.

Although the solid matrix (sediment grains) and the pore fluid are both considered incompressible, the bulk material is compressible because as fluid is expelled from the pores, porosity and bulk volume decrease. The bulk volumetric strain rate $\dot{\varepsilon}_v$ is

directly linked to the rate of porosity change and balances the volumetric deformation of the solid skeleton to the pore fluid flow by conserving total mass:

$$\dot{\varepsilon}_v = \frac{1}{1-n}\frac{Dn}{Dt} = \nabla \boldsymbol{v}_s = -\nabla \boldsymbol{q}_D \tag{3.2}$$

$\frac{Dn}{Dt}$ is a total, material derivative that follows the flow of the solid matrix ($\frac{Dn}{Dt} = \frac{\partial n}{\partial t} + \boldsymbol{v}_s \cdot \nabla n$). The flow of pore fluids in permeable sediments is controlled by the hydraulic conductivity, K, and relates to the Darcy velocity $\boldsymbol{q}_D$ through Darcy's law:

$$\boldsymbol{q}_D = -K\nabla\frac{P_{ex}}{\rho_f g} = -\frac{k}{\eta_f}\nabla P_{ex} \tag{3.3}$$

where P_{ex}, the excess fluid pressure (also referred to as overpressure), is the difference between the fluid pressure and the hydrostatic pressure ($P_{ex} = P_f - P_h$), ρ_f is the fluid density, η_f is the fluid viscosity, and $k{=}\frac{K\,\rho_f\,g}{\eta_f}$ is the sediment permeability. Thus, fluid flows in response to the gradient in excess pressure ∇P_{ex}, which is equivalent to the seepage force exerted by the fluid on the matrix (*Mourgues and Cobbold*, 2003). Seepage forces can modify the stress regime, in particular the orientation of the principal stresses. In this study a power-law relationship (*Smith*, 1971; *Mello et al.*, 1994) is used to link porosity and conductivity:

$$K = K_0\left(\frac{n}{n_0}\right)^m \tag{3.4}$$

where K_0 is the hydraulic conductivity at a reference porosity n_0, and m is the exponent.

Pressure and Effective Pressure

We use the effective stress principle, $P_{eff} = P - P_f$ (*Terzaghi*, 1943), where P is the dynamic pressure (mean stress), to determine the pressure that acts on the solid rock matrix and causes it to fail and deform. As discussed in the following section 3.2.3, this reduction of the pressure to the effective pressure decreases the effective strength of a material and facilitates failure.

Pore-fluid pressure is commonly described as the ratio of fluid pressure to mean stress (see Chapter 2), but can also be described in terms of the Hubbert-Rubey pore-fluid pressure ratio λ_{HR} (*Hubbert and Rubey*, 1959), the ratio of fluid pressure

to lithostatic pressure. Lithostatic pressure (P_{litho}) and mean stress (P) are identical only in a neutral stress system. Following *Davis et al.* (1983) we use $\lambda_{HR} = \frac{P_f - P_w}{P_{litho} - P_w}$ for submarine conditions, where P_w is the pressure of the water column.

Sediment Compaction

Compaction of clastic sediments during burial results in a decrease in porosity with increasing depth. Compaction is inhibited where fluid expulsion is hindered, giving rise to undercompacted sediment associated with fluid overpressure. Other mechanisms of overpressure generation aside from compaction disequilibrium include hydrocarbon generation or mineral reactions, these are not considered here.

Two primary compaction mechanisms exist. Mechanical compaction occurs owing to grain rearrangement to closer packing in response to changes in effective pressure and can be described macroscopically by the effective bulk compressibility of the medium, β_b (e.g. *Revil et al.*, 2002). Viscous compaction occurs owing to pressure solution at grain boundaries (grain dissolution) and local re-precipitation within the residual pore space. Viscous compaction includes the processes of pressure-enhanced dissolution, diffusive transport and re-precipitation, of which diffusive transport has generally been considered to be the rate-limiting mechanism (*Angevine and Turcotte*, 1983). Recent work, however, demonstrates that dissolution and precipitation may equally determine the rate of compaction (*Revil*, 2001). In either case, the compaction is, from a macroscopic perspective, the volumetric equivalent of viscous shear flow and can be described through an effective bulk (volumetric) viscosity ξ of the porous medium. Both mechanical and viscous compaction depend on porosity and diminish in more compacted material. The porosity dependency is to first order linear; $\beta_b(n) = n\beta_p$ for mechanical compaction, where β_p is the pore compressibility, defined as $-\frac{1}{V_p}\frac{\partial V_p}{\partial P_{eff}}$. However, mechanical compaction is known to stop at the closest packing limit (without considering grain crushing), therefore, we use a minimum, or 'lock-off', porosity n_c for mechanical compaction and modify β_b following *Revil et al.* (2002)

$$\beta_b(n) = (n - n_c)\beta_p \tag{3.5}$$

For viscous compaction the porosity dependence is given by $\xi(n) = \mu/n$, where μ is the matrix compactional shear viscosity. This viscosity is often considered identical to the regular shear viscosity η of a material, but this equality likely only holds for strongly compacting material and not for nearly fully compacted material (such as salt in the present models). We therefore treat the compactional shear viscosity as an independent parameter, not related to shear viscosity.

We model viscous compaction in this chapter as decreasing linearly with porosity, but compaction never fully ceases with this formulation. This problem is addressed by introducing an improved description of viscous compaction in *Gradmann and Beaumont* (2012, Chapter 4).

The combined effects of mechanical and viscous compaction change the bulk volume of the porous sediment at the rate $\dot{\varepsilon}_v$ such that:

$$\dot{\varepsilon}_v = \frac{1}{1-n}\frac{Dn}{Dt} = -\beta_b(n)\frac{DP_{eff}}{Dt} - \frac{P_{eff}}{\xi(n)} \tag{3.6}$$

(e.g. *Schneider et al.*, 1996; *Connolly and Podladchikov*, 2000). Equation (3.6) therefore describes how the rate of porosity change relates to mechanical and viscous compaction of clastic sediments, whereas equation (3.2) shows how this same rate relates to matrix deformation and fluid flow. The general diffusion equation for excess pressure can be derived by combining equations (3.2), (3.3), and (3.6)

$$\beta_p(n)\frac{DP_{ex}}{Dt} + \frac{P_{ex}}{\xi(n)} - \nabla(\frac{k}{\eta_f}\nabla P_{ex}) = \beta_p(n)\frac{D}{Dt}(P - P_h) + \frac{P - P_h}{\xi(n)}. \tag{3.7}$$

This equation can be solved numerically to obtain excess pressure once the mean stress P has been determined.

3.2.3 Large-Scale Viscous and Plastic Deformation of the Matrix

In addition to compaction, the porous sedimentary material also deforms by large-scale post-yield flow which is calculated by solving the force balance equation for creeping flow (i.e. without inertial terms, equation 3.8) and conservation of mass for

the compacting material (equation 3.9):

$$\begin{aligned}\nabla\boldsymbol{\sigma} + \rho\, g &= (1-n)\nabla(\boldsymbol{S_s} - P_s\boldsymbol{I}) + n(-\nabla P_f\boldsymbol{I}) + \rho g \\ &= (1-n)\nabla\boldsymbol{S_s} - \nabla(P\boldsymbol{I}) + \rho\, g = 0 \end{aligned} \tag{3.8}$$

$$\nabla\boldsymbol{v}_s = -\nabla\boldsymbol{q}_D = -\beta_b(n)\frac{D\,P_{eff}}{D\,t} - \frac{P_{eff}}{\xi(n)} \tag{3.9}$$

where $\boldsymbol{S_s}$ and P_s are the deviatoric stress tensor and mean stress of the solid phase, P_f is the mean pressure of the fluid phase. It is assumed that the deviatoric stress component in the fluid phase is negligible, such that $\boldsymbol{S_f}$=0. ρ is the bulk sediment density, g is the gravitational acceleration and $\boldsymbol{I}$ is the identity matrix.

The above set of equations is a modification of the penalty method used by *Fullsack* (1995), in which porosity n=0 in equation (3.8) and equation (3.9) describes incompressibility ($\nabla\boldsymbol{v}_s$=0). The penalty parameter now has the physical meaning of a compaction coefficient (equation 3.9) (*Morency et al.*, 2007).

In the case of viscous flow of the solid matrix or salt, the stress tensor is related to the strain rate tensor $\dot{\boldsymbol{\varepsilon}}$ of the solid by

$$\sigma_{ij} = 2\,\eta_{eff}\,\dot{\varepsilon}_{ij} - P\,\delta_{ij} = \eta_{eff}\left(\frac{\partial v_{si}}{\partial x_j} + \frac{\partial v_{sj}}{\partial x_i}\right) - P\,\delta_{ij} \tag{3.10}$$

where δ_{ij} is the Kronecker delta, v_s is the solid velocity, and η_{eff} is the effective viscosity of the solid matrix or the salt viscosity.

Frictional-plastic failure of the clastic sediments is calculated using the Drucker-Prager yield criterion given by:

$$\sigma_Y = J_2'^{1/2} = (P - P_f)\sin\varphi_0 + C\cos\varphi_0 = P_{eff}\sin\varphi_0 + C\cos\varphi_0 \tag{3.11}$$

where σ_Y is the yield stress, φ_0 is the internal angle of friction, and C is the cohesion. Below yield, clastic sediment is assigned a high effective viscosity which precludes significant deformation on the timescales considered here. The post-yield plastic flow is calculated in the same way as viscous flow (equation 3.10) but in this case η_{eff} is the post-failure effective viscosity of frictional plastic material, given by η_{eff}=$\frac{1}{2}\sqrt{\frac{J_2'}{I_2'}}$, where J_2' and $\dot{I}_2'$=$\frac{1}{2}\dot{\varepsilon}_{ij}'\,\dot{\varepsilon}_{ij}'$ are the second invariants of the deviatoric stress and strain

rate, respectively (*Willett*, 1999). That is, the effective viscosity takes the value required to keep the material at yield during the deformation. Deformation is therefore strictly viscous-plastic, that is flow is viscous when the state of stress is below yield, and frictional-plastic when on yield.

3.2.4 Coupling of Compaction and Deformation

Coupling between fluid flow processes and mechanical deformation of the matrix occurs in two ways. First, the fluid pressure P_f reduces the effective pressure P_{eff}, which in turn reduces the effective strength of the material (equation 3.11) and facilitates failure. Second, the compaction parameters for mechanical and viscous compaction enter the equation that is solved for the matrix deformational velocity v_s (combination of equations 3.8 and 3.9), thus determining the compressibility of the large-scale flow. Shear flow (mechanical deformation) and dilatational flow (volumetric deformation) can only be solved for independently under special circumstances. In the current model these parts are coupled because the volumetric deformation changes the mean stress, which affects the stress field for plastic yield.

All equations are solved using the finite element technique (*Fullsack*, 1995). The velocity field v_s and mean stress P are solved for from equations (3.8) and (3.9) with an initial, predicted value of P_{ex}; equation (3.7) is solved for P_{ex} and both systems are iteratively refined (*Morency et al.*, 2007).

Boundary conditions are defined such that there are no fluid and material fluxes across the base or sides of the model domain. Side boundaries allow vertical free slip and the base is a no-slip boundary. The top of the model domain (seafloor) is treated as a free surface that adapts to material flow and the prograding sediment and permits fluid to leave the model domain. Moreover, models comprise an initial phase of sediment deposition and compaction that serves to create self-consistent model properties prior to the start of sediment progradation.

After the iterations for pressure and velocity converge, the porosity is updated according to equation (3.6), which can be rewritten as:

$$\frac{1}{1-n}\frac{Dn}{Dt} = -n\,A + B \quad \text{, with } A = \beta_p \frac{dP_{eff}}{dt} + \frac{1}{\mu}P_{eff} \quad \text{and } B = n_c\beta_p \frac{dP_{eff}}{dt} \quad (3.12)$$

The above equation can be solved analytically as an ordinary differential equation and the new porosity $n(t+\Delta t)$ expressed as a function of the old porosity $n(t)$:

$$n(t+\Delta t) = \frac{n(t)\cdot(e^{-(A-B)\Delta t} - \frac{B}{A}) - \frac{B}{A}\,(e^{-(A-B)\Delta t} - 1)}{n(t)\cdot(e^{-(A-B)\Delta t} - 1) + 1 - \frac{B}{A}\,e^{-(A-B)\Delta t}} \tag{3.13}$$

where Δt is the time step length. If mechanical compaction is not limited, i.e. not 'locked off', B is zero and the above equation simplifies to the form used by *Morency et al.* (2007):

$$n(t+\Delta t) = \frac{n(t)\,e^{-A\Delta t}}{n(t)\cdot(e^{-A\Delta t} - 1) + 1} \tag{3.14}$$

The new porosity derived from the consistent pressure and velocity fields is used in the following timestep to control compaction and hence the evolving pressure regime and deformation. Time step lengths of 5,000-10,000 a are sufficiently small to capture the relevant processes of the length and time-scales of interest, and obey the Courant-Friedrichs-Lewy condition, a necessary constraint for numerical stability.

The model uses an Arbitrary Lagrangian-Eulerian (ALE) formulation, in which computations are made on an Eulerian grid that adapts vertically to the shape of the evolving model domain while the material properties are tracked and updated using a set of Lagrangian particles. The ALE approach allows the model to undergo both large deformation and strain because the computation grid is not advected with the flow nor distorted during deformation. As a result, the amount of strain that can be accommodated in the calculations is not limited by the method.

3.2.5 Sedimentation

Sedimentation is prescribed by defining a bathymetric profile, the space below which is filled with sediment. Material is not removed if it becomes elevated above the sedimentation profile during deformation. Aggradation is given by a horizontal profile $h(x,t)$=$h(x,0)+v_{agg}\cdot t$ where v_{agg} is the aggradation rate. Progradation is prescribed by a half-Gaussian shape:

$$h(x,t) = \begin{cases} h_1 & x \le x'_0 \\ h_2 + (h_1 - h_2)\,exp\,(-(\frac{x-x'_0}{w})^2) & x > x'_0 \end{cases} \tag{3.15}$$

where h_1 and h_2 are the landward and seaward bathymetries (delta-top and toe), respectively, $x_0' = x_0 + v_{prog} \cdot t$ is the current shelf break position, x_0 its initial position, w is the half-width of the continental slope, and v_{prog} is the seaward progradation rate of the bathymetric profile. The sedimentation pattern used here is intended to approximate the geometry of aggrading and prograding sedimentary systems, but not the physics of natural sedimentation.

3.3 Model Design

The design of the numerical model experiments is similar to that of *Gradmann et al.* (2009) in order to facilitate comparisons of the results. In simple prototype models described in this chapter, all clastic sediments in a given model have the same hydraulic properties, representing either sandstone-type or shale-type sediments. In this way we can demonstrate the characteristic compaction and fluid-flow behavior of each lithology taken in isolation and the suitability of our approach to model these materials. More realistic models, comprising layered sandstone-type and shale-type lithologies, are investigated in *Gradmann and Beaumont* (2012) and provide a better approximation of natural pore fluid pressure variations.

3.3.1 Geometry

The models comprise a 320 km wide and 3 km deep salt basin that tapers linearly at both ends, each over a distance of 60 km, and is laterally enclosed by crustal material (Figure 3.2). Sediment is added above the salt basin during the model calculations in either an aggradational or progradational manner.

The initial configuration is locally isostatically balanced, additional sediment loading is flexurally compensated by an elastic beam at the base of the model and assuming an underlying inviscid fluid with density ρ_m=3300 kg/m^3. The flexural rigidity of D=10^{22} Nm represents relatively stiff lithosphere corresponding to values estimated from older rifted continental margins (*Watts*, 2001). Subsidence owing to cooling and contraction of the margin is not included, nor are crustal thickness variations. These choices were made because the region of interest in the Gulf of Mexico is positioned where the lithosphere beneath had become thermally stable before the time interval of interest.

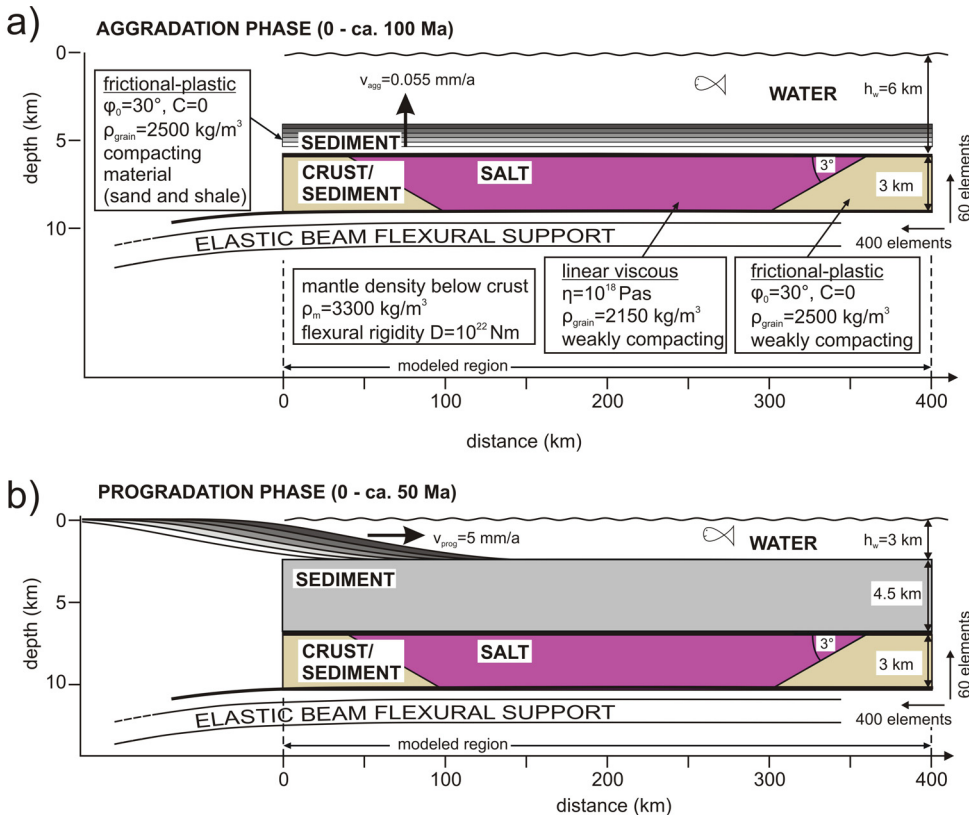

Figure 3.2: Design of model experiments. A 260 km wide, 3 km thick salt basin is embedded in synrift sediment/crustal sequence. a) Phase 1 during which frictional plastic sediments aggrade onto the salt. b) Phase 2 during which sediments prograde onto the salt basin. For a full list of model parameters and their discussion see section 3.3 and Table 3.1.

The models evolve in two phases (Figure 3.2). During phase 1, a laterally uniform sedimentary sequence of 4.5 km aggrades on top of the pre-existing salt layer. During phase 2, sediments prograde onto this sedimentary sequence. Our main interest is the behavior of the system during gravity spreading, which can only occur during phase 2 after a differential load of sediments is deposited onto the salt basin. Phase 1 is, however, necessary to achieve a compacted sediment layer with a self-consistent fluid-pressure regime as a starting configuration for the progradation phase. This phase also illustrates the compaction behavior in absence of differential stresses accompanying progradation.

The sediment aggradation rate of phase 1 (v_{agg}=0.055 mm/a) represents the average aggradation rate of the 4.5 km thick Cretaceous to Oligocene pre-kinematic layer of the Perdido Fold Belt (*Fiduk et al.*, 1999). Model water depth decreases during this phase from ca. 6 km to 3 km owing to combined effects of sedimentation and isostatic compensation. The large initial depth reflects our assumption that thermal subsidence of this region had already occurred or was completed during this phase 1 sedimentation. The water column plays no significant role here, because it merely exerts a laterally uniform load. During phase 2, aggradation ceases and the seaward prograding, half-Gaussian profile has width w=100 km, maximum water depth h_w=3 km, and velocity v_{prog}=5 mm/a. This progradation rate is slightly higher than the average Cenozoic shelf progradation rate of 4 mm/a (*Galloway et al.*, 2000), but reflects increased sediment input rates during the Oligocene, the time when the Perdido Fold Belt formed.

3.3.2 Material Properties

The material properties used in the models (discussed below and listed in Table 3.1) are only one subset of a wide range of values tested during this study. They reflect the choice of mid-range values that best fit the observed compaction trends of sandstone and shale and that yield numerically stable models.

For the calculation of large-scale mechanical deformation, salt is modeled as a linear viscous material with a constant viscosity of $\eta_{salt} = 10^{18}$ Pa s. The crust and sediments are both frictional-plastic materials with an internal angle of friction of φ_0=30° and zero cohesion. *Gradmann et al.* (2009) used φ_0=25° for the sediments,

Table 3.1: Material properties of numerical models.

Parameter	Symbol	Unit	Values (1. set of models)		
			Salt/Crust	Sandstone	Shale
Initial Salt Geometry					
salt width	w_{salt}	km	200 + 2× 60 taper		
salt thickness	h_c	km	3		
taper angle	α	°	3		
Sedimentation					
aggradation velocity	v_{agg}	mm/a	0.055		
progradation velocity	v_{prog}	mm/a	5		
width of progradation profile	w	km	100		
height of progradation profile	h_w	km	3		
Isostatic Compensation					
mantle density	ρ_m	kg/m^3	3300		
water and fluid density	ρ_w	kg/m^3	1000		
flexural rigidity	D	Nm	10^{22}		
Material strength					
internal angle of friction	φ_0		-/30°	30°	30°
shear viscosity	η_{salt}	Pa s	10^{18}/-	-	-
Hydraulic Properties					
grain density	ρ_g	kg/m^3	2150/2500	2500	2500
surface hydraulic conductivity	K_0	m/s	10^{-16}	10^{-6}	10^{-9}
surface porosity	n_0	%	0.1	50	50
K-n exponent	m		1	5	9
pore compressibility	β_p	Pa^{-1}	10^{-14}	10^{-7}	10^{-7}
lock-off porosity (mechanical)	n_c	%	0	30	10
shear viscosity	μ/μ_r	Pa s	10^{28}	10^{23}, 10^{22}	
Finite element grid					
width		km	400		
number of elements (horizontal)			400 (evenly spread)		
number of elements (vertical)			20	40	
time step length	Δt	a	5,000-10,000		
Boundary conditions					
boundary condition at sides			dP_f/dx=0, v_x=0		
boundary condition at base			dP_f/dy=0, v_x=0, v_y=0		
boundary condition at surface			P_f=P_w		

but the effect of this difference is small by comparison with the effect of fluid pressures, which vary in space and time in these models, whereas a constant pore-fluid pressure ratio was assumed by *Gradmann et al.* (2009).

For the fluid pressure calculations there are four different material types in our models: salt, crust, sandstone and shale. Given the large range of permitted parameter values, and that an investigation of all of them is beyond the intent of this paper, we have mostly chosen mid-range values that lead to features that are commonly observed, such as certain depth-to-overpressure development and residual porosity.

Salt and crust are treated as nearly incompactable materials. Rock salt (strictly, halite) is generally assumed to be impermeable, forming 'ideal' seals for hydrocarbons and other fluids (*Downey*, 1984). Recent studies (*Popp et al.*, 2001; *Peach et al.*, 2001) have, however, shown that dilation-induced microcracks in salt can lead to significantly increased permeabilities. This dilation occurs over much smaller scales (millimeters) than those of concern here (*Schoenherr et al.*, 2007; *Schleder et al.*, 2008; *Davison*, 2009). Salt in the current study is therefore considered to be nearly impermeable and incompactable.

Salt compaction occurs mainly within the upper 50 m (*Casas and Lowenstein*, 1989) and is therefore not a significant component of its large-scale behavior. Minimum measured values of salt porosities are on the order of 0.1% (*Urai et al.*, 1986; *Kulenkampff and Yaramanci*, 1993).

In the models presented here, we are interested in the development of overpressures within the sediments and their effect on the stability of the system, while the salt layer acts as a viscous mobile substrate layer but does not contribute to the development of the fluid pressure regime. Hence, it is important to model salt as a low-permeability/low-porosity material that neither absorbs nor expels significant amounts of fluid, which is consistent with the sealing properties of natural salt.

In the models, the salt surface porosity is 0.1% (*Urai et al.*, 1986; *Kulenkampff and Yaramanci*, 1993), the grain density 2150 kg/m^3, and the surface hydraulic conductivity is K_0=10^{-13} m/s (*Carter et al.*, 1993). The coupling of porosity changes to conductivity changes is kept small to avoid large conductivity variations that might generate overpressures (here: m=1, measured values: m=2.5-4.5 (*Cinar et al.*, 2006,

and references therein)). The bulk compressibility is β_p=10^{-14} Pa^{-1}, which corresponds to negligible mechanical compaction for the pressure regimes and timescales considered here. The bulk viscosity is set to a high value (μ=10^{28} Pa s) to avoid viscous compaction of the material. This parameter is not to be equated with the mechanical shear viscosity of salt (η_{salt}=10^{16}-10^{19} Pa s (*van Keken et al.*, 1993)) for this case of essentially fully-compacted salt.

The material laterally surrounding the salt basin, which represents crustal material or fully compacted sediments, is similarly designed not to contribute to the pore-fluid pressure regime of the overlying sediments. Therefore, this material is assigned the same fluid flow properties as salt except for the grain density which is 2500 kg/m^3 (Table 3.1).

Sandstone-type and shale-type sediments are modeled as compacting materials. Sandstones are, for example, known as good aquifers and hydrocarbon reservoir rocks, characterized by generally higher porosities and permeabilities than most other sediments. In contrast, shales are known to be good seals, characterized by low porosities and permeabilities. This difference is largely a consequence of the differently shaped grains and pores of the two materials. In the absence of fracturing, the more equant sand grains can compact mechanically to a densest packing configuration similar to that of spheres, which, for mixed grain size, may reach porosity values of 25-40% (*Revil et al.*, 2002). The more platy clay minerals can compact efficiently down to porosities of ca. 5-10% (*Revil et al.*, 2002). We here use respective mid-range values of 30% (sandstone-type) and 10% (shale-type) as minimum lock-off values for porosity during mechanical compaction. Both materials can have a large range of surface porosities in nature, we chose a value of 50%. Especially in muds, surface porosity can reach values up to 80% (*Neuzil*, 1994), but the rapid very-near-surface compaction trend is not accurately captured by the simplified numerical description used here and is therefore omitted.

The mechanical compaction efficiency is expressed through a combination of lock-off porosity and bulk compressibility (equation 3.5). Bulk compressibilities for sand range from $5 \cdot 10^{-8}$-10^{-10} Pa^{-1} (*Mello et al.*, 1994; *Bradley and Powley*, 1994; *David et al.*, 1994), values for shale are estimated to be $3 \cdot 10^{-8}$-$5 \cdot 10^{-8}$ Pa^{-1} (*Mello et al.*, 1994; *Revil and Cathles*, 1999). These values are often obtained from simplified

porosity-depth curves (*Bradley and Powley*, 1994) or from samples that have already compacted close to their mechanical limit and may therefore not represent reliable values for near-surface mechanical compaction.

We use values of β_p=$10^{-7}\,\mathrm{Pa}^{-1}$ for both sandstone-type and shale-type material, which, in combination with the different lock-off porosities, leads to a much larger compaction efficiency of the shale-type material. Model experiments with lower values of bulk compressibility showed insignificant amounts of mechanical compaction over the depth and timescales considered here. Higher values (which would be justified or even expected for shale-type material) render mechanical compaction calculations very sensitive to numerical inaccuracies. Hence, we control the mechanical compaction efficiency mainly through the lock-off porosities rather than the bulk compressibility *per se*.

The shape of the grains also controls the shape of the resulting pore space, which in turn affects the hydraulic conductivity. The relation between porosity and conductivity is given by the power-law parameter m (equation 3.4), which ranges from 4.5 to 6 for sandstone and from 6 to 12 for shale (*Revil and Cathles*, 1999). Here, values of m=5 and m=9 are chosen for sandstone-type and shale-type material, respectively.

Surface hydraulic conductivities for sand range from $10^{-6}\,\mathrm{m/s}$ to $10^{-2}\,\mathrm{m/s}$ (*Garven*, 1986; *Bradley and Powley*, 1994), surface conductivities of shales range from $10^{-10}\,\mathrm{m/s}$ to $10^{-8}\,\mathrm{m/s}$. With a relatively low value of $10^{-6}\,\mathrm{m/s}$ for sandstone-type material, excess pressure from surrounding overpressured regions cannot diminish rapidly and is maintained for time spans of several hundred thousand to million years. Even with this restriction, hydraulic conductivity in the compacting sandstone-type material remains large enough to prevent significant overpressure.

An intermediate value of $10^{-9}\,\mathrm{m/s}$ for shale-type material ensures that onset of overpressure develops at approximately 2-3 km depth. Additionally, with this hydraulic conductivity shale-type porosities are still on the order of a few percent when the high fluid pressure begins to limit compaction.

The compactional shear viscosity for both materials varies among the model sets. Reference values for shear viscosities or actual bulk viscosities spread over wide ranges in the literature (ξ=$5 \cdot 10^{20}$-$10^{25}\,\mathrm{Pa\,s}$ in *Birchwood and Turcotte*, 1994; *Suetnova and Vasseur*, 2000; *Connolly and Podladchikov*, 2000; *Paterson*, 1973). We present models

with values of ξ=10^{23} and ξ=10^{22} Pa s.

3.4 Results - Single Lithology Models

The set of models presented here demonstrates the contrasting compaction of single lithologies (SL), sandstone-type (Sa) and shale-type (Sh) materials (models SL-Sa and SL-Sh, respectively). Phase 1 corresponds to the aggradation of the 4.5 km thick pre-kinematic sequence of the Perdido Fold Belt. Phase 2 investigates the potential for gravitational spreading during progradation. Standard material properties are as discussed in the previous section and listed in Table 3.1. We present two models with weak viscous compaction (μ=10^{23} Pa s in model SL-Sa1 and SL-Sh1) and two models with stronger viscous compaction (μ=10^{22} Pa s in models SL-Sa2 and SL-Sh2). The sandstone-type and shale-type materials differ in their hydraulic properties, namely with respect to surface hydraulic conductivity (10^{-6} vs. 10^{-9} m/s), the K-n-exponent (5 vs. 9) and the limiting porosity for mechanical compaction (30% vs. 10%), respectively. When combined, these parameters determine the mechanical compaction and associated overpressuring behavior. Viscous compaction is governed by the compactional shear viscosity μ and the evolving porosity and hydraulic conductivity. The progradation phase is only demonstrated for models SL-Sa2 and SL-Sh1, where gravitational failure develops and fluid pressure regimes are to first order realistic (see also Animation_SL-Sh1, supplementary material[1]).

3.4.1 Model SL-Sa1, Weak Viscous Compaction

Model SL-Sa1 illustrates slow compaction in a sandstone-type material with minimal viscous compaction.

Aggradation

Figure 3.3a-d shows the results of model SL-Sa1 (μ=10^{23} Pa s) after 4.5 km of sandstone-type material aggraded slowly over 100 Ma. Material color in Figure 3.3a depicts time of sediment deposition in 10 Ma bands (shades of blue and green). Figure 3.3b shows the distribution of the pore-fluid pressure ratio λ_{HR}=$(P_f - P_w)/(P_{litho} - P_w)$, where

[1]Supplementary material is provided as electronic attachments and is described in Appendix D.

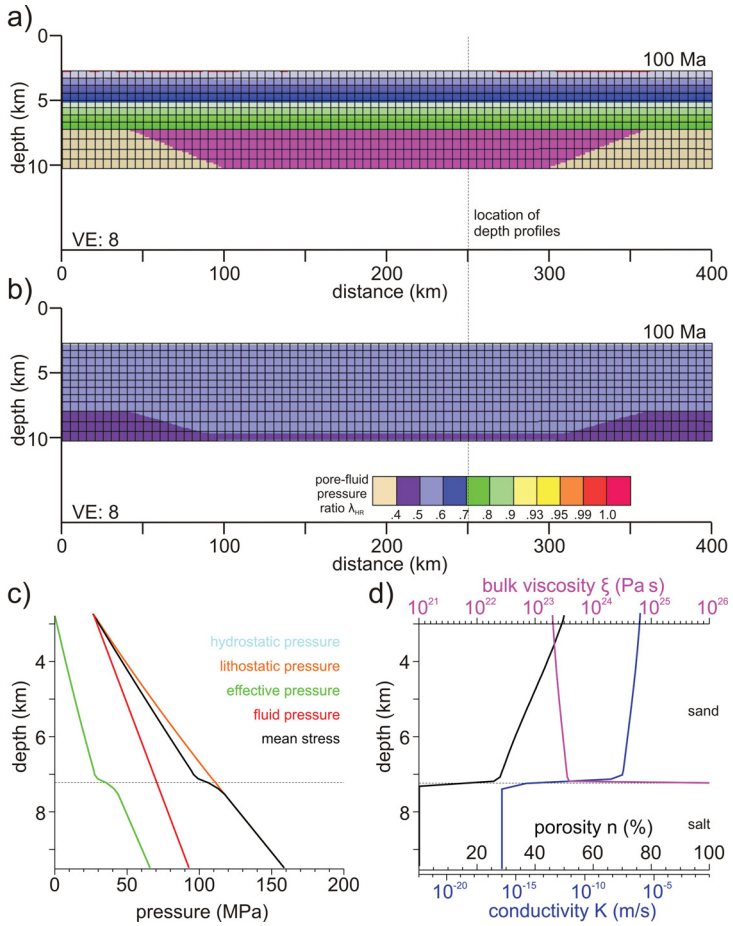

Figure 3.3: Results of model SL-Sa1 with sandstone-type sediments and constant compactional shear viscosity of μ=10^{23} Pa s at end of aggradation phase. (a) Geometry of model. The color scale shows the chronostratigraphy of the sediments in 10 Ma bands. Salt is colored in magenta, crustal material in light brown. Same color coding is used in Figures 3.4-3.6. (b) Pore-fluid pressure ratio λ_{HR}. Blue colors represent low overpressures, red colors represent high overpressures. (c) Pressure-depth profiles at 250 km. Fluid pressure is hydrostatic and overlies the light blue curve. (d) Porosity/conductivity-depth profiles at 250 km.

blue and red colors represent barely and highly overpressured sediments, respectively. Figure 3.3c shows the components of the pressure field at a reference location (250 km) and Figure 3.3d shows variations with depth of porosity, hydraulic conductivity, and bulk viscosity ($\xi(n) = \mu/n$) at the same location.

The fluid pressure remains hydrostatic throughout the entire aggradation phase, leading to pore-fluid pressure ratios of λ_{HR}=0.4-0.5. The pressure at the top of the sediment reflects the overlying water column. The decrease in porosity is nearly linear through the 4.5 km thick sediment column to values approaching the lock-off porosity of 30%. Hydraulic conductivities remain high, decreasing by only one order of magnitude to values of K=10^{-7} m/s.

In the sediments, the mean stress is slightly lower than the lithostatic pressure, indicating a tensile stress system. This is a consequence of the way the sediment deforms during compaction and is discussed in section 3.5 and *Gradmann and Beaumont* (2012, Chapter 4). Within the salt layer and crustal material, fluid pressure remains hydrostatic, and the mean stress remains lithostatic (Figure 3.3c). The progradation phase is not shown because fluid pressures remain hydrostatic throughout and gravitational failure of the overburden does not occur.

3.4.2 Model SL-Sa2, Strong Viscous Compaction

Model SL-Sa2 (Figure 3.4) shows the behavior of a sandstone-type model with enhanced viscous compaction (μ=10^{22} Pa s), which accounts for the differences with respect to model SL-Sa1.

Aggradation

During the aggradation phase, the fluid pressure remains hydrostatic to a depth of approximately 4 km below seafloor, below which it strongly increases with depth (consequence of viscous compaction). Porosity decreases to less than 1%, a much lower value than the 30% lock-off porosity for mechanical compaction. The hydraulic conductivity decreases accordingly to values of K=10^{-17} m/s. The pore-fluid pressure ratios reach values of λ_{HR}=0.95 in a thin layer above the salt (Figure 3.4b). In the salt layer and crust, the fluid pressure follows a hydrostatic gradient but is offset to higher values by the high fluid pressure at the base of the overlying sediments.

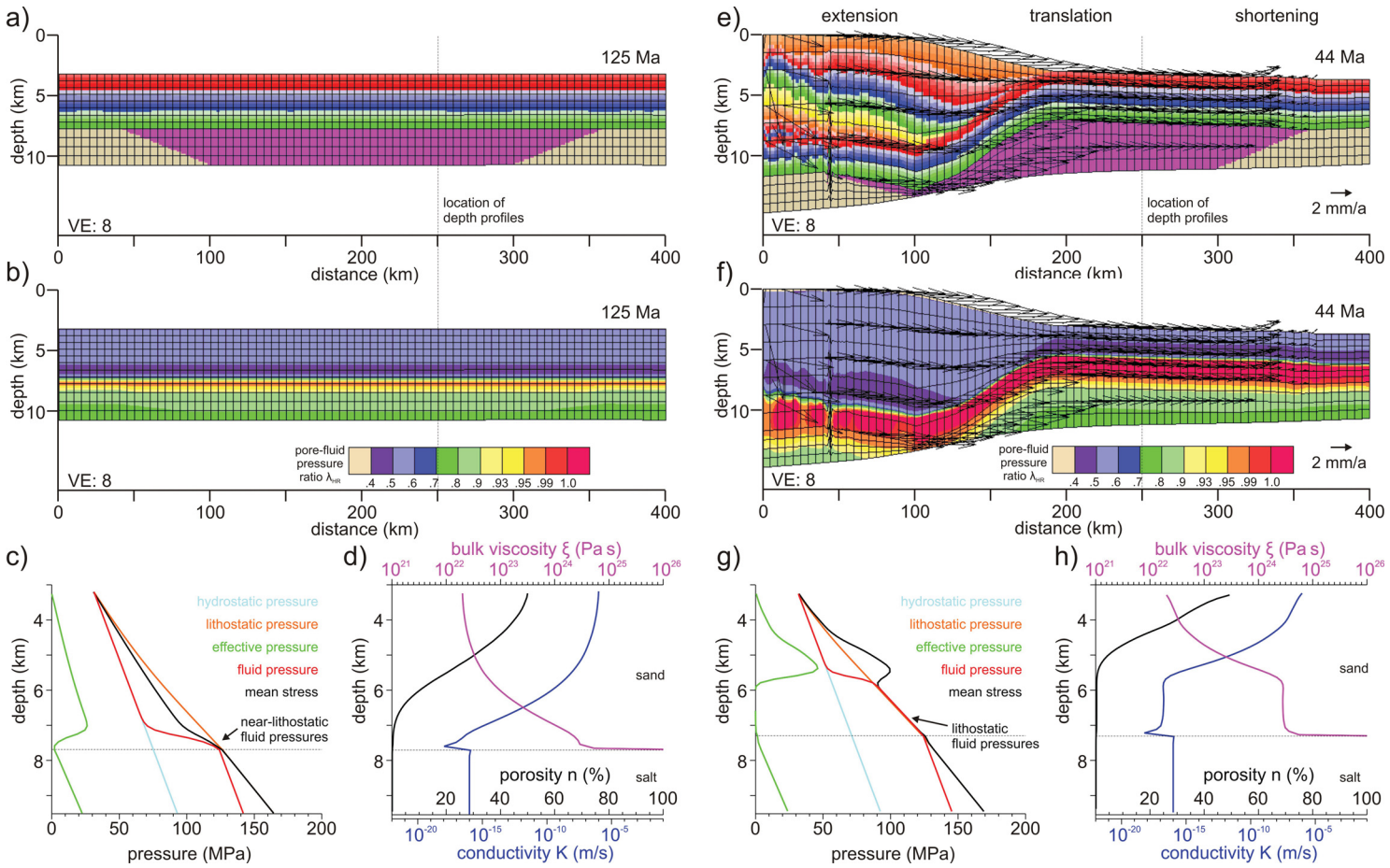

Figure 3.4: Results of model SL-Sa2 with sandstone-type sediments and constant compactional shear viscosity of μ=10^{22} Pa s at end of aggradation phase (a-d) and progradation phase (e-h). (a,e) Geometry of model. Arrows indicate deformational velocities. (b,f) Pore-fluid pressure ratio λ_{HR}. (c,g) Pressure-depth profiles at 250 km. (d,h) Porosity/conductivity-depth profiles at 250 km.

Progradation

During phase 2 (Figure 3.4e-h) model SL-Sa2 becomes gravitationally unstable after approx. 44 Ma of sediment progradation. Velocity arrows indicate that the overburden is moving seaward (Figure 3.4e,f) and there is incipient folding at the seaward end of the salt basin. Pore-fluid pressure ratios (Figure 3.4f) reach values of λ_{HR}=1.0 (lithostatic values) throughout an approximately 2 km thick layer at the base of the sedimentary section. In this region porosities have decreased to approximately 0.5% (Figure 3.4h) as a result of continued viscous compaction. Above the highly overpressured region in the distal part of the system (250 km reference section), the mean stress is now larger than lithostatic values (Figure 3.4g), indicating deviatoric compression and the 'passive Rankine state' of frictional-plastic sediment failure.

3.4.3 Model SL-Sh1, Weak Viscous Compaction

Model SL-Sh1 (Figure 3.5 and Animation_SL-Sh1, supplementary material) demonstrates the behavior of shale-type sediment with minimal viscous compaction (μ=10^{23} Pa s).

Aggradation

The hydraulic properties of the shale-type sediments facilitate stronger mechanical compaction than in models SL-Sa1, and by the end of aggradation porosities decrease to between 20 and 10% at depth, the latter being the lock-off value (Figure 3.5a-d). The corresponding pore-fluid pressure ratios are approximately λ_{HR}=0.6-0.7 in the lower part of the sediment layer (Figure 3.5b,c), but the character of the overpressure regime is different from that in model SL-Sa2 (Figure 3.4c). Now, fluid pressure deviates from hydrostatic pressure at a depth of ca. 3 km (Figure 3.5c) and below this depth largely parallels the mean stress within the sediment layer instead of developing a steep gradient as in model SL-Sa2. Within the salt layer, the fluid pressure again follows a hydrostatic gradient.

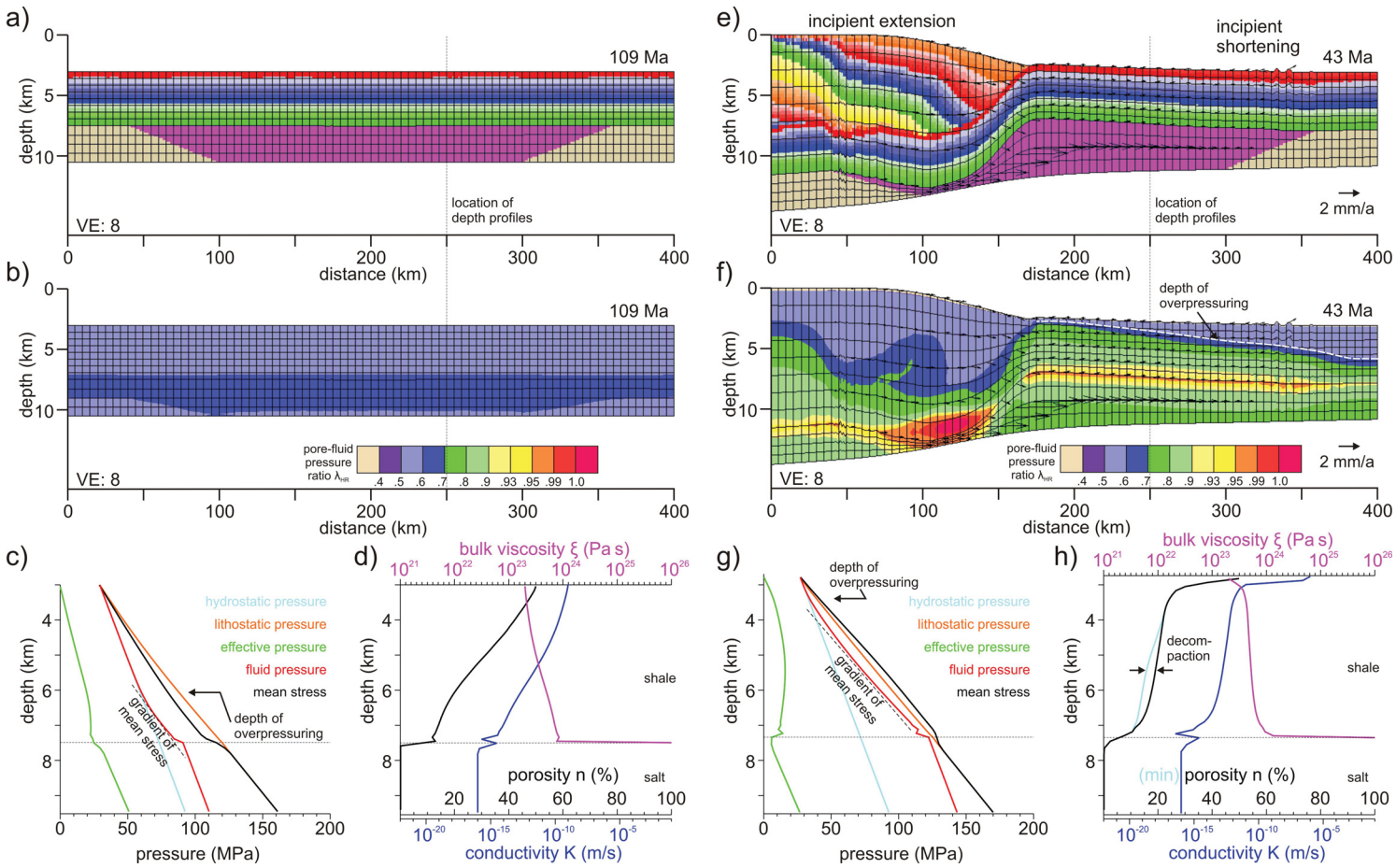

Figure 3.5: Results of model SL-Sh1 with shale-type sediments and constant compactional shear viscosity of μ=10^{23} Pa s at end of aggradation phase (a-d) and progradation phase (e-h). (a,e) Geometry of model. Arrows indicate deformational velocities. (b,f) Pore-fluid pressure ratio λ_{HR}. (c,g) Pressure-depth profiles at 250 km. Light blue curve shows minimum porosity of the material during model evolution. (d,h) Porosity/conductivity-depth profiles at 250 km.

Progradation

After 43 Ma of progradation, the model shows evidence of incipient gravity spreading (Figure 3.5e,f) with minor extension (diverging velocity vectors) and shortening (converging velocity vectors, folding). Overpressures have reached values of approximately λ_{HR}=0.8-0.95 throughout most of the distal part of the basin (Figure 3.5f,g). With the onset of gravity spreading, the top of overpressure is now located at depths of 0.5-2 km above the distal part of the salt basin but remains at depths of 3 km seaward of the salt basin (white line in Figure 3.5f). As in the aggradation phase, the fluid pressures maintain values nearly parallel to the mean stress in the overpressured regions (Figure 3.5g). Porosity decreases rapidly within the upper 1 km of sediment, below which it stabilizes at 15-20% (Figure 3.5h). The corresponding hydraulic conductivities follow the same trend and reach values of 10^{-14} m/s, sufficiently low for moderate, but not 'hard', overpressure to develop. The mean stress in the sediment again exceeds lithostatic pressure (Figure 3.5g), indicating a state close to compressional failure, the 'passive Rankine state'.

The light blue curve (Figure 3.5h) marks the minimum porosity achieved in the 250 km section during the model evolution. Since this is lower than the current porosity (black curve), decompaction must have taken place (see discussion).

3.4.4 Model SL-Sh2, Strong Viscous Compaction

Model SL-Sh2 shows the result of aggradation for shale-type lithology when there is strong, likely excessive, viscous compaction ($\eta = 10^{22}$ Pa s), which accounts for the differences by comparison with model SL-Sh1.

Aggradation

During the aggradation phase, fluid overpressures develop below 2 km and follow a steep gradient leading to lithostatic fluid pressure in the bottom 2 km of the sediments (Figure 3.6b,c). Enhanced viscous compaction has allowed porosities to decrease to ca. 12% in this region with corresponding hydraulic conductivities in the shale-type material of 10^{-15} m/s. This parameter combination results in hard overpressure.

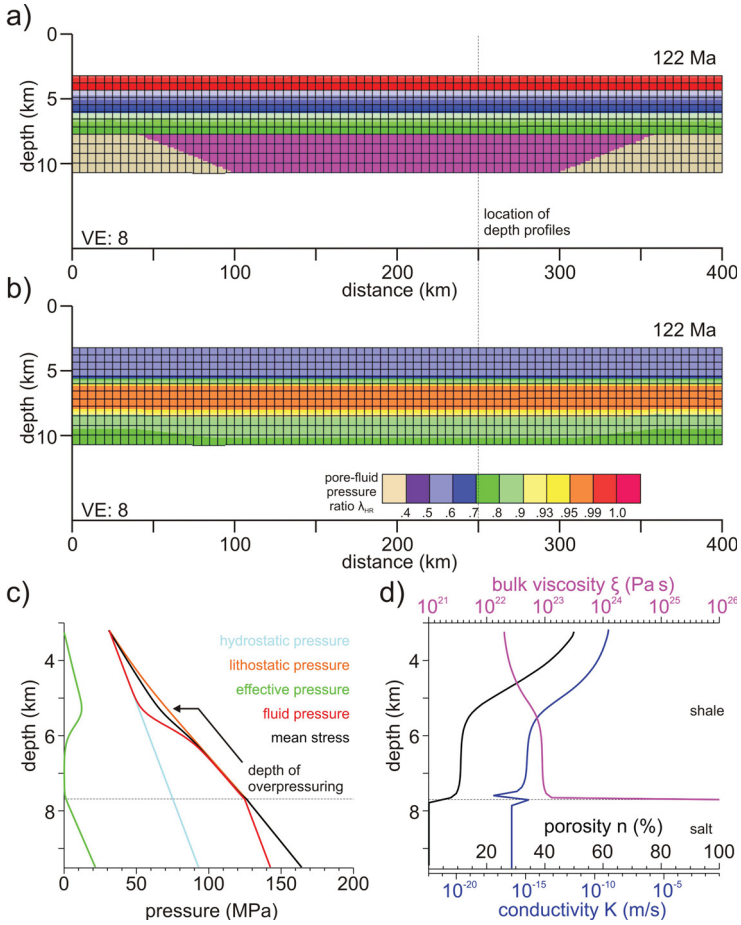

Figure 3.6: Results of model SL-Sh2 with shale-type sediments and constant compactional shear viscosity of μ=10^{22} Pa s at end of aggradation phase. (a) Geometry of model. (b) Pore-fluid pressure ratio λ_{HR}. (c) Pressure-depth profiles at 250 km. (d) Porosity/conductivity-depth profiles at 250 km.

Below the sediment layer, the fluid pressure again follows a hydrostatic gradient. Owing to the unrealistic level of overpressure, the progradation phase is not shown.

3.5 Discussion

The four models presented here show the different mechanical compaction behavior of well-drained sandstone-type material and poorly-drained shale-type material combined with different levels of viscous compaction. The contrasting behavior of the models in regard to compaction, fluid-pressure generation, and gravitational failure is discussed below.

Overpressuring

In the case of sandstone-type model SL-Sa1, fluids expelled by compaction can leave the sediment column through the well-connected pore space (hydraulic conductivity 10^{-6}-10^{-7} m/s). Limited compaction during aggradation also takes place very slowly (from 50% to 30% in 100 Ma), which means the pore-fluid flux is low and this also augments the well-drained nature of the system.

In the other models, overpressure develops where hydraulic conductivity decreases below 10^{-15} m/s. This appears to be the critical value at which fluids can no longer migrate upward fast enough to balance compaction on the characteristic timescales of these models. Fluid escape is hampered by both low hydraulic conductivities and a large thickness of the overlying sediment column, which increases with time. Because fluid expulsion becomes increasingly difficult, further compaction is strongly limited, as is seen from the porosity-depth curves of models SL-Sa2 (Figure 3.4d,h) and SL-Sh2 (Figure 3.6d), leading to near-constant values of porosity and hydraulic conductivity in the lower sediments.

Fluid Pressure in Salt and Crustal Material

The fluid pressures in the salt and crustal material maintain a hydrostatic gradient. The fluid pressure here simply reflects that the fluid is trapped at near-hydrostatic conditions and just responds to the increasing weight of the overburden, so that the

in-situ pressures all increase by the same amount and the hydrostatic gradient is maintained.

In nature there may be interactions among the fluid regimes in the sediments and those in the salt and underlying crust, but we have chosen to suppress these by modeling salt and crust as non-compacting materials containing only very small pockets of fluid. Moreover, the fluid pressure regime in these models does not influence deformation of salt (viscous incompressible flow) or that of the crustal material (effective stresses do not exceed frictional-plastic yield stress).

Mechanical Compaction

Mechanical compaction is best demonstrated in models SL-Sa1 and SL-Sh1, in which viscous compaction is nearly suppressed. During mechanical compaction, the rate of porosity change depends on the rate of change of effective pressure (equation 3.6). In a well-drained case, the time integrated increase of effective pressure will increase with depth of burial and the integrated reduction in porosity should behave accordingly, such that in model SL-Sa1 the porosities decrease uniformly with depth. Hydraulic conductivities remain high enough to maintain hydrostatic fluid pressure.

The situation is different in model SL-Sh1, where the hydraulic conductivities reach much lower values and overpressure develops. Accordingly, the time integrated change of effective pressure with depth is lower than in model SL-Sa1, mechanical compaction is reduced by comparison with the well-drained behavior near the surface, and a less steep porosity gradient ensues (Figure 3.5d,h). In the limit of no additional compaction and no fluid expulsion, the load of aggrading sediments increases the mean stress and the pore fluid pressure equally, so that the effective pressure remains the same (Figure 3.5c,g). The cessation of compaction with depth is only partly related to the lock-off value of 10% porosity for mechanical compaction used here; tests without a limiting minimum porosity showed similar results. The process of mechanical compaction is also activated in the progradation phase during gravitational deformation, as discussed below.

Viscous Compaction

Strong viscous compaction occurs in models SL-Sa2 and SL-Sh2, in addition to the mechanical compaction described above. The rate of viscous compaction increases with the effective pressure (equation 3.6), and the net compaction increases with the time that a sedimentary section is exposed to this pressure. Conversely, the rate decreases with decreasing porosity.

Owing to the time-dependence, viscous compaction may become much stronger in long-lived basins than mechanical compaction as is seen, for example, in the case of model SL-Sa2. This also leads to a reduction of the depth of overpressure with time (compare Figures 3.4b,c and 3.4f,g). This reduction already develops before the onset of gravity spreading, is uniform across the model and affects also the far distal end. Therefore, it cannot be attributed to a changing stress regime during gravity spreading.

Another consequence of the continuing viscous compaction is that the zone of near-lithostatic fluid pressure progressively thickens and reaches approximately 2 km in both model SL-Sa2 (progradation phase) and SL-Sh2 (aggradation phase). These sediments have effectively no strength and could be considered as being in suspension in the pore fluid. Such fluid pressures are unrealistic and a solution to this problem is presented in *Gradmann and Beaumont* (2012, Chapter 4).

In the current formulation, viscous compaction only ceases when either the effective pressure becomes zero (lithostatic fluid pressure values) or the bulk viscosity becomes very high, corresponding to near-zero porosities. In the models presented here, the bulk viscosity, even at values of 10^{24} Pa s (model SL-Sh2), still enables compaction within the time span of tens of millions of years considered here (Figure 3.4h), and compaction doesn't stop until the effective pressure is zero.

The effect of porosity and related hydraulic conductivity on viscous compaction can be seen by comparing sandstone-type and shale-type models. Differences in minimum porosity between the two sandstone-type models are approximately 30%, but between the shale-type models only up to 10%. This demonstrates that viscous compaction in the sandstone-type material with relatively high porosities and high hydraulic conductivities is much more efficient than in the already mechanically compacted shale-type material.

Mean Stress and Lithostatic Pressure

A difference between mean stress and lithostatic pressure can be observed in the sediment column of all models (mean stress is generally lower than lithostatic pressure throughout the aggradation phase and larger than lithostatic pressure in the distal regime after gravitational failure). Deviations from lithostatic stress are common in tensile or compressive stress regimes, where the horizontal stress is smaller or larger, respectively, than the vertical stress, here the load of the overburden. In the frictional-plastic sediments of models SL-Sa2 and SL-Sh1, the high mean stress in the compressional domain (during the progradation phase) indicates compressional failure, the passive failure state, as is also indicated by velocities that show post-yield deformation of the material.

The reduction in mean stress observed in the aggradation phases of all models is generally indicative of a tensile stress system where sub-lithostatic pressure occurs owing to deviatoric tension but is here linked to compaction. Whether the stress state observed during vertical compaction represents tensional failure is a complex question and is addressed in *Gradmann and Beaumont* (2012, Chapter 4).

Effects of Horizontal Shortening

As the system approaches a state of gravitational spreading, the mean stress in the compressional region increases and becomes larger than the lithostatic pressure, as noted above. This means that during gravitational deformation, there is an increase in effective pressure and thus a phase of renewed mechanical compaction and increased viscous compaction in the shortening part of the system. The effects are strongest in the shallow, not yet strongly compacted sediments and fluid pressure increases here. The accompanying decrease in overpressuring depth (white line in model SL-Sh1, Figure 3.5f, see also Animation_SL-Sh1) is then a direct indicator of change in effective pressure, controlled by the horizontal compressive stress. As seen here, the compressive stress is accordingly largest near the base of the slope (where depth of overpressuring is shallowest) and smallest in the distal end of the salt basin. This stress distribution is similar to that of earlier models of *Gradmann et al.* (2009), where deformation localized at the toe of the slope but was absent at the seaward end of the salt basin. Such a deformation pattern is, however, not observed in model SL-Sh1;

and we attribute the folding at the end of the salt basin to the strong influence of developing overpressures.

Decompaction

The increase in porosity (or decompaction) in model SL-Sh1 (Figure 3.5h) only occurs after gravity spreading has started and the region experiences increased horizontal stress. As can be seen from equation (3.6), porosity can only increase if either the effective pressure is negative, which is unrealistic and does not occur in the model set presented here, or if decompaction is mechanical and results from a decrease of effective pressure with time. Such generation of secondary porosity has been observed and studied in basins such as the Gulf of Mexico, and the decreasing effective pressure has commonly been attributed to erosion and unloading (*Corbet and Bethke*, 1992; *Gordon and Flemings*, 1998).

In the context of the present study, compaction itself is a more plausible mechanism for the decrease of effective pressure. Viscous compaction, in particular, can lead to a substantial increase of fluid pressure, which reduces the effective pressure. In the observed case of model SL-Sh1, the net porosity change is positive, suggesting that the process of (mechanical) decompaction is here stronger than that of (viscous) compaction. Another possible decompaction mechanism is the declining mean stress (declining effective pressure) toward the end of deformation, which could allow the sediment to decompact under high ambient fluid pressure. The models shown here are, however, still experiencing deformation and this second mechanism cannot be held responsible for the observed decompaction.

Comparison to Natural Systems

Typically, the fluid pressure in sedimentary basins remains hydrostatic to a depth of 2-3 km, below which it increases and maintains values between hydrostatic and lithostatic. Only model SL-Sh1 shows a similar pressure-depth relation. Other models either develop no overpressure (model SL-Sa1) and accordingly no gravitational failure, or develop essentially lithostatic fluid pressure over thicknesses of several kilometers (models SL-Sa2 and SL-Sh2). Such high and widespread fluid overpressures

are unknown from relatively sand-rich sedimentary basins such as the Gulf of Mexico (*Galloway et al.*, 2000). Models with shale-type sediments and very high fluid pressure would better apply to shale-dominated areas like the Niger delta (*Ings and Beaumont*, 2010). Models with alternating sandstone-type and shale-type layers are presented in *Gradmann and Beaumont* (2012).

3.6 Conclusions

In this study we presented 2D finite element models that couple compaction-induced fluid pressures with mechanical deformation and investigated the compaction and overpressuring behavior of sandstone-type and shale-type materials. Two sets of model parameters were developed that control mechanical and viscous compaction and yield the distinct behavior of the two materials. Primarily mechanically compacting sandstone-type material maintains high porosities and hydrostatic fluid pressures. Porosity in shale-type material, on the other hand, decreases rapidly and overpressure develops.

Where mechanical compaction leads to overpressuring, the fluid pressure maintains a similar gradient as the mean stress. Compaction ceases because there is no further change in effective pressure. Where viscous compaction leads to overpressure, fluid pressure rises to lithostatic values given sufficient time. Decreasing porosities slow this process but do not stop it. An improved formulation that avoids this protracted viscous compaction at low porosity is introduced in *Gradmann and Beaumont* (2012, Chapter 4).

Shortening, as experienced in the distal part of a gravity-spreading system, strongly increases the effective pressure and leads to a renewed phase of mechanical and viscous compaction. Decompaction is disclosed as a process of reverse mechanical compaction, owing to effective pressure that decreases with time, and mainly occurs in regions of strong viscous compaction. This illustrates that the two compaction mechanisms are different, yet coupled processes that need to be analyzed in conjunction with one another.

The single-lithology models described here are only prototypes and cannot satisfactorily reproduce observed pressure-depth profiles from mixed lithology sedimentary basins or from the Oligocene setting of the northwestern Gulf of Mexico in particular.

However, they are useful to demonstrate the basic mechanisms that operate in coupled fluid-mechanical models and how these models can aid in the understanding of gravitational failure in rifted margin salt-siliciclastic systems. Having demonstrated the behavior of these prototypes, we investigate more complex systems, comprising layered sandstone-type and shale-type lithologies, in *Gradmann and Beaumont* (2012, Chapter 4).

3.7 Acknowledgements

Funding for this project was provided by a Killam Scholarship and a Government of Canada Award to SG, an IBM SUR grant and the Canada Research Chair in Geodynamics to CB. We also like to thank Shell International Exploration and Production, Inc. for their kind support and ION/GXT for permission to show their data. Numerical computations were made with the software SOPALEff, developed by Philippe Fullsack and Christina Morency. Post-processing and graphical display of the model results are based on IDL-scripts written by Sergei Medvedev. Jürgen Adam is thanked for reviews of earlier versions of this paper. We also thank Martin Jackson, an anonymous reviewer, Boris Kaus, and the editor for their reviews.

Bibliography

Angevine, C. L., and D. L. Turcotte (1983), Porosity reduction by pressure solution: A theoretical model for quartz arenites, *Geological Society of America Bulletin*, *94*(10), 1129–1134.

Athy, L. F. (1930), Density, porosity, and compaction of sedimentary rocks, *Bulletin of the American Association of Petroleum Geologists*, *14*(1), 1–24.

Audet, D. M., and A. C. Fowler (1992), A mathematical model for compaction in sedimentary basins, *Geophysical Journal International*, *110*(3), 577–590.

Berry, F. A. F. (1973), High fluid potentials in California Coast Ranges and their tectonic significance, *AAPG Bulletin*, *57*(7), 1219–1249.

Biot, M. A. (1941), General theory of three-dimensional consolidation, *Journal of Applied Physics*, *12*(2), 155–164.

Birchwood, R. A., and D. L. Turcotte (1994), A unified approach to geopressuring, seal formation and secondary porosity generation in sedimentary basins, *EOS, Transactions, American Geophysical Union*, *73*(14), 279.

Bjørlykke, K. (1997), An overview of factors controlling rates of compaction, fluid generation and flow in sedimentary basins, in *Growth, dissolution and pattern formation in geosystems*, edited by B. Jamtveit and P. Meakin, pp. 381–404, Kluwer Academic Publishers, Dordrecht, Netherlands, Netherlands.

Bradley, J. S., and D. E. Powley (1994), Pressure compartments in sedimentary basins: A review, in *Basin compartments and seals*, *AAPG Memoir*, vol. 61, edited by P. J. Ortoleva, pp. 3–26, AAPG, Tulsa, Oklahoma.

Bredehoeft, J. D., and B. B. Hanshaw (1968), On the maintenance of anomalous fluid pressures: Part 1, Thick sedimentary sequences, *Geological Society of America Bulletin*, *79*(9), 1097–1106.

Butler, R. W. H., and D. A. Patron (2010), Evaluating lateral compaction in deepwater fold and thrust belts: How much are we missing from "nature's sandbox" ?, *GSA Today*, *20*(3), 4–10.

Carter, N. L., S. T. Horseman, J. E. Russell, and J. Handin (1993), Rheology of rocksalt, *Journal of Structural Geology*, *15*(9-10), 1257–1271.

Casas, E., and T. K. Lowenstein (1989), Diagenesis of saline pan halite: Comparison of petrographic features of modern, Quaternary and Permian halites, *Journal of Sedimentary Petrology*, *59*(5), 724–739.

Cinar, Y., G. Pusch, and V. Reitenbach (2006), Petrophysical and capillary properties of compacted salt, *Transport in Porous Media*, *64*(2), 199–228.

Colten-Bradley, V. A. (1987), Role of pressure in smectite dehydration: Effects on geopressure and smectite-to-illite transformation, *AAPG Bulletin*, *71*(11), 1414–1427.

Connolly, J. A. D., and Y. Y. Podladchikov (2000), Temperature-dependent viscoelastic compaction and compartmentalization in sedimentary basins, *Tectonophysics*, *324*(3), 137–168.

Corbet, T. F., and C. M. Bethke (1992), Disequilibrium fluid pressures and groundwater flow in the Western Canada sedimentary basin, *Journal of Geophysical Research*, *97*(B5), 7203–7217.

David, C., T.-F. Wong, W. Zhu, and J. Zhang (1994), Laboratory measurement of compaction-induced permeability change in porous rocks: Implications for the generation and maintenance of pore pressure excess in the crust, *Pure and Applied Geophysics*, *143*(1-3), 425–456.

Davis, D., J. Suppe, and F. A. Dahlen (1983), Mechanics of fold-and-thrust belts and accretionary wedges, *Journal of Geophysical Research*, *88*(B2), 1153–1172.

Davison, I. (2009), Faulting and fluid flow through salt, *Journal of the Geological Society of London*, *166*(2), 205–216.

Demercian, S., P. Szatmari, and P. R. Cobbold (1993), Style and pattern of salt diapirs due to thin-skinned gravitational gliding, Campos and Santos basins, offshore Brazil, *Tectonophysics*, *228*(3-4), 393–433.

Downey, M. W. (1984), Evaluating seals for hydrocarbon accumulations, *AAPG Bulletin*, *68*(11), 1752–1763.

Fiduk, J. C., P. Weimer, B. D. Trudgill, M. G. Rowan, P. E. Gale, R. L. Phair, B. E. Korn, G. R. Roberts, W. T. Gafford, R. S. Lowe, and T. A. Queffelec (1999), The Perdido fold belt, Northwestern deep Gulf of Mexico, Part 2; Seismic stratigraphy and petroleum systems, *AAPG Bulletin*, *83*(4), 578–612.

Fort, X., J. P. Brun, and F. Chauvel (2004), Contraction induced by block rotation above salt (Angolan margin), *Marine and Petroleum Geology*, *21*(10), 1281–1294.

Fowler, A. C., and X. Yang (1999), Pressure solution and viscous compaction in sedimentary basins, *Journal of Geophysical Research*, *104*(B6), 12,989–12,998.

Freed, R. L., and D. R. Peacor (1989), Geopressured shale and sealing effect of smectite to illite transition, *AAPG Bulletin*, *73*(10), 1223–1232.

Fullsack, P. (1995), An arbitrary Lagrangian-Eulerian formulation for creeping flows and its applications in tectonic models, *Geophysical Journal International*, *120*(1), 1–23.

Galloway, W. E., P. E. Ganey-Curry, X. Li, and R. Buffler (2000), Cenozoic depositional history of the Gulf of Mexico basin, *AAPG Bulletin*, *84*(11), 1743–1774.

Garven, G. (1986), The role of regional fluid flow in the genesis of the Pine Point Deposit, Western Canada sedimentary basin; reply, *Economic Geology and the Bulletin of the Society of Economic Geologists*, *81*(4), 1015–1020.

Ge, H., M. P. A. Jackson, and B. C. Vendeville (1997), Kinematics and dynamics of salt tectonics driven by progradation, *AAPG Bulletin*, *81*, 398–423.

Gemmer, L., S. J. Ings, S. Medvedev, and C. Beaumont (2004), Salt tectonics driven by differential sediment loading: Stability analysis and finite element experiments, *Basin Research*, *16*, 199–219.

Gemmer, L., C. Beaumont, and S. J. Ings (2005), Dynamic modeling of passive margin salt tectonics: Effects of water loading, sediment properties, and sedimentation patterns, *Basin Research*, *17*, 383–402.

Gordon, D. S., and P. B. Flemings (1998), Generation of overpressure and compaction-driven fluid flow in a Plio-Pleistocene growth-faulted basin, Eugene Island 330, offshore Louisiana, *Basin Research*, *10*(2), 177–196.

Gradmann, S., and C. Beaumont (2012), Coupled fluid flow and sediment deformation in margin-scale salt-tectonic systems: 2. Layered sediment models and application to the northwestern Gulf of Mexico, *Tectonics*, *31*(4), doi: 10.1029/2011TC003035.

Gradmann, S., C. Beaumont, and M. Albertz (2009), Factors controlling the evolution of the Perdido Fold Belt, northwestern Gulf of Mexico, determined from numerical models, *Tectonics*, *28*(2).

Hubbert, M. K., and W. W. Rubey (1959), Role of fluid pressure in mechanics of overthrust faulting: Part 1, Mechanics of fluid-filled porous solids and its application to overthrust faulting, *Geological Society of America Bulletin*, *70*(2), 115–166.

Ings, S. J., and C. Beaumont (2010), Continental margin shale tectonics: Preliminary results from coupled fluid-mechanical models of large-scale delta instability, *Journal of the Geological Society of London*, *167*(3), 571–582.

Jackson, M. P. A. (1995), Retrospective salt tectonics, in *Salt Tectonics, A Global Perspective*, *AAPG Memoir*, vol. 65, edited by M. P. A. Jackson, D. G. Roberts, and S. Snelson, pp. 1–28, AAPG, Tulsa, Oklahoma.

Krezsek, C., J. Adam, and D. Grujic (2007), Mechanics of fault/rollover systems developed on passive margins detached on salt: Insights from analogue modelling and optical strain monitoring, in *Structurally Complex Reservoirs*, *Geological Society Special Publications*, vol. 292, edited by S. J. Jolley, D. Barr, J. J. Walsh, and R. J. Knipe, pp. 103–121, Geological Society of London.

Kulenkampff, J. M., and U. Yaramanci (1993), Frequency-dependent complex resistivity of rock-salt samples and related petrophysical parameters, *Geophysical Prospecting*, *41*(8), 995–1008.

Letouzey, J., B. Colletta, R. Vially, and J. C. Chermette (1995), Evolution of salt-related structures in compressional settings, in *Salt Tectonics, A Global Perspective*, *AAPG Memoir*, vol. 65, edited by M. P. A. Jackson, D. G. Roberts, and S. Snelson, pp. 41–60, AAPG, Tulsa, Oklahoma.

Luo, X., and G. Vasseur (1996), Geopressuring mechanism of organic matter cracking: numerical modeling, *AAPG Bulletin*, *80*(6), 856–874.

Maxwell, S. A. (2009), Deformation styles of allochthonous salt sheets during differential loading conditions: Insights from discrete element models, Master's thesis, Rice University, Houston, Texas.

Mello, U. T., G. D. Karner, and R. N. Anderson (1994), A physical explanation for the positioning of the depth to the top of overpressure in shale-dominated sequences in the Gulf Coast basin, United States, *Journal of Geophysical Research*, *99*(B2), 2775–2789.

Morency, C., R. S. Huismans, C. Beaumont, and P. Fullsack (2007), A numerical model for coupled fluid flow and matrix deformation with applications to disequilibrium compaction and delta stability, *Journal of Geophysical Research*, *112*(B10), 407.

Mourgues, R., and P. R. Cobbold (2003), Some tectonic consequences of fluid overpressures and seepage forces as demonstrated by sandbox modelling, *Tectonophysics*, *376*(1-2), 75–97.

Mourgues, R., E. Lecomte, B. Vendeville, and S. Raillard (2009), An experimental investigation of gravity-driven shale tectonics in progradational delta, *Tectonophysics*, *474*(3-4), 643 – 656.

Neuzil, C. E. (1994), How permeable are clays and shales?, *Water Resources Research*, *30*(2), 145–150.

Osborne, M. J., and R. E. Swarbrick (1997), Mechanisms for generating overpressure in sedimentary basins: A reevaluation, *AAPG Bulletin*, *81*(6), 1023–1041.

Paterson, M. S. (1973), Nonhydrostatic thermodynamics and its geologic applications, *Reviews of Geophysics and Space Physics*, *11*(2), 355–389.

Peach, C. J., C. J. Spiers, and P. W. Trimby (2001), Effect of confining pressure on dilatation, recrystallization, and flow of rock salt at 150 degrees C, *Journal of Geophysical Research*, *106*(B7), 13,315–13,328.

Peel, F. J., C. J. Travis, and J. R. Hossack (1995), Genetic structural provinces and salt tectonics of the Cenozoic offshore U.S. Gulf of Mexico: A preliminary analysis, in *Salt Tectonics, A Global Perspective*, *AAPG Memoir*, vol. 65, edited by M. P. A. Jackson, D. G. Roberts, and S. Snelson, pp. 153–175, AAPG, Tulsa, Oklahoma.

Popp, T., H. Kern, and O. Schulze (2001), Evolution of dilatancy and permeability in rock salt during hydrostatic compaction and triaxial deformation, *Journal of Geophysical Research*, *106*(B3), 4061–4078.

Radovich, B., J. Moon, C. Connors, and D. Bird (2007), Insights into structure and stratigraphy of the northern Gulf of Mexico from 2D pre-stack depth migration imaging of mega-regional onshore to deep water, long-offset seismic data, *Transactions - Gulf Coast Association of Geological Societies*, *57*, 633–637.

Revil, A. (2001), Pervasive pressure solution transfer in a quartz sand, *Journal of Geophysical Research*, *106*(B5), 8665–8686.

Revil, A., and L. M. Cathles (1999), Permeability of shaly sands, *Water Resources Research*, *35*(3), 651–662.

Revil, A., D. Grauls, and O. Brevart (2002), Mechanical compaction of sand/clay mixtures, *Journal of Geophysical Research*, *107*(B11), 15.

Rowan, M. G., F. J. Peel, and B. C. Vendeville (2004), Gravity-driven fold belts on passive margins, in *Thrust tectonics and hydrocarbon systems*, *AAPG Memoir*, vol. 82, edited by K. R. McClay, pp. 157–182, AAPG, Tulsa, Oklahoma.

Schleder, Z., J. L. Urai, S. Nollet, and C. Hilgers (2008), Solution-precipitation creep and fluid flow in halite: A case study of Zechstein (Z1) rocksalt from Neuhof salt mine (Germany), *International Journal of Earth Sciences*, *97*(5), 1045–1056.

Schneider, F., J. L. Potdevin, S. Wolf, and I. Faille (1996), Mechanical and chemical compaction model for sedimentary basin simulators, *Tectonophysics*, *263*(1-4), 307–317.

Schoenherr, J., J. L. Urai, P. A. Kukla, R. Littke, Z. Schleder, J.-M. Larroque, M. J. Newall, N. Al-Abry, H. Al-Siyabi, and Z. Rawahi (2007), Limits to the sealing capacity of rock salt: A case study of the infra-Cambrian Ara Salt from the South Oman salt basin, *AAPG Bulletin*, *91*(11), 1541–1557.

Simmons, G. R. (1992), The regional distribution of salt in the northwestern Gulf of Mexico; styles of emplacement and implications for early tectonic history, *Bulletin - Houston Geological Society*, *35*(4), 7.

Smith, J. E. (1971), The dynamics of shale compaction and evolution of pore-fluid pressures, *Journal of the International Association for Mathematical Geology*, *3*(3), 239–263.

Suetnova, E., and G. Vasseur (2000), 1-D modelling rock compaction in sedimentary basins using a visco-elastic rheology, *Earth and Planetary Science Letters*, *178*(3-4), 373–383.

Swarbrick, R. E., and M. J. Osborne (1998), Mechanisms that generate abnormal pressures: an overview, in *Abnormal pressures in hydrocarbon environments*, *AAPG Memoir*, vol. 70, edited by B. Law and C. Spencer, pp. 13–34, AAPG, Tulsa, Oklahoma.

Terzaghi, K. (1936), The shearing resistance of saturated soil and the angle between the planes of shear, *Proc. 1st Int. Conf. Soil Mech*, *1*, 54–56.

Terzaghi, K. (1943), *Theoretical soil Mechanics*, John Wiley and Sons, New York.

Urai, J. L., C. J. Spiers, H. J. Zwart, and G. S. Lister (1986), Weakening of rock salt by water during long-term creep, *Nature*, *324*, 554–557.

van Keken, P. E., C. J. Spiers, A. P. van den Berg, and E. J. Muyzert (1993), The effective viscosity of rocksalt: Implementation of steady-state creep laws in numerical models of salt diapirism, *Tectonophysics*, *225*(4), 457–476.

van Ruth, P., R. Hillis, P. Tingate, and R. Swarbrick (2003), The origin of overpressure in 'old' sedimentary basins: An example from the Cooper Basin, Australia, *Geofluids*, *3*(2), 125–131.

Vendeville, B. C. (2005), Salt tectonics driven by sediment progradation: Part 1, Mechanics and kinematics, *AAPG Bulletin*, *89*(8), 1071–1079.

Watts, A. B. (2001), *Isostasy and flexure of the lithosphere*, University of Cambridge, Cambridge, United Kingdom.

Weimer, P., and R. T. Buffler (1992), Structural geology and evolution of the Mississippi Fan fold belt, deep Gulf of Mexico, *AAPG Bulletin*, *76*(2), 225–251.

Willett, S. D. (1999), Rheological dependence of extension in wedge models of convergent orogens, *Tectonophysics*, *305*(4), 419–435.

Yassir, N. A., and J. S. Bell (1996), Abnormally high fluid pressures and associated porosities and stress regimes in sedimentary basins, *SPE Formation Evaluation*, *11*(1), 5–10.

Chapter 4

Coupled Fluid Flow and Sediment Deformation in Margin-Scale Salt-Tectonic Systems: 2. Layered Sediment Models and Application to the Northwestern Gulf of Mexico

This chapter has been published as "*Gradmann, S., and C. Beaumont (2012), Coupled fluid flow and sediment deformation in margin-scale salt-tectonic systems: 2. Layered sediment models and application to the northwestern Gulf of Mexico, Tectonics, doi:10.1029/2011TC003035.*" Reproduced by permission of American Geophysical Union. Minor editorial corrections have been applied.

4.0 Abstract

In *Gradmann et al.* (2012, Chapter 3) we described a methodology to model coupled fluid flow and deformation in composite salt and siliciclastic tectonic systems and investigated their compaction and overpressuring behavior prior to and during continental margin-scale gravitational spreading. Compaction-driven Darcy fluid flow in clastic sediments is coupled through the effective pressure to their frictional-plastic yield and mechanical deformation. Viscous flow of the underlying salt is independent of fluid pressure. *Gradmann et al.* (2012) presented prototype models that are limited to single uniform sediment lithologies, either sandstone-type or shale-type, that undergo mechanical and volumetric viscous compaction. In this paper we present models with layered sandstone-type and shale-type lithologies designed to better approximate the more complex stratigraphy of the Gulf of Mexico, our natural example. A first set of models demonstrates that layered lithologies can produce fluid pressure regimes similar to those observed in sedimentary basins. We then introduce an improved formulation of viscous compaction that includes a stronger dependence on porosity and depth (used as proxy for temperature), thereby more strongly self-limiting viscous

compaction. A second set of models with the improved viscous compaction formulation demonstrates that the onset of gravity spreading is mainly controlled by the overpressuring in the landward end of the salt basin and that resulting shortening in the distal part is partly accommodated by horizontal compaction. Models with moderately high fluid pressures best reproduce conditions considered to have been necessary for large-scale gravitational spreading in the northwestern Gulf of Mexico, which led to the formation of the Perdido Fold Belt.

4.1 Introduction

In this study we model the effects of coupled fluid flow and deformation in the system of continental-margin scale gravity spreading of sediments above salt. We compare the results with a natural example that is approximately equivalent, the Oligocene setting of the Gulf of Mexico. *Gradmann et al.* (2009) investigated the evolution of the Perdido Fold Belt in the northwestern Gulf of Mexico, a large salt-cored deep-water structure, and concluded that on average a Hubbert-Rubey pore-fluid pressure ratio of approximately λ_{HR}=0.8 would have been needed to enable the system to fail and then fold by gravity spreading. λ_{HR} is the ratio of fluid pressure to lithostatic pressure (*Hubbert and Rubey*, 1959). Following *Davis et al.* (1983) we use $\lambda_{HR} = \frac{P_f - P_w}{P_{litho} - P_w}$ for submarine conditions, where P_f, P_{litho} and P_w are the fluid pressure, lithostatic pressure and the pressure of the water column, respectively.

The results presented in *Gradmann et al.* (2012, Chapter 3) demonstrated that single-lithology models can develop sufficient pore-fluid pressure so that gravity spreading and folding of a Perdido-like system (4.5 km thick clastic sediment layer overlying salt) will occur if efficient viscous compaction generated high overpressures (c.f. models SL-Sa2, SL-Sh1). However, these prototype models are not suitable for direct comparison with the Perdido system because neither the fluid pressure regime that develops nor the modeled sediment lithology corresponds to those reported from sedimentary basins like the northwestern Gulf of Mexico. Here, the sedimentary section comprises deep-water carbonates and several sandstone-dominated layers, which are interlayered with multiple condensed, shale-dominated layers. The main focus of Chapter 4 is therefore to investigate how composite, lithologically layered sediments

above salt behave as gravity-spreading systems and under what pore-fluid pressure regimes the Perdido Fold Belt may have evolved.

Compaction-driven Darcy fluid flow in clastic sediments is coupled through the effective pressure to their frictional-plastic yield and mechanical deformation. Viscous flow of the underlying salt is independent of fluid pressure. *Gradmann et al.* (2012, Chapter 3) presented prototype models that are limited to single uniform sediment lithologies with simple parameterizations of their properties. Sandstone-type and shale-type sediments are discussed and modeled to study their contrasting behavior. Both types of sediment compact by a combination of mechanical and volumetric viscous processes. The single-lithology models are not representative of the more complex stratigraphy of the Gulf of Mexico, our natural example, but serve to illustrate the interactions among compaction, generation of fluid overpressure, and gravitational failure and spreading.

Salt, which is viscously weak, is key to the process of gravity spreading because it reduces basal traction and can act as a décollement layer. Channel (Poiseuille) flow of the salt also assists the failure by applying an additional seaward directed basal drag force on the overburden as it is squeezed and mobilized by differential loading (*Gemmer et al.*, 2004, 2005). The conditions of failure also depend critically on the strength of the overburden and, therefore, on the second key component of the problem, the fluid pressure regime (*Gemmer et al.*, 2005; *Gradmann et al.*, 2009).

We first describe conceptually the effects of alternating sealing and permeable layers, and then relate them to the sedimentary units and current pore-fluid pressure regime of the northwestern Gulf of Mexico (section 4.2). We briefly recap the methodology used in the computations (section 4.3) and then describe simple numerical models of sandstone-type and shale-type layered lithologies (section 4.4). In section 4.5 we introduce an improved model for viscous compaction (pressure solution) that includes the first-order effects of temperature-dependent volumetric viscosity and report on the results of layered lithological models using this improved model. Overall results are discussed and summarized in section 4.7.

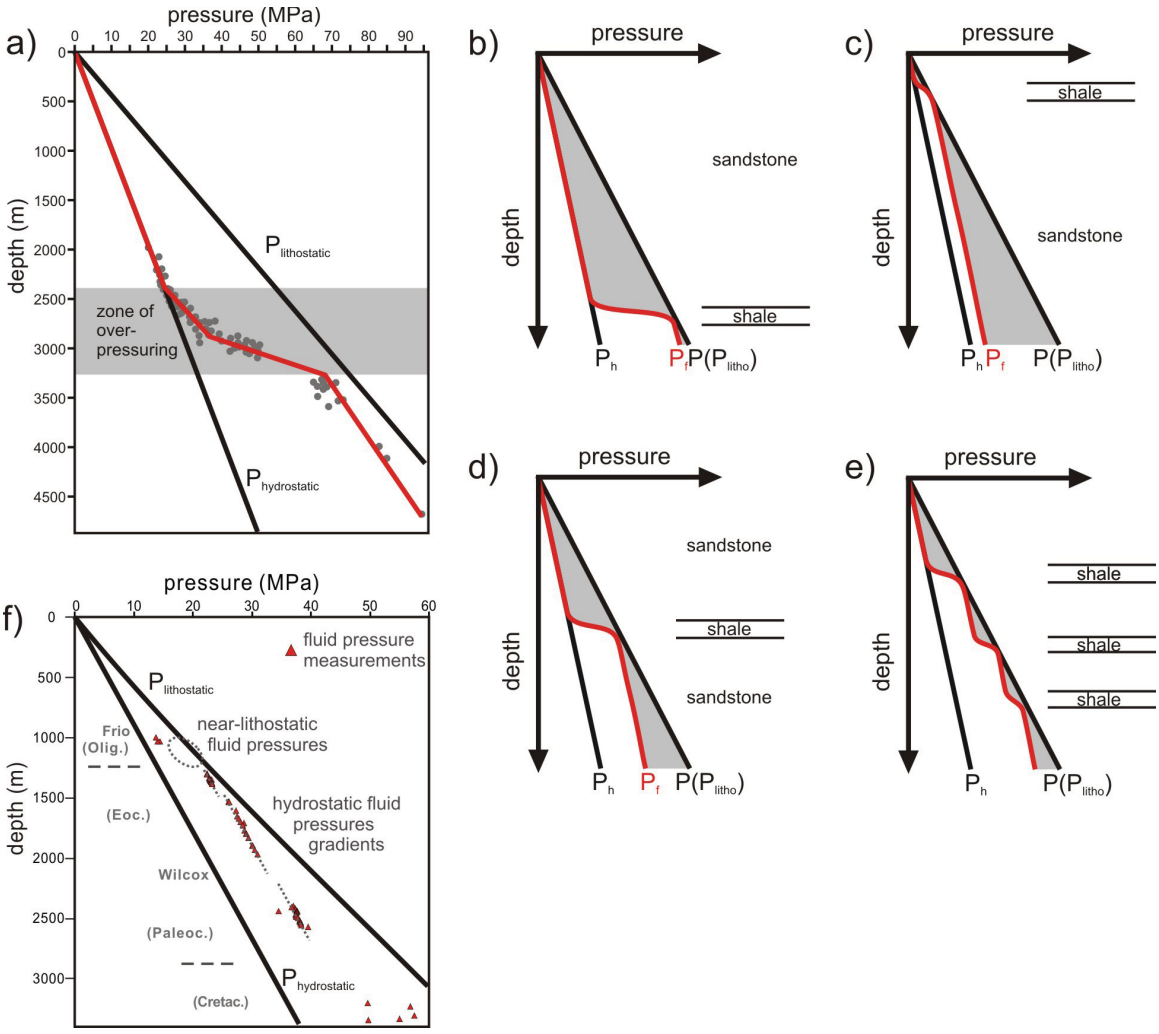

Figure 4.1: Measured and schematic pressure-depth profiles from sedimentary basins. (a) Fluid pressures of the Monte Christo field, Hidalgo County, Texas. (After *Leftwich and Engelder*, 1994). (b) Schematic fluid pressure profile of well-drained sandstone section underlain by sealing shale layer. (c) Schematic fluid pressure profile of well-drained sandstone section overlain by sealing shale layer. (d) Schematic fluid pressure profile of well-drained sandstone section interbedded by sealing shale layer. (e) Schematic fluid pressure profile of well-drained sandstone section interbedded by multiple sealing shale layers. Gray shaded areas mark the integrated effective pressure, representative for the strength of the sediment column. (f) Fluid pressures from the Perdido Fold Belt, northwestern Gulf of Mexico. (After *Couzens-Schultz et al.*, 2007).

4.1.1 Conceptual Effects of Layered Lithologies on Fluid Pressures

Pore-fluid pressure regimes of sedimentary basins commonly look like the one shown in Figure 4.1a, an example from the Gulf Coast of southern Texas. Here, fluid pressure remains hydrostatic to a depth of 2.5 km and then rises rapidly down to a depth of 3.5 km below which the fluid pressure gradient decreases, maintaining a nearly constant value between hydrostatic and lithostatic pressures. Idealized pore-fluid pressure regimes anticipated for a system of shale layers interbedded with sandstone are schematically drawn in Figure 4.1b-e. The idealized materials are assumed to almost perfectly seal (shale) or perfectly drain (sandstone) the sediment column. Fluid pressures in the well-drained material above a shale layer will remain hydrostatic as in models SL-Sa1 and SL-Sa2 (Chapter 3, Figures 3.3 and 3.4). If a shale layer achieves sufficiently low hydraulic conductivity during compaction, pore fluid can no longer be expelled and the fluid pressure will increase as the shale layer is buried, resulting in high (up to lithostatic) overpressures within the shale (similar to the experiment of models SL-Sh1 and SL-Sh2 of Chapter 3, section 3.4). In the permeable sandstone beneath a shale layer fluids continue to circulate freely and have a hydrostatic gradient (Figures 4.1c-e), but the pressure is offset because fluid pressures must be continuous across lithological interfaces (Figure 4.1d). Multiple shale layers cause this pattern to repeat with depth (Figure 4.1e). It is also common for fluid pressure gradients to be larger than hydrostatic where located below seals (Figure 4.1a, *Leftwich and Engelder*, 1994). This may occur in sandstones with low hydraulic conductivities that are mildly overpressured, or because of the effects of interspersed thin layers of clay or shale.

It is easy to appreciate that fluid overpressures caused by one or more sealing shale layers can strongly reduce the yield strength of the entire sediment column, even though the intervening sandstones remain permeable. The effective yield strength σ_Y of the sediment is given by

$$\sigma_Y = P - P_f \cdot \sin(\varphi_0) = P_{eff} \cdot \sin(\varphi_0) = P \cdot (1 - \lambda) \sin(\varphi_0) \tag{4.1}$$

where P, P_f and P_{eff} are the mean stress, the fluid pressure and the effective pressure, respectively, φ_0 is the internal angle of friction and λ is the pore-fluid pressure ratio

based on the mean stress. Only when mean stress and lithostatic pressure are equal does λ=λ_{HR} hold. The overall strength of a sediment layer is obtained by integrating the material strength over the layer thickness. For constant φ_0 this integrated strength is proportional to the integrated effective pressure $\int_0^z P_{eff}$=$\int_0^z P - P_f$, which is shown as grey areas in Figure 4.1b-e. It can be seen that seal layers near the top and base of the section do not reduce the integrated strength significantly (Figure 4.1b,c), but that a seal layer near the middle has a large effect (Figure 4.1d), and multiple seals (Figure 4.1e) reduce the strength most efficiently.

4.2 The Northwestern Gulf of Mexico and the Perdido Fold Belt

The Gulf of Mexico opened as a rift basin in the Late Triassic to Early Jurassic (*Pindell and Dewey*, 1982; *Pindell*, 1985; *Salvador*, 1991; *Bird et al.*, 2005). The Middle Jurassic Louann salt is commonly considered to be a post-rift succession, deposited within a single, up to 3 km thick salt basin (*Trudgill et al.*, 1999; *Hall*, 2002). Recent reconstructions even suggest post- to syn-rift deposition of up to 5-7 km thickness, but much thinner salt, possibly none, in distal parts of the margin (*Pindell and Kennan*, 2007).

Deep-water carbonate deposition prevailed in the Gulf of Mexico throughout the Cretaceous following Late Jurassic subsidence (*Diegel et al.*, 1995; *Peel et al.*, 1995; *Fiduk et al.*, 1999). In the early Paleocene the approximately 100 m thick Midway Formation, a deep marine shale, was deposited (Figure 4.2). Deposition of the up to 1500 m thick clastic Paleocene to early Eocene Wilcox Formation followed, which was the result of tectonic uplift and erosion during the Laramide orogeny in northern Mexico and the southwest US. This turbiditic unit extends 200-300 km away from the contemporaneous shelf edge and has proven to be a major hydrocarbon reservoir rock (*Meyer et al.*, 2007; *McDonnell et al.*, 2008). During the middle to late Eocene, deposition of coarse sediment was mostly confined to the shelf regions, while the deep basin received mud-rich sediments or remained sediment-starved. Oligocene volcanogenic crustal heating, uplift, and erosion of the southwestern United States and northern Mexico resulted in the deposition of the coarse clastics of the Frio Formation. Subsequent sediment deposition in the northwestern Gulf of Mexico was governed by limited supply (*Fiduk et al.*, 1999; *Galloway et al.*, 2000) after the main

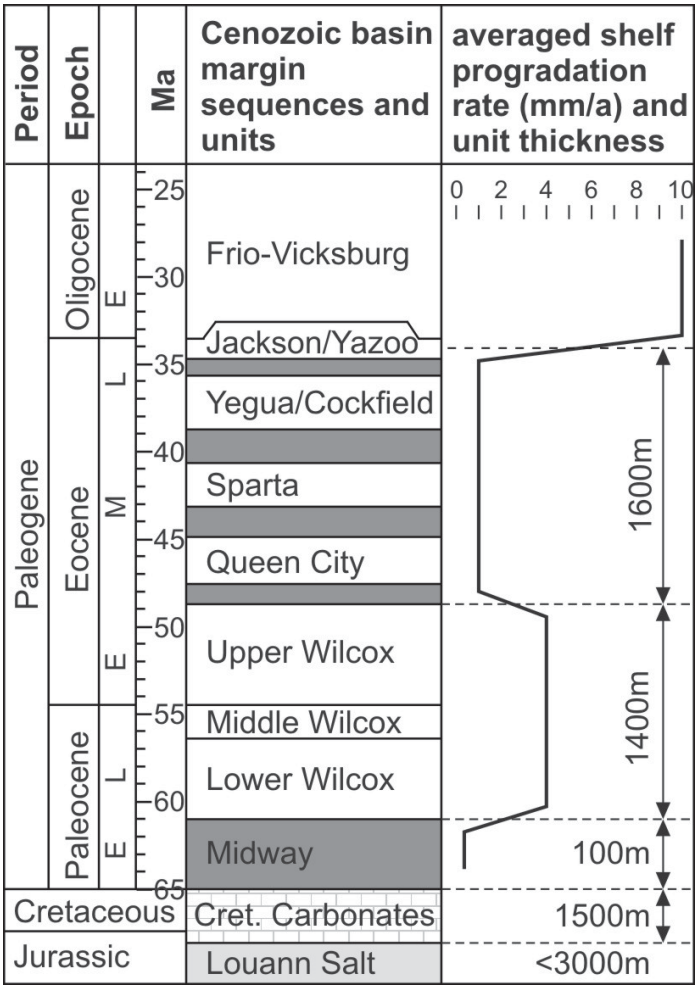

Figure 4.2: Stratigraphic column from the Late Mesozoic to Paleogene section of the northwestern Gulf of Mexico (Modified from *Galloway et al.*, 2000). Average shelf progradation rates from *Galloway et al.* (2000), approximate sediment thicknesses of the deep-water section extracted from *Meyer et al.* (2007) and complemented with data from the mid-basin (*McDonnell et al.*, 2008). Dark gray layers represent shales and condensed sections, white layers represent more sand-rich sections.

sediment input shifted eastward towards the Louisiana shelf and Mississippi delta during the Miocene. Shelf progradation rates during the Cenozoic averaged approximately 4 mm/a in the northwestern Gulf of Mexico, but were highly variable, (Figure 4.2), short-term progradation rates reached up to 10 mm/a in the early Eocene and Oligocene (*Galloway et al.*, 2000).

The salt tectonic evolution of the northwestern Gulf of Mexico is strongly linked to its depositional history. Up to four phases of gravity spreading and gliding have been reported (Figure 4.3a, *Diegel et al.*, 1995; *Peel et al.*, 1995; *Radovich et al.*, 2007a). This paper focusses on the youngest, Oligo-Miocene phase. The oldest observed contractional deformation is connected to Paleocene shortening located landward of the current shelf edge (*Radovich et al.*, 2007a). It was followed by the development of large-scale folds landward of the Perdido Fold Belt in the Eocene (*Peel et al.*, 1995) and the development of an allochthonous salt sheet. A third gravity-spreading system developed above the allochthonous salt layer, as evident from the numerous Oligocene extensional faults and the structures of the Port Isabel Fold Belt (*Peel et al.*, 1995; *Rowan et al.*, 2004). The final phase of gravity spreading developed the Corsair fault system and the Perdido Fold Belt as two linked domains of extension and shortening.

The Perdido Fold Belt is characterized by a train of symmetric, kink-banded detachment folds, formed from a uniform, 4.5 km thick pre-kinematic layer (Figure 4.3c). Its landward end is partly obscured by allochthonous salt but additional shortening structures, located landward, have been identified, either as a separate Eocene folding structure (*Peel et al.*, 1995) or a landward continuation of the Oligo-Miocene Perdido Fold Belt (*Rowan et al.*, 2005; *Radovich et al.*, 2007b). It is estimated that the distal part of this fold belt primarily formed within 10 Ma from late Oligocene to early Miocene, since syn-kinematic sedimentation is largely absent (*Trudgill et al.*, 1999), though some deformation of individual folds continued into the Neogene (*Waller*, 2007).

4.2.1 Current Fluid Pressure Regime in the Northwestern Gulf of Mexico

We lack direct information on the pore-fluid pressure regime in the Oligo-Miocene Gulf of Mexico but summarize the present regime which may be broadly similar to

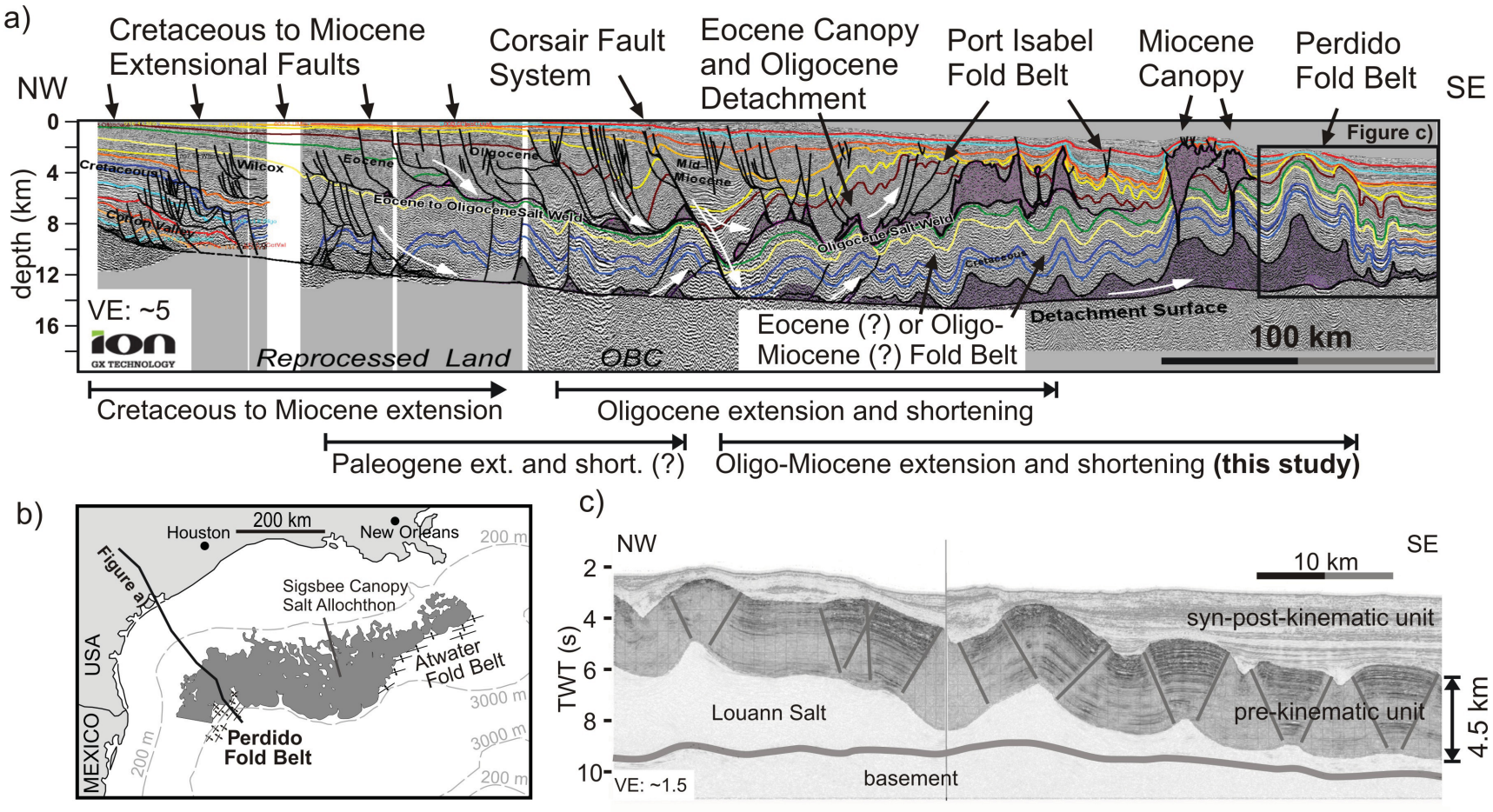

Figure 4.3: (a) Regional NW-SE trending seismic profile from the northwestern Gulf of Mexico extending from onshore into deep water (after *Radovich et al.* (2007a), published with permission of ION/GXT and SEI). Large-scale gravity spreading domains and structures (extensional faults, allochthonous salt, fold belts) are indicated. More detailed figure descriptions can be found in the original publication and Figure 5.2. (b) Regional map of northern Gulf of Mexico showing the location of the allochthonous salt and the Cenozoic fold belts after *Fiduk et al.* (1999), salt outline is from *Simmons* (1992). (c) Interpreted seismic line across the Perdido Fold Belt from *Camerlo and Benson* (2006).

paleo-pressures in places where little sediment has been added since deformation. The Perdido Fold Belt is currently stable although the stresses induced by the differential sediment load across the salt basin remain. As demonstrated by *Gradmann et al.* (2009) and *Gradmann et al.* (2012), a system with a general pre-PFB geometry like that of the northwestern Gulf of Mexico is gravitationally stable unless the overburden sediments are exceptionally weak. High fluid pressures are considered the most likely cause for destabilizing such a system. Lack of significant modern overpressures would bring into question their putative role in triggering failure and ensuing gravitational spreading of the system as a whole.

The fluid pressure regime of Figure 4.1a is representative of those reported from along the entire US Gulf coast. In the western part, where there was little Neogene sedimentation, the depth of overpressures lies within Oligocene sediments (*Leftwich and Engelder*, 1994). In the northern and eastern part, where Neogene sedimentation was abundant, overpressuring occurs in Miocene-Pliocene sediments (*Hart et al.*, 1995). The nature of fluid pressures in the lower Cenozoic sediments above the landward end of the salt basin is unknown.

By contrast, in the offshore, deep-water Gulf of Mexico several occurrences of shallow overpressure have recently been reported (*Behrmann et al.*, 2006; *Flemings et al.*, 2008; *Reilly and Flemings*, 2010). Overpressuring can occur at depths as shallow as 1-1.5 km. Such values are also reported from the Perdido Fold Belt (Figure 4.1f, *Couzens-Schultz et al.*, 2007). Here, the fluid pressures increase to near-lithostatic values at the top of the Eocene Wilcox section and are hydrostatic above. Below the maximum overpressures, they follow a hydrostatic gradient but a slight increase is observed towards the Cretaceous section (*Couzens-Schultz et al.*, 2007). This pattern is broadly similar to the one shown in Figure 4.1d, where low permeability shale is interbedded in highly permeable sandstone. Strong overpressures in the Perdido Fold Belt also coincide roughly with the location of Eocene shales. We investigate similar situations in the numerical experiments.

4.3 Computational Methods and Model Design

4.3.1 Computational Method

The methodology for calculating the coupled fluid-mechanical deformation is summarized in *Gradmann et al.* (2012) and discussed in detail in *Morency et al.* (2007). The calculations comprise two parts which are coupled via the effective stress: compaction combined with pore-fluid pressure development and the mechanical deformation of the solid matrix. The most prominent effects of the coupling are that increasing pore-fluid pressure (decreasing effective pressure) reduces the yield strength of the sediment and facilitates deformation (section 4.1, equation 4.1), and that the mechanical deformation has a feedback effect on the stress regime and therefore influences the compaction behavior and evolving fluid pressures.

Equations for Darcy flow describe the pore-fluid flow in fully-saturated, porous media, and compaction of the pore space provide the source and sink terms. Pore-space reduction occurs as mechanical and viscous compaction (*Gradmann et al.*, 2012, section 3.2):

$$\frac{1}{1-n}\frac{Dn}{Dt} = -\beta_b(n)\frac{DP_{eff}}{Dt} - \frac{P_{eff}}{\xi(n)} \tag{4.2}$$

where n is the porosity, t is time, β_b is the bulk compressibility that macroscopically describes mechanical compaction (e.g. *Birchwood and Turcotte*, 1994), and ξ is the bulk viscosity describing viscous compaction. The bulk compressibility $\beta_b(n) = (n - n_c)\beta_p$ depends here on the pore compressibility β_p and the lock-off porosity for mechanical compaction n_c (*Revil et al.*, 2002). In the case of decreasing effective pressure ($\frac{DP_{eff}}{Dt} < 0$), which would result in a porosity increase (mechanical decompaction), the bulk compressibility in a given element is set to the lowest value of β_b that had been achieved during the previous model evolution. Viscous compaction is determined by the bulk viscosity $\xi(n) = \mu/n^r$ where μ is the matrix compactional shear viscosity and r an empirical number that controls the decrease in compaction efficiency with decreasing porosity.

Deformation of the porous material by large-scale plastic and viscous flow is calculated by solving the force balance equation for creeping flow and conservation of mass for the compacting material. We solve for the velocity field v_s which comprises

the large-scale flow as well as the volumetric compaction of the material. Frictional-plastic failure is calculated using the Drucker-Prager yield criterion (equation 4.1). The post-yield plastic flow is based on relation of stress and strain for viscous flow $2\,\eta_{eff}\,\sqrt{\dot{I}_2'}=\sqrt{J_2'}$, where η_{eff} is the effective viscosity and J_2' and $\dot{I}_2'$ are the second invariants of the deviatoric stress and strain rate, respectively (*Willett*, 1999). In the frictional-plastic case the effective viscosity takes the value required to keep the material at yield during the deformation.

The model uses an Arbitrary Lagrangian-Eulerian (ALE) formulation, in which computations are made on an Eulerian grid that adapts vertically to the shape of the evolving model domain while the material properties are tracked and updated using a set of Lagrangian particles. The ALE approach allows the model to undergo both large deformation and strain because the computation grid is not advected with the flow nor distorted during deformation. As a result, the amount of strain that can be accommodated in the calculations is not limited by the method.

4.3.2 Model Geometry

The models presented here have the same geometry as in *Gradmann et al.* (2012), comprising an isostatically balanced, waterloaded, 260 km wide and 3 km deep salt basin, tapering at both ends over a distance of 60 km, and laterally enclosed by crustal material. All model parameters are listed in Table 4.1 and explained in detail in *Gradmann et al.* (2012).

The models evolve in two phases. During phase 1, a laterally uniform sedimentary sequence aggrades on top of the pre-existing salt layer with a vertical velocity of v_{agg}. Deposition of different materials results in interbedded shale-type layers within the otherwise sandstone-like sediment package. In the northwestern Gulf of Mexico at least five major shale-dominated sections have been identified (Figure 4.2). Unfortunately, their thicknesses (meters to tens of meters) are below the resolution of our models. However, we can demonstrate their first-order aggregate behaviour by choosing a model with only two, but thicker, shale-type layers; the first is deposited above the lower third of the sediment column (Midway shale equivalent, Figure 4.2), the second is deposited in the top third of the sediment column (representing the

Table 4.1: Material properties of numerical models.

Parameter	Symbol	Unit	Values (models ML-1, ML-2) Salt/Crust	Sandstone	Shale	(models ML-Q20 to ML-Q35) (where different)
Initial Salt Geometry						
salt width	w_{salt}	km	140 + 2× 60 taper			
salt thickness	h_c	km	3			
taper angle	α	°	3			
Sedimentation						
rate of aggradation | progradation	v_{agg} | v_{prog}	mm/a	0.055 | 5			
width | height of progradation profile	w | h_w	km	100 | 3			
shale-type layers			2			multiple
Isostatic Compensation						
density of mantle | of water and fluid	ρ_m | ρ_w	kg/m^3	3300 | 1000			
flexural rigidity	D	Nm	10^{22}			
Finite element grid						
width		km	400			
number of elements (horizontal | vertical)			400 | 20	400 | 40		
time step length	Δt	a	5,000-10,000			
Boundary conditions						
boundary condition at sides			dP_f/dx=0, v_x=0			
boundary condition at base			dP_f/dy=0, v_x=0, v_y=0			
boundary condition at surface			P_f=P_w			
Material strength						
internal angle of friction	φ_0		- / 30°	30°	30°	
shear viscosity	η_{salt}	Pa s	10^{18} / -	-	-	
Hydraulic Properties						
grain density	ρ_g	kg/m^3	2150/2500	2500	2500	
surface hydraulic conductivity	K_0	m/s	10^{-16}	10^{-6}	10^{-9}	
surface porosity	n_0	%	0.1	50	50	
K-n exponent	m		1	5	9	
pore compressibility	β_p	Pa^{-1}	10^{-14}	10^{-7}	10^{-7}	
lock-off porosity (mechanical)	n_c	%	0	30	10	
shear viscosity (const./ref.)	μ/μ_r	Pa s	10^{28}	10^{22}, $2 \cdot 10^{22}$		$5\,10^{22}$
reference depth	z_r	mbsf	-	-	-	0
thermal gradient	dT/dz	K/km	-	-	-	25
activation energy	Q	kJ/mole	-	-	-	20, 25, 30, 35
ξ-n exponent	r		1	1	1	2

multiple Eocene shale layers, Figure 4.2). We also simplify the models by considering only sand-type and shale-type lithologies.

As in *Gradmann et al.* (2012), we assume that the mainly aggradational phase that resulted in a 4.5 km thick sediment column lasted approximately 100 Ma and accordingly set v_{agg}=0.055 mm/a, thereby accounting for compaction of the aggrading material. The two shale-type layers are then deposited during 40-60 Ma and 90-110 Ma of elapsed model time. This simplified design does not allow for the often very variable rates and durations of carbonate, shale and sandstone deposition in the Cretaceous to Palaeogene northwestern Gulf of Mexico.

During phase 2, sediments prograde onto this sedimentary sequence in the form of a seaward moving half-Gaussian profile. This profile is specified by the landward and seaward bathymetries (delta-top and toe, h_1 and h_2) and the margin height ($h_1 - h_2$=3 km), margin width (w=100 km), initial position of the shelf break, and progradation velocity (v_{prog}=5 mm/a). Sediment is added to fill the accommodation space below the profile, sediment above the profile is not removed. The additional sediment loading is flexurally compensated by an elastic beam (D=10^{22} Nm) at the base of the model and assuming an underlying inviscid fluid with density ρ_m=3300 kg/m^3.

The main interest again lies in the system's behavior during gravity spreading occurring in phase 2. Phase 1 is necessary to achieve a compacted sediment layer with a self-consistent fluid-pressure regime as a starting configuration for the progradation phase.

4.3.3 Material Properties

In the models, salt is a linear viscous material with constant viscosity (η_{salt} = 10^{18} Pa s). Crust and sediments are frictional-plastic materials with an internal angle of friction of φ_0=30° and zero cohesion. Crust and salt are treated as low porosity, nearly non-compacting materials that maintain a hydrostatic pore-fluid pressure gradient.

Sediments undergo mechanical and viscous compaction, both controlled by the parameters of surface porosity (n_0=50% for sandstone-type and shale-type material), surface hydraulic conductivity (k_0=10^{-6} and 10^{-9} m/s for sandstone-type and shale-type, respectively), and the power law relationship between porosity and hydraulic

conductivity $K{=}K_0\left(\frac{n}{n_0}\right)^m$ (m=5 and 9 for sandstone-type and shale-type material, respectively).

Mechanical compaction is furthermore controlled by the pore compressibility ($\beta_p{=}10^{-7}$ Pa^{-1} for both sandstone-type and shale-type material) and the lock-off porosity (n_c=30% and 10% for sandstone-type and shale-type material, respectively). Viscous compaction in models presented in section 4.4 is controlled by the compactional shear viscosity ($\mu = 10^{22}$ or $2 \cdot 10^{22}$ Pa s for both sandstone-type and shale-type material) and the porosity-viscosity exponent $r = 1$. In the second set of models (section 4.5) the compactional shear viscosity varies with depth ($\mu = \mu(z)$) and $r = 2$.

The choice of parameters results in distinct compaction behavior for the two materials (see *Gradmann et al.*, 2012). Mechanical compaction of the shale-type material results in rapid porosity loss within the upper two kilometers and additional viscous compaction leads to strong overpressuring. The sandstone-type material exhibits more gentle compaction with depth and is mainly affected by mechanical compaction.

4.4 Multiple Lithology Models

The two model experiments ML-1 and ML-2 (ML=Multiple Lithology) differ only in the compactional shear viscosity of $\mu{=}10^{22}$ Pa s and $\mu{=}2 \cdot 10^{22}$ Pa s. The deposition of shale-type layers during sandstone-type aggradation and following progradation phase are identical. All other material properties are the same as the ones used in the single lithology models of *Gradmann et al.* (2012) and as listed in Table 4.1.

4.4.1 Model Results

Model ML-1, $\mu{=}10^{22}$ Pa s (strong viscous compaction)

Aggradation phase

At the end of the aggradation phase of model ML-1 (Figure 4.4) the highest pore-fluid pressure ratios can be found at a depth of 2-3 km within the lower shale-type layer (Figure 4.4b). The pressure-depth plot at 250 km (Figure 4.4c) shows that fluid pressures remain hydrostatic above the lower shale-type layer and increase to near-lithostatic values within it. In the underlying sandstone-type layer the fluid pressure

mostly maintains a hydrostatic pressure gradient but increases near the bottom. Figure 4.4d shows the corresponding porosity and conductivity variations.

Progradation phase

After 50 Ma of sediment progradation (Figures 4.4e-h) the fluid pressures have increased strongly, weakened the sedimentary material and allowed gravity spreading to occur (Figure 4.4e,f). The resulting deformation comprises zones of extension in the landward end and pure-shear thickening and minor folding in the seaward end. The folding is focussed above the distal pinch-out of the salt layer and even continues beyond it. The regions of overpressures that were observed at the end of the aggradation phase (lower shale-type layer and bottom of lower sandstone-type layer) broadened. In the landward half, fluid pressures reach lithostatic values only in the lowermost 2-3 km of the sediment column at 9-15 km depth (Figure 4.4f). The fluid pressure above the distal half of the salt basin is now close to lithostatic throughout the sediment column. Prior to gravitational failure, overpressures in the upper shale-type layer remain hydrostatic (Figure 4.4c), but increase as this region experiences lateral compression (Figure 4.4g). Porosities in the shale-type layers are here approximately 18% and 15% for the upper and lower layer, respectively (Figure 4.4h). Both layers have experienced decompaction where the minimum porosity during model evolution (light blue curve in Figure 4.4h) is lower than the current porosity. Porosities in the sandstone-type layers have decreased to a few percent.

Model ML-2, μ=$2 \cdot 10^{22}$ Pa s (less viscous compaction)

Aggradation phase

At the end of the aggradation phase of model ML-2 (Figure 4.5), overpressures have developed in the lower shale-type layer (Figure 4.5b) but to a lesser extent than in model ML-1 (Figure 4.4b). No overpressures developed in the lowermost sandstone-type layer where the fluid pressure gradient remains hydrostatic (Figures 4.5c). Figure 4.5d shows the corresponding porosity and conductivity variations.

Progradation phase

During the progradation phase, gravity spreading does not develop and the system remains immobile (Figure 4.5e). Significant overpressures develop only in the lower shale-type layer and the underlying sandstone with near-lithostatic values at the

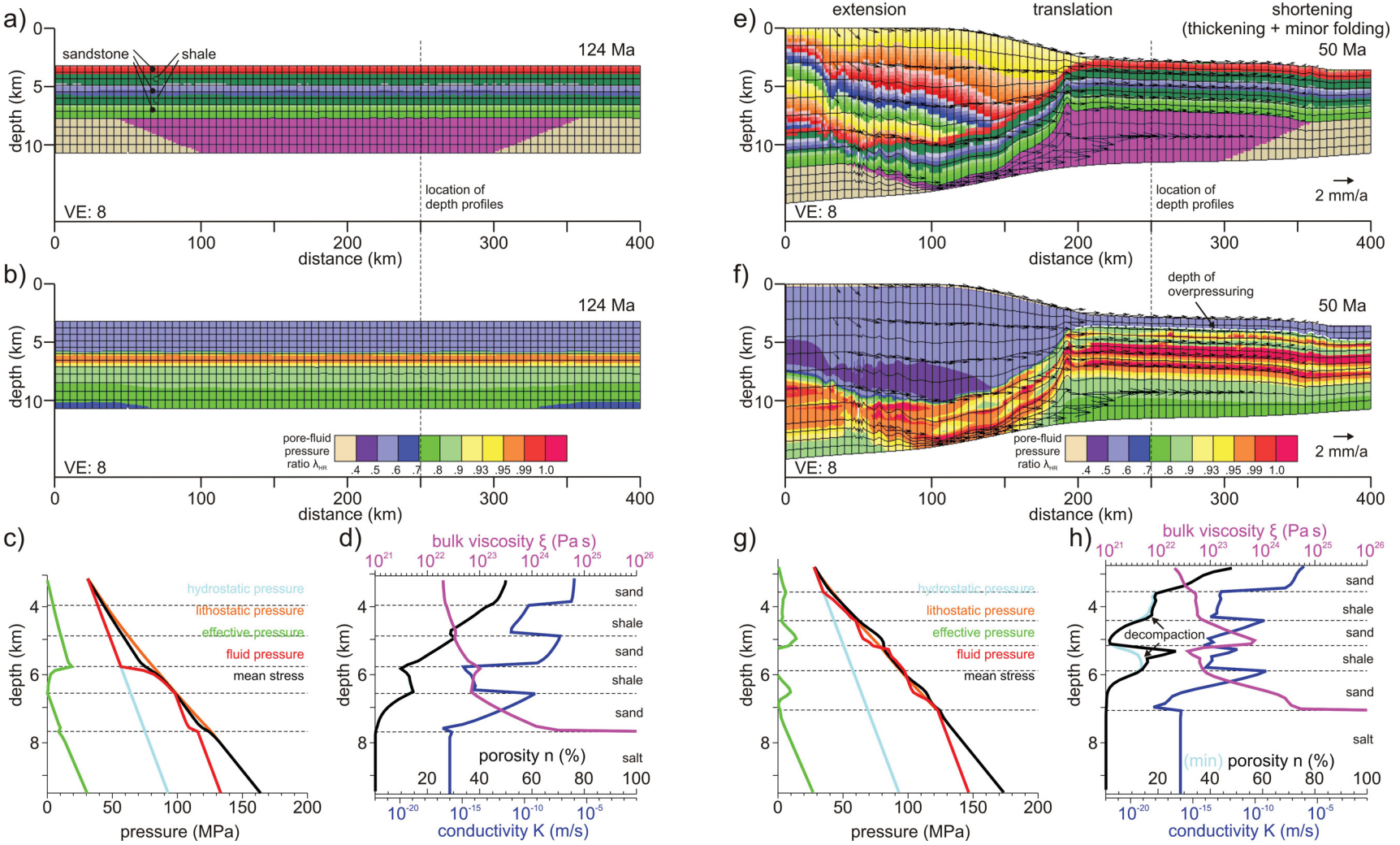

Figure 4.4: Results of model ML-1 with constant compactional shear viscosity of μ=10^{22} Pa s at end of aggradation phase (a-d) and progradation phase (e-h). (a,e) Geometry of model. Shale layers are represented in dark green. (b,f) Pore-fluid pressure ratio λ_{HR}. (c,g) Pressure-depth profiles at 250 km. (d,h) Porosity/conductivity-depth profiles at 250 km.

landward end and values of λ_{HR} <0.9 at the seaward end. Here, minor overpressures also develop in the upper shale-type layer and at the base of the lowermost sandstone-type layer (Figure 4.5g). Porosities in both shale-type and sandstone-type material remain higher in the seaward section than in model ML-1; shale-type porosities are approximately 20% and sandstone-type porosities approximately 5-20% except for very low values at the base (Figure 4.5h). Decompaction has only taken place in the lower shale layer.

4.4.2 Discussion

Effects of layered lithologies

In the two models of layered lithologies with differing viscous compaction efficiency, overpressures develop in the deeply buried shale-type layer during the aggradation phase, whereas the fluid pressures in the permeable sandstone-type layers generally maintain a hydrostatic gradient. In the upper shale layers no overpressure develops during the aggradation phase, partly because the thinner overburden allows excess fluid to escape and because there is less compaction in the upper shale layer than in the lower one (lower effective pressure and compaction has operated for less time). The overall pressure-depth curves are similar to the conceptually drawn ones (Figure 4.1b-e) and those obtained from bore hole measurements in sedimentary basins (compare Figures 4.4c, 4.5c and 4.1a). In the natural and both of the model cases, overpressures start to develop at depths of 2-3 km. Below this interval, the hydrostatic model gradients are somewhat lower than those obtained from bore-hole measurements, which is not surprising because the natural material is likely less permeable than the idealized sandstone-type model material. We conclude that a typical pressure-depth profile of a sedimentary basin (e.g. Figure 4.1a) can be generated by aggradation of sediments of alternating compaction characteristics.

The increase in fluid pressures at the very base of the lower sandstone-type layer in model ML-1 (Figure 4.4c) occurs in the same manner as in model SL-Sa2 (*Gradmann et al.*, 2012, Figure 3.4) and is a consequence of strong viscous compaction generated by the high overburden load and the long time the material is exposed to viscous compaction (>100 Ma).

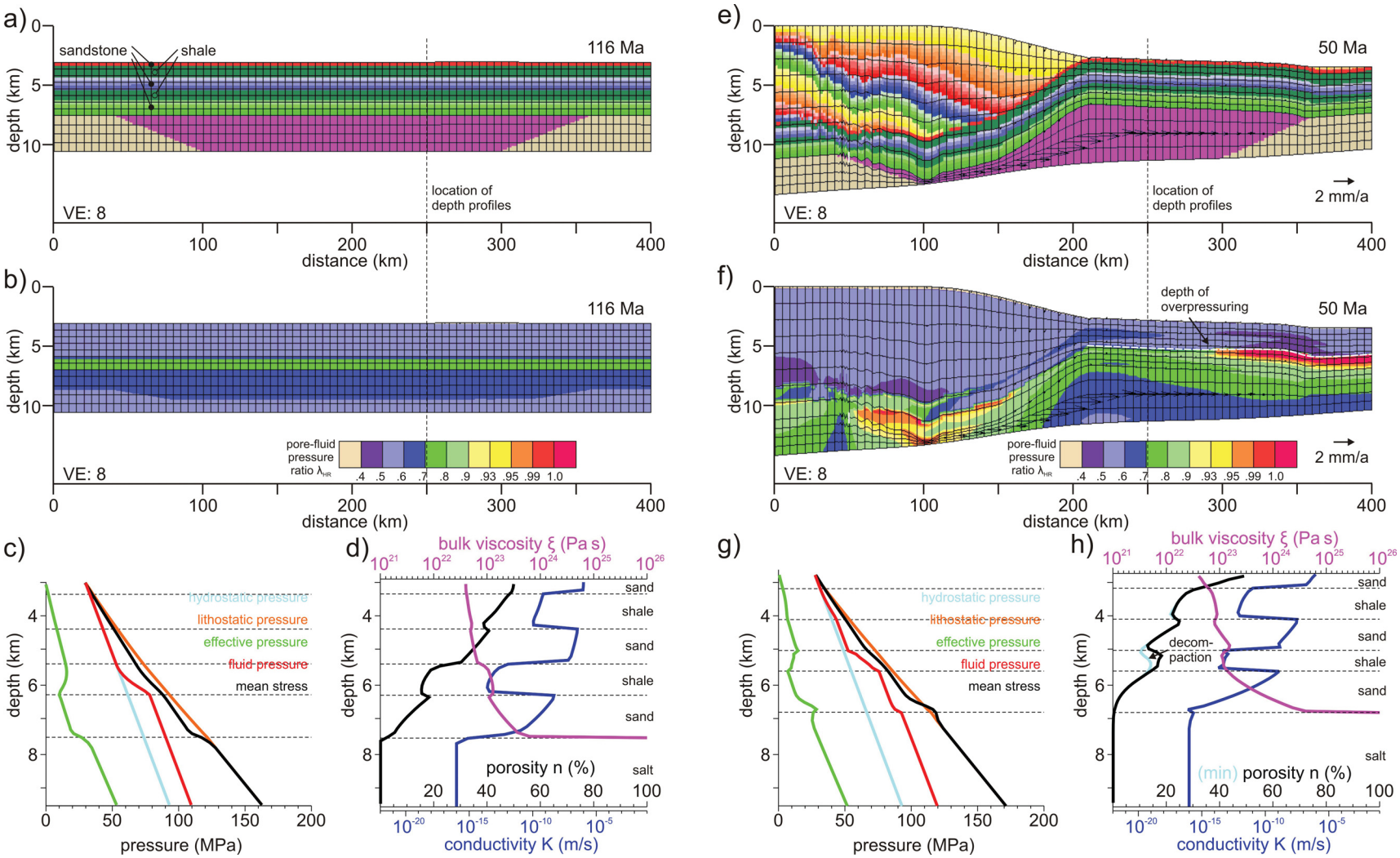

Figure 4.5: Results of model ML-2 with constant compactional shear viscosity of μ=$2 \cdot 10^{22}$ Pa s at end of aggradation phase (a-d) and progradation phase (e-h). (a,e) Geometry of model. (b,f) Pore-fluid pressure ratio λ_{HR}. (c,g) Pressure-depth profiles at 250 km. (d,h) Porosity/conductivity-depth profiles at 250 km.

Gravitational failure

During the progradation phase, only model ML-1 with the more strongly compacting materials undergoes gravitational failure. This must be attributed to the earlier and stronger overpressuring and associated sediment weakening in this model. Whereas the fluid pressure in model ML-1 has reached lithostatic values (in >10 km depth at the landward end and >1 km depth at the seaward end), the fluid pressure of model ML-2 remains much lower throughout the entire model domain (λ_{HR} <0.95 in the deep landward sediments, λ_{HR} <0.8 in the seaward sediments). *Gradmann et al.* (2009) predicted a minimum value of λ_{HR} ≈0.75-0.8 in order for gravitational failure to occur in approximately the same system when fluid pressures are uniform. The current results show that gravitational spreading can occur when overpressures are relatively low in the shallower sediments provided overpressures are high in the deeper sediments. The threshold for failure lies somewhere between the conditions in model ML-1 and ML-2, demonstrating that the system is in its current description very sensitive to relatively small variations in viscous compaction. Variations of other parameter values can, of course, also trigger gravitational failure, as the current models are non-unique.

Decompaction

Both models ML-1 and ML-2 experience decompaction in the shale-type layers, despite the implementation of a minimum bulk compressibility. As discussed in *Gradmann et al.* (2012, model SL-Sh1 and section 3.5), this can again be traced back to decreasing effective pressures during enhanced compaction and overpressuring as the region experiences enhanced lateral stresses. In the models, decreasing effective pressure reverses mechanical compaction, leading to porosity increases. The strong porosity increase in the upper part of the lower shale-type layer of model ML-1 (Figure 4.4h) is likely different as it correlates with unrealistic, supra-lithostatic fluid pressures and negative effective pressures. Here, decompaction probably operates via the inverse viscous compaction mechanism. In natural systems such high fluid pressures would induce hydrofracturing and subsequent fluid and pressure release by leaking or fault-valving. Such a mechanism has been tested in the numerical experiments but was so far only successful in decreasing the fluid pressures locally. Despite this

unrealistic development, however, the modeled systems can be considered to behave reasonably up to the point where fluid pressures become lithostatic.

Fold belt evolution

Folding as a result of gravity spreading initiates at the distal pinch-out of the salt layer (Figure 4.4e). Subsequent shortening is accommodated by folding seaward of this location, forming a fold belt by detaching on the highly overpressured shale-type layers but not above the viscous salt layer (corresponding model output later than 50 Ma is not shown here). This is a major discrepancy with respect to the structure of the Perdido Fold Belt and, moreover, demonstrates that overpressures are most likely too high in the basal sediments of model ML-1. As Figure 4.4g shows, fluid pressures are now close to lithostatic everywhere, and the strength of the sediment column is therefore almost completely eliminated.

Sensitivity to compactional shear viscosity

Models ML-1 and ML-2 demonstrate that variations as small as a factor of two in compactional shear viscosity can lead to large changes in overpressure and can induce gravitational failure. The strong viscous compaction in model ML-1 leads to what are likely unrealistically high overpressures in both compacting materials and to porosities in the lowermost part of the sandstone-type layer, which are an order of magnitude smaller than observed in natural sandstones. Similar behavior was also seen in the models with low compactional shear viscosity of *Gradmann et al.* (2012, models SL-Sa2 and SL-Sh2).

The high sensitivity with respect to the compactional shear viscosity indicates that this parameter needs more careful treatment. Whereas it remains constant with depth in models ML-1 and ML-2, pressure solution is known to depend, for example, on temperature and grain contact area.

4.5 Models with Depth-Dependent Compaction Viscosity

In this section we present models that again consist of layered lithologies but also include an improved formulation of the compactional shear viscosity. We first explain the motivation and implementation of a depth-dependent compactional shear viscosity, then present and discuss several numerical experiments. These improved models now focus on the evolution of a distal fold belt and the interaction among deformation, compaction, and fluid pressures.

4.5.1 Motivation for Depth-Dependent Compactional Shear Viscosity

In the models described in the previous section, the compactional shear viscosity μ is assumed to be constant and the bulk viscosity is estimated by $\xi(n) = \mu/n$. This simple approach has the effect that even sediments with low porosities continue to compact given large enough time scales of several tens of millions of years. As shown in models SL-Sa1 (*Gradmann et al.*, 2012) and ML-1, porosities decrease to values of $<0.5\%$ and fluid pressures may then increase to near-lithostatic values over unrealistic thicknesses of a few kilometers. Minimum porosities of most compacted siliciclastic sediments are on the order of several percent and higher (*Revil et al.*, 2002). In a natural system, increasing grain contact area during compaction will decrease the locally acting stresses, and compaction by pressure solution must therefore ultimately cease at sufficiently low porosities. We therefore introduce an improved but simple model for viscous compaction by pressure solution in which $\xi(n) = \mu/n^r$, where $1 \leq r \leq 2$ (e.g. *Scott and Stevenson*, 1984). Lower values for r are considered suitable for porosities above 10% (*Helle et al.*, 1985) or uncemented material (*Yang*, 2001; *Paterson*, 1973), whereas the compaction behavior of cemented material with very small porosities is best described with r=2. With such higher values for r, the bulk viscosity increases rapidly as the porosity decreases, thereby approximating the stress-limiting process accompanying increasing grain contact area.

Although we model pressure solution as a viscous process following, for example, *Rutter* (1976), *Dewers and Ortoleva* (1990), *Schneider et al.* (1996) and *Connolly and Podladchikov* (2000), others have argued that pressure solution is like a chemical reaction and proceeds rapidly to a thermodynamic equilibrium state such that the

time dependence of compaction is not important (*Palciauskas and Domenico*, 1989; *Stephenson et al.*, 1992; *Revil*, 2001). Our model now considers that the compacting system tends to a level where porosities do not decrease further on the timescale of interest, thereby approximating the 'equilibrium state', unless the effective stress subsequently increases (equation 4.2).

4.5.2 Formulation of Depth-Dependent Compactional Shear Viscosity

Because pressure solution is a thermally activated process, viscous compaction must also be a function of temperature T, i.e. $\mu = \mu(T)$. Pressure-solution creep essentially consists of three phases: pressure-enhanced solution, solute transport (diffusion) and precipitation. Diffusion is generally considered the slowest and therefore rate-limiting process (*Rutter*, 1976; *Angevine and Turcotte*, 1983; *Gratz*, 1991). The strain rate is described by $\dot{\varepsilon} = \sigma \cdot C \cdot exp(\frac{-Q}{RT})$, where C is a material-specific value that includes the effects of geometry and grain size, Q is the activation energy, and R is the universal gas constant. The temperature-dependent compactional shear viscosity can then be written as

$$\mu = \mu_r \cdot \exp\left(\frac{Q}{RT} - \frac{Q}{RT_r}\right) \tag{4.3}$$

where μ_r is the reference compactional shear viscosity at reference temperature T_r. The activation energy for diffusion-controlled creep in sedimentary rocks ranges from 20-60 kJ/mole (*Schneider et al.*, 1996; *Kawabata et al.*, 2009). This value can be considered as a combination of the activation energies of temperature-dependent diffusion (Q_D ≈15-30 kJ/mole) and solubility (Q_S ≈20 kJ/mole) (*Kawabata et al.*, 2009).

Given that our current model does not calculate the temperature field, we test the effect of temperature dependence of shear viscosity by assuming a uniform geothermal gradient and use depth as proxy for temperature

$$T = T_0 + \frac{dT}{dz} \cdot z \tag{4.4}$$

where T_0 is the temperature at the sea floor, z is burial depth, and dT/dz is the geothermal gradient.

Under these circumstances the compactional shear viscosity can also be written as a function of the e-folding length l, which represents the depth over which the value of the compactional shear viscosity increases by a factor of e.

$$\mu = \mu_r \cdot \exp\left(\frac{z_r - z}{l}\right) \tag{4.5}$$

where $l \approx \frac{RT^2}{QdT/dz}$ (*Connolly and Podladchikov*, 1998).

With the combined effects of temperature and porosity dependence, the bulk viscosity is now given as

$$\xi = \mu_r \cdot \exp\left(\frac{Q}{RT} - \frac{Q}{RT_r}\right)/n^r \tag{4.6}$$

4.5.3 Implications of Depth-Dependent Compactional Shear Viscosity

Reference values for shear viscosities or actual bulk viscosities spread over wide ranges in the literature. Most commonly, values of $5 \cdot 10^{20}$-$5 \cdot 10^{21}$ Pa s are used for formulations where shear viscosity is constant (*Paterson*, 1973; *Birchwood and Turcotte*, 1994; *Suetnova and Vasseur*, 2000). *Connolly and Podladchikov* (2000) calculate viscosity-depth trends for various parameter combinations and apply these models to the porosity-depth profiles of the Pannonian basin. They conclude that in order for fluid pressures to remain hydrostatic to depths of 3 km, shear viscosities of μ_r=10^{20}-10^{21} Pa s are required (at reference depth 3 km) for activation energies of Q=20-40 kJ/mole. Over depths of several kilometers, viscosities then range from μ=10^{19}-10^{23} Pa s and are consistent with the values cited for constant shear viscosities.

Figure 4.6 shows the variation of the compactional shear viscosity and bulk viscosity with depth given by equation (4.6). The reference compactional shear viscosity is μ_r=$5 \cdot 10^{22}$ Pa s at the seafloor (z_r = 0 m and T_r=277 K), the thermal gradient is dT/dz=25 K/km, and the activation energy is Q=35 kJ/mole. Porosity is approximated as decreasing linearly over depth from 50% at the surface to 0% at 5 km depth. A non-linear porosity-depth curve, as it is expected for the compacting sediments, would slightly modify the viscosity-depth curve.

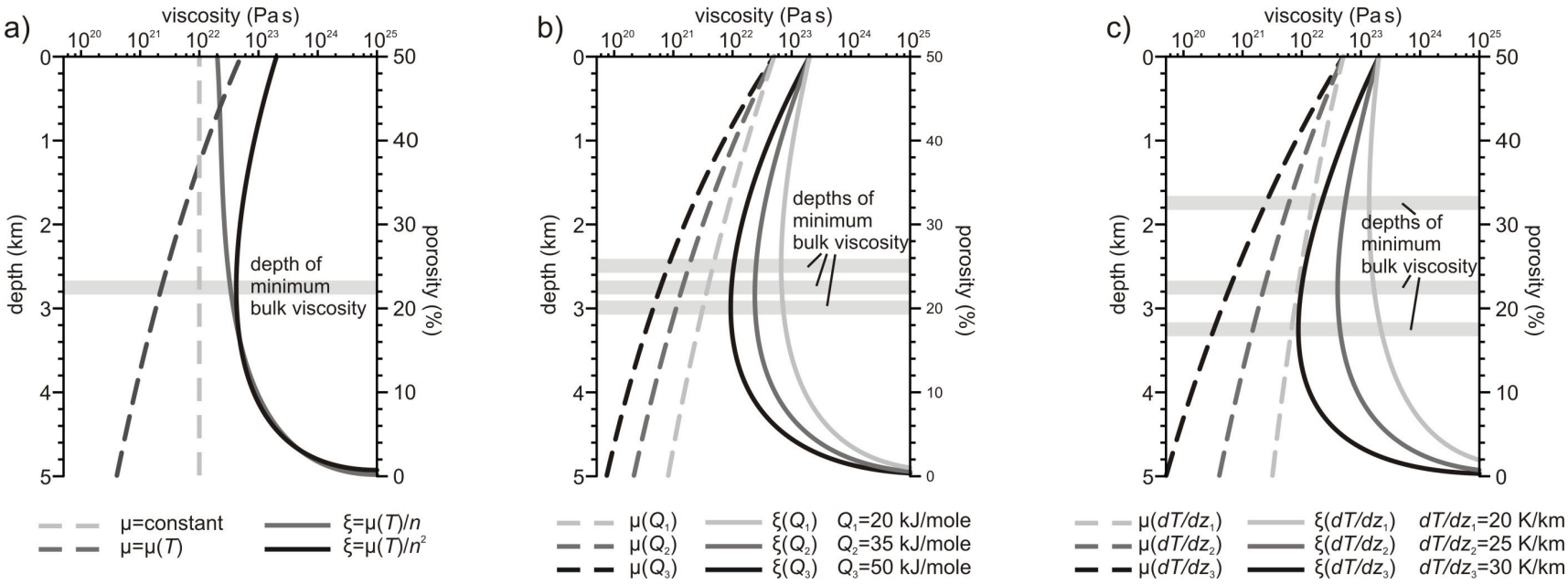

Figure 4.6: Plots of bulk and compactional shear viscosity with depth after equation (4.6). Parameter values are μ_r=5·10^{22} Pa s, Q=35 kJ/mole, T_r=277 K, dT/dz=25 K/km, z_r=0 m, r=2, dn/dz=50%/5 km, and n_0=50% unless otherwise indicated. (a) Old and new formulation of bulk and shear viscosities. (b) Dependency of bulk and compactional shear viscosity on activation energy Q. (c) Dependency of bulk and compactional shear viscosity on temperature gradient dT/dz.

The temperature (or depth) dependency of the compactional shear viscosity decreases the bulk viscosity with depth, but the porosity dependence increases the bulk viscosity with depth (Figure 4.6a). These two competing trends result in a minimum of the bulk viscosity at a certain depth below which the porosity dependence dominates and the bulk viscosity increases.

Depending on the values of Q, T_r and dT/dz, the location and magnitude of the minimum bulk viscosity (maximum viscous compaction) will vary. Figure 4.6b shows this behavior with different e-folding lengths, here achieved through different activation energies Q=20, 35 and 50 kJ/mole, which correspond to the range of natural values for activation energies for sandstones or shales (*Rutter and Mainprice*, 1978; *Angevine and Turcotte*, 1983; *Schneider et al.*, 1996; *Kawabata et al.*, 2009). The minima of the bulk viscosities now lie within the range of 2.5-3 km depth or 20-25% porosity. The temperature gradient has a similar influence on the compactional shear viscosity and bulk viscosity to that of the activation energy (Figure 4.6c).

4.5.4 Model Design

For the numerical experiments presented in this section, we keep all parameters except for the activation energy Q constant. Its value is only poorly constrained by measurements but has a large influence on the resulting compactional shear viscosity values. We vary Q from 20 to 35 kJ/mole (e-folding lengths l between ca. 750 and 1250 m). Other parameters are set to μ_r=$5 \cdot 10^{22}$ Pa s, T_r=277 K, dT/dz=25 K/km and r=2. This yields minimum values of compactional shear viscosity at a depth of 2-3 km (Figure 4.6b), the approximate depth where overpressuring is expected to occur in a tectonically quiet setting, such as that of the Gulf of Mexico (section 4.2). The temperature gradient of 25 K/km represents a low to medium value as expected for sedimentary basins and consistent with the values calculated for the northwestern Gulf of Mexico (*Husson et al.*, 2008). As in the previous models, we do not differentiate between shear viscosities of sandstone-type and shale-type material because estimates are not sufficiently comprehensive or accurate to distinguish between Q-values for shale-type and sandstone-type material. We again attribute the differing compaction behavior of the two end-member materials to the porosities and associated hydraulic conductivities which control both mechanical and viscous compaction.

The models again include an aggradation phase that includes the deposition of two shale-type layers. During the progradation phase, additional shale-type layers are deposited for 3 Ma every 10 Ma in order to represent the younger sediments of mixed lithology landward of the Perdido Fold Belt.

4.5.5 Model Results: Gravity Spreading, Shortening, Fluid Pressure, and Compaction

Figures 4.7-4.10 show the evolution of models ML-Q20, ML-Q25, ML-Q30 and ML-Q35 with corresponding activation energies Q of 20, 25, 30 and 35 kJ/mole. Each model is only shown in the progradation phase: at the onset of gravity spreading (a,e), at the time of strongest folding (b,f,h,i), and at the time when the fold belt has fully developed (c,d,g). The progradation phase of model ML-Q30 is additionally shown as an animated version for better visualization of the model evolution (Animation_MLQ30.mov, supplementary material[1]).

All four models become gravitationally unstable, but model ML-Q20, the least mobile, exhibits only minor amounts of shortening (Figures 4.7-4.10, a-d). At the onset of gravity spreading, the fluid pressure beneath the shelf has reached similar values in all four models across a zone of *c.* 1 km thickness (Figures 4.7-4.10e). More time is required to achieve these pressures in models with lower activation energies (39 Ma vs. 26 Ma), reflecting the less efficient compaction.

The amount of shortening that occurs during gravity spreading is larger in the models with stronger compaction, as is shown by the displacement of passive markers, originally located at 250, 300 and 350 km (Figures 4.7-4.10d). Cumulative shortening within the distal 100 km of the model amounts to approximately 6, 18, 20, and 22 km for models ML-Q20 to ML-Q35, respectively. It is accommodated by folding in models ML-Q25 to ML-Q35, but model ML-Q20 does not develop a fold belt. The fold belt length (60, 90 and 110 km in models ML-Q25 to ML-Q35, respectively) increases with compaction efficiency. The same progression does not hold for the fold amplitude, where model ML-Q30 with a moderately high compactional shear viscosity develops

[1]Supplementary material is provided as electronic attachments and is described in Appendix D.

Figure 4.7: Results of model ML-Q20 with activation energy Q=20 kJ/mole at onset of gravity spreading (a,e), strongest lateral shortening (b,f,h,i), and end of lateral shortening (c,d,g). (a-c) Geometry of entire model. (d) Close-up of distal section with passive markers placed every 50 km. (e-g) Pore-fluid pressure ratio λ_{HR}. (h) Pressure-depth profiles at 250 km. (i) Porosity/conductivity-depth profiles at 250 km.

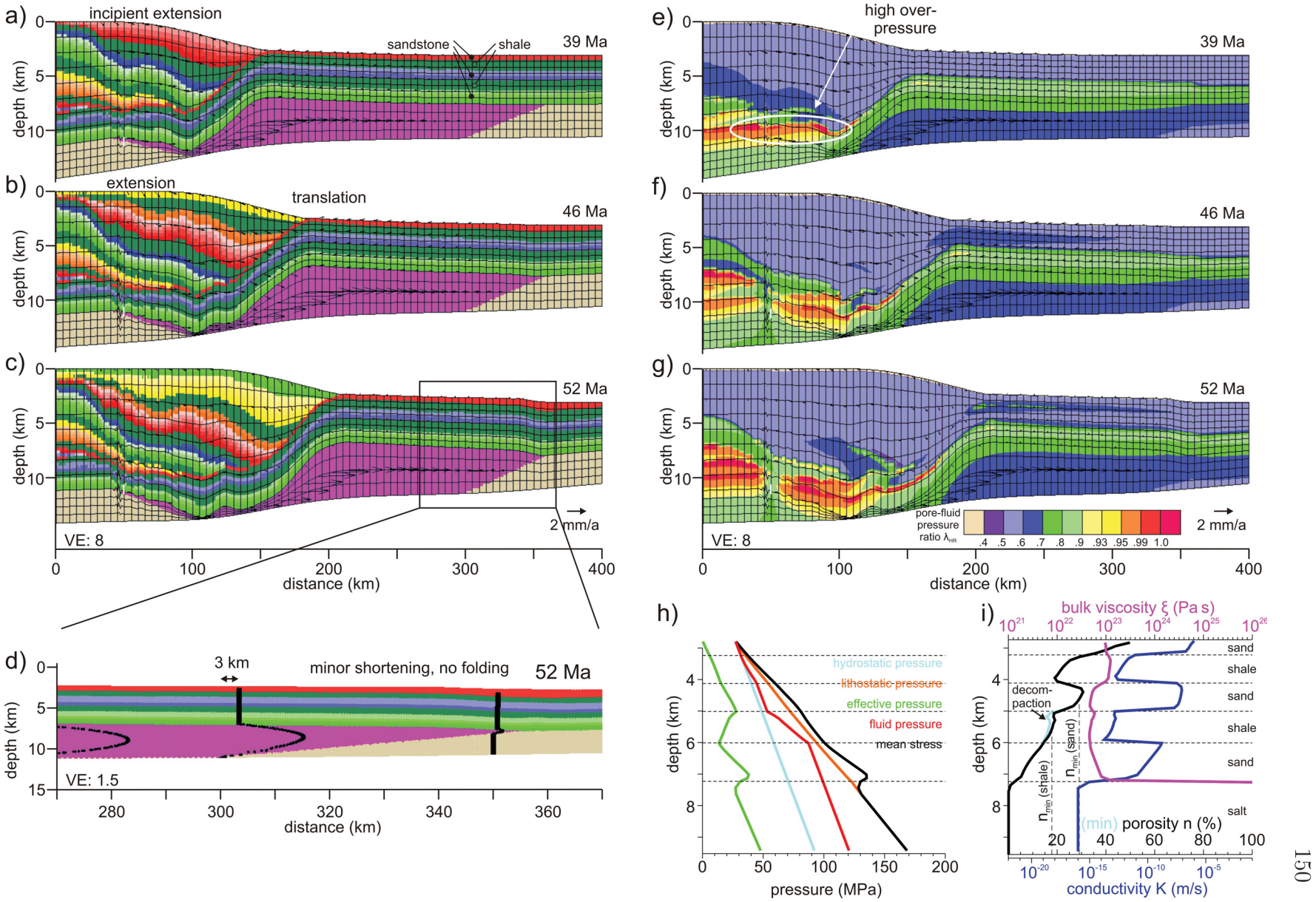
a)
incipient extension
sandstone
shale
39 Ma
b)
extension
translation
46 Ma
c)
52 Ma
2 mm/a
VE: 8
depth (km)
distance (km)
d)
3 km
minor shortening, no folding
52 Ma
VE: 1.5
e)
high over-
pressure
39 Ma
f)
46 Ma
g)
52 Ma
pore-fluid
pressure
ratio λ
h)
hydrostatic pressure
lithostatic pressure
effective pressure
fluid pressure
mean stress
pressure (MPa)
i)
bulk viscosity ξ (Pa s)
sand
shale
sand
shale
sand
salt
decom-
paction
porosity n (%)
conductivity K (m/s)

Figure 4.8: Results of model ML-Q25 with activation energy Q=25 kJ/mole at onset of gravity spreading (a,e), onset of folding (b,f,h,i), and end of lateral shortening (c,d,g). (a-c) Geometry of entire model. (d) Close-up of folded distal section with passive markers placed every 50 km. (e-g) Pore-fluid pressure ratio λ_{HR}. (h) Pressure-depth profiles at 250 km. (i) Porosity/conductivity-depth profiles at 250 km.

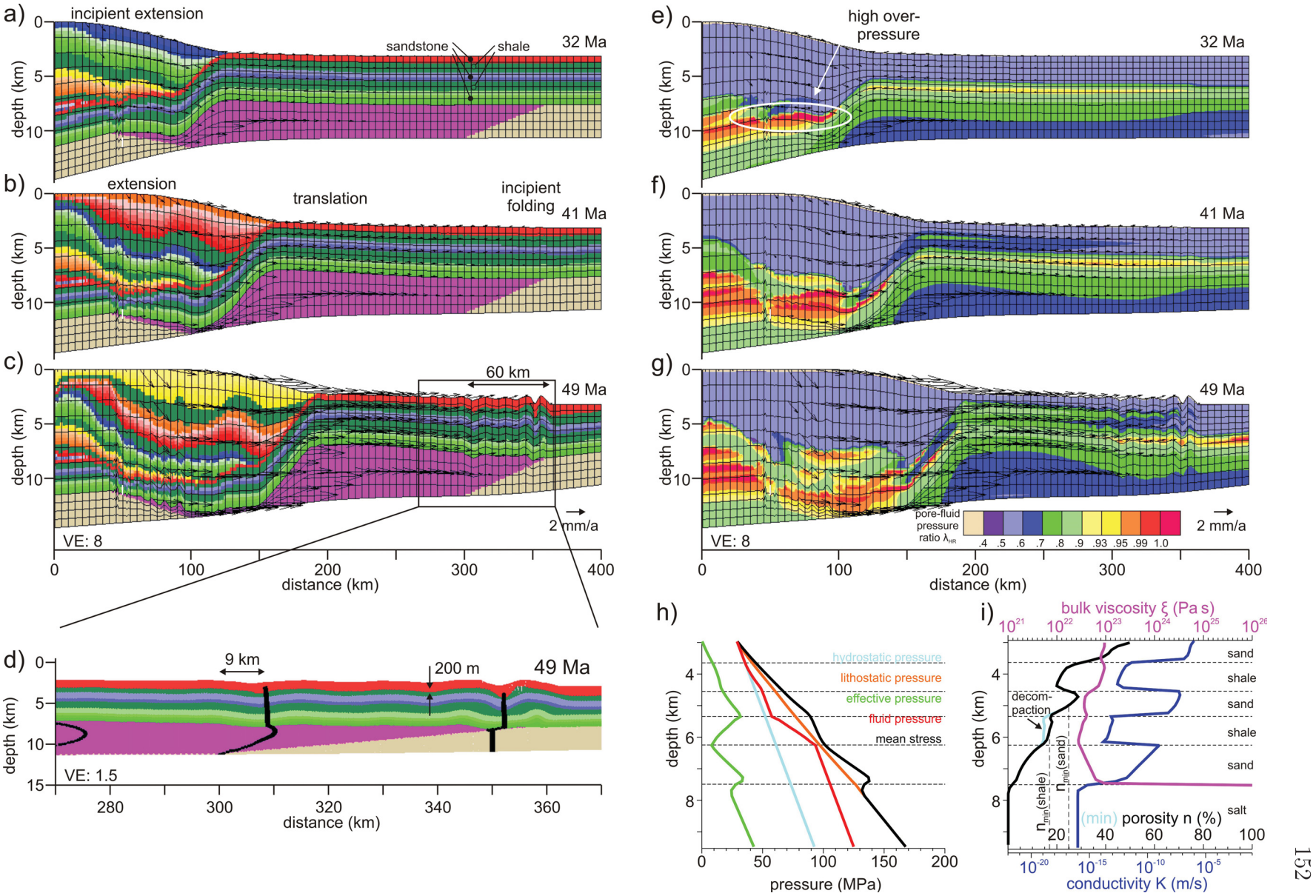
a)
incipient extension
sandstone
shale
32 Ma
depth (km)
b)
extension
translation
incipient folding
41 Ma
c)
60 km
49 Ma
2 mm/a
VE: 8
distance (km)
d)
9 km
200 m
49 Ma
VE: 1.5
e)
high over-pressure
32 Ma
f)
41 Ma
g)
49 Ma
pore-fluid pressure ratio λHR
.4 .5 .6 .7 .8 .9 .93 .95 .99 1.0
h)
hydrostatic pressure
lithostatic pressure
effective pressure
fluid pressure
mean stress
pressure (MPa)
i)
bulk viscosity ξ (Pa s)
sand
shale
decom-paction
salt
porosity n (%)
conductivity K (m/s)

Figure 4.9: Results of model ML-Q30 with activation energy Q=30 kJ/mole at onset of gravity spreading (a,e), onset of folding (b,f,h,i), and end of lateral shortening (c,d,g). (a-c) Geometry of entire model. (d) Close-up of folded distal section with passive markers placed every 50 km. (e-g) Pore-fluid pressure ratio λ_{HR}. (h) Pressure-depth profiles at 250 km. (i) Porosity/conductivity-depth profiles at 250 km.

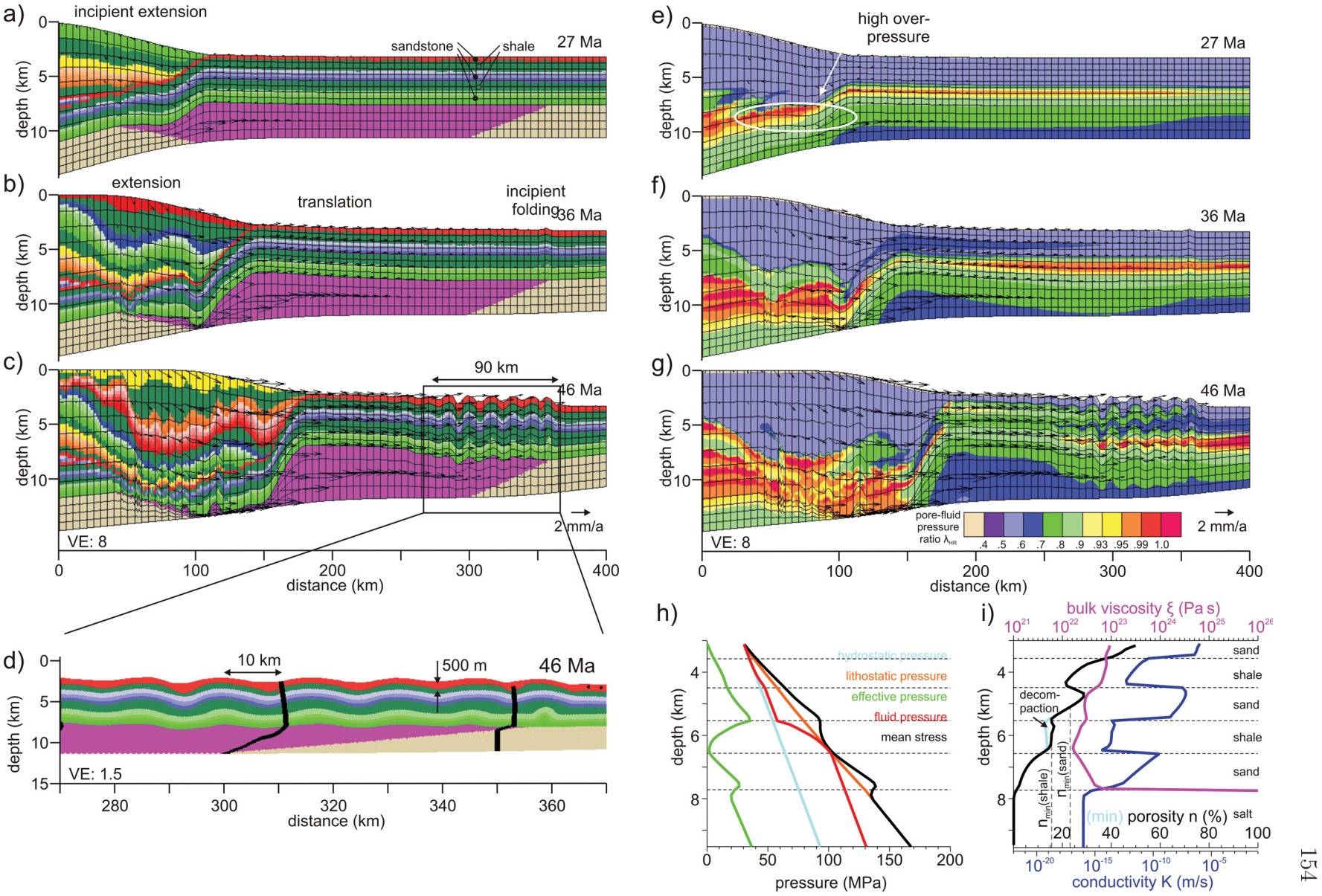
a)
incipient extension
sandstone
shale
27 Ma
b)
extension
translation
incipient folding
36 Ma
c)
90 km
46 Ma
2 mm/a
VE: 8
depth (km)
distance (km)
d)
10 km
500 m
46 Ma
VE: 1.5
e)
high over-pressure
27 Ma
f)
36 Ma
g)
46 Ma
pore-fluid pressure ratio λHR
.4 .5 .6 .7 .8 .9 .93 .95 .99 1.0
h)
hydrostatic pressure
lithostatic pressure
effective pressure
fluid pressure
mean stress
pressure (MPa)
i)
bulk viscosity ξ (Pa s)
sand
shale
sand
shale
sand
salt
decom-paction
porosity n (%)
conductivity K (m/s)

Figure 4.10: Results of model ML-Q35 with activation energy Q=35 kJ/mole at onset of gravity spreading (a,e), onset of folding (b,f,h,i), and end of lateral shortening (c,d,g). (a-c) Geometry of entire model. (d) Close-up of folded distal section with passive markers placed every 50 km. (e-g) Pore-fluid pressure ratio λ_{HR}. (h) Pressure-depth profiles at 250 km. (i) Porosity/conductivity-depth profiles at 250 km.

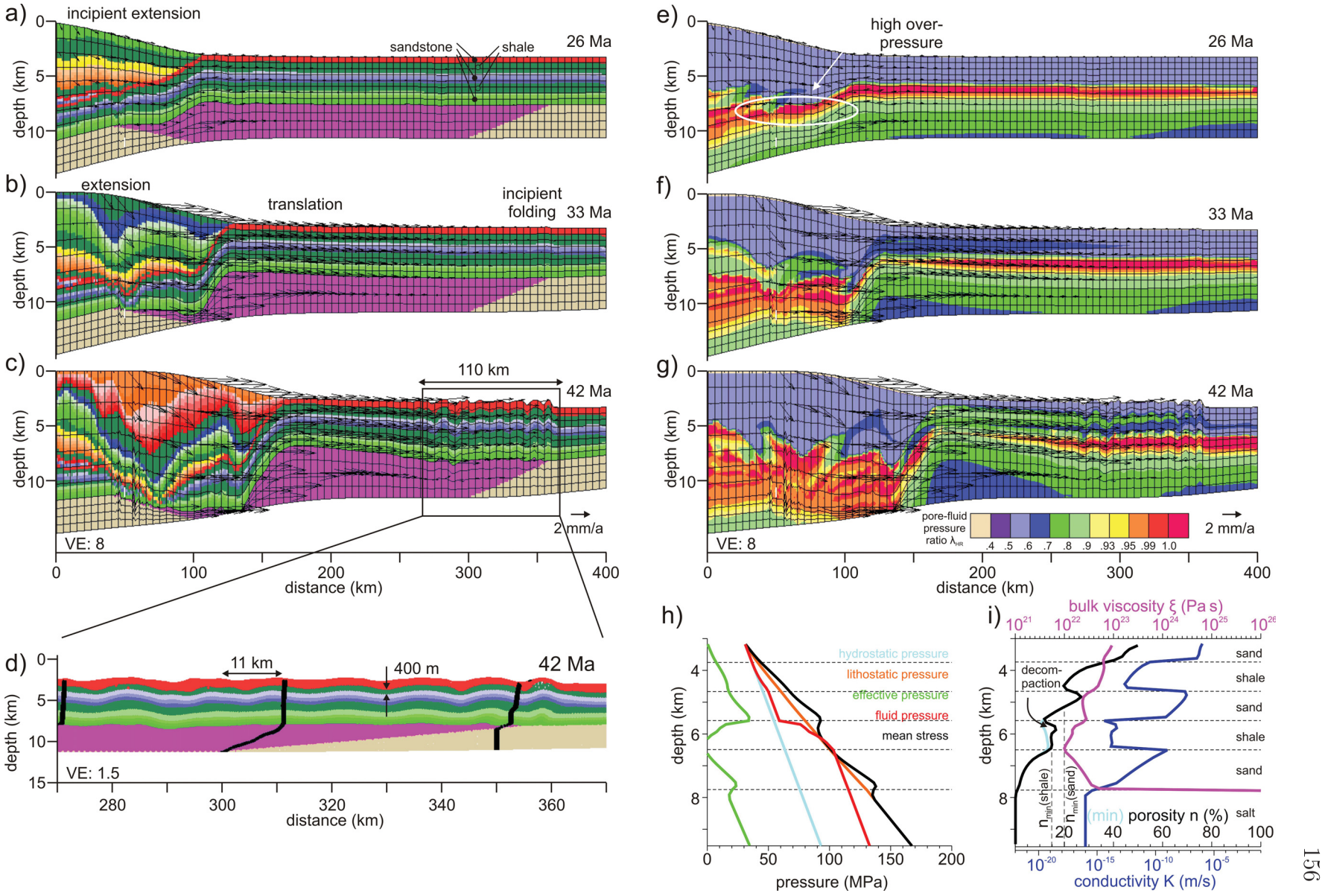
a)
incipient extension
sandstone
shale
26 Ma
b)
extension
translation
incipient folding
33 Ma
c)
110 km
42 Ma
2 mm/a
VE: 8
depth (km)
distance (km)
d)
11 km
400 m
42 Ma
VE: 1.5
e)
high over-pressure
26 Ma
f)
33 Ma
g)
42 Ma
pore-fluid pressure ratio λHR
.4 .5 .6 .7 .8 .9 .93 .95 .99 1.0
h)
hydrostatic pressure
lithostatic pressure
effective pressure
fluid pressure
mean stress
pressure (MPa)
i)
bulk viscosity ξ (Pa s)
decom-paction
sand
shale
sand
shale
sand
salt
nmin(shale)
nmin(sand)
(min) porosity n (%)
conductivity K (m/s)

the largest fold amplitudes (200, 500 and 400 m in models ML-Q25 to ML-Q35, respectively). In all three fold belts, the thickness of the folded layer has increased by approximately 12-15% by the end of folding, indicating pure-shear thickening.

In the landward regions of all four models, the pore-fluid pressures are similar (near-lithostatic) at the onset of gravity spreading (Figures 4.7-4.10e). At the end of the folding phase (Figures 4.7-4.10g), both stronger and shallower overpressures developed in the models with higher viscous compaction efficiency. Near-lithostatic fluid pressures occur at depths of 10 km in the mobilized part of model ML-Q20, and correspondingly at depth of 5-6 km in the mobilized, landward part of model ML-Q35.

The pore-fluid pressures above the seaward part of the salt basin differ significantly among the different models, even at similar stages of evolution (Figures 4.7-4.10, e-g). In general, the models with higher activation energies (stronger viscous compaction) develop higher overpressures both prior to deformation (Figures 4.7-4.10e) and after it (Figures 4.7-4.10, f-h). The zones of high overpressures correspond to the shale-type layers with reduced porosity and hydraulic conductivity (Figures 4.7-4.10i). The shale-type porosity has decreased to progressively lower minimum values from model ML-Q20 (minimum shale-type porosity of c. 18%) to model ML-Q35 (minimum shale-type porosity of c. 15%) at the end of folding. The differences in the minimum porosities of the central sandstone-type layer are larger (28, 25, 23 and 20% for models ML-Q20 to ML-Q35, respectively).

Decompaction occurred in the lower shale-type layer of all four models during the gravity-driven deformation (Figures 4.7-4.10i), despite the implementation of a minimum bulk compressibility. The resulting porosity increase (2-3% in each model) is due to inverse mechanical compaction, which occurs in the models when effective fluid pressures decrease during overpressuring (see *Gradmann et al.*, 2012). The fluid pressure exceeds the mean stress only in model ML-Q35 in the lower part of the deeper shale-type layer. This is physically not correct and the corresponding porosity values in this region therefore need to be considered with caution.

4.5.6 Discussion

Onset of Gravity Spreading

All four models become unstable when a similar level of overpressure evolves in the landward end of the margin. This suggests that the overpressure of the landward sediments controls the stability of the system to a much larger degree than that at the distal end of the basin. This can be explained by the shear force of the décollement layer that counteracts the seaward translation of the overburden and decreases linearly with the thickness of the décollement layer. The landward end of the tapering salt layer constitutes a thin décollement layer, highly resistant to deformation. High overpressure in the sediments above the salt taper effectively widens the weak layer and allows deformation to occur under less friction. The finding that the onset of gravity spreading primarily depends on the deep but not the shallow overpressures modifies the statement of *Gradmann et al.* (2009) that uniform overpressures of λ=0.8 would have been needed for gravity spreading of a Perdido-like system. The fact that higher fluid pressures develop faster in the models with higher activation energies is a direct consequence of the stronger viscous compaction, operating on shorter timescales.

Folding and Shortening

As discussed in section 4.5.5, increased shortening across model ML-Q20 to ML-Q35 does not directly correlate with increased fold amplitudes. This indicates that shortening is not solely accommodated by folding; pure-shear thickening and lateral shortening by compaction also play a role.

The amount of pure-shear thickening (given by the thickness increase of the folded compared to the unfolded section, approximately 5.2 vs. 4.5 km) is similar in all three fold belts (Figures 4.8-4.10c). It suggests that this type of deformation does not contribute to the different fold amplitudes of the models but that lateral shortening owing to compaction may be responsible for the smaller fold amplitudes of model ML-Q35. In order to separate the contributions of folding, compaction and pure-shear deformation that constitute the shortening of a gravity-driven system, a clear separation of the respective strains as well as a clear definition of the terms is needed.

Discussion of 'vertical' and 'horizontal' compaction

The terms 'vertical' and 'horizontal' compaction are often used to describe porosity loss as a result of a vertically or horizontally compressive stress regime. These are misleading terms for the models described here, since compaction (volume loss) occurs only in response to pressure (equation 4.2) and is therefore a volumetric process, implying that it is independent of direction. This formulation of pressure-dependent compaction is widely used in soil mechanic theories. The process usually denoted by the term 'vertical' compaction can be understood notionally as the superposition of volume loss by compaction, which leads to shortening both horizontally and vertically (Figure 4.11, central panel), plus superimposed pure-shear flattening which increases the vertical shortening of the matrix and expands it laterally to its original width (Figure 4.11, top right panel). The net strain is here only vertical, corresponding, for example, to compaction of uniformly aggraded sediments in the absence of any tectonic stress, where fluid expulsion results in vertical, but no horizontal, shortening. During this process of so-called vertical compaction, pure-shear flattening accompanies volumetric compaction because the maximum principal stress is vertical. Equivalently, horizontal compaction is here the product of porosity loss by volumetric compaction plus superimposed pure-shear shortening and thickening in response to a horizontal maximum principal stress (Figure 4.11, bottom right panel). Both deformations must be closely coupled such that the deviatoric deformation of the matrix keeps pace with the compaction.

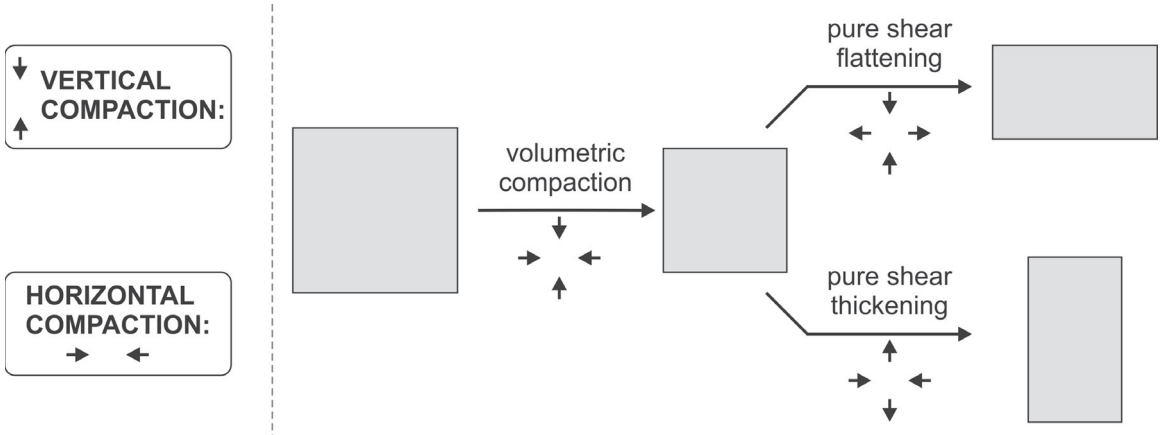

Figure 4.11: Schematic of vertical and horizontal compaction, representing the superposition of volumetric compaction and pure-shear flattening or pure-shear thickening.

This coupled volumetric compaction and pure-shear deformation must be taking place in the numerical models, because compaction is strictly defined as a volumetric process. Accompanying pure-shear deformation implies that the matrix must undergo frictional-plastic failure.

Whether this concept of directional compaction can be transferred to the natural system is not easily answered. Support for this interpretation comes from shear failure in compacting sediments. Numerical and analogue experiments of *Shin et al.* (2008) demonstrate that small volume loss by compaction reduces the horizontal stress exerted by the sediment to the point that the sediment fails under deviatoric tension. This is exactly the first stage notional behavior described above, followed by shear deformation of the sediment that results in the pure-shear vertical flattening accompanying the volumetric compaction in the models.

Vertical and horizontal compaction in the numerical models

We established that the amount of shortening in models ML-Q20 to ML-Q35 can be accommodated by folding (simple-shear deformation), pure-shear thickening and horizontal compaction, where the latter process here comprises the superposition of volumetric compaction and associated pure-shear deformation. The numerical models distinguish between total volumetric, total pure-shear and total simple-shear strain rates. It is not possible, however, to directly separate the fraction of volumetric and pure-shear deformation that stem from horizontal compaction from those stemming from vertical compaction and self-contained pure-shear thickening.

Nevertheless, certain conclusions can be drawn from the plots of accumulated volumetric strain and porosities and the comparison of these parameters from the folded and unfolded section of each model. The differences in volumetric strain between models ML-Q25 to ML-Q35 are not large (Figure 4.12a-c), only model ML-Q35 shows a larger total volumetric strain - and therefore larger total volumetric compaction - in the central sandstone-type layer. Decompaction occurs in the lower shale-type layer of all models with largest intensity in model ML-Q30. The porosities in the fold belt (Figure 4.12d-f, black curve) generally reflect the compaction associated with combined vertical and horizontal shortening. The sediments in the region beyond the salt basin (Figure 4.12d-f, gray curve), however, only experienced vertical shortening. The

difference between the porosities of the fold belt and of the distal section therefore indicates the process of horizontal compaction and is marked as grey areas in Figure 4.12d-f. Porosity is additionally affected by decompaction, which occurs mainly in the lower shale-type layer of all models (Figure 4.12a-c). This layer is therefore omitted here from the consideration of porosity changes.

All three models show generally lower porosities in the folded than in the unfolded section (Figure 4.12d-f) indicating that the folded layers all experience horizontal compaction. The porosity difference in model ML-Q30 is much smaller than that in model ML-Q35, which supports the idea that less shortening was accommodated by horizontal compaction here. However, the porosity difference of model ML-Q30 is also smaller than that of model ML-Q25, although it experienced less shortening and operates with less efficient viscous compaction. A possible explanation may be that compaction efficiency is limited more by the higher pore-fluid pressure in the upper sediments of models ML-Q30 and ML-Q35 than it is enhanced by the higher activation energy Q.

There isn't sufficient evidence to conclude that horizontal compaction would be the primary cause for the different fold amplitudes of models ML-Q30 and ML-Q35. An additional cause may be decompaction, which strongly affects the shale-type layers of model ML-Q30, especially in the fold anticlines (Figure 4.12b,e), and may add to the growth of folds. Furthermore, the shale-type layers of model ML-Q30 are slightly thicker than in model ML-Q35, due to less compaction but equal duration of deposition during the aggradation phase, and may 'host' more decompaction. Without proper elimination of decompaction we cannot draw a final conclusion on the mechanisms affecting the growth of folds. Nevertheless, we can state that higher viscous compaction efficiency must play a role in accommodating more shortening as evidenced by the behavior of models ML-Q30 and ML-Q35. The activation energy Q is only one parameter that characterizes viscous compaction and other parameters that also have a direct control (thermal gradient, reference compactional shear viscosity) are expected to show a similar influence on the system's deformational behavior.

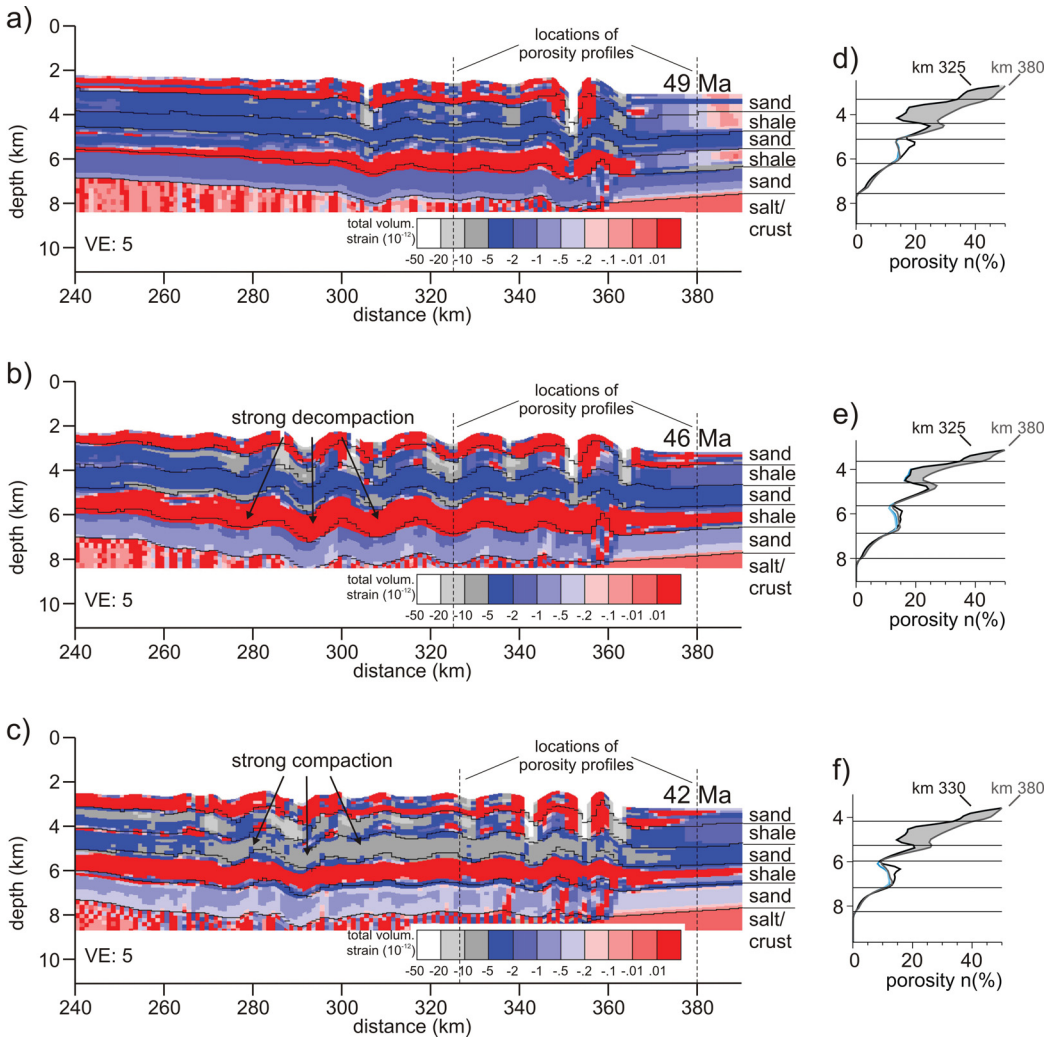

Figure 4.12: (a-c) Plots of the total volumetric strain of the fully developed fold belts of models ML-Q25, ML-Q30, and ML-Q35 accumulated during the progradation phase. Model ML-Q30 exhibits the strongest decompaction (b), model ML-Q35 the strongest volumetric strains (c). (d-f) Porosity-depth profiles of the three models from the folded and unfolded sections. The segments of the profiles within a single layer from the distal section have been stretched to match those of the folded section. The grey areas mark the current differences in porosity, and hence differences in total volumetric strain, and can be taken as an indicator of *horizontal compaction* in the fold belt. See text for more details.

Comparison with Northwestern Gulf of Mexico

When comparing the fold belts that develop in the models to the Perdido Fold Belt of the northwestern Gulf of Mexico, criteria such as duration of folding, fold-belt length, fold amplitude, and fold shape can be used. The fluid pressure regimes that develop in the models can to some degree be compared with the current observations from the northwestern Gulf of Mexico.

The Perdido Fold Belt likely formed in a relatively short period of *c.* 10 Ma (*Trudgill et al.*, 1999) with minor folding activity continuing into the Neogene (*Waller*, 2007). This time frame correlates best with the more unstable models ML-Q30 and ML-Q35, in which fluid pressures develop more quickly and to higher values. Equally, the fold belt lengths of these two models correspond better to the natural system than that of model ML-Q25. Regarding the fold amplitudes, only model ML-Q30 exhibits larger folds although these are still about half the size of the natural folds. Too little deformation (owing to the lower fluid pressures of model ML-Q20) or potentially too strong lateral compaction (owing to the high viscous compaction of model ML-Q35) both yield very small fold amplitudes. The overall discrepancy of the amplitudes of modeled and natural folds is likely related to pure-shear thickening within the model fold belt which accommodates a significant part of the shortening (here 12-15%) but has not been identified in the Perdido Fold Belt. However, given the likely small magnitude of pure-shear thickening, it may be difficult to image with seismic methods.

The folds of the Perdido Fold Belt are characterized as kink-banded folds (*Camerlo and Benson*, 2006), but our models show more sinusoidal folds. This can, for example, be attributed to the chosen implementation of flow laws for rocks and the limited model resolution that cannot reproduce the thinly layered sediments commonly associated with kink folds.

The fluid pressures in the numerical models show certain similarities to the current fluid pressure regime of the northwestern Gulf of Mexico. Onset of overpressures in the onshore and shelf areas of the Gulf of Mexico occurs at depths of approximately 3 km (*Leftwich and Engelder*, 1994, and section 4.2) but at depth of 5-10 km in the numerical models (shallowest overpressures in model ML-Q35). These relatively large differences likely reflect the comparison of the outcome of the time-dependent process of viscous compaction at different times in the evolution of the system. Furthermore,

the local sedimentation rates, which can be very high in the extensional domain of the modeled systems, can influence the timing of overpressure development. In the deep-water domains of the Gulf of Mexico anomalously high shallow overpressures (depth 1-1.5 km) have been reported from several locations (Figure 4.1f and *Behrmann et al.*, 2006; *Couzens-Schultz et al.*, 2007; *Flemings et al.*, 2008; *Reilly and Flemings*, 2010). Such fluid pressure regimes develop in the numerical models only where horizontal compression leads to overpressuring of shale-type layers at this depth (see *Gradmann et al.*, 2012, and section 4.4) and is therefore consistent with model ML-Q25 to ML-Q35. Additionally, the lithology-dependent fluid-pressure variations in the models are consistent with those of the Perdido Fold Belt (Figure 4.1f). Here, overpressures develop in the uppermost Eocene section that contains several shale layers (equivalent to the upper shale-type layer in the models) and fluid pressures in the underlying Wilcox Formation remain hydrostatic (equivalent to the central sandstone-type layer of the models).

4.6 Limitations of the Models

The models presented here can only be regarded as a first approximation of the fluid-deformation interactions that operate on a continental margin on various time and length scales. However, our models give insights into the fundamental large-scale processes related to fluid-pressure evolution and salt tectonics. Certain limitations of the models are imposed by the software, others by its application to our problem of the northwestern Gulf of Mexico.

Simplifications and assumptions that enter the mathematical description of Darcy fluid flow in compacting material are discussed in *Morency et al.* (2007). The software does not include fluid-pressure generation driven by other mechanisms than compaction (e.g. mineral transformations, like the smectite-illite transition, or hydrocarbon generation). We therefore assume here that all strong overpressuring can be captured by the description of compaction-driven fluid pressure generation. The implementation of compaction is currently incomplete, as it is not treated as a fully irreversible process and decompaction can occur. A better implementation will be needed for more detailed analysis of the models.

We here consider gravity spreading on a continental margin as a primarily two-dimensional process because the structures of the northwestern Gulf of Mexico extend for several tens of kilometers along strike. Effects of three-dimensional deformation and fluid flow can then be omitted. Averaging and upscaling of model parameters, which are commonly obtained from bore-hole or laboratory measurements, was necessary in order to investigate the large-scale problem of gravity spreading on a continental margin: Several thin shale layers were approximated by a few thick ones, hydraulic properties of the model material are considered to represent large-scale behavior (not necessarily laboratory measurements), and sedimentation rates were averaged over several tens of millions of years. We expect certain effects on overpressure generation of the smaller-scale variations of model parameters (thinly layered shale, faulting as mechanism for rapid fluid pressure release, variable sedimentation rates), but consider these of secondary importance to the large-scale behavior.

4.7 Summary and Conclusions

In section 4.4 we showed that models with alternating sandstone-type and shale-type lithologies can yield fluid pressure regimes that are consistent with those observed in sedimentary basins. Here, overpressures develop in the less permeable shale-type sediments, whereas fluid pressures within the sandstone-type layers maintain a hydrostatic gradient; overpressures develop at approximately 3 km depth. Interspersal of overpressured layers (shale layers) can effectively reduce the strength of the sediment column.

In section 4.5 a new formulation of the compactional shear viscosity is presented that includes a stronger porosity-dependency and depth-dependency of the compactional shear viscosity. This entails a stronger self-limiting nature of viscous compaction and impedes the development of unreasonably large zones of very high overpressures. A set of models with varying viscous compaction efficiency (models ML-Q20 to ML-Q35) demonstrates that the occurrence of gravity spreading is mainly controlled by the overpressuring in the landward end of the salt basin, where near-lithostatic fluid pressures are required locally within a layer of c. 1 km thickness. These results put into perspective the calculations of *Gradmann et al.* (2009), where uniform,

high overpressures were assumed throughout the sediment columns of the landward and distal end of the salt basin.

Shallow overpressures, as observed in the deep-water region of the Gulf of Mexico, only occur in the numerical models where the system experiences compression, which augments the effective pressure and hence drives compaction and decreases permeability.

Models with higher compaction efficiency develop higher overpressures; the gravity spreading system is more mobile and experiences more distal shortening. However, strongest shortening does not correlate with strongest folding. We conclude that other modes of shortening, in particular so-called horizontal compaction, accommodate shortening in the models with high compaction efficiency. Effects of mechanical decompaction during overpressuring and effects of varying thickness of the shale-type layers between the models may also play a role.

The model with moderately high compaction efficiency (model ML-Q30) shows the strongest resemblance to the natural system of the Perdido Fold Belt in the northwestern Gulf of Mexico with respect to the fold-belt length, duration of folding and to fluid pressures across the folded layers. This indicates that strong overpressures must have developed prior to and during the formation of the Perdido Fold Belt but that too strong compaction and overpressuring of the sediments might again have decreased the efficiency of fold belt evolution.

The models presented in this paper demonstrate that fluid-pressure generation and deformation are strongly coupled in a salt-tectonic system experiencing gravity spreading. Compaction (and associated shortening) is strongly influenced by the changes in stress caused by overpressuring and by large-scale mechanical deformation.

4.8 Acknowledgements

Funding for this project was provided by a Killam Scholarship and a Government of Canada Award to SG, an IBM SUR grant and the Canada Research Chair in Geodynamics to CB. We also like to thank Shell International Exploration and Production, Inc. for their kind support and ION/GXT for permission to show their data. Numerical computations were made with the software SOPALEff, developed by Philippe Fullsack and Christina Morency. Post-processing and graphical display of the model

results are based on IDL-scripts written by Sergei Medvedev. Jürgen Adam and Steve Ings are thanked for reviews of earlier versions of this paper. We also thank Martin Jackson, an anonymous reviewer, and the editor for their reviews.

Bibliography

Angevine, C. L., and D. L. Turcotte (1983), Porosity reduction by pressure solution: A theoretical model for quartz arenites, *Geological Society of America Bulletin*, *94*(10), 1129–1134.

Behrmann, J. H., P. B. Flemings, C. M. John, and the IODP Expedition 308 Scientists (2006), Rapid sedimentation, overpressure, and focused fluid flow, Gulf of Mexico continental margin, *Scientific Drilling*, *3*, 12–17.

Birchwood, R. A., and D. L. Turcotte (1994), A unified approach to geopressuring, seal formation and secondary porosity generation in sedimentary basins, *EOS, Transactions, American Geophysical Union*, *73*(14), 279.

Bird, D. E., K. Burke, S. A. Hall, and J. F. Casey (2005), Gulf of Mexico tectonic history; hotspot tracks, crustal boundaries, and early salt distribution, *AAPG Bulletin*, *89*(3), 311–328.

Camerlo, R. H., and E. F. Benson (2006), Geometric and seismic interpretation of the Perdido fold belt: Northwestern deep-water Gulf of Mexico, *AAPG Bulletin*, *90*(3), 363–386.

Connolly, J. A. D., and Y. Y. Podladchikov (1998), Compaction-driven fluid flow in viscoelastic rocks, *Geodin. Acta*, *11*, 55–84.

Connolly, J. A. D., and Y. Y. Podladchikov (2000), Temperature-dependent viscoelastic compaction and compartmentalization in sedimentary basins, *Tectonophysics*, *324*(3), 137–168.

Couzens-Schultz, B. A., C. A. Hedlund, and C. Guzman (2007), Integrating geology and velocity data to constrain pressure prediction in foldbelts, *Abstracts: Annual Meeting - American Association of Petroleum Geologists*, *2007*, 28.

Davis, D., J. Suppe, and F. A. Dahlen (1983), Mechanics of fold-and-thrust belts and accretionary wedges, *Journal of Geophysical Research*, *88*(B2), 1153–1172.

Dewers, T., and P. J. Ortoleva (1990), Interaction of reaction, mass transport, and rock deformation during diagenesis: Mathematical modeling of intergranular pressure solution, stylolites, and differential compaction/cementation, in *Prediction of reservoir quality through chemical modeling*, vol. 49, edited by I. D. Meshri and P. J. Ortoleva, pp. 147–160, AAPG, Tulsa, Oklahoma.

Diegel, F. A., J. F. Karlo, D. C. Schuster, R. C. Shoup, and P. R. Tauvers (1995), Cenozoic structural evolution and tectono-stratigraphic framework of the northern Gulf Coast continental margin, in *Salt Tectonics, A Global Perspective*, *AAPG Memoir*, vol. 65, edited by M. P. A. Jackson, D. G. Roberts, and S. Snelson, pp. 109–151, AAPG, Tulsa, Oklahoma.

Fiduk, J. C., P. Weimer, B. D. Trudgill, M. G. Rowan, P. E. Gale, R. L. Phair, B. E. Korn, G. R. Roberts, W. T. Gafford, R. S. Lowe, and T. A. Queffelec (1999), The Perdido fold belt, Northwestern deep Gulf of Mexico, Part 2; Seismic stratigraphy and petroleum systems, *AAPG Bulletin*, *83*(4), 578–612.

Flemings, P. B., H. Long, B. Dugan, J. Germaine, C. M. John, J. H. Behrmann, D. Sawyer, and the IODP Expedition 308 Scientists (2008), Pore pressure penetrometers document high overpressure near the seafloor where multiple submarine landslides have occurred on the continental slope, offshore Louisiana, Gulf of Mexico, *Earth and Planetary Science Letters*, *269*(3-4), 309–324.

Galloway, W. E., P. E. Ganey-Curry, X. Li, and R. Buffler (2000), Cenozoic depositional history of the Gulf of Mexico basin, *AAPG Bulletin*, *84*(11), 1743–1774.

Gemmer, L., S. J. Ings, S. Medvedev, and C. Beaumont (2004), Salt tectonics driven by differential sediment loading: Stability analysis and finite element experiments, *Basin Research*, *16*, 199–219.

Gemmer, L., C. Beaumont, and S. J. Ings (2005), Dynamic modeling of passive margin salt tectonics: Effects of water loading, sediment properties, and sedimentation patterns, *Basin Research*, *17*, 383–402.

Gradmann, S., C. Beaumont, and M. Albertz (2009), Factors controlling the evolution of the Perdido Fold Belt, northwestern Gulf of Mexico, determined from numerical models, *Tectonics*, *28*(2).

Gradmann, S., C. Beaumont, and S. Ings (2012), Coupled fluid flow and sediment deformation in margin-scale salt-tectonic systems: 1. Development and application of simple, single-lithology models, *Tectonics*, *31*(4), doi: 10.1029/2011TC003033.

Gratz, A. J. (1991), Solution-transfer compaction of quartzites: Progress toward a rate law, *Geology*, *19*(9), 901–904.

Hall, S. H. (2002), The role of autochthonous salt inflation and deflation in the northern Gulf of Mexico, *Marine and Petroleum Geology*, *19*(6), 649–682.

Hart, B., P. Flemings, and A. Deshpande (1995), Porosity and pressure: Role of compaction disequilibrium in the development of geopressures in a Gulf Coast Pleistocene basin, *Geology*, *23*(1), 45–48.

Helle, H., K. Easterling, and M. Ashby (1985), Hot-isostatic pressing diagrams: New developments, *Acta Metallurgica*, *33*, 2163–2174.

Hubbert, M. K., and W. W. Rubey (1959), Role of fluid pressure in mechanics of overthrust faulting: Part 1, Mechanics of fluid-filled porous solids and its application to overthrust faulting, *Geological Society of America Bulletin*, *70*(2), 115–166.

Husson, L., P. Henry, and X. L. Pichon (2008), Thermal regime of the NW shelf of the Gulf of Mexico: Part A, Thermal and pressure fields, *Bulletin de la Societe Geologique de France*, *179*(2), 129–137.

Kawabata, K., H. Tanaka, Y. Kitamura, and K.-F. Ma (2009), Apparent activation energy and rate-limiting process estimation from natural shale deformed by pressure solution in shallow subduction zone, *Earth and Planetary Science Letters*, *287*(1-2), 57–63.

Leftwich, J. T., and T. Engelder (1994), The characteristics of geopressure profiles in the Gulf of Mexico Basin, in *Basin compartments and seals*, *AAPG Memoir*, vol. 61, edited by P. J. Ortoleva, pp. 119–129, AAPG, Tulsa, Oklahoma.

McDonnell, A., R. G. Loucks, and W. E. Galloway (2008), Paleocene to Eocene deep-water slope canyons, western Gulf of Mexico: Further insights for the provenance of deep-water offshore Wilcox Group plays, *AAPG Bulletin*, *92*(9), 1169–1189.

Meyer, D., L. Zarra, and J. Yun (2007), From BAHA to Jack, evolution of the Lower Tertiary Wilcox trend in the deepwater Gulf of Mexico, *The Sedimentary Record*, *5*(3), 4–9.

Morency, C., R. S. Huismans, C. Beaumont, and P. Fullsack (2007), A numerical model for coupled fluid flow and matrix deformation with applications to disequilibrium compaction and delta stability, *Journal of Geophysical Research*, *112*(B10), 407.

Palciauskas, V. V., and P. A. Domenico (1989), Fluid pressures in deforming porous rocks, *Water Resources Research*, *25*(2), 203–213.

Paterson, M. S. (1973), Nonhydrostatic thermodynamics and its geologic applications, *Reviews of Geophysics and Space Physics*, *11*(2), 355–389.

Peel, F. J., C. J. Travis, and J. R. Hossack (1995), Genetic structural provinces and salt tectonics of the Cenozoic offshore U.S. Gulf of Mexico: A preliminary analysis, in *Salt Tectonics, A Global Perspective*, *AAPG Memoir*, vol. 65, edited by M. P. A. Jackson, D. G. Roberts, and S. Snelson, pp. 153–175, AAPG, Tulsa, Oklahoma.

Pindell, J., and J. F. Dewey (1982), Permo-Triassic reconstruction of western Pangea and the evolution of the Gulf of Mexico/Caribbean region, *Tectonics*, *1*(2), 179–211.

Pindell, J., and L. Kennan (2007), Rift models and the salt-cored marginal wedge in the northern Gulf of Mexico: Implications for deep water Paleogene Wilcox deposition and basinwide maturation, in *Transactions of GCSSEPM 27th Annual Bob F. Perkins Research Conference*, pp. 146–186, (CD Rom).

Pindell, J. L. (1985), Alleghenian reconstruction and subsequent evolution of the Gulf of Mexico, Bahamas, and proto-Caribbean, *Tectonics*, *4*(1), 1–39.

Radovich, B., J. Moon, C. Connors, and D. Bird (2007a), Insights into structure and stratigraphy of the northern Gulf of Mexico from 2D pre-stack depth migration imaging of mega-regional onshore to deep water, long-offset seismic data, *Transactions - Gulf Coast Association of Geological Societies*, *57*, 633–637.

Radovich, B., C. Connors, and J. Moon (2007b), Deep imaging of the Paleogene, Miocene structure and stratigraphy of the western Gulf of Mexico using 2D pre-stack depth migration of mega-regional onshore to deep water, long-offset seismic data, in *The Paleogene of the Gulf of Mexico and Caribbean Basins: Processes, Events, and Petroleum Systems. GCSSEPM Conference Proceedings*, pp. 307–322, (CD Rom).

Reilly, M. J., and P. B. Flemings (2010), Deep pore pressures and seafloor venting in the Auger Basin, Gulf of Mexico, *Basin Research*, *22*(4), 380–397.

Revil, A. (2001), Pervasive pressure solution transfer in a quartz sand, *Journal of Geophysical Research*, *106*(B5), 8665–8686.

Revil, A., D. Grauls, and O. Brevart (2002), Mechanical compaction of sand/clay mixtures, *Journal of Geophysical Research*, *107*(B11), 15.

Rowan, M. G., F. J. Peel, and B. C. Vendeville (2004), Gravity-driven fold belts on passive margins, in *Thrust tectonics and hydrocarbon systems*, *AAPG Memoir*, vol. 82, edited by K. R. McClay, pp. 157–182, AAPG, Tulsa, Oklahoma.

Rowan, M. G., K. F. Inman, and J. C. Fiduk (2005), Oligo-Miocene extension at the Louann level in the northern Gulf of Mexico: Kinematic models and examples, *Transactions - Gulf Coast Association of Geological Societies*, *55*, 725–732.

Rutter, E. H. (1976), The kinetics of rock deformation by pressure solution, *Philosophical Transactions of the Royal Society of London, Series A: Mathematical and Physical Sciences*, *283*(1312), 203–219.

Rutter, E. H., and D. H. Mainprice (1978), The effect of water on stress relaxation of faulted and unfaulted sandstone, in *Rock friction and earthquake prediction*, vol. 116, edited by J. D. Byerlee and M. Wyss, pp. 634–654, Birkhäuser Verlag.

Salvador, A. (1991), Origin and development of the Gulf of Mexico Basin, in *The Gulf of Mexico Basin*, *The geology of North America*, vol. J, edited by A. Salvador, pp. 389–444, GSA, USA.

Schneider, F., J. L. Potdevin, S. Wolf, and I. Faille (1996), Mechanical and chemical compaction model for sedimentary basin simulators, *Tectonophysics*, *263*(1-4), 307–317.

Scott, D. R., and D. J. Stevenson (1984), Magma solitons, *Geophysical Research Letters*, *11*(11), 1161–1164.

Shin, H., J. C. Santamarina, and J. A. Cartwright (2008), Contraction-driven shear failure in compacting uncemented sediments, *Geology*, *36*(12), 931–934.

Simmons, G. R. (1992), The regional distribution of salt in the northwestern Gulf of Mexico; styles of emplacement and implications for early tectonic history, *Bulletin - Houston Geological Society*, *35*(4), 7.

Stephenson, L. P., W. J. Plumley, and V. V. Palciauskas (1992), A model for sandstone compaction by grain interpenetration, *Journal of Sedimentary Research*, *62*(1), 11–22.

Suetnova, E., and G. Vasseur (2000), 1-D modelling rock compaction in sedimentary basins using a visco-elastic rheology, *Earth and Planetary Science Letters*, *178*(3-4), 373–383.

Trudgill, B. D., M. G. Rowan, J. C. Fiduk, P. Weimer, P. E. Gale, B. E. Korn, R. L. Phair, W. T. Gafford, G. R. Roberts, and S. W. Dobbs (1999), The Perdido fold belt, northwestern deep Gulf of Mexico: Part 1, Structural geometry, evolution and regional implications, *AAPG Bulletin*, *83*(1), 88–113.

Waller, T. D. (2007), Structural Analysis of the Perdido Fold Belt: Timing, Evolution and Structural Cycle, Master's thesis, Texas A&M University.

Willett, S. D. (1999), Rheological dependence of extension in wedge models of convergent orogens, *Tectonophysics*, *305*(4), 419–435.

Yang, X. S. (2001), A unified approach to mechanical compaction, pressure solution, mineral reactions and the temperature distribution in hydrocarbon basins, *Tectonophysics*, *330*(1-2), 141–151.

Chapter 5

Numerical Modeling Study of Mechanisms of Salt Canopy Evolution and their Application to the Northwestern Gulf of Mexico

5.0 Abstract

Salt canopies are common salt-tectonic structures and are key players in the structural evolution of a salt basin as well as in the associated development of hydrocarbon systems. This study employs 2D finite-element models, which involve the dynamical interaction of viscous salt and frictional-plastic sediments in a gravity-spreading system, to investigate the evolution of an Eocene canopy that developed in the center of a large autochthonous salt basin in the northwestern Gulf of Mexico (GoM).

Three different salt expulsion and canopy formation concepts are tested that have been proposed in the salt-tectonic literature. 1) The squeezed diapir mechanism holds that shortening of a region containing pre-existing diapirs will be absorbed by the salt (the weakest part of the system), which is then expelled onto the seafloor. 2) The expulsion rollover mechanism causes salt to be expelled laterally and to the surface from beneath evolving rollover structures and can operate in a neutral stress regime. 3) The breached anticline mechanism requires substantial shortening of salt-cored folds such that the salt breaches the anticlines and is expelled to the seafloor. Where diapirs are required as precursory structures for canopy formation, their evolution is included in the models to assure a continuous, non-abrupt evolution of the salt-sediment system.

All three canopy mechanisms can, in general, produce allochthonous salt structures. But only the squeezed diapir models capture a large number of key features of the Eocene paleocanopy of the northwestern GoM: the sub-canopy structures, the canopy's lateral extent, as well as the delayed deformation of the cover above the distal part of the salt basin. It is also possible that the three different mechanisms may

have acted in combination or sequentially. The mechanism of breached anticlines, for example, may best explain the evolution of a younger, further seaward located canopy.

5.1 Introduction

Allochthonous salt is defined as a body of salt at a stratigraphic level higher than its own depositional (autochthonous) level (*Jackson and Talbot*, 1991). A salt sheet is loosely defined as an allochthonous salt body with a subhorizontal dimension that is several times larger than its vertical dimension. A canopy strictly consists of two or more coalesced salt sheets (*Jackson and Talbot*, 1991). However, the term canopy is often applied to single large salt sheets where it is not feasible to determine the number of feeders as they may have been pinched off or are obscured in seismic data by the overlying salt. Definitions of the salt-tectonic terminology used in this chapter are given in the glossary (Appendix A).

Allochthonous salt sheets have been reported from many onshore and offshore sedimentary basins worldwide (see *Jackson*, 1995; *Hudec and Jackson*, 2006, and references therein). Nevertheless, the mechanisms of emplacement and advance of salt sheets remain poorly understood. This is related to a number of factors, including difficulties in sub-salt seismic imaging and resulting poorly defined kinematic structural relationships below salt sheets; as well as limited quantitative understanding of the rheological and mechanical processes at work during salt-sheet evolution. This study addresses the latter issue through forward quantitative modeling of salt-sheet evolution.

The work focuses on both the general mechanisms of salt-sheet and canopy development and on the particular case of an Eocene canopy in the northwestern GoM (GoM, Figures 5.1 and 5.2a,b), which today is only preserved as a detachment layer that was active during the Oligocene. Even though the salt has been evacuated, many features of this paleocanopy and the timing of subsequent salt-tectonic deformation of the region can be reconstructed from the seismically well imaged overlying and adjacent strata. The aim of this study is to find out how this Eocene canopy most likely evolved by first investigating three different canopy emplacement mechanisms with numerical experiments and subsequently comparing them to the Oligocene-Eocene

setting of the northwestern GoM. The canopy has been a laterally extensive structure, sprawling along the continental margin. It is therefore considered suitable to investigate its first-order evolution with 2D numerical models, but relevance of out-of-plane salt flow for the regional evolution cannot be excluded.

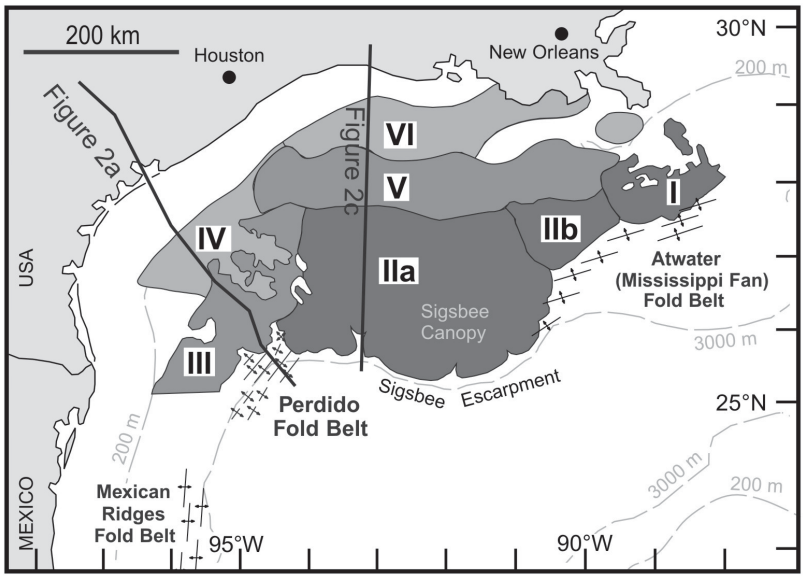

Figure 5.1: Regional map of northern Gulf of Mexico showing the Cenozoic fold belts as well as the location of salt canopies and their classification (after *Peel et al.*, 1995; *Fiduk et al.*, 1999). Neogene canopies are shown in dark grey (I-II), Paleogene to Miocene canopies in medium grey (III&V) and Eocene-Oligocene canopies in light grey (IV&VI). The Sigsbee canopy (canopy II) is the largest Neogene canopy. Canopy IV is subject of this study.

5.1.1 Development of the Northwestern Gulf of Mexico

Depositional History

The Gulf of Mexico (GoM) opened as a rift basin in the Late Triassic to Early Jurassic (*Pindell and Dewey*, 1982; *Pindell*, 1985; *Salvador*, 1991; *Bird et al.*, 2005). The Middle Jurassic Louann salt is commonly considered to be a post-rift succession, deposited within a single, up to 3 km thick salt basin (*Trudgill et al.*, 1999; *Hall*, 2002). Recent reconstructions even suggest post- to syn-rift deposition of up to 5-7 km thickness (*Pindell and Kennan*, 2007). Deep-water carbonate deposition prevailed in the GoM throughout the Cretaceous (*Diegel et al.*, 1995; *Peel et al.*, 1995; *Fiduk et al.*, 1999). Two major episodes of clastic sediment input occurred during the Paleogene.

Figure 5.2: (a) Regional NW-SE trending seismic profile from the northwestern GoM extending from onshore into deep water (from *Radovich et al.*, 2007a). Large-scale gravity spreading structures (extensional faults, allochthonous salt, fold belts) are indicated. Location is shown in Figure 5.1. (b) Detail of panel (a) showing interpreted faults and folding structures beneath the paleocanopy (from *Radovich et al.*, 2007b). (c) Profile across northern GoM, interpreted from seismic data. Two allochthonous salt levels are interpreted. Location is shown in Figure 5.1. (d) Reconstruction of panel (c) showing a vast canopy evolving from numerous diapirs. Annotations indicate common salt-tectonic structures; Mb: minibasin, S: salt sheet, Tu: turtle structure, W: salt weld, D: diapir, To: salt tongue, C: salt canopy ,F: salt feeder. ((c) and (d) from *Diegel et al.*, 1995)

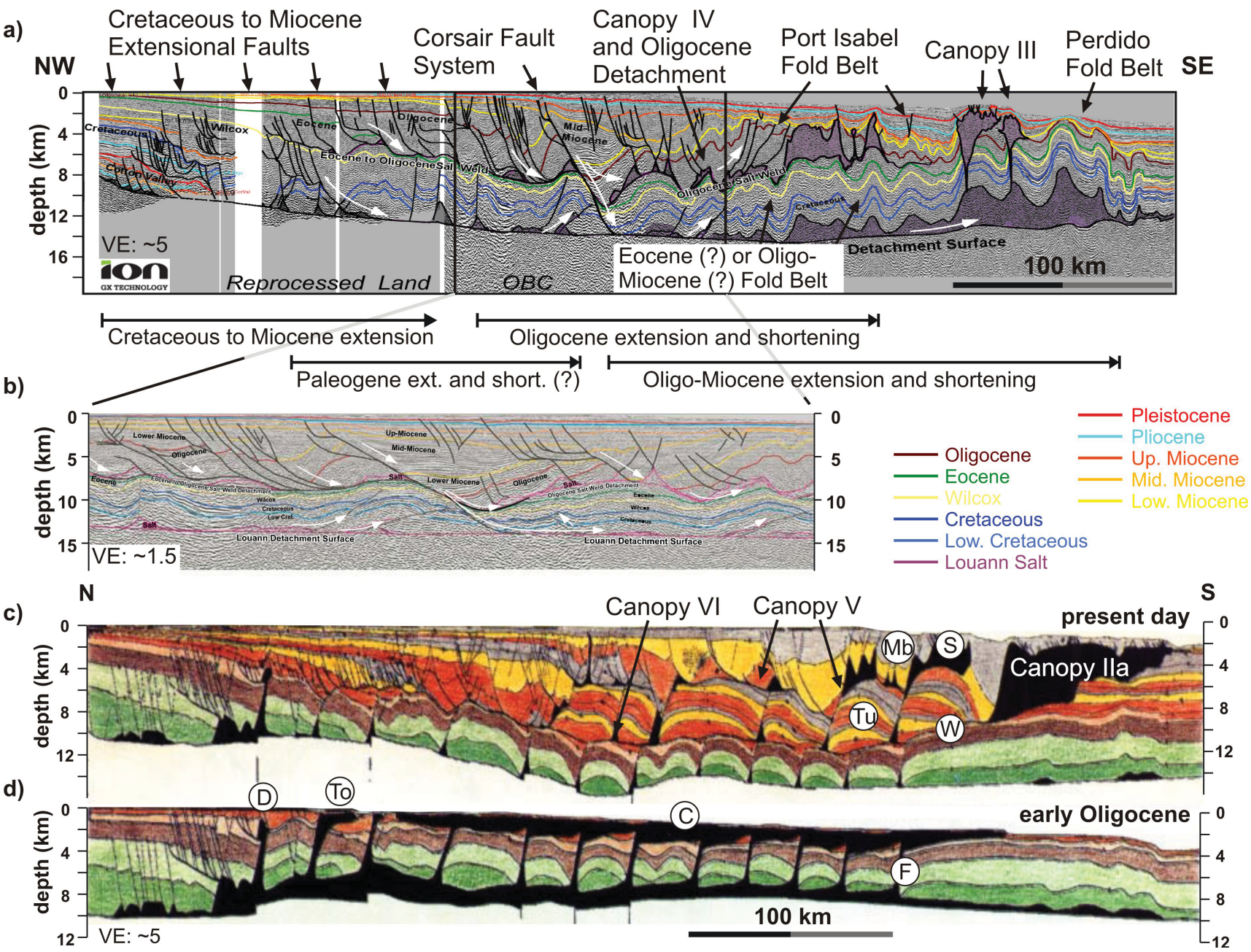
a)
NW
SE
Cretaceous to Miocene Extensional Faults
Corsair Fault System
Canopy IV and Oligocene Detachment
Port Isabel Fold Belt
Canopy III
Perdido Fold Belt
depth (km)
VE: ~5
Reprocessed Land
OBC
Eocene (?) or Oligo-Miocene (?) Fold Belt
Detachment Surface
100 km
Cretaceous to Miocene extension
Oligocene extension and shortening
Paleogene ext. and short. (?)
Oligo-Miocene extension and shortening
b)
depth (km)
VE: ~1.5
Louann Detachment Surface
Pleistocene
Pliocene
Up. Miocene
Mid. Miocene
Low. Miocene
Oligocene
Eocene
Wilcox
Cretaceous
Low. Cretaceous
Louann Salt
N
S
c)
Canopy VI
Canopy V
present day
Canopy IIa
Mb
S
Tu
W
d)
D
To
C
F
early Oligocene
100 km
VE: ~5

The lower Eocene Wilcox Formation was deposited as the result of tectonic uplift and associated erosion during the Laramide orogeny in northern Mexico and in the southwest US. This turbiditic unit extends 200-300 km away from the contemporaneous shelf edge and has proven to be a major hydrocarbon reservoir (*Meyer et al.*, 2007; *McDonnell et al.*, 2008). Rejuvenated uplift and erosion during Oligocene volcanogenic crustal heating in the southwestern United States and northern Mexico caused renewed influx of coarse clastics of the Frio Formation.

During the Miocene the main sediment input shifted eastward towards the Louisiana shelf and Mississippi delta (*Fiduk et al.*, 1999; *Galloway et al.*, 2000), and Neogene sedimentation in the northwestern GoM accordingly slowed down. Shelf progradation rates during the Cenozoic averaged approximately 4 mm/a in the northwestern GoM, but were quite variable (Figure 5.3), shorter-term progradation rates reached up to 10 mm/a in the early Eocene and Oligocene (*Galloway et al.*, 2000).

The Late Mesozoic to Paleogene sedimentary succession of the northwestern GoM has a relatively uniform thickness across most of the distal half of the salt basin (Figure 5.2a, *Trudgill et al.*, 1999; *Meyer et al.*, 2007; *McDonnell et al.*, 2008). Reasons for this uniform deposition are only poorly understood but are possibly related to a very wide, salt-cored marginal wedge that shaped the continental slope (*Pindell and Kennan*, 2007).

The influence of thermal subsidence on sediment distribution and salt movement in the GoM remains unsatisfactorily understood. Various models for rifting and associated thermal subsidence have been proposed (classic McKenzie model (*Salvador*, 1991; *Diegel et al.*, 1995), asymmetric rifting (*Pindell and Kennan*, 2007), back-arc basin formation (*Stern and Dickinson*, 2010)). But because salt movement and lithospheric tectonothermal processes additionally influenced the subsidence history, no consistent picture has been assembled yet.

Salt Tectonic Structures in the Northwestern Gulf of Mexico

The salt-tectonic evolution of the northwestern GoM is strongly linked to its depositional history. Up to four phases of gravity spreading and gravity gliding have been reported for the northwestern GoM (Figure 5.2a, *Diegel et al.*, 1995; *Peel et al.*, 1995; *Radovich et al.*, 2007b) and multiple Cenozoic canopies evolved in this region

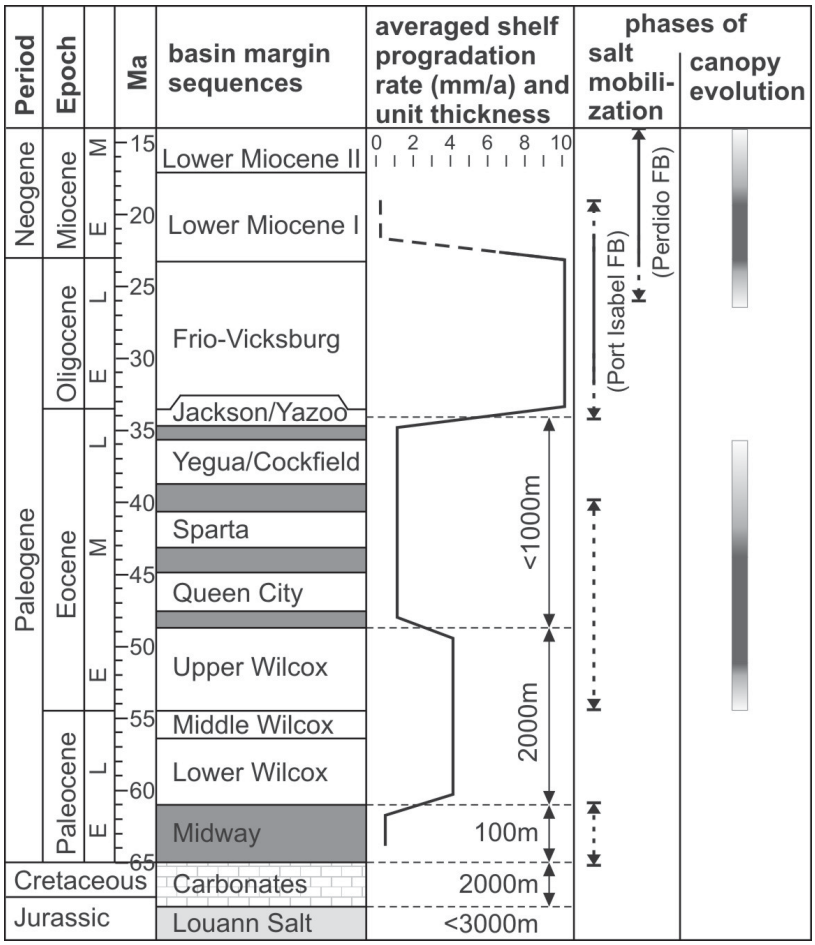

Figure 5.3: Sediment succession of the Texan shelf for the Late Mesozoic to Paleogene. Dark gray layers mark shale-dominated lithologies. Average shelf progradation rates from *Galloway et al.* (2000). Approximate sediment thicknesses extracted from pre-kinematic section of Perdido Fold Belt (*Meyer et al.*, 2007) and central part of salt basin (*Rowan et al.*, 2005; *McDonnell et al.*, 2008). Approximate phases of deformation and canopy evolution from *Peel et al.* (1995); *Diegel et al.* (1995); *Radovich et al.* (2007b) and *Rowan et al.* (2005).

(Figure 5.1, *Peel et al.*, 1995). During both gravity spreading and gravity gliding, mobilized underlying salt assists gravitational deformation (see glossary). Many linked systems of extension and shortening show a combination of these two mechanisms (*Schultz-Ela*, 2001).

Widespread extension occurred during Late Cretaceous to Miocene times in the northwestern GoM with the majority of faults soling out in the autochthonous salt sheet. The oldest observed contractional deformation is connected to Paleocene shortening located landward of the current shelf edge (*Radovich et al.*, 2007b). It was followed by the development of large-scale folds landward of the Perdido Fold Belt in the Eocene (*Peel et al.*, 1995) and the development of the salt canopy investigated in this study. The increased sediment input during the deposition of the early Eocene Wilcox Formation and subsequent sediment starvation may have influenced, perhaps controlled, the expulsion and spreading of the allochthonous salt during this time. None of the multiple landward-situated extensional features have been directly correlated with the formation of the paleocanopy.

The subsequent evolution of the northwestern GoM is conceptually shown in Figure 5.4, as proposed by *Rowan et al.* (2005) and in parts modeled by *Gradmann et al.* (2009). With continuing deposition of the Frio sediments in the Oligocene, a third gravity-spreading system developed above the allochthonous salt layer, as is evident from the numerous Oligocene extensional faults and the structures of the Port Isabel Fold Belt (*Peel et al.*, 1995; *Rowan et al.*, 2004) (Figure 5.4b). Shales deposited during the late Eocene sea-level lowstand likely participated as additional detachment surfaces (*Peel et al.*, 1995; *Diegel et al.*, 1995; *McDonnell et al.*, 2009). During the final, late Oligocene to Miocene phase of gravity spreading the enhanced sediment load above the autochthonous and allochthonous salt activated the Corsair fault system and caused the folding of the Perdido Fold Belt (Figure 5.4c, *Rowan et al.*, 2005; *Radovich et al.*, 2007b; *McDonnell et al.*, 2009; *Gradmann et al.*, 2009).

As evident from the 4.5 km thick pre-kinematic section of the Perdido Fold Belt, this last phase of gravity spreading was the first salt-tectonic deformation to affect the distal end of the salt basin. Slightly different dates for the fold belt evolution (first minor folding event occurred in early Oligocene) as well as additional minor activity phases (reactivation during late Miocene-Pliocene) have been proposed (*Fuqua*, 1990;

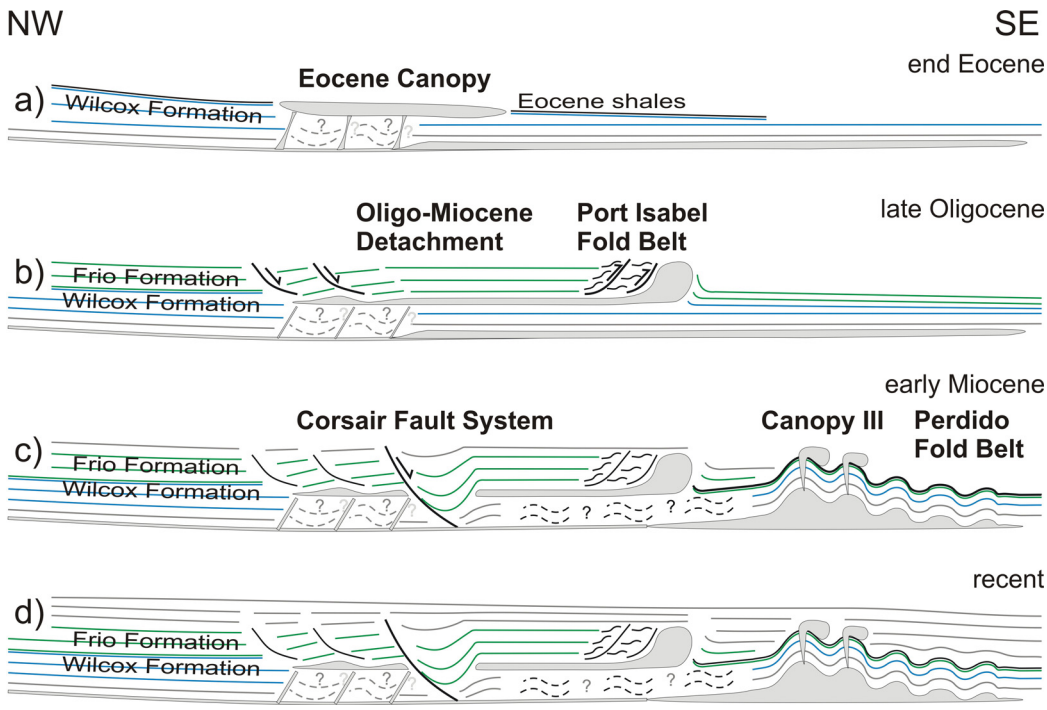

Figure 5.4: Schematic salt-tectonic evolution of the northwestern GoM from Eocene to recent as outlined in *Rowan et al.* (2005). Light grey represents autochthonous and allochthonous salt bodies. The Eocene canopy shown in (a) is equivalent to canopy IV shown in Figure 5.1. Active faults and deformational surfaces are indicated by arrows. Not to scale.

Diegel et al., 1995; *Peel et al.*, 1995; *Trudgill et al.*, 1999; *Waller*, 2007). Folding structures landward of the Perdido Fold Belt, which are partly obscured by allochthonous salt, have been interpreted either as a separate Eocene fold belt (*Peel et al.*, 1995) or as a landward continuation of the Oligo-Miocene Perdido Fold Belt (*Rowan et al.*, 2005; *Radovich et al.*, 2007b). A second canopy is located just landward and above the fold belt and must therefore be of same age or younger.

The two canopies of the northwestern GoM are only two of a large set of canopies in the GoM that exhibit a large variety of sizes and temporal evolution (Figure 5.1). The most notable is the Sigsbee salt canopy (labeled canopy IIa & IIb in Figure 5.1), which extends several hundred kilometers along and up to 200 km across the margin (*Peel et al.*, 1995; *Diegel et al.*, 1995). The oldest of the mapped, large-scale canopies are the two Eocene-Oligocene canopies in the northwestern and northern GoM (canopy IV and VI of Figure 5.1) which acted as large-scale detachment systems in the Oligocene-Miocene. Because of later sediment loading, reactivation and possibly dissolution these canopies are in most places only preserved as salt welds. Consequently their timing and extent are poorly constrained; a joint evolution of both canopies has also been suggested (*Diegel et al.*, 1995). Allochthonous salt sheets are also found to the west and east of the Sigsbee canopy (canopies I & III, Figure 5.1), but have been inferred to have different emplacement histories than that of the central canopy (*Peel et al.*, 1995). This study focuses on the northwestern GoM and its Eocene canopy (canopy IV). Possible similarities to the northern canopy (canopy VI, Figure 5.2c,d) and implications for the western canopy (canopy III) are also discussed.

5.1.2 Evolution of Salt Sheets and Canopies

This study focusses on salt sheets and canopies that evolved during thin-skinned, gravity-driven salt tectonics in passive margin environments but were never exposed to the tectonic extension or shortening of the underlying crust. Salt sheets can extend for several tens of kilometers, have thicknesses of several hundreds to thousands of meters and generally overlie sedimentary strata, which can also be several kilometers thick (*Peel et al.*, 1995). Salt sheets may even occur as tiered systems, as reported from the GoM (*Diegel et al.*, 1995). Salt sheet emplacement, originally interpreted as sill-like intrusion (*Nelson and Fairchild*, 1989), is now considered to be generally

extrusive along the land surface or seafloor (*Fletcher et al.*, 1995), although some cases of smaller, sill-like intrusions (salt wings) are known from the North German Basin (*Hudec*, 2004). The mechanisms by which the salt, which is often denser than the surrounding near-surface sediments, is brought up to the surface or seafloor, and the early stages of its spreading as it develops into a sheet, remain mostly conceptual. Only the salt-sediment interaction occurring near the top of the diapirs has been studied on outcrops in Iran, Romania and Mexico (see references in *Jackson*, 1995; *Giles and Lawton*, 2002). Factors influencing salt-sheet advance that follows the earlier 'extrusion' phase, have been studied and documented in detail (*Fletcher et al.*, 1995; *McBride et al.*, 1998; *Hudec and Jackson*, 2006).

The primary driver of salt-sheet advance is the slope of the basal surface and the pressure difference across the salt sheet stemming from varying thicknesses of the salt or from the load of a sedimentary overburden. Crestal bulges indicate locally thickened salt and have been observed near the centers of subaerial salt glaciers. They are an expression of additional regional pressure, over and above buoyancy forces, that squeezes the feeders and expels salt upward. Crestal bulges may rise several hundreds of meters above the surrounding salt plateau during phases of intensive salt-sheet advance (*Talbot*, 1998; *Talbot and Aftabi*, 2004). Similarly, submarine salt sheets usually have a frontal relief of several hundreds of meters at their toes (*Fletcher et al.*, 1995; *Hudec and Jackson*, 2006), indicating that such a large pressure difference is necessary to drive salt-sheet advance. In contrast to thick salt sheets, subaerial mobile tongues of salt glaciers (namakiers) can be as thin as several tens of meters (*Talbot*, 1998; *Talbot and Aftabi*, 2004) when they flow downslope and are weakened by meteoric waters (*Talbot and Rogers*, 1980).

The rate of salt-sheet advance additionally depends on the salt viscosity, estimated to range from $4 \cdot 10^{18} - 10^{19}$ Pa s in extruding submarine salt (*Fletcher et al.*, 1995). Whether individual salt sheets will coalesce into canopies depends on their spreading rate, the amount of salt available, the distance between individual feeders and the contemporaneous sedimentation.

Here, the less well-studied mechanisms of salt extrusion are investigated. Three conceptual mechanisms are named after the principal structures involved (Figure 5.5):

(1) squeezed diapirs, (2) expulsion rollovers, and (3) breached anticlines. These mechanisms have been proposed in the salt-tectonic literature (*Diegel et al.*, 1995; *Rowan et al.*, 2005; *Gradmann et al.*, 2009), but have not yet been quantitatively studied. All three mechanisms may occur in a submarine post-rift margin setting and can be considered responsible for the evacuation of salt, its extrusion and emplacement at a higher structural levels. Furthermore they may drive lateral salt flow and amalgamation of salt sheets into canopies with multiple salt feeders. For the first two mechanisms of canopy evolution, diapirs can be important precursory structures. In the models presented here they evolve through a new mechanism (based on uneven sedimentation) that can take place in a neutral regional stress system and thereby does not interfere with the subsequent canopy phase (section 5.3 and Appendix 5.9).

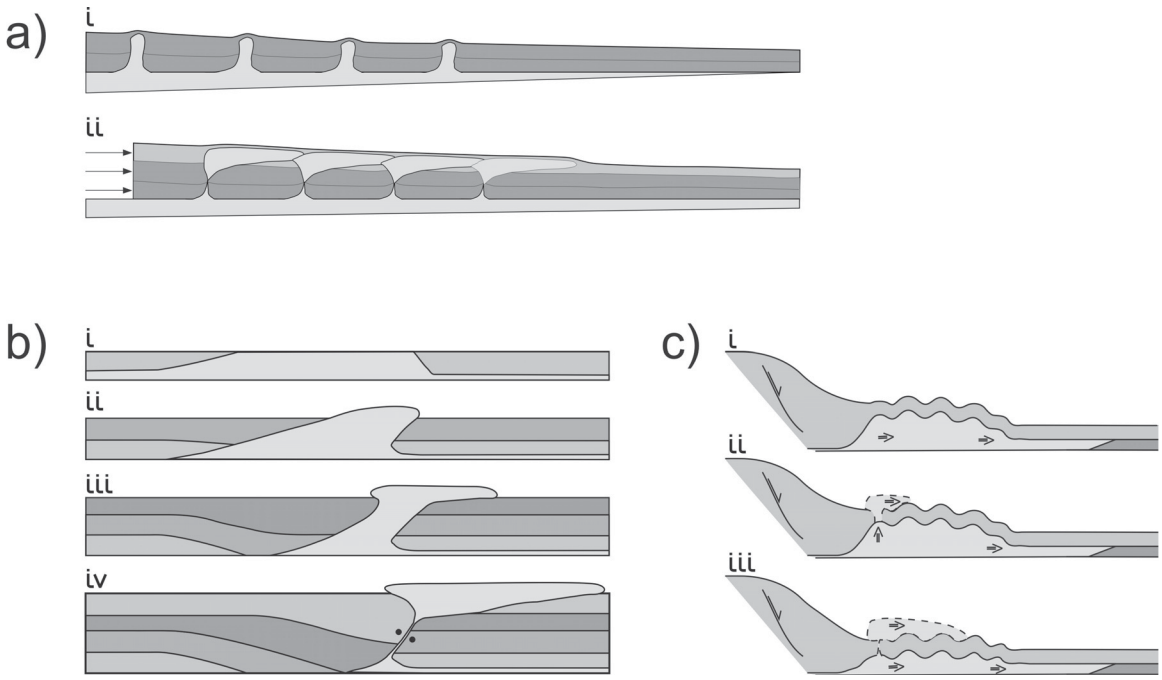

Figure 5.5: Schematic diagrams of different concepts for canopy evolution. (a) Squeezed diapir mechanism (after *Rowan et al.*, 2004). (b) Expulsion rollover mechanism. Black dots mark location of salt weld (after *Rowan and Inman*, 2005). (c) Breached anticline mechanism. Shortening is here generated by gravity spreading (after *Gradmann et al.*, 2009).

Canopy Concept I: Evolution from Squeezed Diapirs

The squeezed diapir mechanism for the evolution of a salt canopy (Figure 5.5a) operates in a compressive stress regime where shortening is more easily absorbed by the diapirs because they are the weakest part of the system (*Diegel et al.*, 1995). The squeezing and shortening of the diapirs pump salt to the surface where it may advance as a salt sheet. The pressures evolving in the diapirs are crucial as they must assist in rupturing the sedimentary roof, if this exists, and the rate of upward salt flow must be sufficiently high to exceed sedimentation rates in adjacent basins. A high flow rate furthermore amplifies the crestal bulge and thereby enhances the rate of salt advance, allowing adjacent salt sheets to coalesce. The squeezed diapir mechanism has, for example, been proposed by *Diegel et al.* (1995) to have formed the canopy in the northern GoM (Figure 5.2c). The mechanism of salt canopy formation requires pre-existing diapirs as well as regional shortening. These processes are addressed separately in section 5.4 and Appendix 5.9.

Canopy Concept II: Evolution from Expulsion Rollovers

The evolution of an allochthonous salt sheet formed by an expulsion rollover against a salt high requires pre-existing thickened salt - either a diapir, or salt inflating landward of a basement high (Figure 5.5b i). As sediments prograde onto the thick salt layer (Figure 5.5b ii), the differential load squeezes the underlying salt seaward, which then further inflates the distal salt and ultimately lifts it up onto the seafloor (Figure 5.5b iii). Sediment above the elevated salt will likely be thin owing to the positive relief generated by the inflated salt and possibly enhanced erosion here. Under these circumstances cover strata may be more easily pierced by the inflating salt. Extrusion will cease when the expulsion rollover fully closes off the feeder, leaving a landward-dipping (counter-regional) salt weld (Figure 5.5b iv). Sediment progradation may continue and transfer the process of lateral salt evacuation onto the allochthonous level.

Two end-members of this process of salt-expulsion have been described. *Ge et al.* (1997) and *Adam and Krezsek* (2012) demonstrate with analogue models in which silicone represents salt, that basin-wide expulsion rollovers (several tens of kilometers wide) can evacuate salt and develop allochthonous structures. Here, salt pinches out against basement highs, where salt inflation and expulsion are localized. If several

basement steps are present, this type of behavior has the potential to develop a true canopy that is supplied by more than one feeder (*Ge et al.*, 1997, their Figure 10).

Rowan et al. (2005) invoke several smaller-scale expulsion rollovers to explain canopy evolution in the northern GoM, where no direct evidence of extension or shortening has been brought forward. They interpret a series of seaward-leaning welded feeders to be the remnants of diapirs between minibasins through which salt was expelled onto the seafloor as the minibasins became asymmetrically loaded and developed into expulsion rollover structures. The term minibasin is used for a sedimentary basin of several kilometers extent that exhibits rapid growth owing to expulsion of underlying salt (see glossary).

Both cases of salt-sheet evolution are investigated, distinguished by the lateral extent over which differential sedimentation acts (regional and local scale). Our end-member scenarios of expulsion rollovers develop in a neutral stress regime in order to separate them from the effects of other canopy evolution mechanisms.

Canopy Concept III: Evolution from Breached Anticlines

Canopies may also evolve through the mechanism of breached anticlines (Figure 5.5c), whereby substantial shortening, induced for example by gravity spreading or gliding, can generate a salt-cored fold belt above the autochthonous salt layer (Figure 5.5c i). As folds are progressively shortened and tightened, high bending stresses develop along the fold hinges and bring the overburden closer to failure. Buoyant salt can eventually breach the anticlines and extrude to the seafloor (Figure 5.5c ii and iii), generating salt sheets. This process may also be enhanced by erosion common above shortening structures (e.g. *Coward and Stewart*, 1995; *Heiniö and Davies*, 2006).

If the distance between the diapirs extruded from each anticline is sufficiently short, a true salt canopy can form with only moderate amounts of salt required from each breached anticline. *Gradmann et al.* (2009) demonstrated with numerical models that this process can explain the evolution of the salt canopy adjacent to the Perdido Fold Belt (canopy II, Figures 5.1 and 5.2a)

5.2 Finite Element Numerical Modeling

Two-dimensional mechanical finite element models are used here to investigate the evolution of salt canopies in a rifted continental margin setting.

Viscous Creeping Flow

The models calculate plane-strain, incompressible, viscous-plastic fluid flow (*Fullsack*, 1995; *Willett*, 1999). Deformation is governed by the equation of motion (creeping flow with conservation of momentum and no inertial forces) and the equation for conservation of mass, which, for incompressible flow (sediment compaction is treated separately), can be written as zero divergence of the velocity.

$$\frac{\partial P}{\partial x_j} + \frac{\partial \sigma_{ij}}{\partial x_i} + \rho\, g_j = 0 \qquad i,j = 1,2 \tag{5.1}$$

$$\frac{\partial v_i}{\partial x_i} = 0 \tag{5.2}$$

where summation is implied over repeated indices, v_i are the spatial velocity components, P is the mean stress, x_i are the spatial dimensions, ρ is the density, and g is the gravitational acceleration acting in the $j = 2$ direction. σ_{ij} is the stress tensor that relates to strain rates by the constitutive law for incompressible viscous deformation

$$\sigma_{ij} = P\,\delta_{ij} + 2\,\eta_e\,\dot{\varepsilon}_{ij} \tag{5.3}$$

where $\delta_{ij} = 1$ when $i = j$ and $\delta_{ij} = 0$ when $i \neq j$, η_e is the effective viscosity, and $\dot{\varepsilon}_{ij}$ is the strain rate tensor defined by

$$\dot{\varepsilon}_{ij} = \frac{1}{2}\left(\frac{\partial v_i}{\partial x_j} + \frac{\partial v_j}{\partial x_i}\right). \tag{5.4}$$

η_e is constant for linear viscous materials (salt) and stress dependent for the non-linear viscous sediment overburden (equation 5.6). Equations (5.1) and (5.2) are solved using an Arbitrary Lagrangian-Eulerian (ALE) finite element method in which computations are made on an Eulerian grid that stretches vertically to adapt to the evolving model geometry (*Fullsack*, 1995). The material properties are tracked and updated

using a set of Lagrangian particles that move with the calculated velocity field. This approach allows calculations to be made for very large deformation.

Material Rheology

Sediments and basement are modeled as brittle frictional-plastic materials with strength that increases with pressure and that follow a Drucker-Prager yield criterion, which is equivalent to the Coulomb criterion for incompressible, plane-strain deformation:

$$J_2'^{1/2} = P\,(1-\lambda)\,\sin\varphi_0 + C\,\cos\varphi_0 \tag{5.5}$$

where $J_2' = \frac{1}{2}\sigma_{ij}'\,\sigma_{ij}'$ is the second invariant of the deviatoric stress ($J_2'^{1/2}$ is the yield stress), λ is the pore-fluid pressure ratio (ratio of fluid pressure to mean stress; note that this differs from the Hubbert-Rubey definition of λ_{HR}, the ratio of fluid pressure to lithostatic pressure), φ_0 is the internal angle of friction and C is the cohesion. The effects of pore-fluid pressure on the material strength can alternatively be considered to be included in an effective angle of friction $\sin\varphi_e{=}(1-\lambda)\sin\varphi_0$ that describes the strength of the fluid-saturated sediments. When fluid pressures are hydrostatic, λ is approximately 0.4-0.5. Fluid overpressures increase λ to >0.9, and at λ=1, when fluid pressure equals lithostatic pressure, the fluid-filled sediments have effectively no strength (other than cohesion).

The plastic flow at yield is also described by equations (5.1) to (5.4) but in this case the effective viscosity is stress dependent:

$$\eta_e = \frac{1}{2}\left(\frac{J_2'}{\dot{I}_2'}\right)^{1/2} \tag{5.6}$$

where $\dot{I}_2' = \frac{1}{2}\dot{\varepsilon}_{ij}'\,\dot{\varepsilon}_{ij}'$ is the second invariant of the deviatoric strain rate (*Willett*, 1999). By assigning this numerical viscosity to a material at yield, it is assured that the flow stress satisfies the yield condition (equation 5.5).

Salt (here to first order considered pure halite) is treated as a linear viscous material with constant viscosity, η, and no cohesion. Viscous material has no yield strength.

Compaction

Compaction of model sediments is achieved through a prescribed density-depth dependence (*Korvin*, 1984), that reflects porosity reduction with increasing burial depth z:

$$\rho_{sed} = \rho_g - (\rho_g - \rho_w)\,\Phi_0\,e^{-c\,z} \tag{5.7}$$

where ρ_{sed}, ρ_g, and ρ_w are the densities of the fluid-filled sediment, the grain matrix, and the pore fluid, respectively. Φ_0 is the initial surface porosity and c is the compaction coefficient. The current density of each sedimentary finite element is calculated in each timestep depending on its burial depth z. Densities increase with burial but do not decrease during exhumation, becasue sediments are assumed not to decompact. In addition, in order to account for mass loss as fluid is expelled, the volume of each element decreases kinematically by vertical contraction as the density increases. It is assumed that expelled fluids are lost from the system, but mass of the grains and of the remaining pore fluid is conserved. Horizontal compaction likely also occurs in the natural systems, but it is not taken into account. Effects of compaction on sediment strength or coupling with pore-fluid pressures are not included except in that the pressure includes the effect of increasing density with burial depths (equation 5.5). Other model materials (salt, crust) have constant densities, are thereby incompressible.

Geometry, Isostasy, and Sedimentation

The numerical models presented here represent a simplified continental margin setting in which a layer of salt is overlain by pre-existing and aggrading/prograding sediments. A detailed description of the model geometry is given in section 5.3 and listed in Table 5.1. The entire system is submarine. The weight of the water column is applied as a force acting normal to the seafloor, thereby increasing the solid and fluid pressures within the model materials. The initial model configuration is in local isostatic equilibrium. During the model evolution additional and redistributed loads, exerted by sediments, salt and water, are isostatically compensated at each

timestep using an elastic beam at the base of the model with flexural rigidity D and an underlying inviscid fluid with density ρ_m.

The model bathymetry $z_{sed}(x)$ (positive upward) is determined according to the chosen sedimentation model (Figure 5.6). A prograding shelf-to-slope sedimentary wedge is represented by a profile with a half-Gaussian shape

$$z_{sed}(x) = \begin{cases} 0 & x \leq x_s \\ h_w \, exp\,(-(\frac{x-x_s}{w})^2) & x > x_s \end{cases} \tag{5.8}$$

where h_w is the total increase in water depth across the margin, w is the width of the slope region, and x_s is the location of the edge of the shelf (Figure 5.6a).

Sediment progradation is treated kinematically by translating this profile horizontally at a prescribed rate v_{prog} and filling of accommodation space within the model domain below the profile with compacting sediments. Sediments above the profile are not eroded.

Aggradation is modeled similarly by using a sedimentation profile that moves vertically at rate v_{agg}. The position of this profile is calculated incrementally relative to the position of the model surface of the previous time step (Figure 5.6b)

$$z_{sed}(x,t) = z_{sed}(x_0, t - \Delta t) + v_{agg} \cdot \Delta t \tag{5.9}$$

where Δt is the incremental time step and x_0 is the position at which the aggradation profile is calculated. x_0 is chosen to be at the distal end of the model domain, which is not affected by deformation but only by the processes of isostatic adjustment and vertical compaction which are laterally uniform here. The aggradation profile is defined relative to its previous position so that the sediment surface moves upward at the aggradation rate v_{agg} but the effective rate of sediment thickening is larger due to isostatic response to the sediment load.

All sedimentation models used here completely fill the accommodation space below the prescribed sedimentation profile, possibly leading to locally unreasonably high sedimentation rates. Given the multiple factors that may influence the system's strain rates and behavior, it is here assumed that the sedimentation pattern is not directly biasing the model result and constitutes a valid, simplified model of sediment

deposition on a continental margin.

Models described in sections 5.4, 5.5.2 and Appendix 5.9 include a first-order idealization of uneven sediment aggradation. A sinusoidal modulation, $S(x)$, is added to the aggradation profile described above to represent the effects of local to regional bathymetric features such as channel-levee systems or submarine lobes (Appendix 5.9). The modified aggradation profile is defined between locations x_1 and x_2 (Figure 5.6c) by

$$z_{sed}(x,t) = z_{sed}(x_0, t-\Delta t) + v_{agg} \cdot \Delta t + S(x) \tag{5.10}$$

$$S(x) = \begin{cases} 0 & x \le x_1 \\ \frac{A}{2} \cdot \sin(2\pi \frac{x-x_1}{L}) * \frac{x-x_1}{T} & x_1 < x < x_1 + T \\ \frac{A}{2} \cdot \sin(2\pi \frac{x-x_1}{L}) & x_1 < x < x_2 \\ \frac{A}{2} \cdot \sin(2\pi \frac{x-x_1}{L}) * \frac{x_2-x}{T} & x_2 - T < x < x_2 \\ 0 & x \ge x_2 \end{cases} \tag{5.11}$$

where A and L are the peak-to-trough range and wavelength of the sinusoid, respectively. The sinusoidal perturbation tapers off linearly at either end over a length T.

Models described in section 5.5.2 additionally include a tilt of the aggradation profile (Figure 5.6d) so that

$$z_{sed}(x,t) = z_{sed}(x_0, t-\Delta t) + \frac{\Delta h}{x_0}(x_0 - x) + v_{agg} \cdot \Delta t + S(x) \tag{5.12}$$

where x_0 is again the position relative to which the aggradation profile is calculated and $\frac{\Delta h}{x_0}$ is the gradient of the profile. Models in which the tilt of the aggradation profile changes use the following bathymetric profile (Figure 5.6e)

$$z_{sed}(x,t) = z_{sed}(x_0, t-\Delta t) + \frac{v_{agg} \cdot t}{x_0}(x_0 - x) + S(x). \tag{5.13}$$

If progradation and aggradation both occur, the higher of the two sedimentation profiles is chosen as the filling-level for sediments. This choice is made before the profile is modulated. The sinusoidal perturbation is not included in models with both progradation and aggradation (section 5.4).

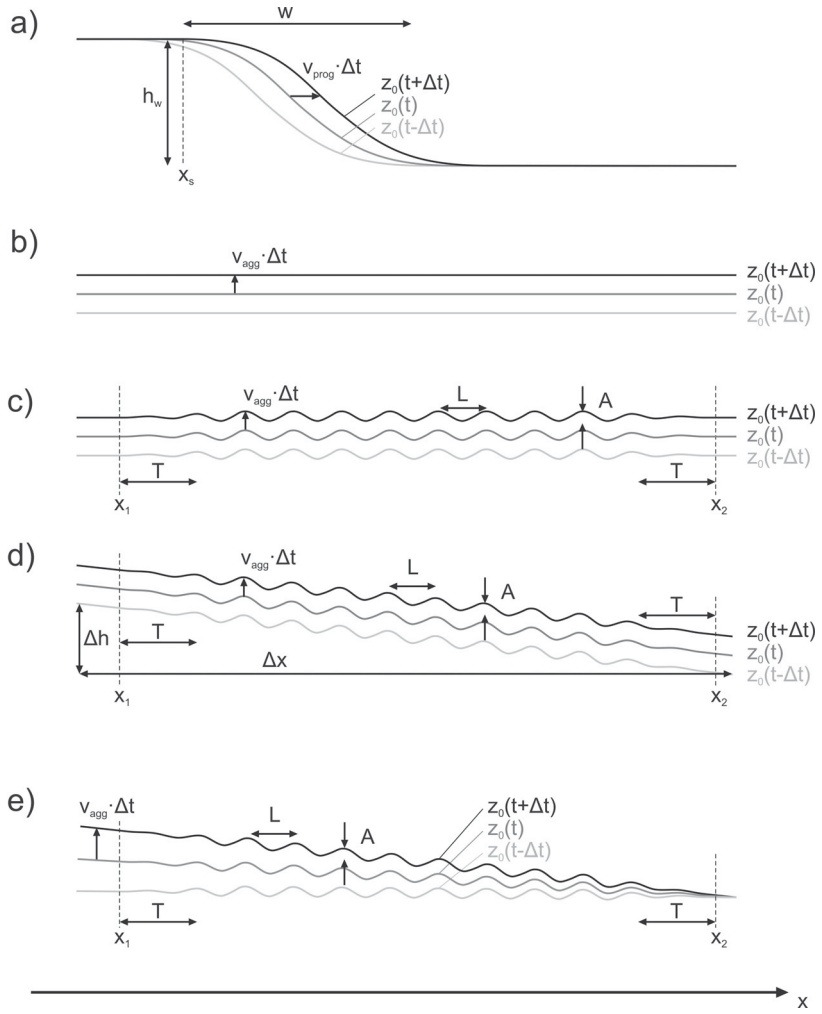

Figure 5.6: Schematic diagrams of sedimentation types used. All types consist of a sedimentation profile up to which sediment is added. (a) Progradation profile. (b) Aggradation profile. (c) Aggradation profile modulated by a sinusoid. (d) Tilted aggradation profile modulated by a sinusoid. (e) Rotating profile modulated by a sinusoid.

5.3 Model Design

Two of the canopy mechanisms investigated in this study require the existence of diapirs prior to salt expulsion onto the seafloor (section 5.4 and 5.5.2). Their initiation and evolution is still debated (*Hudec et al.*, 2009; *Ings and Beaumont*, 2010) and cannot be thoroughly addressed in this study of canopy evolution. Nevertheless, a starting model with pre-existing diapirs is needed in order to investigate mechanisms of canopy evolution. Such a starting model must not contain artificial stress regimes that affect the subsequent phase of canopy development, such as a salt-sediment system in disequilibrium. A starting configuration is therefore chosen that has been dynamically modeled, as described in Appendix 5.9. Here, a new concept of diapir evolution is employed, which is based on uneven sedimentation and operates in a neutral stress regime. These conditions assure that the models evolve continuously and with no abrupt change towards the phase of canopy evolution and permit an independent investigation of the different concepts described in section 5.1.2. The evolution of diapirs (termed phase 1) is only summarized here and discussed in more detail in Appendix 5.9. The subsequent phases of sedimentation that lead to canopy evolution (phase 2) are discussed in the respective sections 5.4 and 5.5.

5.3.1 Model Design and Diapir Evolution

All models consist of a salt basin encased by non-deforming material, onto which sediment are subsequently deposited (Figure 5.7). The salt basin geometry (salt basin width, thickness, and seaward taper) was chosen to be similar to the authochthonous salt basin in the northwestern GoM (Figure 5.2a) (*Peel et al.*, 1995; *Diegel et al.*, 1995; *Hall*, 2002). The 2 km initial salt layer thickness is likely a minimum estimate for this region (*Diegel et al.*, 1995; *Trudgill et al.*, 1999).

The salt is assumed to be halite with uniform viscosity (η=10^{18} Pa s) and constant density (ρ_{salt}=2150 kg/m^3). The encasing material (syn-rift sediments or crustal basement) as well as the sediments are frictional-plastic materials with an internal angle of friction of φ_0=25°. The pore-fluid pressure is assumed to be hydrostatic (pore-fluid pressure ratio λ approximately 0.45), such that effective internal angle of friction φ_e

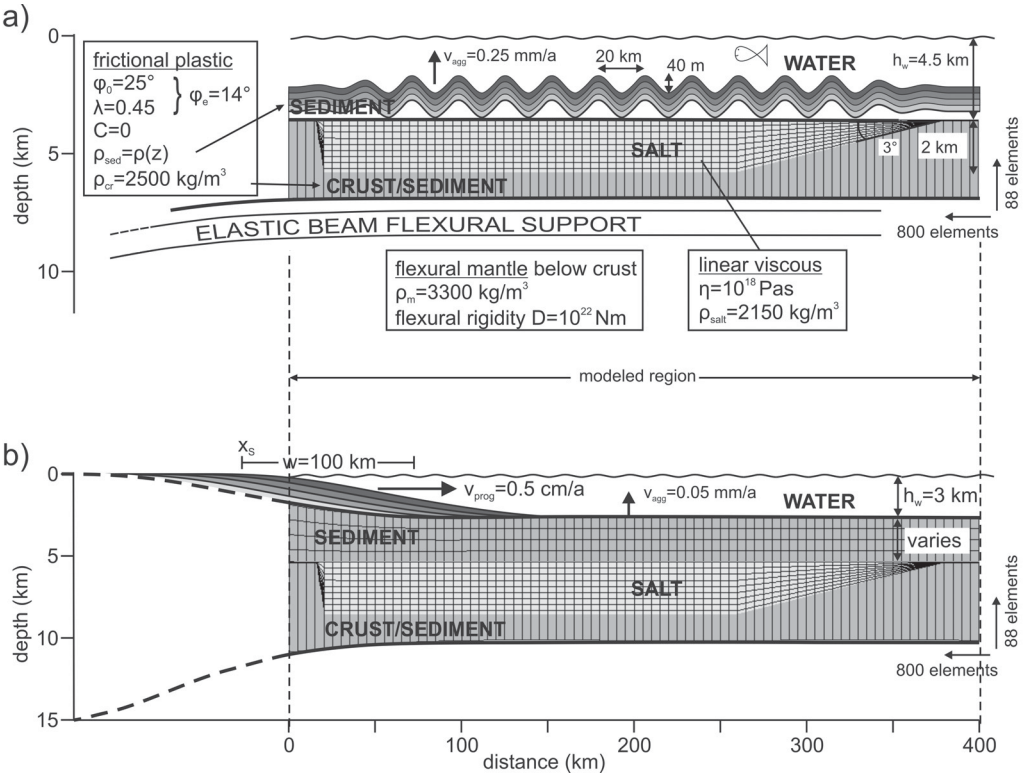

Figure 5.7: Design of model experiments. A 360 km-wide, 2 km-thick salt basin is embedded in synrift sediment/crustal sequence and progressively overlain by sediments. The model includes sediment compaction, parametric effects of pore-fluid pressures, isostatic adjustment, and the loading effects of the water column. (a) Model design for diapir phase. Aggradation occurs following a sinusoidal profile (shown strongly exaggerated). (b) Model design for canopy phase. Sedimentation occurs following a prograding, half-Gaussian profile. For a full list of model parameters and their discussion see section 5.3 and Table 5.1.

Table 5.1: Material properties of numerical models.

Parameter	Symbol	Unit	reference value	differing value	differing for model
Sediment					
sediment density	ρ_{sed}	kg/m^3	$\rho_g - (\rho_g - \rho_w)\,\Phi_0\,exp(-cz)$		
sediment grain density	ρ_g	kg/m^3	2500	2700*	D4*
pore-fluid/ water density	ρ_w	kg/m^3	1000	-	-
initial porosity	Φ_0		0.4	-	-
compaction coefficient	c	1/m	$7 \cdot 10^{-4}$	-	-
internal angle of friction	φ_0	°	25	-	-
pore-fluid pressure ratio	λ		hyd.	0.8	BA1
effective angle of friction	φ_e	°	≈14	≈5	BA1
cohesion	C	MPa	0.0	-	-
Salt					
density	ρ_{salt}	kg/m^3	2150	-	-
viscosity	η	Pa s	10^{18}	$5 \cdot 10^{18}$	BA1
Crustal/Synrift Material					
density	ρ_{cr}	kg/m^3	2500	-	-
internal angle of friction	φ_0	°	25	-	-
pore-fluid pressure ratio	λ		hyd.	0.5	BA1
effective angle of friction	φ_e	°	14	5	BA1
cohesion	C	MPa	0.0	-	-
Lithosphere					
density	ρ_m	kg/m^3	3300	-	-
flexural rigidity	D	Nm	10^{22}	-	-
Initial Salt Basin					
thickness	h_c	m	2000	-	-
width	w	km	360	2x100	ER1
of which tapered		km	60	0	ER1
initial taper angle	α	°	1	90	ER1
Sedimentation Profile (aggradation phase of models D1, ER2, ER3, D2-D4*)					
amplitude of sinusoid	A	m	20	5*	D3*,D4*
wavelength of sinusoid	L	km	20	50	ER2,ER3
start, end of perturbation	x_1, x_2	km	20,350	20,150	SD3
taper of perturbation	T	km	20	-	-
tilt of aggradation profile		°	-	0.07/0-3	ER2/ER3
aggradation rate	v_{agg}	mm/a	0.25	0-0.5/0.5*	ER3/D2*
Sedimentation Profile (progradation phase of models SD1-SD3, ER1, BA1)					
width	w	km	100	200/50	ER1/BA1
initial max. water height	h_w	km	4	3.5/3	ER1/BA1
final max. water height	h_w	km	3	3.5	ER1
progradation rate	v_{prog}	mm/a	5	2	ER1
aggradation rate	v_{agg}	mm/a	0	0.05	SD1-SD3
Finite Element Grid					
width		km	400	-	-
number of elements (horizontal x vertical)			800 x 88	-	-
width of elements		m	500	-	-
time-stepping length	Δt	a	$5{\cdot}10^3$-10^4	-	-

* models shown in Appendix 5.9

is approximately 14° ($\sin\varphi_e = (1-\lambda)\sin\varphi_0$, section 5.2). Cohesion is not considered in order to simplify the model.

Sediments compact following a depth-dependent density curve (Figure 5.8 and equation 5.7) which was calibrated using data derived from several well data sets from the GoM (Table 5.1, *Jackson and Talbot*, 1986). With this compaction curve the local sediment density equals that of salt (2150 kg/m^3) at a depth of 770 m, and the average density of the sediment column equals that of salt when the compacted thickness is 1710 m. The encasing material has a constant density of ρ_{cr}=2500 kg/m^3.

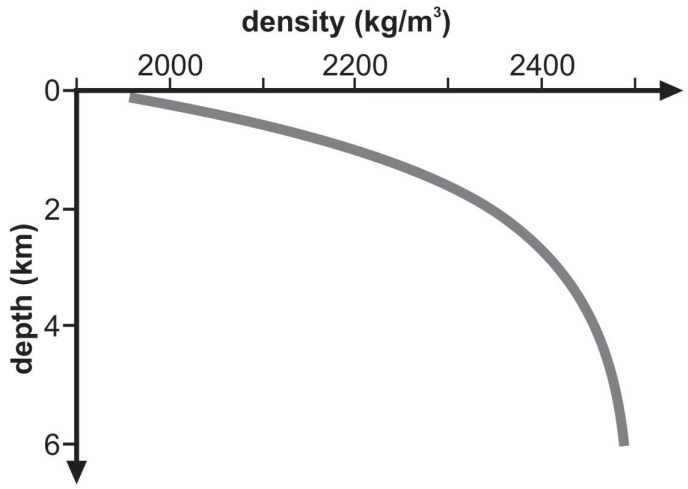

Figure 5.8: Average compaction trend for sediments in the Gulf of Mexico used in the numerical models. Curve simplified from *Jackson and Talbot* (1986) with sediment density defined as $\rho_{sed} = \rho_g - (\rho_g - \rho_w)\,\Phi_0\,exp(-cz)$, where grain density ρ_g=2500 kg/m^3, pore fluid density ρ_w=1000 kg/m^3, initial porosity Φ_0=0.4 and compaction coefficient c=0.0007 m^{-1}. z is burial depth.

Sediment deposition occurs according to a sinusoidally modified aggradation profile (equation 5.10) or by a combination of progradation and uniform aggradation (equations 5.8 and 5.9). The first is employed during phase 1 (the diapir phase); the sinusoidal perturbations remain stationary, so that a constant bathymetric relief is maintained. Local isostatic balancing of these bathymetric highs drives flow of the underlying salt. Continuing sedimentation sustains the pressure differences, which, assisted by the evolving density contrast between salt and compacting sediments, can eventually lead to diapir evolution. A detailed analytic description of this process as well as corresponding model experiments are given in Appendix 5.9.

Figure 5.9 shows model D1 (D ≡ Diapir) of diapir evolution after 5 and 10 Ma m.t. (Ma m.t. ≡ million years model time). The geometric values of the aggradation profile were chosen to facilitate diapir evolution (peak to trough range A=40 m, wavelength L=20 km, aggradation rate v_{agg}=0.25 mm/a) and are likely on the far end of the values of natural systems (Appendix 5.9). After 5 of aggradation (Figure 5.9a), salt highs have grown nearly 2 km tall, their roofs are covered by a thin (300 m thick) sedimentary layer. The sediment pockets between the diapirs (minibasins) have grown continuously, and where they are thickest their average density has reached that of the underlying salt. During subsequent evolution (Figure 5.9b) the diapirs grow narrow and tall (nearly 4 km), and the minibasins are close to grounding. The asymmetry evident from the minibasins likely results from the minor, overall asymmetry of the model or from numerical uncertainties (Appendix 5.9).

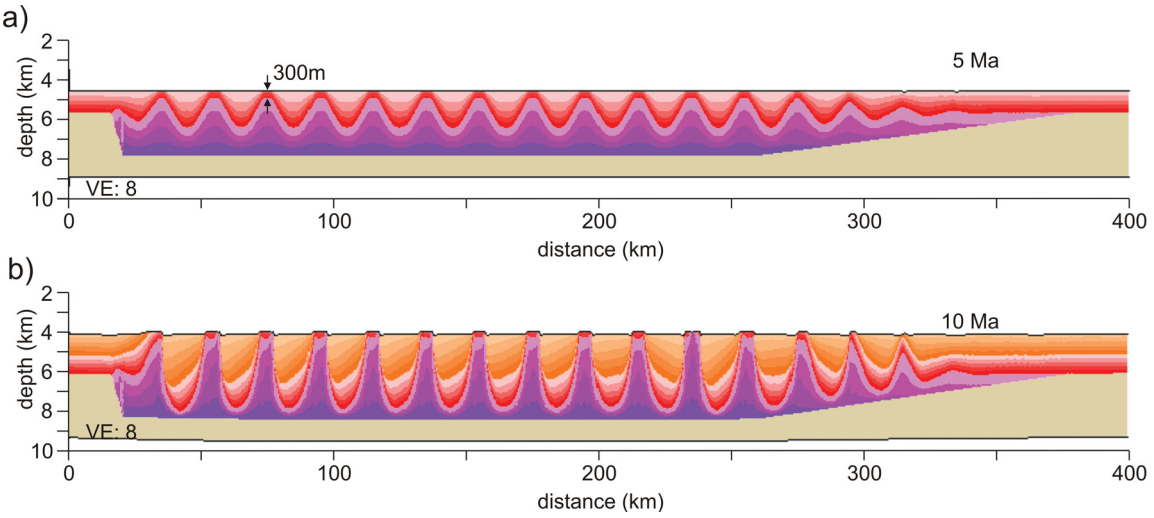

Figure 5.9: Results from model D1 (reference model for diapir evolution) with aggrading sedimentation with sinusoidal bathymetric perturbations that have constant amplitude (A=40 m) and wavelength (L=20 km). See text for details of model evolution. The color scale shows the chronostratigraphy of the sediments in 1 Ma m.t. bands. Salt is colored in magenta, synrift/crustal material in light brown. Same color coding is used in all subsequent model figures.

Model D1 demonstrates that uneven sedimentation that preserves bathymetric features can drive diapirism if appropriate values of the control parameters are chosen. Discussion and sensitivity of these parameters as well as a quantitative assessment of the sedimentation-driven diapir mechanism is given in Appendix 5.9. The diapirs of model D1 serve as precursory structures for the subsequent evolution of canopies,

without introducing an additional stress regime or requiring a change of material properties. It should nevertheless be pointed out that this diapir evolution may be only one of several mechanisms that could produce the precursory structures required for subsequent canopy evolution.

5.4 Canopy Mechanism I: Squeezed Diapirs

5.4.1 Model Design

The following numerical experiments, designed to investigate canopy evolution by diapir squeezing, combine diapir model D1 (termed phase 1) with progradational sedimentation (termed phase 2). Progradation follows a half-Gaussian profile (section 5.2, equation 5.8) with a Gaussian slope width of w=100 km and an initial maximum water depth of ca. 4 km. Aggradation following a strictly horizontal profile occurs coevally with a rate of $v_{agg} = 0.05$ mm/a. Water depth decreases during the model evolution from approximately 4 km to 3 km and is thus intermediate between the water depths of 4-5 km estimated for the late Cretaceous GoM (*Winker and Buffler*, 1988) and current water depths of 2-3 km. The aggradation profile is now strictly horizontal, no sinusoidal perturbations are included. The slope profile is initially located outside the model domain and progrades onto the salt basin at a rate of v_{prog}=5 mm/a, slightly higher than the Cenozoic average of 4 mm/a (*Galloway et al.*, 2000). All other parameter values are the same as in model D1.

Three models are discussed here. Model SD1 (SD ≡ squeezed diapir) uses model D1 at 10 Ma m.t. as a starting configuration. Model SD2 is identical to model SD1 except that the starting configuration is model D1 at 5 Ma m.t. Model SD3 is a variation of model SD1, in which the sinusoidal undulations during phase 1 are confined to the landward end of the salt basin (extending from 20-150 km). The motivation to restrict the diapir evolution to the landward part of the salt basin was to impede the development of allochthonous salt structures in the distal part. It is also more realistic because seafloor sediment undulations in natural systems are likely larger in more proximal settings like near the toe-of-slope. All model parameters of models SD1-SD3 are listed in Table 5.1.

5.4.2 Results of Model SD1

The evolution of model SD1 is shown in Figure 5.10 and Animation_SD1.wmv[1]. Prograding sediments reach the salt basin after ca. 5 Ma m.t. of phase 2, and gravity spreading begins soon after (Figure 5.10a), marked by extensional faulting and a growth wedge at the landward end of the basin. Shortening occurs in a region spanning nearly 100 km beyond the toe of the slope, where diapirs become squeezed and minibasins are rotated and become asymmetric (Figure 5.10a).

After an additional 7 Ma m.t. of sediment progradation and gravity spreading (Figure 5.10b), a large rollover structure develops along the flank of the most proximal diapir (later a feeder and its weld). This diapir is progressively deformed and squeezed seaward by the prograding sediment wedge. All three landward-located salt rollers in Figure 5.10b originate from this same diapir. The salt of the adjacent diapirs has extruded onto the seafloor and three of the sheets have begun to coalesce into a canopy. As each salt sheet advances over the sediments of the adjacent minibasin, the sediments sink deeper into the underlying salt, thereby expelling more salt laterally and into the salt sheet. This leads to a rotational swapping of positions of salt sheet and minibasin fill (Figure 5.10b).

After an additional 13 Ma m.t. (Figure 5.10c), a ca. 50 km long canopy has developed. The minibasins, which were rotated during regional shortening, have rotated back into their original position in the landward end of the system and the intervening feeders have closed. The most proximal minibasins have been inverted into turtle structures. Extension is now accommodated along a several tens of kilometers long detachment system, located partly on autochthonous salt (translation of turtle structures) and partly on allochthonous salt (faults soling out into it).

5.4.3 Results of Model SD2

In model SD2, prograding sediment at the landward end of the salt basin (phase 2) arrives 5 Ma m.t. earlier than in model SD1, when the diapirs are not yet as well developed. Figure 5.11 shows model SD2 at the same times in model evolution (relative to phase 1) as those shown in Figure 5.10 of model SD1. Gravity spreading again begins a few Ma m.t. after the prograding sediment wedge has reached the salt basin.

[1]Supplementary material is provided as electronic attachments and is described in Appendix D.

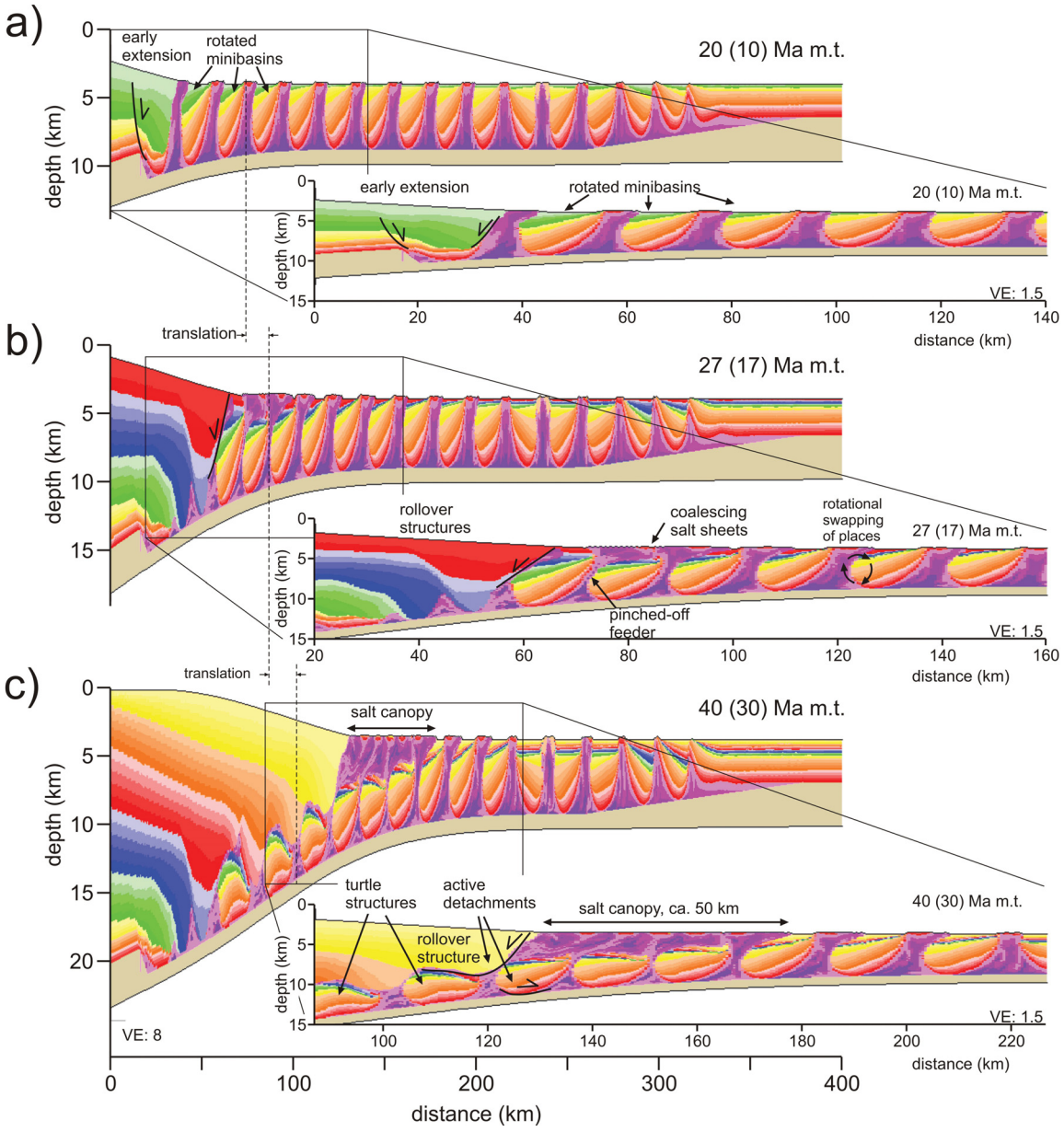

Figure 5.10: Results of model SD1 (reference squeezed-diapir model for canopy evolution). Starting configuration is model D1 at 10 Ma m.t. Time denotes elapsed model time. Time in parentheses denotes time since onset of progradational sedimentation. Open arrows indicate relative displacement. See text for discussion.

At this time, diapirs are less mature than in model SD1, minibasins are less deep and the autochthonous salt layer is still more than 1 km thick (Figure 5.11a). Further differential sedimentation leads to a wide zone of landward extension (Figures 5.11b and c) as it was also observed in model SD1. Compression, however, is accommodated by shortening of the minibasins and inflation of the underlying autochthonous salt layer. Diapirs cease to evolve and no allochthonous salt structures develop.

The distal diapirs and minibasins still grow throughout the model evolution although no sinusoidal variations of the sedimentation profile were included. This shows that the density contrast between salt and sediment is large enough for successful diapir growth driven by a combination of buoyancy and sedimentation at the seaward end of the system. In contrast, compression at the landward end of the system inhibits minibasin development because the uplift rate, generated by the thickening salt, likely exceeds the buoyancy-driven sinking rate. Consequently, the sea floor is above the prescribed sedimentation profile and no sediment deposition occurs in the model.

5.4.4 Results of Model SD3

Because sinusoidal sedimentation is restricted to the landward part of the salt basin during phase 1 of model SD3, diapirs only develop in the landward parts of the model while the distal domain remains undeformed. As in model SD1, progradation commences after a 10 Ma m.t. long aggradation phase (phase 1), the sediment wedge reaches the salt basin after ca. 5 Ma m.t. of progradation and gravity spreading begins soon after (Figure 5.12a). Diapirs are again squeezed during regional shortening and salt extrudes to the seafloor and coalesces into a canopy (Figure 5.12b). Minibasins again rotate during shortening and rotate back to form turtle structures below and behind the landward end of the canopy. Sedimentation is accommodated in several large growth wedges which represent rollover structures in the extensional domain.

The sediments within the seaward half of the salt basin remain nearly undeformed during the first 25 Ma m.t. Merely the sediment carapace directly adjacent to the diapir domain is slightly elevated owing to moderate inflation of the underlying salt layer. Shortening has been accommodated in the relatively narrow diapir-minibasin domain during this time. After 30 Ma m.t. of progradation the distal sediments are

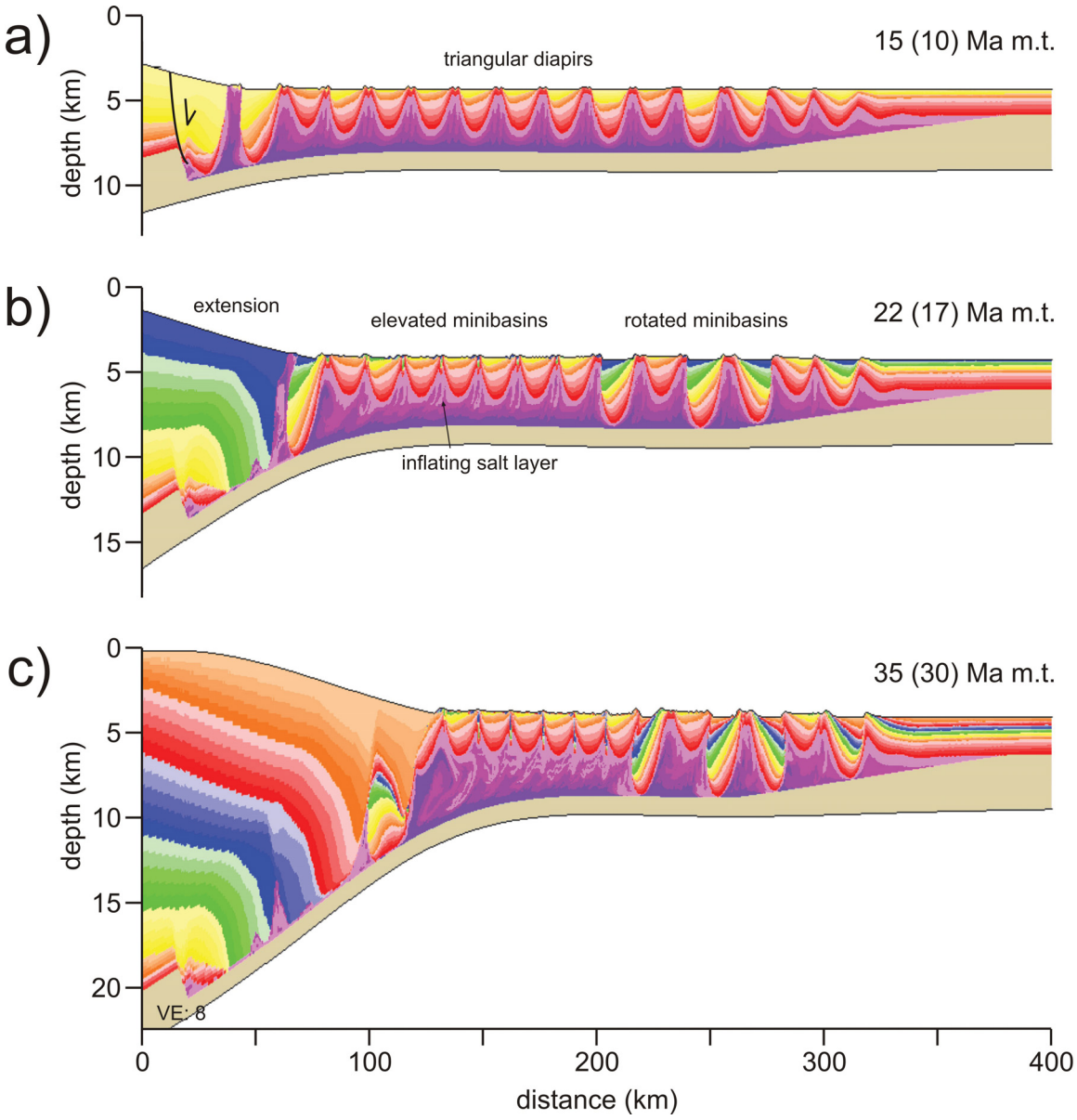

Figure 5.11: Results of model SD2 (squeezed-diapir model with shorter diapir phase). Starting configuration is model D1 at 5 Ma m.t. Time denotes elapsed model time. Time in parentheses denotes time since onset of progradational sedimentation. Open arrows indicate relative displacement. See text for discussion.

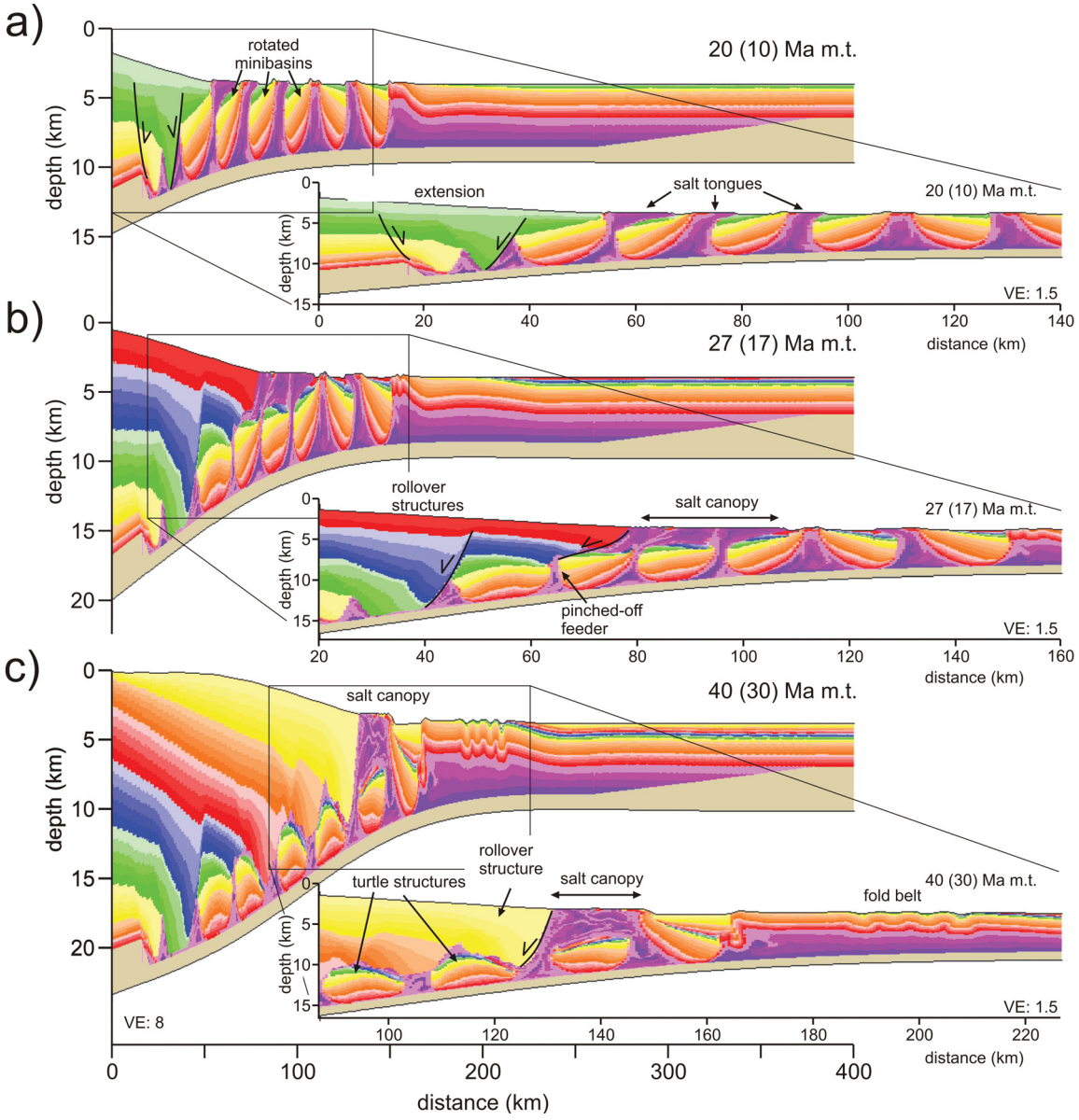

Figure 5.12: Results of model SD3 (squeezed-diapir model with landward diapirs only). Time denotes elapsed model time. Time in parentheses denotes time since onset of progradational sedimentation. Open arrows indicate relative displacement. See text for discussion.

eventually folded into a ca. 20 km wide fold belt. The canopy in model SD3 is initially >20 km wide (Figure 5.12b) but narrows during the later evolution of the model (Figure 5.12c) and never grows as large as the canopy in model SD1.

5.4.5 Discussion of Models SD1-SD3

Squeezing of Diapirs

The model results demonstrate that shortening induced by gravity spreading first localizes in the diapirs, which accordingly narrow and expel salt. In the two contrasting cases of models SD1 and SD2 (Figures 5.10 and 5.11), in which gravity spreading occurs when the minibasin-diapir system is 'mature' and 'immature', the squeezed salt is respectively expelled upward onto the seafloor or is pushed downward into the underlying salt layer, which consequently inflates as the diapirs narrow. In the latter case, no allochthonous salt structures develop. The key to this difference is the pressure that develops in the salt and that also acts on the minibasins. If the pressure in the autochthonous salt layer exceeds the weight of a minibasin, the minibasin will float upward as the underlying salt layer thickens and the adjacent diapirs thin (Figure 5.11). This process is not only controlled by the minibasin weight but is also facilitated if the salt is thick below the minibasin and impeded if the minibasin is grounded. If the upward velocity of the minibasin exceeds the model's aggradation rate, no sediment is deposited in the basins. The basins merely float upward until the total pressure is in equilibrium with the weight of the system (Figure 5.11). In contrast, more mature systems have minbasins that are too heavy to be floated by the squeezing pressure or the underlying salt layer is too thin to inflate efficiently. These minibasins continue to sink or remain grounded while the system shortens (Figures 5.10). The excess pressure leads to a rise of salt within the diapirs that accordingly stretch vertically and narrow. The transfer of the stress to the top of the diapirs causes failure between the minibasin and the roof of the diapir, a necessary precursor to expulsion of salt to the surface. Both sinking and floating behaviors are seen in model SD2, where some minibasins were sufficiently mature to overcome the tendency to float upward as the salt thickens (right-hand side of Figure 5.11).

Additional models that are not shown here suggest that the shape of diapirs, in particular the steepness of their flanks, can also influence the creation of allochthonous

salt structures. Salt from diapirs with less steep flanks and a more triangular shape (e.g., model D2 of Appendix 5.9) tends to be pushed downward during compression whereas salt from more rectangular shaped diapirs with steeper flanks (e.g., model D1 or D4 of Appendix 5.9) is more easily expelled upwards.

Diapir squeezing will be influenced by the lateral flow velocities of the unstable part of the system and the corresponding horizontal strain rates. These are controlled, e.g., through the sedimentation profile, the rate of progradation, or the mobility of the system (*Gemmer et al.*, 2004), but these factors are not investigated in further detail here.

Canopy Formation

Salt expelled onto the seafloor in models SD1 and SD3 forms large canopies of several tens of kilometers. The advance of the salt sheets is not only driven by the ≈200 m bathymetric expression of the expelled salt, but by the thickness of several kilometers of the entire salt sheet. A positive feedback loop exists between the advance of the overlying salt sheet and the subsidence of the minibasins that are located at the toe of the salt sheet: The advancing salt sheet exerts extra load on the minibasins, whose sinking in turn provides the necessary space and also expels additional salt from underneath as long as the feeders remain open. This is similar to the Rayleigh-Taylor instability behavior when the less dense material rises and flows on top of the denser material. Corresponding systems evolving in a neutral stress regime (models D1-D4 of Appendix 5.9) do not exhibit this behavior.

As described in section 5.1.2, salt-sheet advance has so far only been associated with the propagation of the thinning salt tip (*Hudec and Jackson*, 2006). The contemporaneous movement of the underlying sediments together with expulsion of the autochthonous salt, which can create new space for the advancing salt sheet, provides a new concept that has not yet been considered in the salt-tectonic literature.

The location and extent of the early diapir region exerts a primary control on the location and extent of the allochthonous salt structures (compare model SD1 and SD3), because diapirs must exist before they can be squeezed to produce salt sheets. The amount of shortening naturally also controls the amount of salt expulsion. The more subtle aspect is that salt expulsion also depends on the timing of squeezing

in relation to the diapir growth (maturity). Variable diapir maturity across the salt basin (also controlled by the landward sediment input) may determine the salt sheet distribution and ultimately the way they coalesce into canopies.

5.5 Canopy Mechanism II: Expulsion Rollover

The aim of the expulsion rollover models is to investigate under which circumstances a canopy can evolve in the center of a salt basin in a neutral regional stress regime (section 5.1.2). Two cases are investigated exploring regional and local differential sedimentation.

5.5.1 Large-Scale Expulsion Rollover

Following the analogue model design of *Ge et al.* (1997), a basement high is included in the salt basin of the numerical experiments to buttress salt flow and initiate a salt diapir during sediment progradation (section 5.1.2). The experiments include basement highs of variable heights, centered in the salt basin. Salt inflates next to the basement high and flows over it but is never extruded onto the seafloor unless the basement high fully separated the salt into two sub-basins. This end-member model is described below, followed by the possible reasons for the failure of the other models to develop allochthonous salt structures.

Model Design

Model ER1 (ER ≡ expulsion rollover) comprises two salt basins (each 2 km thick and 100 km wide) separated by a 20 km wide basement high of rectangular cross-section (Figure 5.13). The salt basins are not tapered as in the previous models to avoid slowing of the salt flow out of the basin by the thinning salt channel. The salt layer is overlain by an initial 300 m thick sediment layer and a water column of 4 km. The densities and rheologies of the model materials are the same as in the earlier models and as listed in Table 5.1.

Sedimentation is modeled using a prograding half-Gaussian profile (w=200 km, h_w=4.5 km, v_{prog}=2 mm/a) that intersects the top of the initial salt and sediment layers (Figure 5.13) to achieve a relatively steep front to the sediment wedge that can

drive salt expulsion efficiently. Progradation rate is low (2 mm/a) to allow for efficient salt flow. No sediment aggradation is included because a thickening sediment layer above the basement high would inhibit salt expulsion. This sedimentation pattern follows the principle that a distal margin setting only experiences minor, pelagic sedimentation.

Results of Model ER1

After 50 Ma m.t. (Figure 5.13a) the prograding sediment wedge has evacuated the salt from the landward half of its autochthonous basin, formed a large-scale expulsion rollover and inflated the distal salt. Flexural compensation of the sediment load tilts the model landward. At ca. 55 Ma m.t. the salt has inflated to 600 m above the sediments covering the basement high and begins to flow onto it, covering two thirds of the basement high by 60 Ma m.t. (Figure 5.13b). The salt sheet is almost one kilometer thick and advances seaward at 2-3 mm/a, slightly faster than the sediment progradation rate. By 67 Ma m.t. the front of the salt sheet has sunk into the second salt basin, pushing its salt seaward and inflating it (Figure 5.13c). The salt sheet is now more than one kilometer thick and advances by shear flow with a surface velocity up to 4 mm/a.

Discussion of Model ER1

General Evolution

As model ER1 demonstrates, a large-scale expulsion rollover can expel salt into an allochthonous sheet that can become 20 km long and likely much longer. The structure formed here is a single salt sheet, not a canopy.

The advance of the salt sheet is relatively fast compared to the time it takes to begin expulsion of allochthonous salt (more than 50 Ma m.t.). This time span depends strongly on the progradation rate, initial salt layer thickness, salt basin width and salt viscosity. Values other than those used in model ER1, which could reduce the timescale of salt expulsion by several times, would still be consistent with continental margin settings such as the northwestern GoM. The timing can therefore not be used directly as a criterion to validate or discard this mechanism.

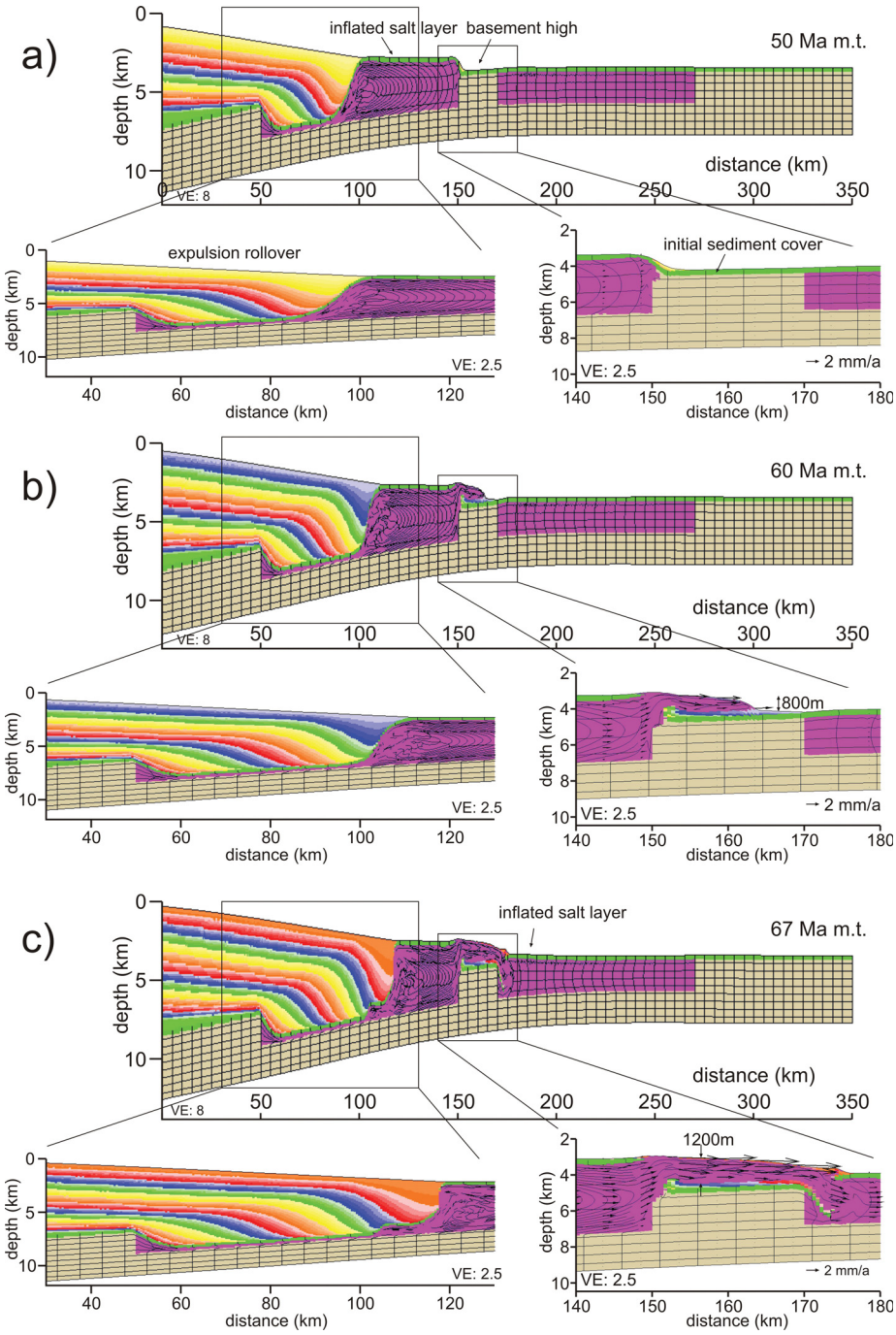

Figure 5.13: Results of model ER1 showing the evolution of a salt sheet via the large-scale expulsion rollover mechanism.

Importance of the Basement High

The evolution of allochthonous salt in model ER1 is fundamentally dependent on the presence of the basement high or an equivalent, possibly sedimentary, buttress structure that forces salt inflation. Models with lower basement highs, even just 10% less, allowed salt to flow efficiently across them after modest inflation and did not develop diapirs or allochthonous salt structures, even when the salt viscosity was increased to $5 \cdot 10^{18}$ Pa s. These results are similar to the numerical experiments of *Albertz and Beaumont* (2010), where basement obstacles required relief comparable to the thickness of the salt in order to strongly impede the salt flow. In contrast, *Ge et al.* (1997) show analogue models in which diapirs evolve above basement steps that are less than half the thickness of the surrounding salt layer.

A major difference between the analogue and numerical models is the density contrast between salt and sediments (up to 700 kg/m^3 in analogue models, 50 kg/m^3 in numerical models). This difference is likely responsible for the different capabilities for salt extrusion in the models. Analogue models with lower density contrast (300 kg/m^3) also showed no diapir or salt-sheet evolution (*Ge et al.*, 1997).

Salt-Sheet Advance

In model ER1, salt only remains at an allochthonous level where located above the basement high. Only 2-3 Ma m.t. after advancing onto the second salt basin, the underlying sediment layer fails, the salt sheet sinks and merges with the autochthonous salt of the second basin. This sinking is facilitated by the additional load, the higher density of the salt with respect to the thin sediment layer, the low mechanical strength of the sediments, and the low salt viscosity. A much thicker and stronger distal sediment cover prevents this sinking of the salt sheet into the second basin. Instead, the sediment layer over the second salt basin is depressed and evacuates the underlying salt, inflating it further seaward, similar to the evacuation of the first salt basin in model ER1. A thicker sediment cover across the entire model domain would, however, strongly inhibit the formation and advance of allochthonous salt, since the salt now has to inflate and climb higher in order to build up a sufficient pressure head.

5.5.2 Small-Scale Expulsion Rollover

Design of Models ER2 and ER3

Following the conceptual mechanism suggested by *Rowan and Inman* (2005), a number of pre-existing diapirs are covered by differential sedimentation, giving rise to asymmetric minibasins and rollover structures. The forcibly narrowed diapirs then expel salt onto the seafloor.

For the current study, diapir evolution is achieved by the mechanism introduced and discussed in section 5.3 and Appendix 5.9. The model design is initially identical to model D1 (Figure 5.9), only that a sinusoid wavelength of L=50 km is chosen in order to develop diapirs sufficiently large to form allochthonous structures. The densities and rheologies are as in the previous models and as in Table 5.1. At 10 Ma m.t., when diapirs have developed and minibasins begin to ground, asymmetric sediment aggradation commences (phase 2).

The sedimentation in model ER2 is equivalent to that of a seaward-prograding wedge with a constant slope (equation 5.12, Figure 5.6d). The tilt of the aggradation profile remains constant throughout phase 2 and the entire profile is elevated with an aggradation rate of v_{agg}=0.25 mm/a. The seaward tilt of the aggradation profile (500 m over 400 km) is of the same order as the average slope between the maximum and minimum of the sinusoidal undulations of phase 1 (40 m over 25 km). The sedimentation of model ER3 is equivalent to a seaward prograding wedge with a progressively steepening slope profile (equation 5.13, Figure 5.6e). The tilt of the aggradation profile is steadily increased such that its landward end rises at 0.5 mm/a and the profile pivots about a point located near the end of the salt basin at 350 km. The resulting taper of the sediment wedge is larger than the mere tilt of the seafloor owing to the effects of isostatic balancing. The sinusoidal modulation of the aggradation profile of phase 1 is maintained throughout phase 2 in order to facilitate salt rise.

Results of Model ER2

The diapirs developing during phase 1 (Figure 5.14a) develop more slowly than in model D1 because the isostatic relaxation time is longer owing to the longer wavelength (50 km rather than 20 km; Appendix 5.9). Approximately 700 m of sediment form the roof of the diapirs.

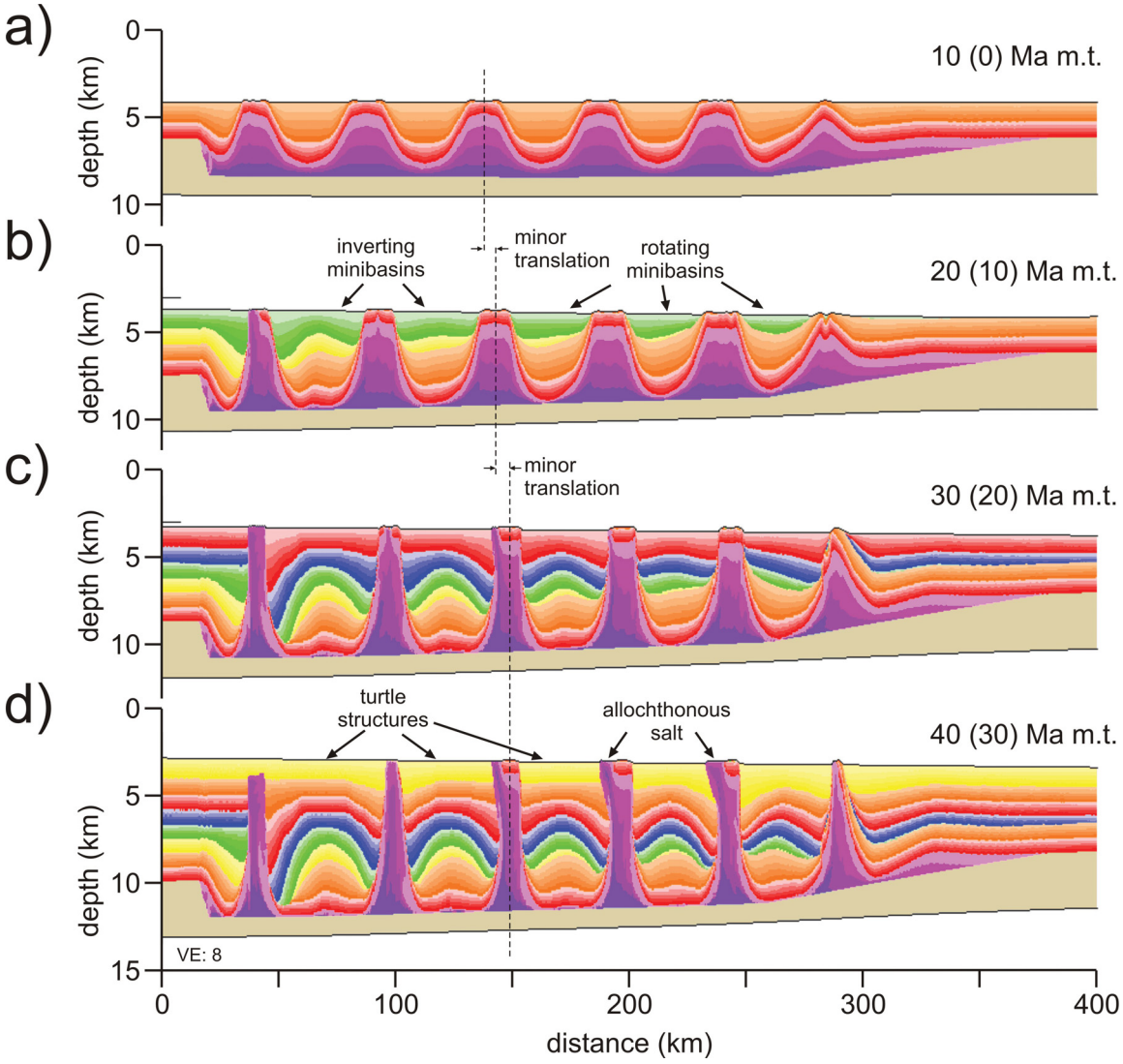

Figure 5.14: Results of model ER2 (small-scale expulsion-rollover model with constant bathymetric slope). Time denotes elapsed model time. Time in parentheses denotes time since onset of asymmetric aggradation.

After 10 Ma m.t. of gently tilted aggradation of phase 2 of model ER2 (Figure 5.14b), the two most landward minibasins are inverted into turtle structures, the

most seaward minibasins are rotated landward. During continued sediment deposition (Figure 5.14c and d), the seaward minibasins also invert into turtle structures and the salt evacuation from all minibasins becomes progressively more symmetric. The intervening diapirs grow and narrow. No asymmetric expulsion rollovers develop. The roofs of some diapirs begin to be pierced by salt after 20 Ma m.t. of phase 2 (Figure 5.14c), and salt structures form near the seafloor (Figure 5.14d). Two of these salt structures have minor allochthonous tongues. Small amounts (< 10 km) of lateral movement of the salt diapirs occur.

Results of Model ER3

Phase 1 of model ER3 is identical to that of model ER2. Like model ER2, minibasins rotate landward with initial asymmetric sedimentation of phase 2 (distal minibasins of Figure 5.15a) and subsequently evolve into turtle structures as sedimentation continues. The turtle structures retain slight asymmetry, with their landward flanks subsiding somewhat faster. The diapirs narrow and rise, leading to small bathymetric relief of less than 50 m at the seafloor.

After 20 Ma m.t. of increasingly tilted phase 2 aggradation (Figure 5.15b), the overburden has failed and the system becomes mobile. Extension is focussed in the most landward diapir where a sedimentary growth wedge forms, the more distal mininbasins and diapirs translate seaward, and, in contrast to model ER3, the previously undeformed sediment layer above the distal salt taper folds.

Discussion of Models ER2 and ER3

The mechanism of asymmetric loading of the minibasins leading to the development of expulsion rollover structures does not produce allochthonous salt structures under the conditions investigated in models ER2 and ER3, and accordingly remains conceptual. The processes that operate in these models are nevertheless discussed here to understand why no allochthonous salt structures develop and how subsequent models could be improved.

The minibasins invert to turtle structures, which can be regarded as double-sided expulsion rollovers in the case of 2D structures. The initial asymmetry of the minibasins can be explained by the effects of asymmetric loading on the subsidence of the

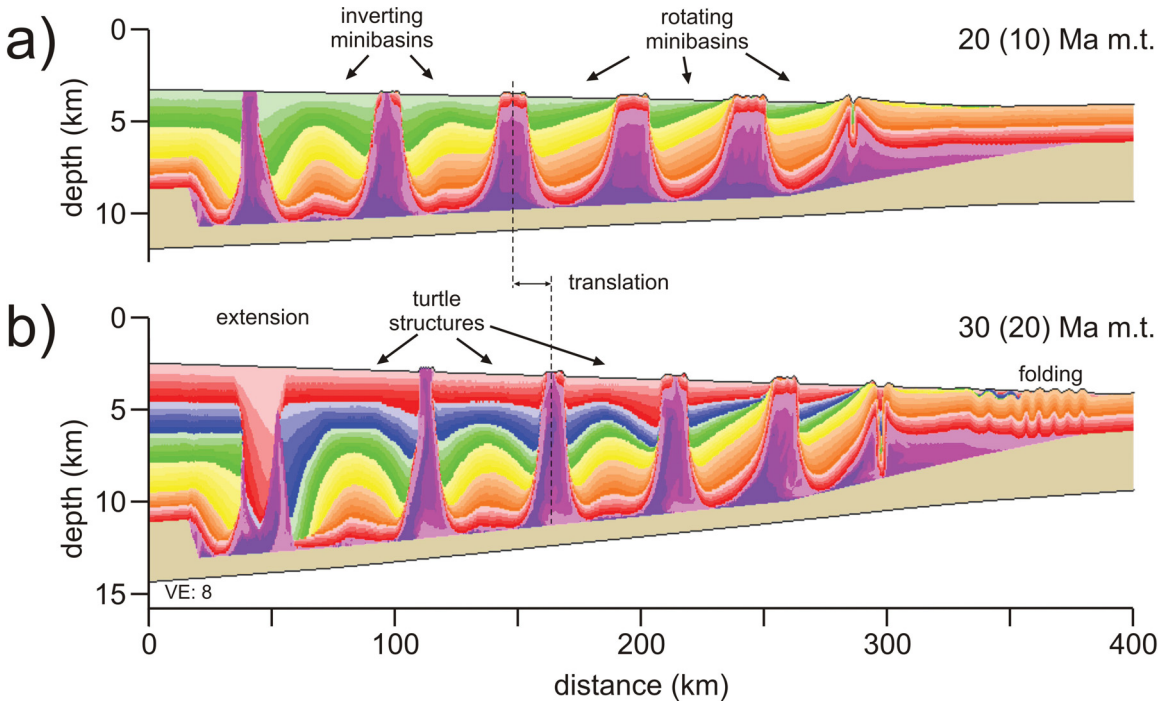

Figure 5.15: Results of model ER3 (small-scale expulsion-rollover model with growing bathymetric slope). Time denotes elapsed model time. Time in parentheses denotes time since onset of asymmetric aggradation.

minibasin flanks. The later shift towards symmetry in model ER2 represents the negative feedback effect from the thinning autochthonous salt layer underneath. Once a minibasin is grounded, its flanks spread laterally, developing a turtle structure. The highly tilted aggradation profile of model ER3 can sustain a slight asymmetry (Figure 5.15a).

Diapirs grow throughout the evolution of models ER2 and ER3. Salt initially flows into the diapirs from underneath the sinking minibasins, later it rises as the diapirs are squeezed and narrow between the widening turtle structures. The growth rate of the diapirs is here similar to the aggradation rate at the seafloor, with the result that salt does not extrude to form allochthonous structures.

The distal fold belt of model ER3 develops coeval with widening of the most landward diapir, development of extensional rollover structures here, seaward translation of the central section by approximately 20 km, and accelerated narrowing of the basin's diapirs. These events are direct evidence for gravity spreading, which suggests that the observed processes, the narrowing of the diapirs in particular, are primarily

driven by the regional, compressive stress regime. It also indicates that the mechanism of squeezed diapirs dominates over the mechanism of expulsion rollovers. A reduction of the sedimentation rate does not lead to salt expulsion, but to an equally reduced rate of salt rise. Thus, the diapirs grow synchronously with the sedimentation.

The current sedimentation model results in higher sediment deposition at the landward side of a minibasin, leading to asymmetric subsidence and landward salt evacuation. It is, however, the salt evacuation in a seaward direction that would be more efficient for seaward prograding salt sheets. A sedimentation pattern that could provide seaward salt evacuation could be based on the concept that bathymetric highs of the diapirs shelter the accommodation space from the landward sediment input. Additionally, 3D effects of sedimentation may play a strong role in the natural evolution of diapirs and minibasin. Different sedimentation models have not been tested here.

The concept of asymmetric salt evacuation by differential loading of minibasins can narrow diapirs, as the numerical models show. But they fail to expel significant quantities of salt onto the seafloor and do not generate salt sheets.

5.6 Canopy Mechanism III: Breached Anticlines

Canopy evolution through breached anticlines was modeled numerically by *Gradmann et al.* (2009). Their results are briefly described here to achieve a more complete overview on possible mechanisms of canopy evolution in the northwestern GoM, but no new models are presented.

5.6.1 Design of Model BA1

Model BA1 (BA ≡ breached anticlines) is model RM2 of *Gradmann et al.* (2009). Their study focusses on the evolution of the Perdido Fold Belt but also addresses the evolution of the Eocene mid-basin canopy. Model BA1 was designed to investigate the evolution of a canopy in the central part of a salt basin before the post-salt sediment succession in the distal part started to deform and to develop into a detached fold belt. It is also designed to be consistent with the prevailing conditions in the northwestern GoM during the Paleocene.

The mechanism of breached anticlines requires folding of strata above autochthonous salt prior to rupture of the anticlines. Shortening is localized in the center of the salt basin, where the canopy is meant to develop, through toe-of-slope folding. *Gradmann et al.* (2009) demonstrated that localization of gravity spreading-driven shortening depends on the 'strength' (resistance to flow) of the salt layer.

The large 'strength' of the salt layer in Model BA1 (Figure 5.16) is achieved using values of 2 km for salt thickness and $5 \cdot 10^{18}$ Pa s for salt viscosity. The salt basin is 360 km wide and is covered by a 4.5 km uniformly thick pre-existing sediment unit (Figure 5.16a). This unit was initially designed to represent the more seaward Cretaceous to Oligocene pre-kinematic sequence of the Perdido Fold Belt (*Trudgill et al.*, 1999; *Rowan et al.*, 2000). The thickness is approximately the same as that of the Cretaceous to Eocene sequence in the more landward part of the salt basin in the northwestern GoM (Figure 5.2a).

All densities and sediment properties are the same as in model D1 except that sediments are highly overpressured (pore-fluid pressure ratio of λ=0.8, φ_e=5°). Such high overpressures were necessary to bring a system with very thick overburden to gravitational failure and allow a fold belt to develop (*Gradmann et al.*, 2009). With respect to canopy formation, the low effective strength of the sediments under high pore-fluid pressure also facilitates the breaching of the anticlines by the extruding salt. Sedimentation takes the form of progradation, without aggradation, with a half-Gaussian profile width of w=50 km, a water depth of approximately 3 km and a progradation rate of v_{prog}=5 mm/a.

5.6.2 Results of Model BA1

In model BA1 early margin instability induced by differential loading of the prograding sediment wedge leads to gravity spreading and folding at the toe of the slope (Figure 5.16a, Animation_BA1.wmv). Shortening and folding propagate seaward faster than the sediment profile progrades (Figure 5.16b), creating a fold belt with the most substantial deformation at the toe of the slope. At 19 Ma m.t. after gravity spreading started, a diapir has breached the anticline of the most landward fold (Figure 5.16b). This breaching process is controlled by the bending stresses during intense shortening and the buoyancy force of the underlying, inflating salt. Local

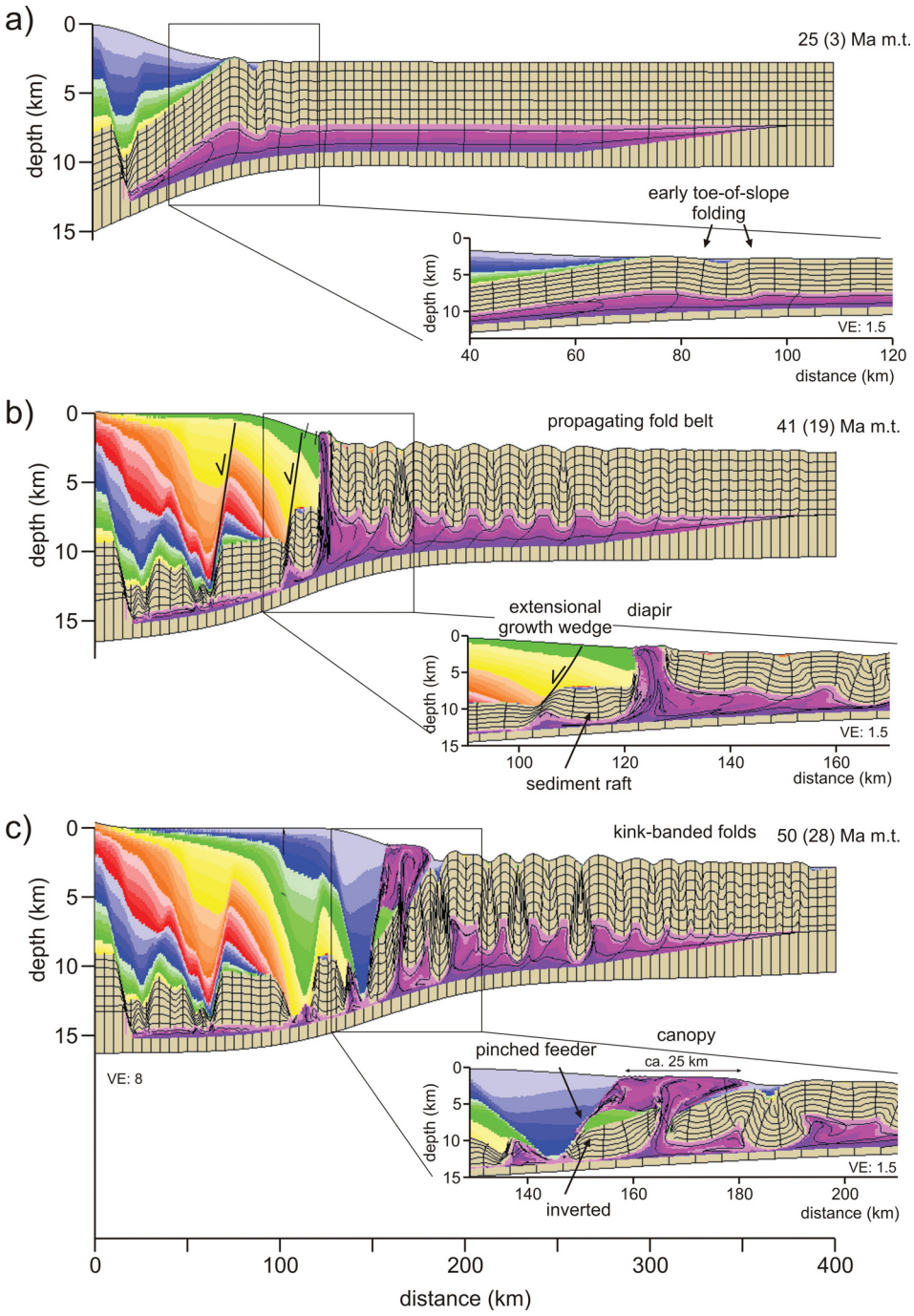

Figure 5.16: Results from model BA1 (breached-anticline model for canopy evolution). Time denotes elapsed model time. Time in parentheses denotes time since onset of gravity spreading. Open arrows indicate relative displacement. (a) Model evolution at time of early toe-of-slope folding. (b) Model evolution at time when diapir extrudes at the toe of slope. The distal section is basically undeformed at this stage. (c) Model evolution at time when the first salt sheet coalesces with the second one.

extension occurs in the strata above the largest salt high (Figure 5.17a,b) accompanied and followed by shearing on the diapir flanks (Figure 5.17c). Salt rapidly pierces through its roof in 1.5 Ma m.t. (Figure 5.17b-d). Figure 5.17e and 5.17f show the salt when it has just reached the seafloor. Extension and piercing of the anticline coincides with significant extensional shear offset at the trailing edge of the rollover structure immediately landward of the diapir.

At this stage shortening and folding of the sedimentary overburden have propagated across almost the entire salt basin (Figure 5.16b). The salt in the anticline underlying the diapir is evacuated within a few million years, and the ongoing shortening and propagation of the expulsion rollover closes off the salt feeder (Figure 5.16c).

The shortening also continues to inflate the adjacent salt pocket seaward of the diapir and tightens its overlying folds. A second diapir and salt sheet forms in the same manner as the first and coalesces with it to form a canopy 4 km thick and 25 km wide.

5.6.3 Discussion of Model BA1

Model BA1 shows that allochthonous salt structures including canopies can develop in a shortening system through the mechanism of breached anticlines as a consequence of local bending stresses and buoyancy forces leading to rupture of overburden. Once the overburden is breached the salt expulsion occurs in a similar manner as in the squeezed diapir mechanism, perhaps assisted by a developing rollover structure. The allochthonous salt structures develop in the transition between the extensional domain (extensional shear zone landward of diapir) and the shortening domain (continued shortening of folds seaward of diapir). The boundary between these domains is not sharp, nor does it remain stationary in any reference frame (such as basement, diapirs, or shelf edge) during model evolution. This migration of the kinematic domains seems responsible for the evolution of diapiric structures forming in superimposed tensional and compressive stress regimes (Animation_BA1.wmv).

The overall mechanism may be interpreted as a first stage of crestal collapse of the anticlines and early active diapirism, followed by a later stage of accelerated salt rise that occurs similarly to that of the squeezed diapir mechanism, assisted by a

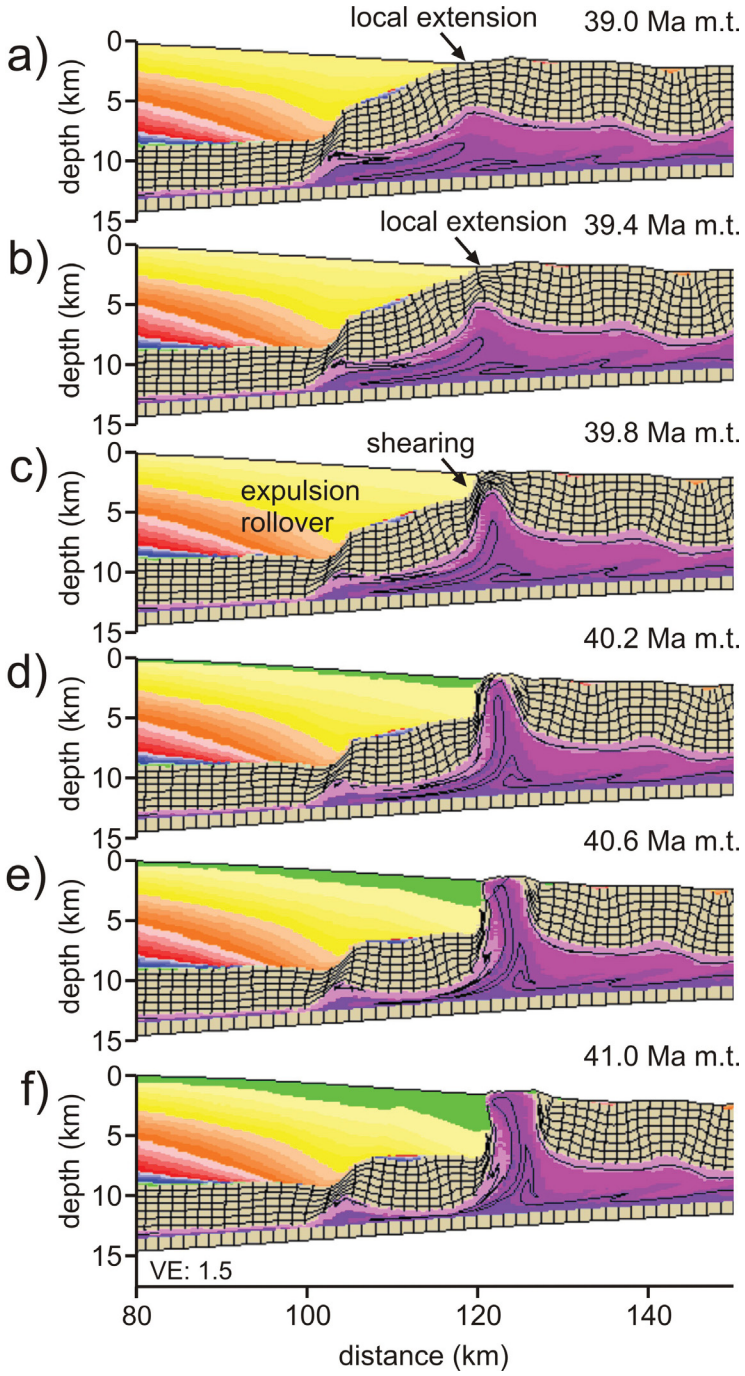

Figure 5.17: Closeup of model BA1 (Figure 5.16) showing the evolution of a diapir breaching an anticline. (f) corresponds to Figure 5.16b.

developing expulsion rollover. The contributions of the individual processes are difficult to quantify. Buoyancy must be an important factor because models with a higher salt density ($\rho_{salt} = 2200\,\mathrm{kg/m^3}$) do not develop allochthonous salt structures (*Gradmann et al.*, 2009). The load of the rollover growth wedge drives salt evacuation and lateral salt flow. Enhanced vertical salt flow (during thinning and closing off of the diapir), however, does not occur while the adjacent rollover grows fastest (40 Ma m.t.), but only after the main zone of extension shifts slightly landward (42-44 ma) and the diapir again experiences lateral compression driving vertical salt flow (see Animation_BA1.wmv). This suggests that the mechanism of squeezed diapirs is operating here. In conclusion, the mechanism of breached anticlines is more complex than conceptually introduced in section 5.1.2, and it may result from several processes acting together.

A major obstacle to the viability of the breached anticline mechanism is that local shortening must be sufficient to tighten the folds and thereby weaken the fold crests. Model BA1 only develops two such anticlines, resulting in a modest (25 km wide) canopy. Additional shortening is accommodated by folding of the sediments above the distal end of the salt basin. To develop a wider canopy, either more breached anticlines or more total salt expulsion is required. More rupturing folds and contributing feeders could be achieved by a higher salt viscosity which would on the other hand slow the rate of salt flow. A thicker salt layer could provide more salt to be expelled through each anticline but would also lower the salt layer's strength and impede toe-of-slope folding.

Other model properties, such as sediment strength and salt-sediment density contrast, are already at that end of the range of possible values where they most strongly assist formation of allochthonous salt structures. Erosion of the anticlinal fold crests could also weaken the overburden and reduce the force needed for the salt to pierce through.

Although the breached anticline mechanism may not operate efficiently in the center of a salt basin, it may be more efficient at the distal end. (*Gradmann et al.*, 2009, their model RM1). Such a setting would be analogous to the development of Canopy III in the northwestern GoM (Figure 5.2a).

5.7 Comparison of Canopy Emplacement Mechanisms with the Northwestern Gulf of Mexico

Similarities and differences between the Eocene canopy of the northwestern GoM and the modeled canopies are depicted in Figure 5.18. A number of key features of the salt-sediment system are chosen as comparison criteria.

5.7.1 Sedimentation Pattern and Evolving Kinematic Regime

The Eocene canopy of the northwestern GoM developed in the center of a salt basin above slowly aggraded shallow- to deep-water Cretaceous carbonates and the Paleocene to Eocene age clastics of the Wilcox Formation. The latter may have formed as slope and toe-of-slope deposits (*Pindell and Kennan*, 2007). Differential sediment load (such as generated by progradational sedimentation) was likely a prerequisite for the occurrence of gravity spreading since the Late Cretaceous.

The mechanism of squeezed diapirs and small-scale expulsion rollovers require that diapirs already existed in the salt basin prior to canopy formation. A primarily aggradational environment and neutral kinematic regime are consistent with this early evolution. Such an environment is equally suited for the breached anticline mechanism, where a thick sediment cover is required prior to folding. The large-scale expulsion rollover mechanism cannot account for significant sediment aggradation, since it would generate a thicker sediment cover and higher buttress, which would impede the salt both from extruding and advancing.

The squeezed diapir and breached anticline mechanisms both operate under a phase of increased progradational sediment input, which induces gravity spreading and, accordingly, shortening at the toe of the slope. This is in good agreement with the increased sand-rich sediment input of the Wilcox Formation during the Paleocene to Eocene in the northwestern GoM. The large-scale expulsion rollover mechanism also invokes large-scale deltaic sedimentation yet with less differential loading so that gravity spreading is not occurring. The small-scale expulsion rollover mechanism involves even smaller differential loads, preferably only acting on local scales. This is in disagreement with the sediment deposition at the time of canopy emplacement in the northwestern GoM. Both expulsion rollover mechanisms operate in a neutral

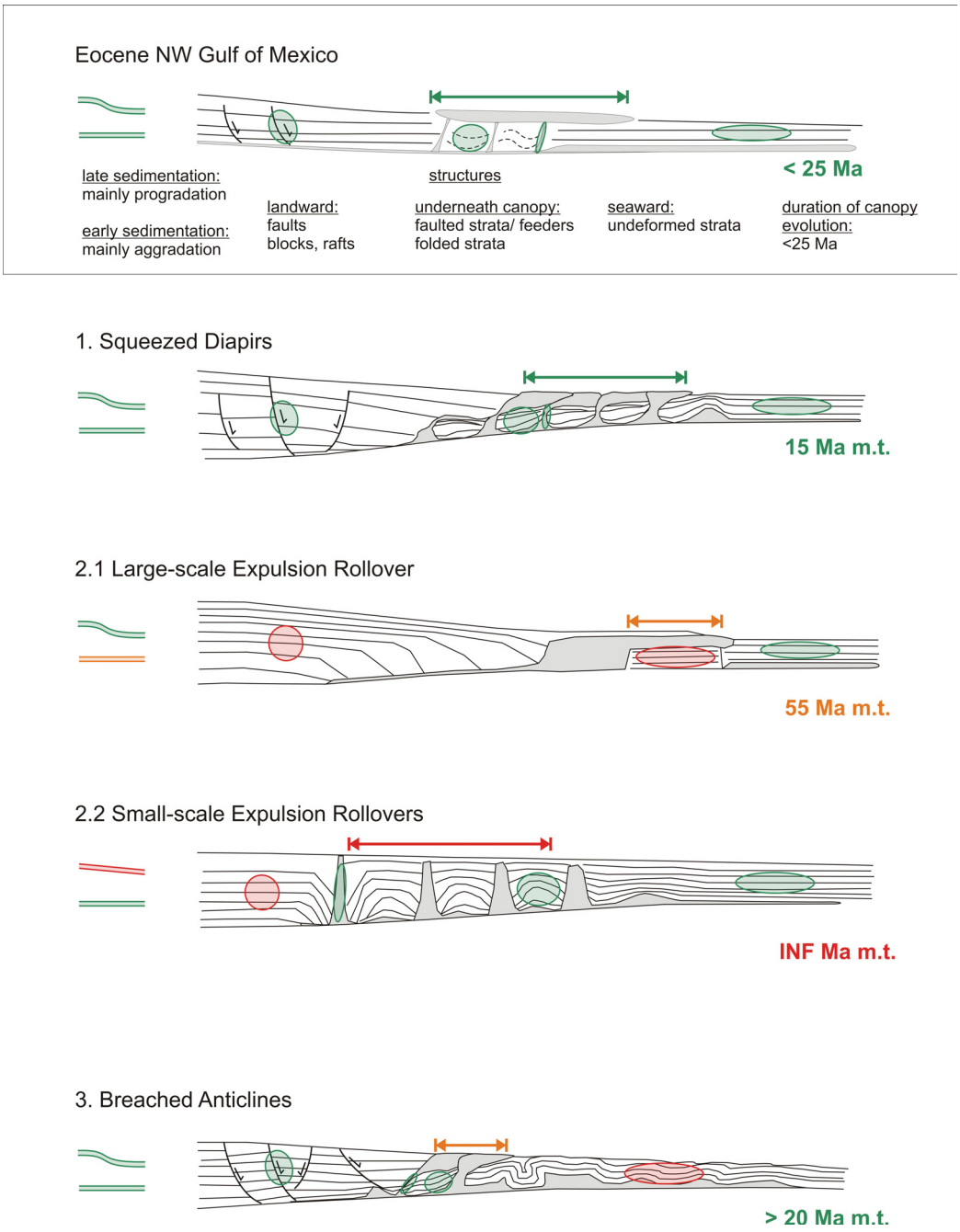

Figure 5.18: Schematic comparison of Eocene canopy in the northwestern GoM with those developing in the numerical models of section 5.4-5.6. All drawings are schematic and have similar but conceptual scales. They are based either on the seismic profile shown in Figure 5.2a or on the model results presented in this study. Characteristics of the GoM canopy are listed and highlighted in green. Their similarities with the model features are marked as the following. Green: Good agreement between model results and natural example. Orange: features don't match but would likely do so with small changes in model parameters as discussed in text. Red: Model and natural example mismatch. Best agreement with the structures of the Eocene canopy is provided by the squeezed diapir mechanism. The small-scale expulsion rollover mechanism does not develop allochthonous salt structures, which is marked here as 'infinite' duration of canopy evolution.

kinematic regime. This may be correlated with intermittent quiescent phases during the highly prevalent gravity spreading in the northwestern GoM, but leads to potential conflicts in the duration of canopy formation (see below).

5.7.2 Sediment Structures Around Canopy

Landward of Canopy

Multiple extensional faults landward of the canopy indicate deformation owing to gravity spreading since the Cretaceous. The timing of these faults has not been directly linked to the canopy evolution but indicates the overall Cenozoic kinematic regime.

Substantial gravity spreading is required for the squeezed diapir and breached anticline mechanisms, as mentioned above, and landward domains of extension develop here. In contrast, this region remains stable under the expulsion rollover mechanisms. In particular, the extensive growth wedge developing in the large-scale expulsion rollover model has no equivalent in the seismically well-imaged structures of the northwestern GoM.

Underneath Canopy

The paleocanopy is underlain by 4-5 km thick sediments, which remain relatively uniform throughout the basin (*McDonnell et al.*, 2009). The structures within this sub-canopy sequence are poorly imaged but likely include folds and thrusts (Figure 5.2a, *Radovich et al.*, 2007b; *Rowan et al.*, 2005). An array of turtle structures and pinched-off feeders has been inferred underneath a similar paleocanopy in the northern GoM (Figure 5.2c *Diegel et al.*, 1995; *Rowan and Inman*, 2005).

Sub-salt structures of the squeezed diapir mechanism include rotated and inverted minibasins (turtle structures) as well as closed feeders. Similarly, the small-scale expulsion rollover mechanism develops distinctive turtle structures and very narrow diapirs in the salt basin center. The structures under the canopy that evolved from breached anticlines consist primarily of folds that have been rotated and deformed anew. Re-deformed folds cannot easily be discerned from turtle structures in the sub-salt seismic data and all the above mechanisms can be considered as developing

structures consistent with observational data. The canopy developing from a large-scale expulsion rollover covers a prominent basement high, possibly also undeformed sediments. Such a major basement high has not been seen in the seismic data from the northwestern GoM.

Seaward of Canopy

The sediments seaward of the paleocanopy remained undeformed for approx. 10-20 Ma after canopy evolution until the Perdido Fold Belt evolved in the late Oligocene-Miocene. The canopy may have been less extensive prior to Oligocene sediment loading, and structures currently under the distal end of the paleocanopy may once have been located beyond the toe of the allochthonous salt sheet. The structures found here are mainly folds, which may have already formed during the Eocene (*Peel et al.*, 1995), or later during folding of the Perdido Fold Belt (*Radovich et al.*, 2007b; *Rowan et al.*, 2005).

The small-scale expulsion rollover mechanism leaves the distal strata undeformed. The salt-sheet generated by the large-scale mechanism deforms the distal strata a few million years after its extrusion, as soon as it advances across the basement high. During the squeezed diapir mechanism, the distal sediments remain undeformed if the pre-existing diapirs do not extend across the entire salt basin, and additional sediment deposition strengthens this region. The breached anticline mechanism folds all sedimentary overburden including the distal end of the salt basin. Limiting deformation in the distal end of the already mobilized salt basin is difficult (*Gradmann et al.*, 2009), which constitutes a flaw of this mechanism. Both squeezed diapir and breached anticline mechanisms can provide for the fold structures observed underneath the current end of the paleocanopy.

5.7.3 Timing of Evolution and Extent of Canopy

The extent of the Oligo-Miocene detachment surface that developed on the canopy was approximately 100-200 km. It is likely that the canopy was not as extensive prior to the sediment loading and the ensuing gravity spreading. The canopy likely evolved in less than 20 Ma during the deposition of the Wilcox Formation and expanded during subsequent sedimentation phases.

The small-scale expulsion rollover mechanism does not develop a salt sheet, only minor allochthonous structures develop where the diapirs reach the seafloor. Expulsion rollovers occur in combination with the other canopy emplacement mechanisms but play only a subordinate role in salt extrusion (section 5.5.2). This mechanism is, in the form tested here, not applicable to the northwestern GoM.

The canopy developing from a large-scale expulsion rollover extends as far as the basement high. The numerical models showed that it plunges into the second salt basin during further advance. It takes the model canopy 55 Ma m.t. to develop. A faster evolution could be achieved by a different salt-basin geometry and higher sedimentation rates (compare section 5.5.1). It nevertheless remains problematic to justify a long period without gravity spreading for the Cenozoic GoM.

Salt expulsion under the breached anticline mechanism only occurs after an extended period of shortening (here >20 Ma m.t.), but a more rapid canopy evolution is possible within the range of model parameters. The model canopy is only 20 km wide but different initial salt geometry and sedimentation patterns could provide for a larger allochthonous salt volume (compare section 5.6). The model canopy could spread and extend further if sediment were deposited above, especially if shale also played a role in the detachment system, as has been suggested for the northwestern GoM (*Peel et al.*, 1995; *Diegel et al.*, 1995; *McDonnell et al.*, 2009). Both time period and salt volume are generally comparable to the values proposed for the Eocene canopy evolution.

The most rapid evolution and most voluminous salt canopy occurs in the squeezed diapir models. Here a canopy develops in 15 Ma m.t., is several kilometers thick, and extends up to 50 km. These values best match the Eocene evolution of the northwestern GoM.

5.7.4 Summary

None of the numerical models presented in this chapter satisfactorily reproduces all of the observed characteristics of the Eocene canopy in the northwestern GoM. The squeezed diapir mechanism represents the most promising candidate for the development of such a canopy, because of the associated sedimentation regimes (firstly primarily aggradational, later progradational), the structures that develop around the

canopy (landward faults, folded and faulted strata underneath the canopy, delayed deformation of the distal section), and the amount of salt expelled onto the seafloor (several thousand meters by up to 50 km). Major shortcomings of the other mechanisms are little or no salt extrusion (small-scale expulsion rollover mechanism and breached anticline mechanism, respectively), different structures surrounding the allochthonous salt (basement high and growth wedge for large-scale expulsion rollover mechanism), and premature deformation of the sedimentary overburden above the distal end of the salt basin (breached anticline mechanism and large-scale expulsion rollover mechanism).

The squeezed diapir mechanism had also been proposed for the canopy of the northern GoM (Figure 5.2c), which likely evolved in an environment similar to the Eocene canopy of this study (*Diegel et al.*, 1995). The breached anticline mechanism is considered to be well suited for creating the salt canopy adjacent to the Perdido Fold Belt, in agreement with the interpretation of *Gradmann et al.* (2009) and with recent interpretations of seismic data (*Hall*, 2002; *Rowan et al.*, 2005; *Radovich et al.*, 2007b). This mechanism has not yet been sufficiently investigated for different sedimentation rates and sediment strengths in order to discard it as a mechanism for the evolution of the mid-basin canopy. A combination of different mechanisms may have operated in the Eocene GoM, yet the salt-extrusion generated by expulsion rollovers would likely have contributed the least to the canopy evolution.

5.8 Conclusions

The study presented here investigates three possible mechanisms of canopy evolution, first in a general context and then in relation to the allochthonous salt sheet formed during the Eocene in the northwestern Gulf of Mexico (GoM). The numerical experiments are idealized models of salt-bearing, rifted continental margins and do not account for many of the complexities of the natural system.

The squeezed diapir mechanism (section 5.4 and models SD1-SD3) requires pre-existing diapirs subsequently shortened during gravity spreading. The growth of diapirs (phase 1) must here occur in a tectonically quiet regime and allow a non-abrupt transition towards progradational sedimentation. This is achieved via a new mechanism of uneven sedimentation, explained in detail in Appendix 5.9. The phase

of canopy evolution (phase 2) requires shortening, here evoked by gravity spreading common to a salt-bearing continental margin. As diapirs are squeezed, salt is efficiently expelled to the seafloor to form allochthonous salt sheets that coalesce into canopies. This process is only successful if diapirs are 'mature' (mainly buoyancy-driven diapir growth, advanced depletion of autochthonous salt layer, thick intervening minibasins). Squeezing of 'immature' diapir pushes salt downward, re-inflates the autochthonous salt layer, and lifts the minibasins, and no salt extrudes to the seafloor. Salt-sheet advance occurs primarily by rotational swapping of positions of salt sheet and adjacent minibasins. Sedimentation regimes, timing and extent of diapir evolution, as well as the structures evolving underneath the canopy (inverted minibasins, pinched-off feeders) are in good agreement with those observed in the northwestern GoM.

Two possibilities for canopies that develop through the expulsion rollover mechanism are investigated, which both take place in the neutral stress regime of a stable continental margin. In the first mechanism (section 5.5.1, model ER1) a single large expulsion rollover develops landward of a sediment or basement buttress and salt is expelled up and over the buttress to form an allochthonous salt sheet. This mechanism is only successful if the buttress all but separates the salt basin into two, thus representing the development of a salt nappe at the end of a salt basin. The key structures of this mechanism (enormous growth wedge, mid-basin basement high) have no counterparts in the northwestern GoM.

In the second mechanism, a set of expulsion rollovers is thought to develop from asymmetric minibasins when they are subject to local differential sediment loading and expel salt upward and onto the seafloor (section 5.5.2, models ER2, ER3). Initial diapirs again develop by the mechanism of uneven sedimentation (Appendix 5.9). The small-scale expulsion rollover mechanism has not been successful for the parameter space tested here. Local differential loading evacuates underlying salt and narrows the diapirs. But diapir growth occurs apace to the sedimentation rate and salt does not extrude onto the seafloor. This canopy-forming mechanism thus could not be validated and remains conceptual for the time being.

Canopies developing through the breached anticline mechanism require that strata above autochthonous salt be folded as a prelude to further shortening of the salt-cored

anticlines, followed by rupture of the anticlines (section 5.6 and model BA1). In order for a salt canopy to develop in the center of the salt basin, vigorous toe-of-slope folding is necessary. This can be achieved with appropriate choices of salt-layer thickness and viscosity, but propagation of the folding across the distal end of the salt basin could not be suppressed. Salt extrusion is sparse compared to the squeezed diapir mechanism, but a broad range of parameter changes that could increase salt extrusion has not yet been considered. The overall sedimentation and kinematic regimes comply with the northwestern GoM, as well as the structures forming underneath the model canopy (folded strata and pinched-off feeders). Coeval deformation of the distal overburden is in disagreement with the Eocene canopy evolution.

In conclusion, both squeezed diapir and breached anticline mechanisms can successfully generate mid-basin canopies. The large-scale expulsion rollover mechanism is successful at the end of a salt basin, the small-scale expulsion rollover mechanism is not successful (under the circumstances tested here). The squeezed diapir mechanism works in agreement with the sedimentation and kinematic regimes of the Cenozoic GoM as well as with the salt and sediment structures mapped here. The breached anticline mechanism likely formed the allochthonous salt structures observed above the Perdido Fold Belt (see *Gradmann et al.*, 2009). More than one mechanism may have been active, and combined mechanisms are certainly possible.

5.9 Appendix: Diapir Evolution Induced by Uneven Sedimentation

This appendix describes and discusses the diapir mechanism introduced in section 5.3. The evolving diapirs serve as precursory structures for the canopy evolution of sections 5.4 and 5.5.2.

5.9.1 Introduction and Motivation

After more than a century of salt-tectonic research, the initiation and evolution of salt diapirs is still debated. Diapirs are often considered to grow as Rayleigh-Taylor instabilities in response to buoyancy when the overburden (vertically averaged) is denser than the salt. This will work when the overlying sediment is sufficiently thick and dense, but many diapirs already began to develop under a thin sediment cover, and this early initiation phase is still not properly resolved (*Hudec et al.*, 2009; *Ings and*

Beaumont, 2010). The vertically averaged density of clastic marine sediments commonly only exceeds that of the underlying salt when the sediments are 1.5-3 km thick (*Hudec et al.*, 2009, and references therein). At this thickness, buoyancy forces alone are rarely enough to overcome the strength of the overburden and thus an additional stress regime, often assumed to be tensional, must also be invoked (e.g. *Vendeville and Jackson*, 1992; *Jackson and Vendeville*, 1994). Growing evidence, mostly from deep-water environments, indicates that diapirs may also evolve in compressional settings (*Coward and Stewart*, 1995; *Hall*, 2002; *Grando and McClay*, 2004; *Vendeville and Gaullier*, 2005; *Gradmann et al.*, 2009; *Ings and Beaumont*, 2010).

This study investigates a mechanism of diapir evolution that can operate in a neutral regional stress regime and is purely driven by differential sedimentation. This approach provides suitable starting models for the subsequent canopy development that assure a non-abrupt, continuous evolution between the two model phases, and furthermore elucidates the general processes acting during early diapir evolution.

A sediment pattern is employed which maintains small bathymetric highs in fixed positions (termed uneven sedimentation). This bathymetric relief could represent channel-levee systems, turbidite deposits, or slumps, features that are commonly observed in slope and toe-of-slope settings on most continental margins. These natural features shift locations on the margin, averaging out to a relatively smooth bathymetric relief over large enough time scales. However, on relatively brief timescales ($10^4 - 10^5$ years), channels and their wedge-shaped levees maintain their location and aggrade vertically, and lobes grow through compensation stacking of individual beds (*Deptuck et al.*, 2008). A worldwide comparison shows that the size of submarine lobes can range in width from 1-25 km, in length from 3-43 km, and in height from 3-42 m (*Prelat et al.*, 2010). Extreme cases even achieve hundreds of meters relief and widths up to several tens of kilometers (*Skene et al.*, 2002).

A first-order approximation of this type of uneven bathymetry is achieved by the sinusoidal modulation of an otherwise horizontal aggradation profile (equation 5.10, Figure 5.6c). Here the range (double amplitude) approximates the bathymetric relief, and the wavelength approximates the spatial scale of what are here termed sediment lenses, i.e. the half-convex bathymetric expression. The bathymetric relief is maintained during model evolution, existing depressions are not leveled out, but material

is deposited where the sinusoidal sediment highs existed previously. This sedimentation pattern may to some degree be compared to compensation stacking observed from submarine lobes, where subsequent areas of deposition partly overlap, though their centers shift laterally. The sedimentation profile is here applied across the entire salt basin, perpendicular to the margin, whereas series of channel-levee systems and submarine lobes rather occur parallel to the margin along the slope and toe of the slope. The salt displacement during the evolution of a single diapir can trigger the evolution of adjacent diapirs (*Warsitzka et al.*, 2011), and a succession of diapirs of staggered evolution across a salt basin is possible. Although the employed sedimentation pattern deviates from the natural processes observed on the seafloor (no sediment infill, margin-perpendicular bathymetric undulations), the view is taken here that it is nevertheless suitable to demonstrate a mechanism that can play a role in early salt-sediment interaction and may contribute to diapir evolution.

In a more theoretical sense, the single sinusoid of the employed sedimentation profile does not need to be considered as the true bathymetric expression at the seafloor, but can be seen as only one of a range of wavelengths and amplitudes of sediment lenses that form the natural seafloor bathymetry. In an idealized viscous-rigid salt-sediment system, sediment bodies of the same thickness (amplitude) but different spatial extent (wavelength) adjust isostatically at different rates. Bodies of larger wavelength generally adjust (relax) faster if the salt is sufficiently thick. However, sinking bodies with wavelengths significantly larger than the salt thickness start to 'feel' the bottom of the salt layer and adjust more slowly because expulsion of the salt becomes progressively more difficult as the wavelength increases. Sediment bodies with wavelengths approximately 3-4 times the thickness of the viscous layer adjust at the fastest rate (*Cathles*, 1975; *Ings*, 2006). This simple relationship only holds if the overburden thickness is small with respect to the salt thickness. The relaxation time varies little with wavelength for wavelengths close to this preferred (fastest relaxing) one, therefore a finite range of wavelengths, covering 2-12 times the salt thickness, are expected to sink rapidly (*Ings*, 2006).

The concept of preferred wavelengths with shorter relaxation times implies that if a salt layer is overlain by a random distribution of sediment loads, the loads with the preferred wavelengths will relax fastest and with time appear as the dominant

wavelength of diapirism. In other words, even if bathymetric structures of wavelengths in this range are not the ones with the largest amplitudes, they may still be the ones that displace the underlying salt most efficiently and can determine the spatial scale of diapirs and intervening minibasins.

In regard to the application to the Gulf of Mexico (GoM), assuming that the autochthonous salt basin was approximately 2-3 km thick (*Hall*, 2002), bodies of 4-36 km extent are expected to sink the fastest. These values fit fairly well with the observed spacing of diapirs and canopy feeders of 10-20 km reported by several authors (*Diegel et al.*, 1995; *Heaton et al.*, 1995; *Hall*, 2002). Also, minibasins developing between growing diapirs are observed on a number of continental margins and are typically 10-15 km wide (*Ings*, 2006; *Hudec et al.*, 2009).

5.9.2 Models of Diapir Evolution Induced by Uneven Sedimentation

Section 5.3 introduced a model showing sedimentation-induced diapirism (Figure 5.9). This model D1 was only shown during its later stages of model evolution when diapirs had already formed. Here, the entire model evolution is shown and discussed, followed by three additional models that demonstrate the mechanism's sensitivity to different model parameters.

All models include a salt basin that is encased by non-deforming material, onto which sediment are subsequently deposited (Figure 5.7a). Salt basin geometry as well as salt and sediment rheology are same as in the models of sections 5.3-5.6 (Table 5.1). Salt density is constant, sediment density is exponentially increasing with burial depth, simulating burial compaction (equation 5.7, Figure 5.8). Sediments are deposited following a horizontal, sinusoidally modified aggradation profile (equation 5.10) with peak to trough range A=40 m, wavelength L=20 km and aggradation rate v_{agg}=0.25 mm/a. The modulation extends across the entire basin and tapers off over a distance of T=20 km at both ends. The sinusoidal perturbations remain stationary, so that a constant bathymetric relief is maintained. The geometric values may be on the far end of the values of natural systems, but are here chosen such that the diapir mechanism can be well demonstrated. The water depth (initially 6 km) plays no role during the aggradation phase because the water merely exerts a laterally uniform load.

Results of Model D1

During the evolution of model D1 (Figure 5.19) sedimentary roots develop under the sediment lenses, which grow continuously as the sediments displace underlying salt during isostatic adjustment. The roots are much thicker than the bathymetric expression of the lens owing to their small density contrast with the salt. Vertical aggradation results in the deposition of a uniform background layer of sediment (thickness h_2, Figure 5.19c). The thickening of this layer results in increasing densities of sediments in the underlying root. This in turn decreases the density contrast to the salt and results in growth of the roots in order to maintain local isostatic compensation. The growing roots displace underlying salt laterally into the diapirs, which accordingly rise and lift their sediment cover. This reduces and eventually stalls the thickening of the cover layer (thickness h_2) under the prescribed aggradation profile (Figure 5.19d).

The evolving system can be described as one of diapirs and minibasins (Figure 5.19d,e). Deformation localizes between diapir and adjacent minibasin, with discordances between the diapir flanks and the younger strata. These may be equivalent to shear zones or drag zones in the natural system. After 10 Ma m.t., the minibasins have almost grounded (Figure 5.19e) and the diapirs have reached heights that now significantly exceed the initial thickness of the salt layer, elevating their cover above the adjacent seafloor. The minibasins develop an irregular asymmetry, which must be caused by the inaccuracies of the numerical model. Neither the sedimentation profile nor the salt basin geometry provides for significant asymmetry. Minor differences (e.g. in timing of salt breaching its overburden) can locally influence the salt dynamics and generate self-enhancing asymmetry.

Results of Models D2, D3 and D4

Models D2, D3 and D4 are variations of model D1, designed to demonstrate how different parameters can affect the diapir evolution. In model D2 the aggradation rate is doubled to v_{agg}=0.5 mm/a. In model D3 the peak-to-trough amplitude of the seafloor undulations is 10 m instead of 40 m. Model D4 is the same as model D3 but with a higher sediment grain density of 2700 kg/m^3 instead of 2500 kg/m^3 to simulate calcareous sediments (*Sclater and Christie*, 1980; *Schmoker and Halley*, 1982). Sediment compaction again follows the compaction curve described in equation

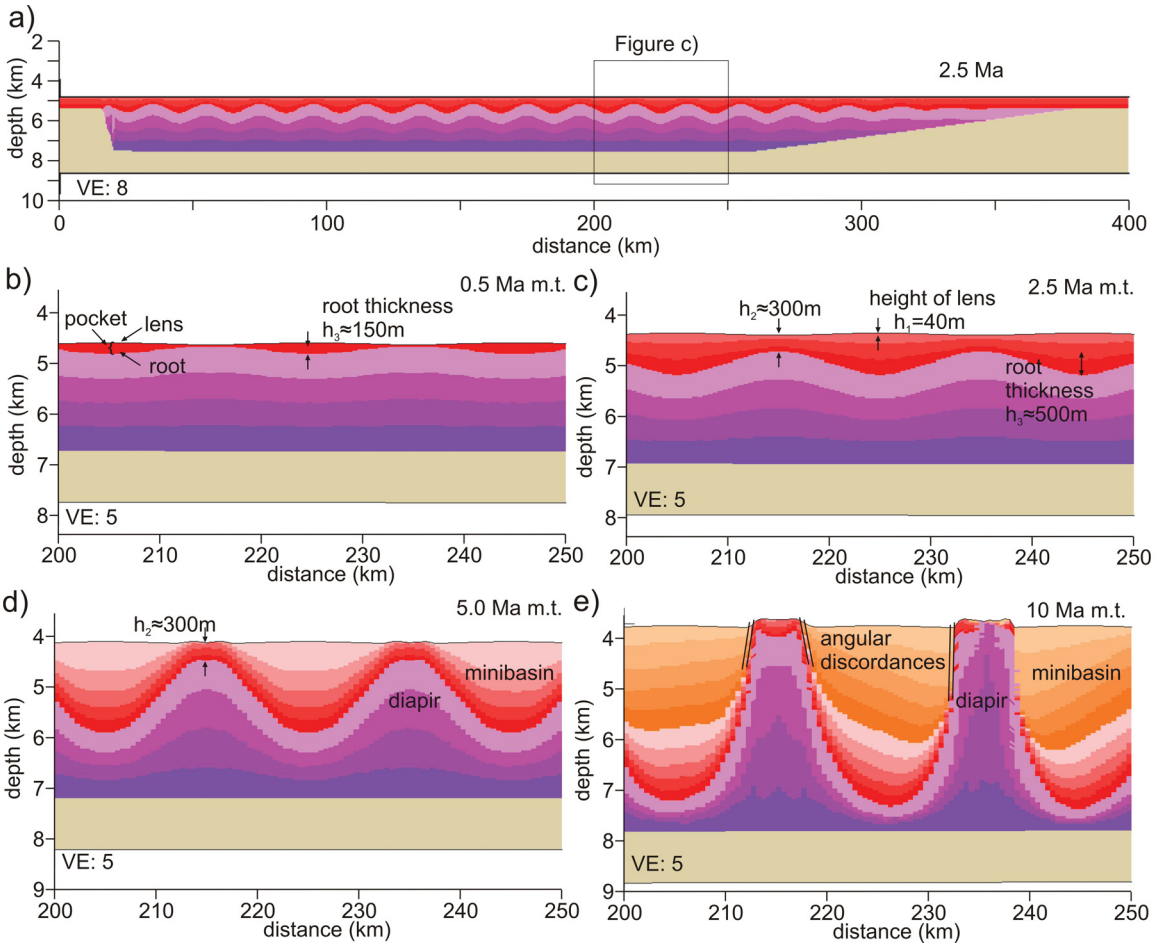

Figure 5.19: Results from model D1 with aggrading sedimentation with sinusoidal bathymetric perturbations that have constant amplitude (A=40 m) and wavelength (L=20 km). The color coding is the same as in previous model figures. See text for details of model evolution.

(5.7) and Figure 5.8. Owing to the increased grain density, sediment densities are now equal to that of salt at a depth of 300 m, and the average density of a sediment column reaches salt density at a thickness of 630 m. All other properties of the three models are the same as in model D1.

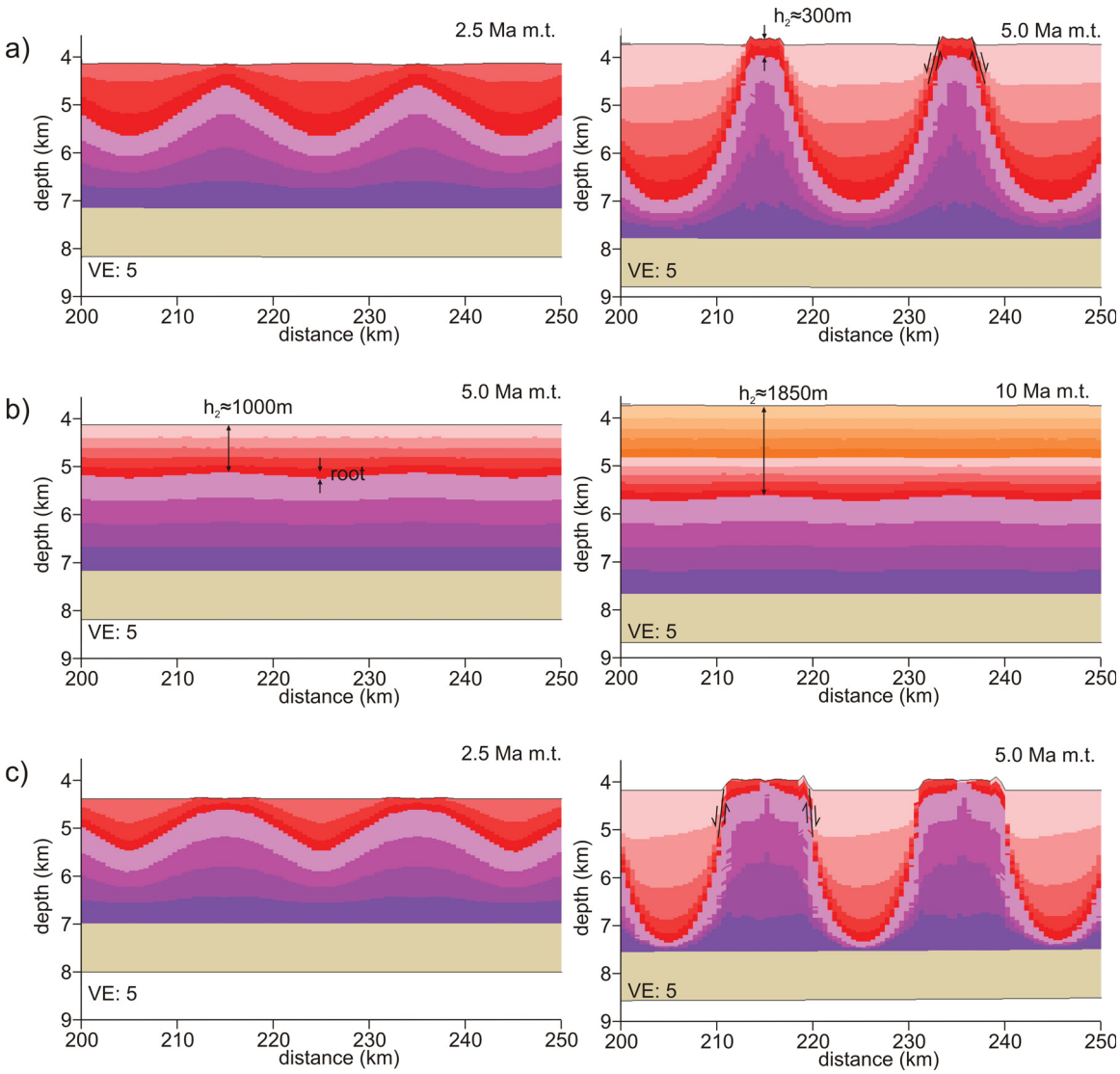

Figure 5.20: Results from models D2, D3 and D4. (a) Model D2 with doubled aggradation rate of v_{agg}=0.5 mm/a. Diapirs form faster and obtain a more triangular shape. (b) Model D3 with smaller bathymetric expressions of 10 m. Diapirs do not develop. (c) Model D4 with increased sediment grain density of 2700 kg/m^3. Diapirs develop faster and into wider structures. Open arrows indicate relative displacement.

In the details of model D2 at 5 and 10 Ma m.t. (Figure 5.20a), the amount of sediment deposited corresponds to that in Figures 5.19d and 5.19e of model D1. The

diapirs in model D2 grow faster under the increased aggradation rate and are more pointed and triangular-shaped by comparison with the more flat-topped diapirs of model D1. Sediment deposition above the salt highs ceases after approx. 2.5 Ma m.t., as the diapir growth rate exceeds the aggradation rate v_{agg} of the prescribed bathymetric profile.

In model D3 (Figure 5.20b) with 10 m high sediment lenses, only the very first stage of model evolution, during which isolated sediment lenses are compensated by a sedimentary root, is similar to that of model D1. In the subsequent evolution, during which the layer of thickness h_2 steadily grows by aggradation, the thickness of the sedimentary roots no longer increases. No diapirs develop in this scenario.

Diapirs grow rapidly in model D4 by comparison to the other models, owing to the much higher grain density, and attain a very broad, flat-topped shape (Figure 5.20c). Sedimentation above the salt highs ceases after less than 1.5 Ma m.t.

5.9.3 Discussion of Diapir Mechanism

Models D1-D4 demonstrated that the employed uneven sedimentation can initiate and drive salt diapirism. Local isostatic balancing of the bathymetric highs drives flow of the underlying salt. Continuing sedimentation sustains the pressure differences, which, assisted by the evolving density contrast between salt and compacting sediments, can eventually lead to diapir evolution.

For the quantitative assessment of sedimentation-driven diapirism, a simplified case in a unconfined salt basin is considered, in which displaced salt is not retained (Figure 5.21). For simplicity it is also assumed that salt is inviscid (instantaneous local isostatic equilibration). Additionally, sediments are assumed to have negligible strength, which in the natural case may only hold for very thin, newly deposited sediments.

Static equilibrium implies that the pressure at the base of the sediment root must be the same as the pressure at the same level in the salt ($P_{sed} = P_{salt}$, Figure 5.21a). This is the case in the early stages when the sediment lenses are not connected by aggrading sediments (Figure 5.21a i) and must be equally true when an aggrading

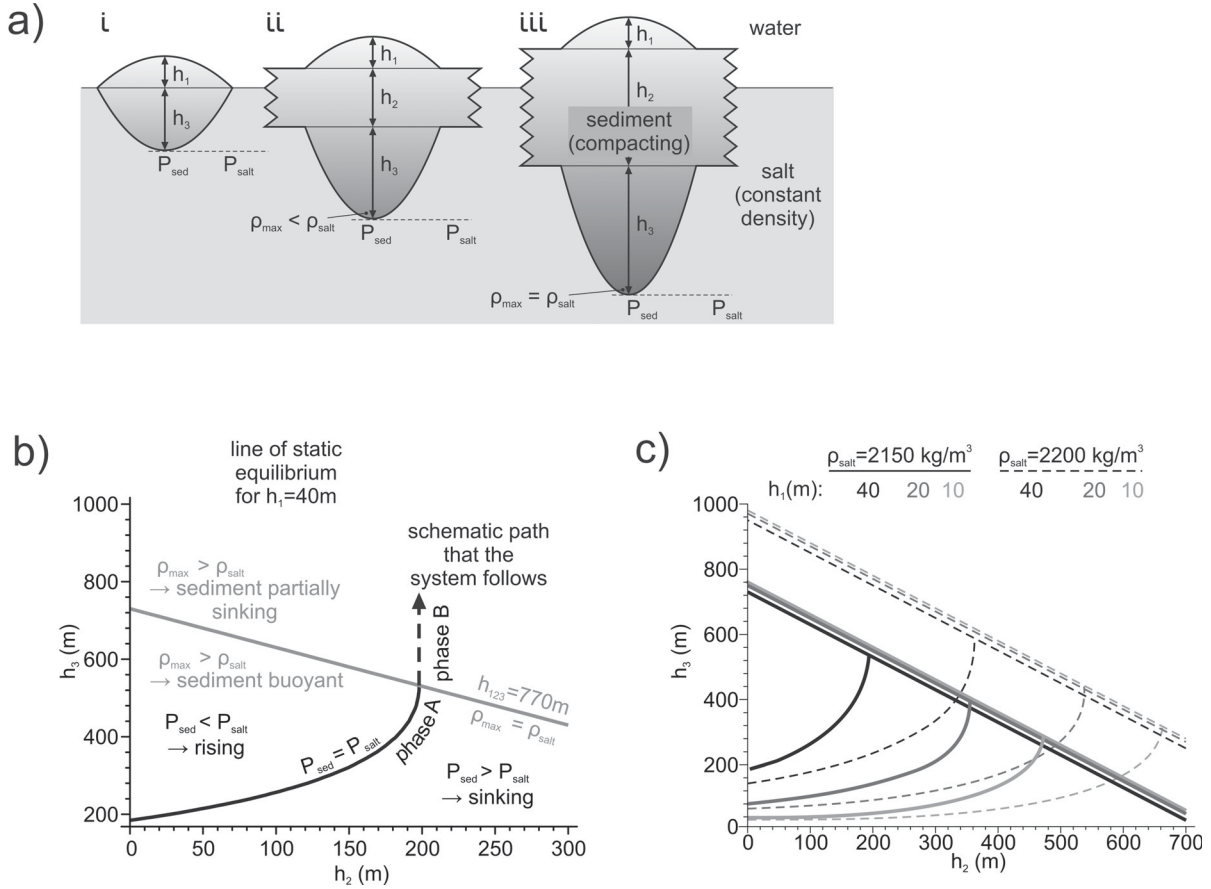

Figure 5.21: Conceptual model of diapir evolution driven by fixed bathymetric relief. (a) Evolution of sediment pocket with growing root (thickness h_3) as uniform layer thickens (thickness h_2) and bathymetric expression (h_1) remains constant. (b) Graph showing the thickness h_3 needed to isostatically balance a sediment pocket with variable thickness h_2 (black curve) and the thickness h_3 needed to achieve a density ρ_{max} at the bottom of the sediment pocket equal to the salt density ρ_{salt} (gray curve). h_1 remains constant at 40 m, salt and sediment densities are as discussed in the text. (c) Graph similar to (b) but for variable thicknesses h_1 and salt densities ρ_{salt}.

layer (thickness h_2) is added (Figure 5.21a ii and iii). The pressure balance implies

$$\bar{\rho}_{123}\, g\, h_{123} = \rho_{water}\, g\, h_1 + \bar{\rho}_2\, g\, h_2 + \rho_{salt}\, g\, h_3, \tag{5.14}$$

where g is the gravitational acceleration, $h_{123} = h_1 + h_2 + h_3$ is the total thickness of the sediment pocket with average density $\bar{\rho}_{123}$, and h_2 and ρ_2 are the thickness and average density of the uniform layer where there is no sediment lens. The average densities are given by

$$\bar{\rho}(h_{123}) = \int_0^{h_{123}} \rho_{sed}(z)\, dz \qquad \text{and} \tag{5.15}$$

$$\bar{\rho}(h_2) = \int_0^{h_2} \rho_{sed}(z)\, dz \qquad \text{with} \tag{5.16}$$

$$\rho_{sed}(z) = \rho_g - (\rho_g - \rho_w)\, \Phi_0\, e^{-cz}, \tag{5.17}$$

where ρ_{sed} is the local sediment density and depends on burial depth z measured below the local sediment surface (equation 5.7).

During aggradation, h_1 remains constant, h_2 grows according to the aggradation rate, and h_3 grows such that the root can isostatically support the sediment lens (Figure 5.21a ii and iii), provided sediment supply is sufficient. The growth of the sediment pockets leading to increased height of the adjacent salt highs is termed downbuilding. As h_2 increases, the sediment density in the underlying root increases and a thicker root is now needed to maintain the isostatic balance (phase A, Figure 5.21a ii). The 'line of static equilibrium' (Figure 5.21b) shows how h_3 increases with increasing h_2 for a constant h_1 of 40 m under assumed instantaneous isostatic equilibration. When the thickness of the sediment pocket (h_{123}) exceeds 770 m (Figure 5.21a iii), the density at the bottom of the sedimentary root becomes larger than the surrounding salt density, and an increase in root thickness can no longer isostatically support the entire thickness h_1 of the sediment lens. Continued aggradation increases the pressure P_{sed} at the base of the sediment pocket (minibasin) more than that in the adjacent salt, and the minibasin consequently sinks deeper (phase B). Only when the vertically averaged density of the sediment exceeds that of the salt (h_{123}>1710 m) can the minibasins grow without additional sedimentation (phase C, active diapirism).

While the thickness of the sediment lens, h_1, determines the root thickness and

is crucial for the first growth stage (phase A), it is of minor importance once the basal sediment density exceeds the salt density (phase B). Here minibasin subsidence can continue during aggradation even if h_1=0, provided the mechanical strength of the sediment is sufficiently low. Diapir growth becomes more efficient when entering phase B, which occurs when h_2=200 m (Figure 5.21c) according to the simplified calculations. This value is similar to h_2=300 m, the thickness at which the model diapir growth rate exceeds the sedimentation rate (Figure 5.19d).

The rates of diapir growth and minibasin subsidence are not exclusively controlled by the sedimentation rate but also depend on the salt viscosity, the failure strength of the sediments, and the width and spacing of the minibasins. Furthermore, in a confined salt basin (as in the numerical experiment) or where thick minibasins prevent large-scale lateral salt flow, salt must be conserved locally by transfer into adjacent developing diapirs and an increase in the diapirs' growth rate is expected. Despite these factors, the predictions of the simplified analytical solution reasonably matches the numerical models.

Amplitude of Bathymetric Relief

For systems with smaller surface undulations than in model D1, the point in time at which the sediment density at the bottom of the minibasin reaches the salt density (transition from phase A to phase B) is expected to occur later, since h_3 will be smaller and a larger aggraded thickness of h_2 is required. Figure 5.21c shows the simplified system behavior with smaller surface undulations (h_1=40 m, 20 m and 10 m) and the different thicknesses of h_2 necessary to start efficient downbuilding of diapirs. A larger thickness h_2 implies a greater strength of the sediment layer, which needs to be overcome by larger buoyancy forces to allow diapir growth. In the models, this in turn requires an increase of h_2, which may lead to a too strong overburden that prevents diapir growth. This is seen in model D3 (Figure 5.20b), where h_1=10 m and the overburden thickness required to start phase B is h_2=450 m.

Salt and Sediment Densities

Figure 5.21c also shows the behavior of systems with a higher salt density of 2200 kg/m^3. This is a more accurate value for natural salt that contains impurities (2150 kg/m^3

represents pure halite density, *Hudec et al.*, 2009). Greater burial depths are then required for compacting sediments to be as dense as salt (990 m for local density, 2270 m for average density). This in turn requires larger sediment thickness h_2 for the presented diapir mechanism. For the system considered here, increasing salt density by 50 kg/m^3 has a similar effect to halving the amplitude of the surface undulations. Numerical experiments with a salt density of 2200 kg/m^3 also develop diapirs (not shown here), but they form more slowly, accumulate a thicker sediment carapace, and form pointier structures.

Higher sediment densities will have an effect similar to lower salt density. As model D4 shows, the evolving diapirs grow much faster and attain a more box-like shape with steep flanks. The effects of different compaction models and sedimentation rates for this mechanism of diapir evolution have recently been addressed by *Goteti et al.* (2012).

5.9.4 Uneven Sedimentation as a Mechanism for Early Diapirism in the Northwestern Gulf of Mexico

As demonstrated by model D1, a relief of 40 m is sufficient to generate diapirs. This value is at the upper limit of sediment lobes deposited at basin floors, e.g., *Prelat et al.* (2010) list maximum thicknesses of 20-40 m for sediment lobes in smaller, enclosed basins, with lateral extents of up to 14 km. Sediment lobes in wide, open basins, which often reach lengths of more than 20 km, tend to be only 10-20 m thick (*Prelat et al.*, 2010). Model D1 is therefore considered an end-member case and other factors must facilitate diapir evolution if induced solely by the bathymetric relief of sediment lobes. For example, diapirs may evolve with bathymetric relief that is less than 40 m, if correlated density distributions enhance the pressure effect of uneven bathymetry.

The northwestern GoM represented a deep-water environment during the Cretaceous and early Cenozoic (*Goldhammer and Johnson*, 2001). Sediment deposition was relatively uniform across most of the salt basin, far from deltaic sediment input. Nevertheless, Paleocene-Eocene and Oligocene turbidite deposits are known to exist more than 200 km away from the contemporaneous shelf edge, suggesting that a well-developed slope was present to assist the sediment transport (*Pindell and Kennan*, 2007). Accordingly, sedimentary deposits that are generally found at the toe of the

slope (like channel lobes) may also have been present in the Cretaceous to Cenozoic northwestern GoM.

The early post-salt sediments in the GoM are initially shallow-water, then deep-water carbonates (*Galloway et al.*, 2000). Significant sediment lobes are less likely for precipitated deep-water carbonates, but resedimented carbonates can form lobes or accumulations of slumped material. Carbonates typically have higher grain densities (*Sclater and Christie*, 1980), for which much smaller undulations are required to drive diapirism (model D4). Very little is published in the scientific literature about the seafloor relief of calciclastic sediment lobes. Although any relief will likely be small and the frictional strength of carbonates is higher than that of quartz-dominated sand, especially in submarine conditions (*Obert and Duvall*, 1967), it may be possible that bathymetric variation on the scale of meters may be sufficient to initiate diapirs.

In model D1 it takes a few million years to grow diapirs by stacking, uneven sedimentation to the stage where buoyancy contrast can take over. Deep-water sediment lobes persist for less time ($10^4 - 10^5$ a depending on sediment supply, *Deptuck et al.*, 2008; *Prelat et al.*, 2010). Higher sediment aggradation rates in the models could decrease the necessary duration of bathymetry-maintaining sedimentation. Significantly higher sedimentation rates, however, do not leave enough time for the local isostatic adjustment and thereby suppress the diapir formation. Diapir evolution in a three-dimensional setting (such as the GoM) may be much faster than the two-dimensional setting of the numerical experiments, because growing diapirs can receive salt from all directions, sinking minibasins can expel salt in all directions and both features may hence grow more efficiently. An additional possibility, which has not yet been explored in the numerical models, is that uneven sedimentation develops for a short interval after an extended period of laterally uniform sedimentation. If densities at the bottom of the uniform layer are already close to that of the underlying salt, only a short period of uneven sedimentation may be sufficient to drive the system into the regime of buoyancy driven diapirism (*Goteti et al.*, 2012).

5.9.5 Summary of Diapirism Driven by Uneven Sedimentation

It has been demonstrated with the help of numerical models and simplified calculations, that surface loading akin to uneven sedimentation that preserves bathymetric expressions can drive diapirism if the control parameters take appropriate values. This mechanism is motivated by the observation that local bathymetric highs, termed lenses (such as channel-levee systems or turbidite lobes) can be the locus of persistent sedimentation for a limited, though mechanically significant, period of time. While the sediment is less dense than the salt, these positive structures subside into the salt but remain floating in isostatic equilibrium (phase A). Under regional sediment aggradation the density at the base of the sediment pockets becomes larger than that of the surrounding salt and isostatic equilibrium can no longer be achieved (phase B, passive diapir growth). Eventually, the whole sediment column becomes on average denser than the salt and sinks into the salt under its own weight (phase C, active diapir growth similar to Rayleigh-Taylor instability). Numerical models and simplified calculations show that this mechanism is reasonably efficient for siliciclastic sediments with undulations of amplitude 40 m and wavelengths of 20 km. Smaller bathymetric relief or smaller salt-sediment contrasts hamper or even inhibit diapir evolution. High sedimentation rates can expedite but also swamp diapir growth. The examples discussed here are to be considered as end-members, the chosen parameter values all strongly help the evolution of diapirs.

This mechanism may not be appropriate for the Cretaceous evolution of the northwestern GoM, which was dominated by deep-water carbonate deposition and hence very little early bathymetric relief. Nevertheless, uneven clastic sedimentation above other salt basins worldwide may have had a large effect on diapir growth, and this mechanism deserves consideration in future studies on diapir evolution (see *Goteti et al.*, 2012).

Bibliography

Adam, J., and C. Krezsek (2012), Basin-scale salt tectonic processes of the Laurentian Basin, Eastern Canada: Insights from integrated regional 2D seismic interpretation and 4D physical experiments, in *Salt tectonics, sediments and prospectivity*, *Geological Society Special Publications*, vol. 363, edited by I. Alsop, pp. 331–360, Geological Society of London.

Albertz, M., and C. Beaumont (2010), An investigation of salt tectonic structural styles in the Scotian Basin, offshore Atlantic Canada, Part 2: Comparison of observations with geometrically complex numerical models, *Tectonics*, *29*, doi: 10.1029/2009TC002540.

Bird, D. E., K. Burke, S. A. Hall, and J. F. Casey (2005), Gulf of Mexico tectonic history; hotspot tracks, crustal boundaries, and early salt distribution, *AAPG Bulletin*, *89*(3), 311–328.

Cathles, L. M. (1975), *The viscosity of the Earth's mantle*, Princeton Univ. Press, Princeton, N.J., USA.

Coward, M., and S. Stewart (1995), Salt-influenced structures in the Mesozoic-Tertiary cover of the southern North Sea, U.K, in *Salt Tectonics, A Global Perspective*, *AAPG Memoir*, vol. 65, edited by M. P. A. Jackson, D. G. Roberts, and S. Snelson, pp. 229–250, AAPG, Tulsa, Oklahoma.

Deptuck, M. E., D. J. W. Piper, B. Savoye, and A. Gervais (2008), Dimensions and architecture of late Pleistocene submarine lobes off the northern margin of east Corsica, *Sedimentology*, *55*(4), 869–898.

Diegel, F. A., J. F. Karlo, D. C. Schuster, R. C. Shoup, and P. R. Tauvers (1995), Cenozoic structural evolution and tectono-stratigraphic framework of the northern Gulf Coast continental margin, in *Salt Tectonics, A Global Perspective*, *AAPG Memoir*, vol. 65, edited by M. P. A. Jackson, D. G. Roberts, and S. Snelson, pp. 109–151, AAPG, Tulsa, Oklahoma.

Fiduk, J. C., P. Weimer, B. D. Trudgill, M. G. Rowan, P. E. Gale, R. L. Phair, B. E. Korn, G. R. Roberts, W. T. Gafford, R. S. Lowe, and T. A. Queffelec (1999), The Perdido fold belt, Northwestern deep Gulf of Mexico, Part 2; Seismic stratigraphy and petroleum systems, *AAPG Bulletin*, *83*(4), 578–612.

Fletcher, R. C., M. R. Hudec, and I. A. Watson (1995), Salt glacier and composite sediment-salt glacier models for the emplacement and early burial of allochthonous salt sheets, in *Salt Tectonics, A Global Perspective*, *AAPG Memoir*, vol. 65, edited by M. P. A. Jackson, D. G. Roberts, and S. Snelson, pp. 77–107, AAPG, Tulsa, Oklahoma.

Fullsack, P. (1995), An arbitrary Lagrangian-Eulerian formulation for creeping flows and its applications in tectonic models, *Geophysical Journal International*, *120*(1), 1–23.

Fuqua, D. A. (1990), Seismic structural analysis of the Perdido fold belt, Alaminos Canyon area, northwestern Gulf of Mexico, Master's thesis.

Galloway, W. E., P. E. Ganey-Curry, X. Li, and R. Buffler (2000), Cenozoic depositional history of the Gulf of Mexico basin, *AAPG Bulletin*, *84*(11), 1743–1774.

Ge, H., M. P. A. Jackson, and B. C. Vendeville (1997), Kinematics and dynamics of salt tectonics driven by progradation, *AAPG Bulletin*, *81*, 398–423.

Gemmer, L., S. J. Ings, S. Medvedev, and C. Beaumont (2004), Salt tectonics driven by differential sediment loading: Stability analysis and finite element experiments, *Basin Research*, *16*, 199–219.

Giles, K. A., and T. F. Lawton (2002), Halokinetic sequence stratigraphy adjacent to the El Papalote Diapir, northeastern Mexico, *AAPG Bulletin*, *86*(5), 823–840.

Goldhammer, R. K., and C. A. Johnson (2001), Middle Jurassic-Upper Cretaceous paleogeographic evolution and sequence-stratigraphic framework of the Northwest Gulf of Mexico rim, in *The western Gulf of Mexico basin; tectonics, sedimentary basins, and petroleum systems*, *AAPG Memoir*, vol. 75, edited by C. Bartolini, R. T. Buffler, and A. Cantu-Chapa, pp. 45–81, AAPG, Tulsa, Oklahoma.

Goteti, R., S. Ings, and C. Beaumont (2012), Development of salt mini basins initiated by sedimentary topographic relief, *Earth and Planetary Science Letters*, *339-340*, 103–116.

Gradmann, S., C. Beaumont, and M. Albertz (2009), Factors controlling the evolution of the Perdido Fold Belt, northwestern Gulf of Mexico, determined from numerical models, *Tectonics*, *28*(2).

Grando, G., and K. R. McClay (2004), Structural evolution of the Frampton growth fold system, Atwater Valley-southern Green Canyon area, deep water Gulf of Mexico; Oil and gas in compressional belts, *Marine and Petroleum Geology*, *21*(7), 889–910.

Hall, S. H. (2002), The role of autochthonous salt inflation and deflation in the northern Gulf of Mexico, *Marine and Petroleum Geology*, *19*(6), 649–682.

Heaton, R. C., M. P. A. Jackson, M. Barmahmoud, and S. O. Nani (1995), Superposed Neogene extension, contraction and salt canopy emplacement in the Yemeni Red Sea, in *Salt Tectonics, A Global Perspective*, *AAPG Memoir*, vol. 65, edited by M. P. A. Jackson, D. G. Roberts, and S. Snelson, pp. 333–352, AAPG, Tulsa, Oklahoma.

Heiniö, P., and R. Davies (2006), Degradation of compressional fold belts: Deep-water Niger Delta, *AAPG Bulletin*, *90*(5), 753–770, doi: 10.1306/11210505090.

Hudec, M. R. (2004), Salt intrusion: Time for a comeback?, in *Salt Sediment Interactions and Hydrocarbon Prospectivity: Concepts, Applications, and Case Studies for the 21st Century. GCSSEPM Conference Proceedings*, pp. 119–132, (CD-ROM - ISSN: 1544-2462).

Hudec, M. R., and M. P. A. Jackson (2006), Advance of allochthonous salt sheets in passive margins and orogens, *AAPG Bulletin*, *90*(10), 1535–1564.

Hudec, M. R., M. P. A. Jackson, and D. D. Schultz-Ela (2009), The paradox of minibasin subsidence into salt; clues to the evolution of crustal basins, *Geological Society of America Bulletin*, *121*(1-2), 201–221.

Ings, S. J. (2006), Passive continental margin salt tectonics: Numerical modelling, analytical stability analysis, and applications to the Scotian Margin, offshore Eastern Canada, Ph.D. thesis, Dalhousie University.

Ings, S. J., and C. Beaumont (2010), Shortening viscous pressure ridges, a solution to the enigma of initiating salt "withdrawal" minibasins, *Geology*, *38*(4), 339–342.

Jackson, M. P. A. (1995), Retrospective salt tectonics, in *Salt Tectonics, A Global Perspective*, *AAPG Memoir*, vol. 65, edited by M. P. A. Jackson, D. G. Roberts, and S. Snelson, pp. 1–28, AAPG, Tulsa, Oklahoma.

Jackson, M. P. A., and C. J. Talbot (1986), External shapes, strain rates, and dynamics of salt structures, *GSA Bulletin*, *97*(3), 305–323.

Jackson, M. P. A., and C. J. Talbot (1991), A glossary of salt tectonics, *Tech. Rep. 91-94*, University of Texas at Austin, Bureau of Economic Geology, Austin, TX, United States (USA).

Jackson, M. P. A., and B. C. Vendeville (1994), Regional extension as a geologic trigger for diapirism, *GSA Bulletin*, *106*, 57–73.

Korvin, G. (1984), Shale compaction and statistical physics, *Geophysical Journal of the Royal Astronomical Society*, *78*, 35–50.

McBride, B. C., M. G. Rowan, P. Weimer, N. Hurley, and P. Weimer (1998), The evolution of allochthonous salt systems, northern Green Canyon and Ewing Bank (offshore Louisiana), northern Gulf of Mexico, *AAPG Bulletin*, *82*(5B), 1013–1036.

McDonnell, A., R. G. Loucks, and W. E. Galloway (2008), Paleocene to Eocene deep-water slope canyons, western Gulf of Mexico: Further insights for the provenance of deep-water offshore Wilcox Group plays, *AAPG Bulletin*, *92*(9), 1169–1189.

McDonnell, A., M. R. Hudec, and M. P. Jackson (2009), Distinguishing salt welds from shale detachments on the inner texas shelf, western gulf of mexico, *Basin Research*, *21*, doi: 10.1111/j.1365-2117.2008.00375.x.

Meyer, D., L. Zarra, and J. Yun (2007), From BAHA to Jack, evolution of the Lower Tertiary Wilcox trend in the deepwater Gulf of Mexico, *The Sedimentary Record*, *5*(3), 4–9.

Nelson, T. H., and L. Fairchild (1989), Emplacement and evolution of salt sills in the northern gulf of mexico, *The Bulletin of the Houston Geological Society*, *32*(1), 6–7.

Obert, L., and W. I. Duvall (1967), *Rock mechanics and the design of structures in rock*, John Wiley and Sons, New York.

Peel, F. J., C. J. Travis, and J. R. Hossack (1995), Genetic structural provinces and salt tectonics of the Cenozoic offshore U.S. Gulf of Mexico: A preliminary analysis, in *Salt Tectonics, A Global Perspective*, *AAPG Memoir*, vol. 65, edited by M. P. A. Jackson, D. G. Roberts, and S. Snelson, pp. 153–175, AAPG, Tulsa, Oklahoma.

Pindell, J., and J. F. Dewey (1982), Permo-Triassic reconstruction of western Pangea and the evolution of the Gulf of Mexico/Caribbean region, *Tectonics*, *1*(2), 179–211.

Pindell, J., and L. Kennan (2007), Rift models and the salt-cored marginal wedge in the northern Gulf of Mexico: Implications for deep water Paleogene Wilcox deposition and basinwide maturation, in *Transactions of GCSSEPM 27th Annual Bob F. Perkins Research Conference*, pp. 146–186, (CD Rom).

Pindell, J. L. (1985), Alleghenian reconstruction and subsequent evolution of the Gulf of Mexico, Bahamas, and proto-Caribbean, *Tectonics*, *4*(1), 1–39.

Prelat, A., J. Covault, D. Hodgson, A. Fildani, and S. Flint (2010), Intrinsic controls on the range of volumes, morphologies, and dimensions of submarine lobes, *Sedimentary Geology*, *232*(1-2), 66 – 76.

Radovich, B., J. Moon, C. Connors, and D. Bird (2007a), Insights into structure and stratigraphy of the northern Gulf of Mexico from 2D pre-stack depth migration imaging of mega-regional onshore to deep water, long-offset seismic data, *Transactions - Gulf Coast Association of Geological Societies*, *57*, 633–637.

Radovich, B., C. Connors, and J. Moon (2007b), Deep imaging of the Paleogene, Miocene structure and stratigraphy of the western Gulf of Mexico using 2D pre-stack depth migration of mega-regional onshore to deep water, long-offset seismic data, in *The Paleogene of the Gulf of Mexico and Caribbean Basins: Processes, Events, and Petroleum Systems. GCSSEPM Conference Proceedings*, pp. 307–322, (CD Rom).

Rowan, M. G., and K. F. Inman (2005), Counterregional-style deformation in the deep shelf of the northern Gulf of Mexico, *Transactions - Gulf Coast Association of Geological Societies*, *55*, 716–724.

Rowan, M. G., B. D. Trudgill, and J. C. Fiduk (2000), Deep-water, salt-cored foldbelts: Lessons from the Mississippi Fan and Perdido Foldbelts, northern Gulf of Mexico, in *Atlantic Rifts and Continental Margins*, *Geophysical Monograph*, vol. 115, edited by W. Mohriak and M. Talwani, pp. 173–191, AGU, Washington, D.C.

Rowan, M. G., F. J. Peel, and B. C. Vendeville (2004), Gravity-driven fold belts on passive margins, in *Thrust tectonics and hydrocarbon systems*, *AAPG Memoir*, vol. 82, edited by K. R. McClay, pp. 157–182, AAPG, Tulsa, Oklahoma.

Rowan, M. G., K. F. Inman, and J. C. Fiduk (2005), Oligo-Miocene extension at the Louann level in the northern Gulf of Mexico: Kinematic models and examples, *Transactions - Gulf Coast Association of Geological Societies*, *55*, 725–732.

Salvador, A. (1991), Origin and development of the Gulf of Mexico Basin, in *The Gulf of Mexico Basin*, *The geology of North America*, vol. J, edited by A. Salvador, pp. 389–444, GSA, USA.

Schmoker, J., and R. Halley (1982), Carbonate porosity versus depth: A predictabler-Relation for South Florida, *AAPG Bulletin*, *66*(12), 2561–2570.

Schultz-Ela, D. D. (2001), Excursus on gravity gliding and gravity spreading, *Journal of Structural Geology*, *23*(5), 725–731.

Sclater, J., and P. Christie (1980), Continental stretching: an explanation of the post-mid-Cretaceous subsidence of the Central North Sea Basin, *Journal of Geophysical Research*, *85*, 37113739, doi: 10.1029/JB085iB07p03711.

Skene, K. I., D. J. W. Piper, and P. S. Hill (2002), Quantitative analysis of variations in depositional sequence thickness from submarine channel levees, *Sedimentology*, *49*(6), 1411–1430.

Stern, R. J., and W. R. Dickinson (2010), The Gulf of Mexico is a Jurassic backarc basin, *Geosphere*, *6*(6), 739–754.

Talbot, C. J. (1998), Extrusions of Hormuz salt in Iran, *Geological Society Special Publications*, *143*, 315–334.

Talbot, C. J., and P. Aftabi (2004), Geology and models of salt extrusion at Qum Kuh, central Iran, *Journal of the Geological Society*, *161*(2), 321–334.

Talbot, C. J., and E. A. Rogers (1980), Seasonal movements in a salt glacier in Iran, *Science*, *208*(4442), 395–397.

Trudgill, B. D., M. G. Rowan, J. C. Fiduk, P. Weimer, P. E. Gale, B. E. Korn, R. L. Phair, W. T. Gafford, G. R. Roberts, and S. W. Dobbs (1999), The Perdido fold belt, northwestern deep Gulf of Mexico: Part 1, Structural geometry, evolution and regional implications, *AAPG Bulletin*, *83*(1), 88–113.

Vendeville, B., and V. Gaullier (2005), Salt diapirism generated by shortening and buckle folding, *Abstracts, CDROM, AAPG Annual Convention*.

Vendeville, B. C., and M. P. A. Jackson (1992), The rise of diapirs during thin-skinned extension, *Marine and Petroleum Geology*, *9*(4), 331–353.

Waller, T. D. (2007), Structural Analysis of the Perdido Fold Belt: Timing, Evolution and Structural Cycle, Master's thesis, Texas A&M University.

Warsitzka, M., J. Kley, F. Jahne, and N. Kukowski (2011), Salt diapirism driven by differential loading some insights from analogue modelling, *Tectonophysics*, doi: 10.1016/j.tecto.2011.11.018.

Willett, S. D. (1999), Rheological dependence of extension in wedge models of convergent orogens, *Tectonophysics*, *305*(4), 419–435.

Winker, C. D., and R. Buffler (1988), Paleogeographic evolution of early deep-water Gulf of Mexico and margins, Jurassic to Middle Cretaceous (Comanchean), *AAPG Bulletin*, *72*(3), 318–346.

Chapter 6

Discussion

The intent of the research presented in this thesis is to provide additional insight into the salt-tectonic processes and structures that occur in the deep-water regions of continental margins by employing 2D numerical models. The following aspects of salt-tectonic deformation are addressed in one or more of the four paper-style chapters: (1) the conditions leading to gravity spreading above salt on continental margins; (2) the development of salt tectonic structures (fold belts, canopies, diapirs); and (3) the salt-tectonic evolution of the northwestern Gulf of Mexico (GoM). This chapter reviews the research results with respect to these aspects (summaries of the chapters discussed here may be found in Chapters 2, 3, 4, and 5). Furthermore, the overall contributions to salt-tectonic research and implications for further studies are addressed.

6.1 Gravity Spreading on Continental Margins

Gravity spreading of a continental margin-scale sedimentary wedge above a salt substrate occurs when increasing differential stress in the sedimentary wedge causes it to fail (Figure 6.1). Ensuing deformation results in the formation of an upslope (landward) domain of extension, a central domain of translation and a downslope (seaward) domain of shortening (e.g. *Letouzey et al.*, 1995; *Rowan et al.*, 2004; *Vendeville*, 2005). A weak substrate such as salt or shale can act as a décollement layer and reduce the basal friction. Channel (Poiseuille) flow of the salt assists the failure by applying a basal drag on the overburden as it is squeezed and mobilized by the differential loading. Analytical calculations of the stability conditions (*Gemmer et al.*, 2004, 2005) demonstrated that yielding of the sedimentary overburden depends on factors such as the differential sediment thickness, the basal slope of the salt layer, and the effective sediment strength.

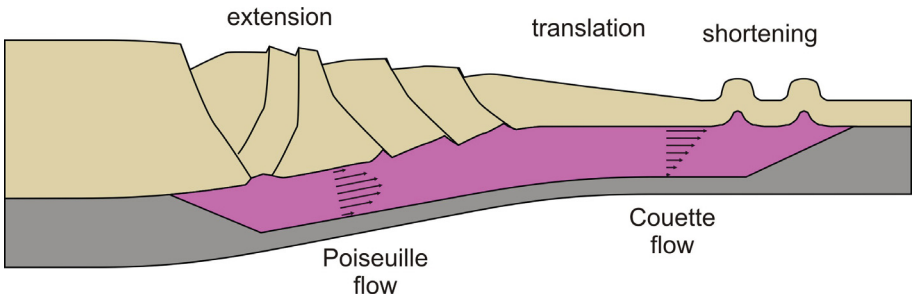

Figure 6.1: Schematic of gravity spreading showing domains of extension, translation and shortening as well as dominant viscous flow in the salt layer. After *Letouzey et al.* (1995).

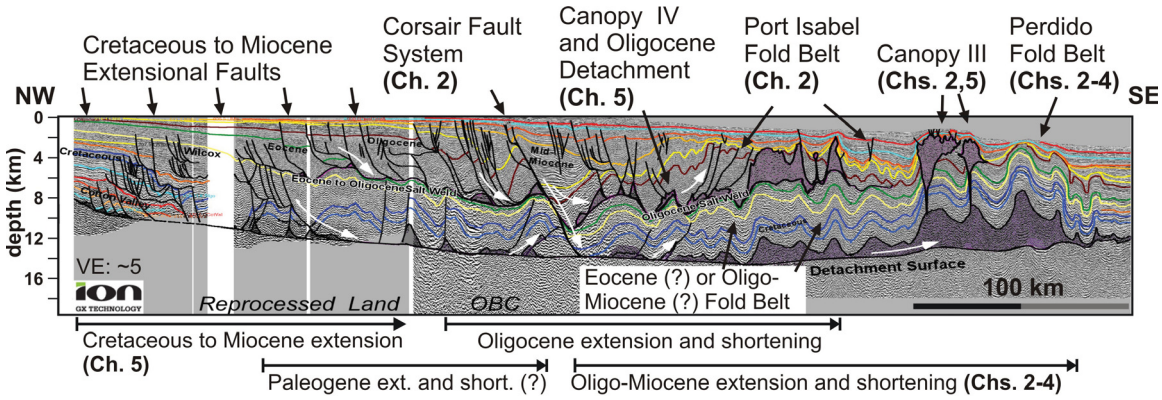

Figure 6.2: Regional NW-SE trending seismic profile from the northwestern Gulf of Mexico extending from onshore into deep water (from *Radovich et al.*, 2007). Large-scale gravity-spreading structures (extensional faults, allochthonous salt, fold belts) are indicated as well as the thesis chapters addressing their evolution.

The results presented have general applications but in order to provide context, the northwestern GoM is used throughout this thesis as a natural example of gravity spreading to study the factors that controlled its destabilization. In the GoM, salt-tectonic deformation during the Oligocene-Miocene created the extensional structures of the Corsair fault system and formed the Perdido Fold Belt, located nearly 200 km further seaward (*Rowan et al.*, 2005) (Figure 6.2). Many parameters influencing this margin's instability are well known (e.g. the geometric extent or thickness of the deformed overburden) or can be estimated reasonably well (e.g. the salt thickness). A key factor that is poorly constrained and subject of this investigation is the sediment strength.

In order to compare numerical models not only to the natural setting but also to analytical calculations, the stability analysis of *Gemmer et al.* (2004) and *Gemmer et al.* (2005) is expanded in Chapter 2 and Appendix B to include the changes of the detachment slope during sedimentary loading (Chapter 2). Local isostatic balancing of a seaward thinning sediment wedge creates a landward tilt of the system and adds a landward directed force (Appendix B). Gravitational failure of the system is hampered and ensuing deformation of the overburden takes place more slowly than in a non-isostatically balanced system. Analytical and numerical calculations of the stability of an isostatically balanced salt-sediment system agree very well (Figure 6.3). An interesting effect of a slightly landward tilted salt-sediment system is that tensile failure does not occur at the shelf edge as in flat-based systems, but can localize along the slope of the sediment wedge (Appendix B). This indicates that there are competing effects of a larger landward overburden (larger tensile forces vs. larger load to translate upslope), that can either stabilize or destabilize the system. The seismic section of the northwestern GoM (Figure 6.2) images a downward convex rather than a landward tilted salt basin as it evolved due to the isostatic effects of the underlying, seaward thinning crust. Such a crustal geometry has not been included in the numerical and analytical calculations and limits their comparison with the natural system to the distal half of the salt basin, where crustal thickness variations are less pronounced and a landward tilt of the system is present.

In both numerical and analytical calculations the sediment strength is controlled via a parametric description of the effects of pore-fluid pressure. The pore-fluid

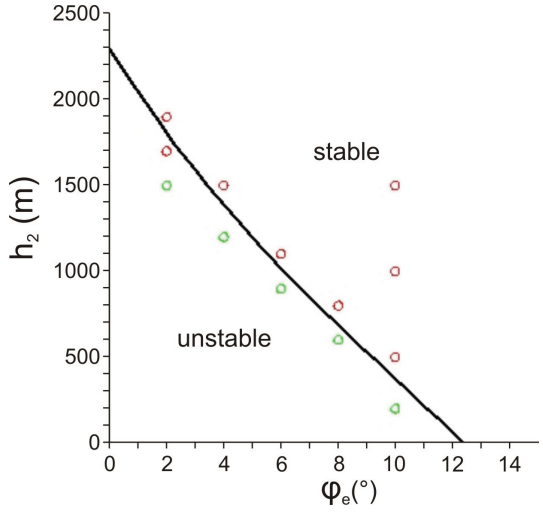

Figure 6.3: Comparison of theoretical and numerical results of stability analysis. The graph shows the necessary landward sediment thickness h_1 for failure to occur in a submerged frictional overburden above a viscous substratum as a function of sediment strength (effective internal angle of friction φ_e). Numerical model results are plotted as red and green dots (stable and unstable models). The numerical results nicely fit the theoretical results except for domains of very low and very high angles of friction.

pressure ratio λ represents the ratio of fluid pressure to mean stress and effectively reduces the internal angle of friction ($\sin\varphi_{eff} = (1-\lambda)\sin\varphi_0$). Both numerical and analytical methods conclude that a setting like the Oligocene northwestern GoM can deform on a landward sloping detachment under gravitational loading if the pore-fluid pressure ratio is sufficiently high ($\lambda = 0.8$ for typical clastic sediments with an internal angle of friction of $\varphi_0 = 30°$).

These results demonstrate that the Perdido Fold Belt could indeed have formed due to gravity spreading alone, as had been suggested but not quantified by many previous authors (*Diegel et al.*, 1995; *Peel et al.*, 1995; *Rowan et al.*, 2005). However, it raises the questions whether the pore-fluid pressure ratios in the Perdido Fold Belt were actually as high and uniform as in the numerical calculations. This issue is addressed in two companion papers (Chapters 3 and 4) that include dynamic calculations of pore-fluid pressure (*Gradmann et al.*, 2012; *Gradmann and Beaumont*, 2012). Here, sediment compaction is included as both viscous and mechanical processes and compaction-driven Darcy fluid flow in clastic sediments is coupled through the effective pressure to their frictional-plastic yielding and mechanical deformation. The strength of a given sediment column is now no longer controlled by a constant value

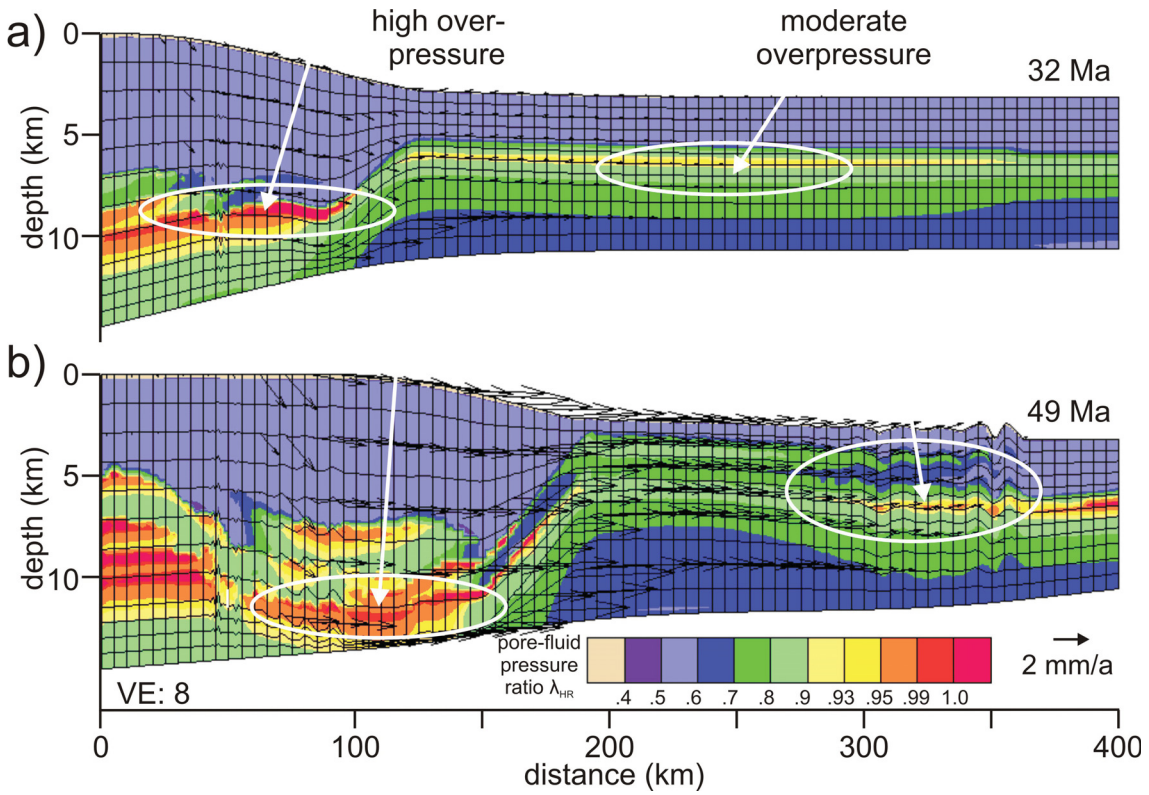

Figure 6.4: Pore-fluid pressure ratio of model ML-Q25 during (a) incipient gravity spreading and (b) strong folding.

of the pore-fluid pressure ratio, but by the location of shale-type layers embedded in sandstone-type material and their burial history. These layers easily overpressure and thereby modify the overall fluid pressure regime.

The results of these more complex models show that, in order to bring a setting like the Oligocene northwestern GoM to gravitational failure, very high pore-fluid pressure needs only to occur in the sediments above the landward end of the salt basin where the detachment surface forms and that uniformly high pore-fluid pressure is not required (Figure 6.4). High pore-fluid pressure in the distal area of the gravity-spreading system enhances deformation rates but is less crucial to gravitational failure. In order to achieve rapid deformation and strong shortening such as witnessed in the northwestern GoM, more than one shale layer, or an equivalent, with strong compaction efficiency is necessary.

6.2 Development of Salt-Tectonic Structures

The salt-tectonic structures investigated in this thesis include fold belts, salt canopies, and salt diapirs.

6.2.1 Fold Belts

Fold belts develop in the shortening domain of a gravity-spreading system (*Rowan et al.*, 2004), which can localize either at the toe-of-slope of the prograding sediment wedge or at the end of the underlying salt basin. In this thesis I demonstrated with 2D numerical models that this localization depends on the integrated shear strength of the underlying salt layer. Above thin or high-viscosity salt, sufficient strain localizes at the toe-of-slope to deform the overburden. Above thick or low-viscosity salt, little strain localizes at the toe-of-slope but more at the end of the salt basin, where subsequent deformation of the overburden occurs (Figure 6.5 and Chapter 2). A fold belt forming at the toe-of-slope grows seaward, where it can more easily mobilize salt and deform the overburden. Fold belts forming at the toe-of-slope will therefore accommodate less shortening in each anticline than those forming at the end of the salt basin, resulting in smaller fold amplitude. However, these fold belts may be longer, often extending all the way to the end of the salt basin (Chapter 2).

In Chapters 3 and 4 (*Gradmann et al.*, 2012; *Gradmann and Beaumont*, 2012), the influence of pore-fluid pressure on fold-belt formation is addressed using an expanded version of the 2D modeling software, which allows for the dynamic calculation of pore-fluid pressure. Excessive overpressure in the sedimentary overburden facilitates detaching on the overpressured sediment layer rather than on salt, leading to continuation of the fold belt beyond the salt basin. Folding is only one mode of horizontal shortening: pure-shear thickening and lateral compaction are additional modes, and their contributions to fold belt evolution are discussed in Chapter 4 (*Gradmann and Beaumont*, 2012). Whereas no clear separation into the different modes of shortening could be performed, it still becomes clear that the weakest sediments do not necessarily lead to the strongest folding. Model ML-Q35, which has a higher compaction efficiency than model ML-Q30 and therefore generates higher overpressure, develops smaller fold amplitude for same amounts of total shortening. This suggests that

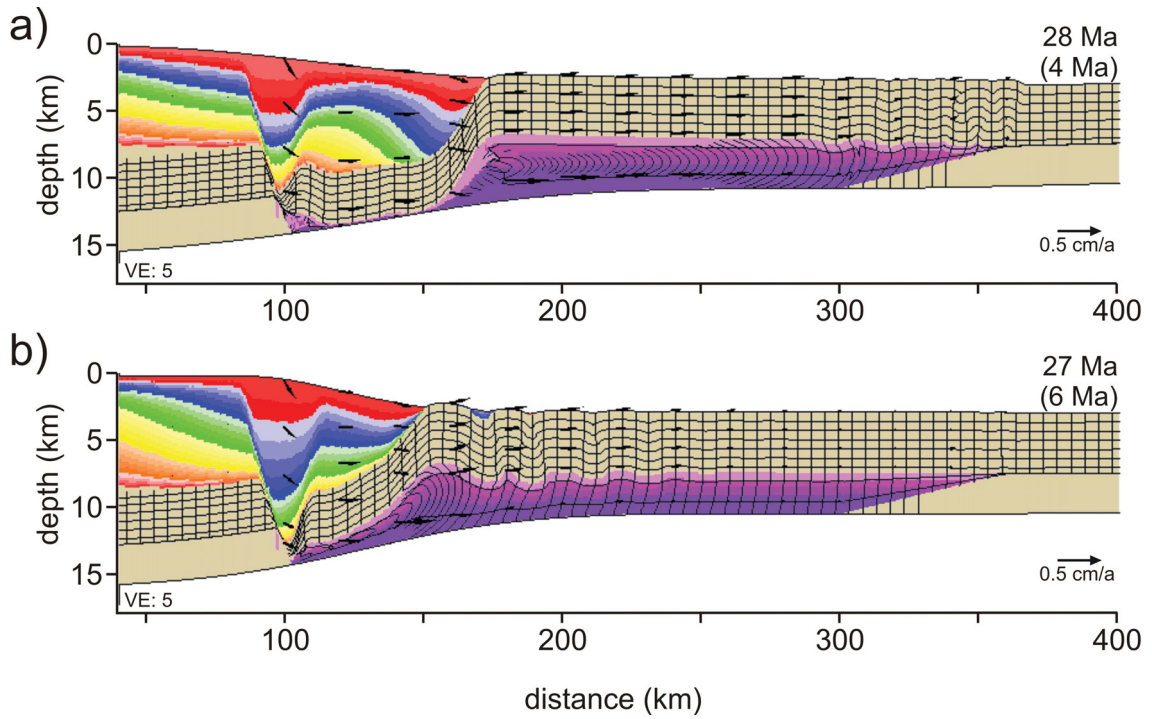

Figure 6.5: foldbelt evolution above (a) low-viscosity salt and (b) high-viscosity salt. Fold belt develops at the end of the salt basin and the toe of the slope, respectively.

compaction efficiency may contribute to shortening by lateral compaction. Another explanation could be that decompaction plays an important role in enhancing the fold anticlines, leading to larger fold amplitudes in model ML-Q30.

6.2.2 Canopies

Salt canopies are voluminous allochthonous salt structures that can extend several tens to even hundreds of kilometers along and across continental margins. They are particularly abundant in the GoM, where different generations and styles of salt canopies exist (*Peel et al.*, 1995). Salt canopies represent an exceptional form of salt mobilization where salt rises from its autochthonous level to the Earth's surface or seafloor and can then move up to several kilometers laterally (*Fletcher et al.*, 1995; *Talbot*, 1998; *Talbot and Aftabi*, 2004). In Chapter 5, the evolution of salt canopies in the center of a large salt basin (similar to the Eocene canopy in the northwestern GoM) is investigated by employing 2D finite-element models, which involve the dynamical interaction of viscous salt and frictional-plastic sediments in a gravity-spreading system.

Three different concepts of salt expulsion and canopy formation, already proposed in the literature, are tested. The squeezed diapir mechanism (1) holds that shortening of a region containing pre-existing diapirs will be absorbed by the salt (the weakest part of the system), which is then expelled onto the seafloor. The expulsion rollover mechanism (2) causes salt to be expelled laterally and to the surface from beneath evolving rollover structures and can operate in a neutral stress regime. The breached anticline mechanism (3) requires strong shortening of salt-cored folds such that the salt breaches the anticlines and is expelled to the seafloor. Where diapirs are required as precursory structures for canopy formation, their evolution is included in the models according to the mechanism of uneven sedimentation discussed in Chapter 5. This approach provides a suitable precursor phase to that of progradational sedimentation.

While all three canopy mechanisms can theoretically produce allochthonous salt structures, a true canopy, which consists of two or more coalesced salt sheets, only develops in the compressive settings of the squeezed-diapir and breached-anticline mechanisms. A mechanism operating in a neutral stress regime like the expulsion-rollover mechanism only succeeds to expel salt adjacent to strong basement highs, which effectively constitute the end of a salt basin. The concept of salt expulsion as a result of a series of minibasin developing into expulsion rollovers was not successful under the conditions tested here.

The squeezed diapir mechanism represents the most promising candidate for the development of the Eocene canopy in the northwestern GoM. It develops under similar sedimentation regimes (initially primarily aggradational, later progradational), develops similar structures around the canopy (landward faults, folded and faulted strata underneath the canopy, delayed deformation of the distal section), and the cross-sectional area of salt expelled onto the sea floor is comparable (several thousand meters by up to 50 km). Major shortcomings of the models of the other mechanisms are little or no salt extrusion (small-scale expulsion rollover mechanism and breached anticline mechanism, respectively), differences of the structures surrounding the allochthonous salt (basement high and growth wedge for large-scale expulsion rollover mechanism), and premature deformation of the sedimentary overburden above the distal end of the salt basin (breached anticline mechanism and large-scale expulsion rollover mechanism). It is also possible that the three different mechanisms may have

acted in combination or sequentially. The mechanism of breached anticlines may best explain the evolution of the younger canopy located further seaward (Figure 6.2).

6.2.3 Salt Diapirs

In recent years, diapir initiation under a brittle overburden has been mostly discussed in the context of regional extension or shortening (*Vendeville and Jackson*, 1992; *Jackson and Vendeville*, 1994; *Ings and Beaumont*, 2010). The contribution of sedimentation patterns to diapir initiation in a neutral stress regime has not been investigated and is one subject of Chapter 5. Here, numerical models are invoked that comprise a viscous salt layer progressively overlain by compacting, frictional-plastic sediments. Sedimentation occurs as uniform aggradation, laterally modulated by sinusoidal undulations. The results demonstrate that the bathymetric relief generated by, for example submarine lobes (e.g. *Deptuck et al.*, 2008), can indeed initiate diapirism when operating over a few millions of years. The sinusoidal undulations here have wavelengths of approximately 20 km and an amplitude of only 10-20 m, which corresponds to the limits of the range of dimensions of submarine lobes and other sediment gravity-flow deposits.

Although these end-member results are still preliminary and the range of parameters that lead to successful diapir evolution needs to be further investigated, they show that laterally varying sedimentation can play an important role in diapir evolution above young salt basins.

6.3 Salt-Tectonic Evolution of the Northwestern Gulf of Mexico

The northwestern Gulf of Mexico experienced at least four phases of gravity spreading (*Peel et al.*, 1995; *Radovich et al.*, 2007) and comprises a multitude of salt-tectonic structures (a salt-cored fold belt, salt-related faults, salt diapirs, salt canopies). A focus of this thesis is the circumstances that led to the youngest, Oligo-Miocene phase of gravity spreading and the associated evolution of the Perdido Fold Belt, but also addresses two older phases. During the Oligocene gravity-spreading phase, deformation took place at the level of an allochthonous salt layer (the Eocene canopy) and resulted in the formation of the Port Isabel Fold Belt. An Eocene phase of gravity

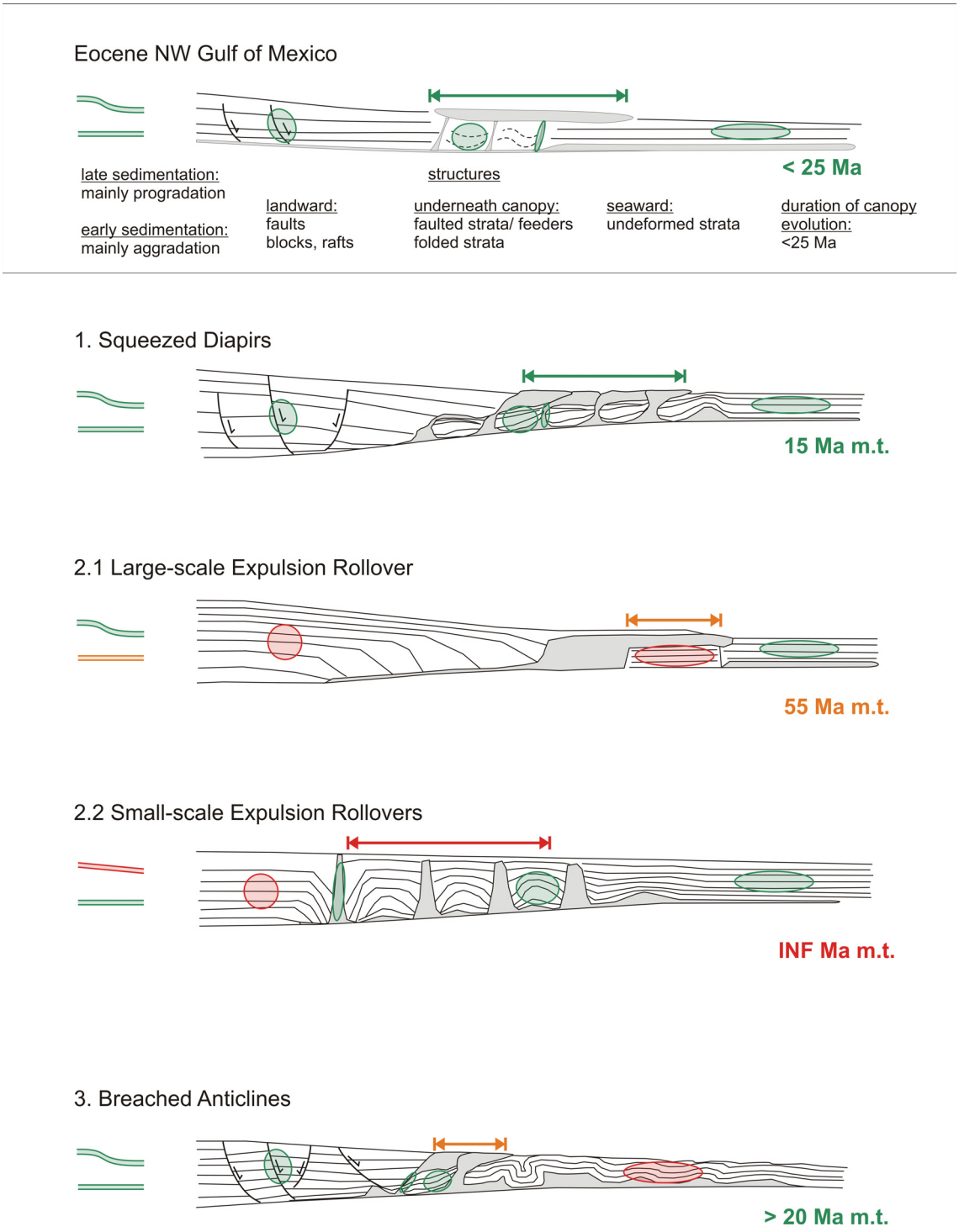

Figure 6.6: Schematic comparison of Eocene canopy in the northwestern Gulf of Mexico with those developing in the numerical models of Chapter 5. All drawings are schematic and have similar but conceptual scales. Characteristics of the Gulf of Mexico canopy are listed and highlighted in green. The markings in green, orange and red display the poor, moderate, and good agreement of the model results with the natural features, respectively. The small-scale expulsion rollover mechanism does not develop allochthonous salt structures, which is marked here as 'infinite' duration of canopy evolution.

spreading was proposed by *Peel et al.* (1995) to have formed the large-scale folding structures landward of the Perdido Fold Belt.

In this thesis, the salt-tectonic evolution of the northwestern GoM is studied beginning with the youngest, best-known and going back in time to the older, less well-known structures. It is however more logical to discuss the structural evolution in chronological order.

Although not completely unambiguous, squeezing of pre-existing diapirs constitutes the most likely mechanism for the development of the Eocene salt canopy. This result implies that a phase of diapirism existed in pre-Eocene times and that a phase of gravity spreading followed, which laterally shortened the salt structures and expelled salt onto the seafloor (Figure 6.7a). This interpretation is supported by modeling results (Chapter 5) and structural interpretation of seismic data. While the late Eocene was a time of reduced sediment supply, the Oligocene was dominated by enhanced supply of coarse clastic sediments (*Galloway et al.*, 2000). Deltaic progradation of sediments above the allochthonous salt layer may have triggered another phase of gravity spreading (model R-C1, Chapter 2). Here the décollement layer likely also comprised layers of shale deposited during the sediment-starved periods of the Oligocene (*Peel et al.*, 1995; *Diegel et al.*, 1995; *McDonnell et al.*, 2009). The autochthonous salt layer underneath the Eocene canopy was presumably already strongly evacuated and was, therefore, not easily activated as a décollement system. Continuing progradation of the deltaic sediment wedge eventually shifted the differential loading to the region where the autochthonous salt layer had not yet been strongly evacuated and triggered the onset of the last major phase of gravity spreading (model R-C1, Chapter 2).

This last phase of gravity spreading folded the 4.5 km thick section above the autochthonous salt basin into the Perdido Fold Belt. In Chapter 2 (*Gradmann et al.*, 2009) it is demonstrated with numerical and analytical calculations that such gravity-driven deformation could only occur if high fluid pressure existed in the overburden. In Chapter 4 (*Gradmann and Beaumont*, 2012), this inference is refined by employing dynamic calculations of compaction-induced fluid pressure. It is shown that very high overpressure only needed to exist in the landward end of the gravity-spreading system. The effective strength of a sediment column can be easily reduced by efficiently

compacting and overpressuring shale layers embedded in more permeable (sandstone-type) material. It is demonstrated that the early Paleocene and Eocene shale layers in the stratigraphic column of the northwestern GoM would have provided sufficiently effective reduction of integrated sediment strength.

The canopy that is located above the most landward part of the Perdido Fold Belt likely formed coevally with this shortening structure. Fold anticlines become weakened when they are strongly shortened and buoyant salt can pierce through its overburden (Chapter 2 and 5). Only small amounts of salt will extrude to the surface forming a patchy canopy as described from seismic data (*Fiduk et al.*, 1999).

The formation of the Perdido Fold Belt and Perdido Canopy were the latest major salt-tectonic activities in the northwestern GoM. Without considering minor reactivation phases during the late Miocene (*Waller*, 2007), this thesis comprises the study of nearly the entire Cenozoic salt-tectonic evolution of the northwestern GoM (latest Paleocene to present). The prior evolution may have involved diapirism (Chapter 5) and a first phase of gravity spreading (*Radovich et al.*, 2007).

6.4 Summary and Outlook

This thesis has addressed several aspects of salt-tectonic deformation on a continental margin - both in general and with respect to the Cenozoic evolution of the northwestern Gulf of Mexico. These aspects include the evolution of a Eocene salt canopy (probably preceded by diapirism), its role as a décollement layer during Oligocene, the re-activation of the allochthonous salt detachment and associated evolution of the Perdido Fold Belt, as well as the development of a late Oligocene-Miocene canopy above the fold belt. The studies employed 2D finite element numerical models that comprise a viscous salt layer overlain by compacting, frictional-plastic sediments.

A new mechanism of diapir evolution has been tested that can operate in a neutral regional stress regime and employs the effects of uneven sedimentation. Local isostatic compensation of bathymetric features leads to formation of salt highs and under continuing sedimentation to evolving diapirs. Though it cannot be resolved whether this mechanism is applicable the early evolution of the GoM, it demonstrates the effects of salt-sediment interaction occurring during diapir evolution.

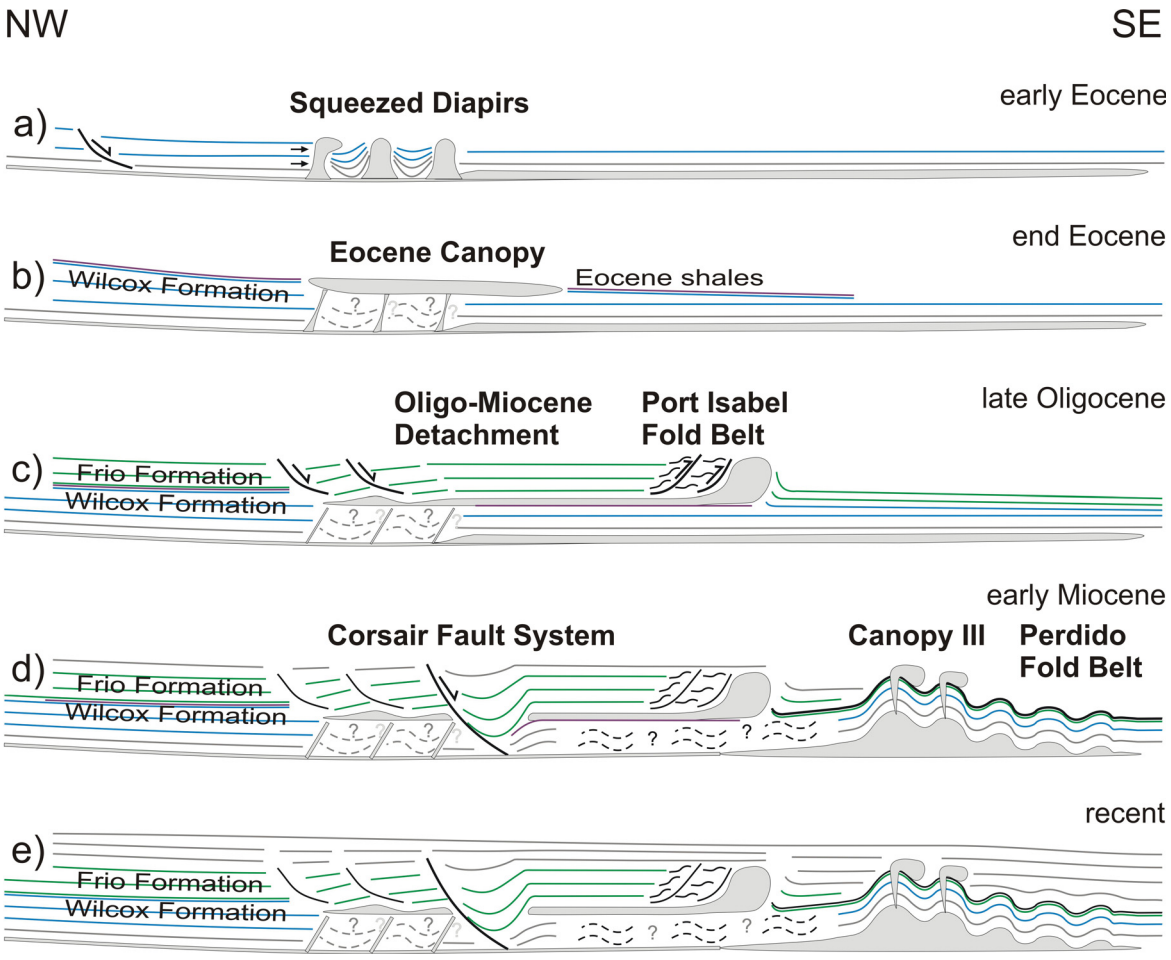

Figure 6.7: Schematic evolution of the northwestern Gulf of Mexico.

Three different mechanisms of canopy evolution have been tested: 1) The mechanism of squeezed diapirs, 2) the mechanism of expulsion rollovers, and 3) the mechanism of breached anticlines. All three canopy mechanisms can, in general, produce allochthonous salt structures, but only the models of squeezed diapirs and breached anticlines develop a true canopy. The first mechanism, which requires the evolution of diapirs as precursory structures, is here considered the most likely candidate for the formation of the Eocene canopy in the northwestern GoM. Its overall sedimentation and stress regimes as well as the evolving structures (inverted minibasins, closed feeders) match well those reported from the natural example.

The evolution of the Perdido Fold Belt occurred much later than the emplacement of the Eocene canopy. In Chapter 2 (*Gradmann et al.*, 2009) we suggested that the autochthonous salt layer underneath the canopy had been mostly evacuated and that increased sediment deposition extending beyond the canopy (associated with Oligocene shelf progradation, *Galloway et al.*, 2000) can successfully trigger a new phase of gravity spreading on the autochthonous salt layer. The quantitative failure conditions of a salt-bearing, isostatically balanced continental margin system were investigated analytically (expanding on previous work by *Gemmer et al.*, 2004, 2005) and numerically. Both approaches revealed that the late Oligocene folding of the 4.5 km thick sequence now forming the Perdido Fold Belt can indeed have been driven by gravitational spreading alone, if fluid pressure weakened the overburden sufficiently (pore-fluid pressure ratio $\lambda = 0.8$). These values were refined using numerical models that couple compaction-induced fluid pressure and mechanical deformation (*Morency et al.*, 2007). Chapters 3 and 4 (*Gradmann et al.*, 2012; *Gradmann and Beaumont*, 2012) show that in order to induce failure, high fluid pressure is primarily required at the base of the extending overburden, while moderate fluid pressure in the remaining overburden (e.g. induced by two or more shale layers) is sufficient.

These coupled models further showed that sediment compaction can accommodate a significant amount of shortening, again applied to the deep-water setting of the Perdido Fold Belt. Consequently, the compaction efficiency of a sedimentary layer can influence the style of folding (e.g. fold amplitudes), depending on the contribution of different modes to shortening (compaction, folding, pure-shear thickening). Folding in a gravity-spreading system can localize at the toe-of-slope of the prograding sediment

wedge or at the end of the underlying salt basin. In Chapter 2 (*Gradmann et al.*, 2009) we demonstrated that this localization depends on the shear strength of the underlying salt layer (thin and high-viscosity salt vs. thick and low-viscosity salt).

Strong folding, as predicted for end-of-salt folding, can effectively weaken the overburden such that buoyant salt can breach the anticlines and extrude to the seafloor. This mechanism has been investigated as one of the concepts of canopy evolution and is here regarded as the process that formed the salt canopy over and adjacent to the Perdido Fold Belt.

The work presented in this thesis has contributed significantly to current salt-tectonic research. The work on the northwestern GoM itself may assist the more detailed understanding of salt-related structures and be of benefit in hydrocarbon exploration. Many findings that were obtained by studying the northwestern GoM can be applied to other continental margin salt basins (such as the stability analysis, the mechanisms of diapir and canopy evolution). The use of numerical models facilitated analysis and visualization of the salt-tectonic processes on a continental margin, which is especially important and helpful for the understanding of the large-scale linking between upslope and downslope processes. Dynamic calculations of pore-fluid pressure have, for the first time, been applied to a salt-tectonic system and revealed strong feedback effects between compaction and deformation, which have been previously known but only poorly understood and quantified.

Deep-water exploration in the northwestern GoM will continue and expand over the next years and it will be interesting to see what new information will be revealed about its salt-tectonic and structural evolution. The basic experiments I did on diapir evolution induced by uneven sedimentation have recently been expanded to investigate the effects of different sediment compaction behavior and sedimentation patterns (*Goteti et al.*, 2012). Many additional investigations on early salt-sediment interaction can be envisaged (effects of lateral density variations, layered salt-sediment system, or regional stress regimes). Effects of three-dimensional salt flow cannot be tested with the current software, but may play a significant role in early salt-sediment interaction (enhanced diapir growth rate, change of preferred minibasin wavelength) and in the regional evolution of canopies (coalescense of adjacent sheets, expulsion of underlying salt). My work on the coupled evolution of fluid pressure in sediments and

salt-tectonic deformation can be seen as a first step in understanding the structural evolution in many sedimentary basins. Of particular interest would be the detailed stress and pressure regimes in fold belts or around diapirs, together with their relative feedback effects. For this, higher resolution models and a better treatment of the numerical effects outlined in Chapter 4 would be required.

The work presented here may thus in many ways help future studies and enable continued research on salt-tectonic processes on continental-margin scale, in deep-water settings or with respect to local salt-sediment and fluid interactions.

Appendix A

Glossary of Salt-Tectonic Terminology

active diapirism Salt piercing through its overburden in response to buoyancy forces.

allochthonous salt Sheet-like body of salt at a stratigraphic level higher than its own depositional (autochthonous) one (*Jackson and Talbot*, 1991).

autochthonous salt Salt at its depositional level.

diapir Mass of salt that has flowed ductilely and appears to have (often together with its roof) discordantly pierced or intruded the overburden (*Jackson and Talbot*, 1991).

downbuilding See passive diapirism.

expulsion rollover Prograding sediment wedge that laterally expels salt.

gravity gliding Movement of a rock mass above a weak detachment surface induced by the slope of the detachment. Internal deformation does not necessarily occur (*Schultz-Ela*, 2001).

gravity spreading Movement of a rock mass above a weak detachment surface (regardless of its slope) induced by the differential loading of the overburden. Lateral extension and vertical contraction of the rock mass occur (*Schultz-Ela*, 2001).

minibasin Sedimentary basin of several kilometers extent surrounded by shallow (near-surface), thick salt, which can subside rapidly owing to withdrawal of the underlying salt (*Hudec et al.*, 2009).

passive diapirism Growth of diapir as sediments accumulate around it. During this process of downbuilding, the additionally deposited sediments exert a load

on the diapirs flanks, squeeze more of the underlying salt into the diapir and create additional accommodation space.

namakier Subaerial allochthonous salt sheet. Equivalent to salt glacier.

reactive diapirism Vertical salt movement in response to local thinning of the overburden during regional extension. Salt is driven by lateral load gradients and fills the space created by extension.

salt canopy Two or more coalesced salt sheets.

salt feeder Sub-vertical salt body that links deep to near-surface salt.

salt glacier Subaerial allochthonous salt sheet. Equivalent to namakier.

salt nappe Allochthonous salt structure forming at the depositional end of the salt basin. Often formed in a thrust-like style.

salt roller Triangular shaped salt body with a single, dominant bounding fault. Common structure below rotating blocks in extensional setting.

salt sheet Body of allochthonous salt with one feeder, the sub-horizontal dimension of which is several times larger than is vertical one (*Jackson and Talbot*, 1991; *Hudec and Jackson*, 2006).

salt tongue Sub-horizontal allochthonous salt structure formed on the seafloor usually from a seaward leaning, extruding diapir.

salt weld Original location of now depleted salt layer which marks a fault-like unconformity between pre- and post-salt strata.

salt wing Sheet-like salt body that intruded from the flank of a diapir into weak, adjacent strata, e.g., into a pre-existing salt layer.

turtle structure Structure of inverted minibasin that develops when the flanks of the minibasin subside owing to salt withdrawal after the minibasin grounds at the base of the salt layer.

Appendix B

Stability Analysis of Continental Margin System over Viscous Substratum

B.1 Introduction

The stability of a continental margin system above salt has been analytically determined by *Gemmer et al.* (2004, 2005) and expanded to the isostatically balanced case in Chapter 2 (*Gradmann et al.*, 2009). A shortcoming of the latter is that tensile failure was assumed to always occur along the shelf edge. This chapter shows that this is not necessarily the case, and additionally compares the results of the analytical solution to numerical experiments, thereby testing both software and calculations.

A simplified continental margin system is shown in Figure B.1 and consists of a wedge-shaped, frictional overburden and a viscous salt layer of constant thickness. Owing to the differential height of the overburden the system may fail and develop an extensional setting upslope and a compressional setting downslope with the central part of the overburden sliding basinward. This behavior of gravity spreading has been observed on many continental margins (Gulf of Mexico, Angola, Eastern Mediterranean, *Worral and Snelson* (1989); *Tari et al.* (2003)) and studied in physical experiment (*Vendeville and Jackson*, 1992; *Letouzey et al.*, 1995; *Koyi*, 1996; *Ge et al.*, 1997; *Krezsek et al.*, 2007).

B.2 Horizontal Force Balance - Isostatically Balanced System Including Water Load

The continental margin can be regarded as a system on which different horizontal forces act (Figure B.2). These forces are the tensile force F_1 that results from the attempt of the wedge-shaped overburden to level out, the force F_2 that resists the thickening or thrusting of the seaward sediment layer, the downhill-slope force F_{iso}, the drag force F_p that results from the Poiseuille flow induced in the viscous layer,

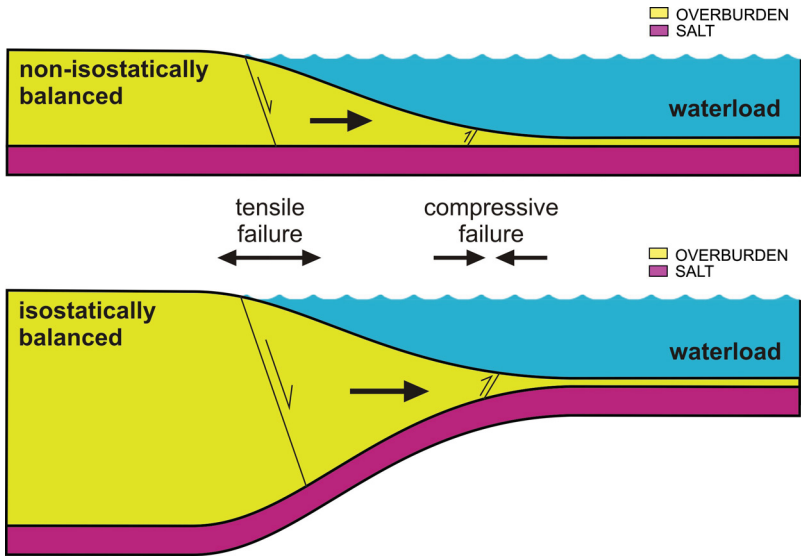

Figure B.1: Schematic picture of gravity spreading in a non-isostatically balanced and an isostatically balanced continental margin system underlain by a layer of salt.

and the force of the water load F_w, which can be regarded as an additional buttressing force. If the forces in the downslope direction prevail, the overburden will fail and start to slide basinward. To be precise, a net force acting basinward cannot exist. It would be counterbalanced by a frictional force that results from the shearing of the substratum. Its magnitude depends on the sliding velocity that induces the Couette flow in the substratum. To determine the conditions for failure, the frictional force of the Couette flow is not needed (since at the point of failure the sliding velocity and therefore the frictional force will be zero). The horizontal force balance then states

$$F_1 + F_2 + F_p + F_{iso} + F_w = 0. \tag{B.1}$$

The different forces are calculated in the following sections. Where possible, the derivations of Chapter 2 (*Gradmann et al.*, 2009) are used. The terminology of the different parameters used in the analytical stability analysis is explained and listed in Figure B.3. The salt-sediment system is here directly underlain by material of the lithospheric mantle, which is displaced during isostatic adjustment. A crustal layer is omitted, as it plays no part in the isostatic considerations.

Table B.1: Parameters used in limit analysis for margin stability.

Symbol	Parameter
Geometry	
x_1, x_2	location of tensile and compressive failure
$h(x)$	thickness of overburden
h_1=$h(x_1)$	thickness of overburden at location of tensile failure
h_2=$h(x_2)$	thickness of overburden at location of compressive failure
h_0	distance from water level to reference level
h_{w1}, h_{w2}	height of the water column at location of tensile and compressive failure
h_c	thickness of salt layer
$h_m(x)$	thickness of lithospheric mantle relative to lowest point of sedimentary system
$\overline{h}_m(x)$	thickness of mantle material expelled by overburden during isostatic adjustment
$\alpha_1(x)$	slope of seafloor
$\alpha_2(x)$	slope of base of the system
Material Properties	
φ_0	internal angle of friction
φ_e	effective angle of friction, modified by pore-fluid pressure
λ	pore-fluid pressure ratio, defined as ratio of fluid pressure to mean stress (equation B.10)
ρ_w	density of water
ρ_s	density of salt and sediment
ρ_m	density of lithospheric mantle

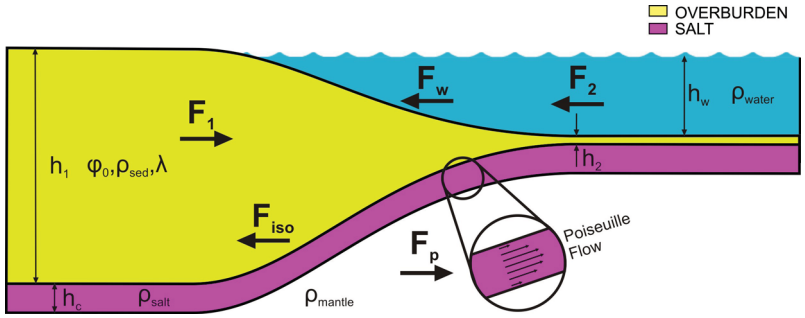

Figure B.2: Forces acting on a continental margin system underlain by a layer of salt. F_1: force of tensile stresses, F_2: force of compressive stresses, F_p: force due to drag of Poiseuille flow induced by pressure difference, F_{iso}: downhill-slope force of sedimentary overburden, F_w: buttress force of water load.

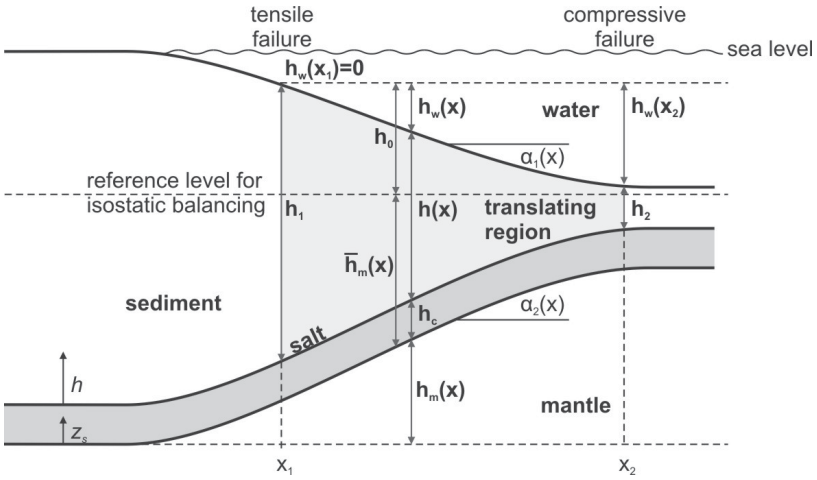

Figure B.3: Schematic of continental margin wedge underlain by a layer of salt. Isostasy bends the landward part down. A crustal layer is omitted here, as it plays no part in the isostatic considerations. The terminology is described in Table B.1.

A few Geometric Relations

Airy isostasy and geometric considerations yield

$$(h(x) + h_c)\,\rho_s + h_w(x)\,\rho_w = \overline{h}_m(x)\,\rho_m \tag{B.2}$$

$$h_w(x) + h(x) + h_c = h_0 + \overline{h}_m(x) \tag{B.3}$$

Combining the above equations yields

$$h_w(x) = h_0 \frac{\rho_m}{\rho_m - \rho_w} - (h(x) + h_c) R \quad \text{with} \tag{B.4}$$

$$R = \frac{\rho_m - \rho_s}{\rho_m - \rho_w}. \tag{B.5}$$

It follows that

$$h_{w1} = h_{w0} - R\, h_1 \tag{B.6}$$

$$h_{w2} = h_{w0} - R\, h_2 = h_{w1} + R\,(h_1 - h_2), \tag{B.7}$$

where $h_{w0} = h_0 \frac{\rho_m}{\rho_m - \rho_w} - h_c R$ corresponds to the water depth over the isostatically balanced salt layer if no sedimentary overburden was present. Equations (B.2) and (B.3) furthermore yield

$$\overline{h}_m(x) = (h(x) + h_c)(1 - R) + h_0 \frac{\rho_w}{\rho_m - \rho_w}$$

$$\frac{d\, h_m(x)}{dx} = (1 - R) \frac{dh(x)}{dx}. \tag{B.8}$$

Tensile and Compressive Forces F_1 and F_2

The deviatoric tensile and compressive stresses in a volume of frictional material are very difficult to calculate in a stress field below yield. However, since we are interested in the behavior at yield, we can make use of the yield criterion:

$$\sigma_{e1} - \sigma_{e3} = (\sigma_{e1} + \sigma_{e3}) \sin\varphi_0 + C \cos\varphi_0 \tag{B.9}$$

where σ_{e1} and σ_{e3} are the minimum and maximum effective stresses, respectively, (the stress reduced by the pore-fluid pressure p_f, $\sigma_e = \sigma - p_f$), φ_0 is the internal angle of friction, and C is the cohesion. In the presented case, the cohesion is considered negligible because the other stresses (e.g. overburden weight) are orders of magnitude larger. The pore-fluid pressure is parameterized by its ratio to the mean stress

(equation B.10), which, for sub-aqueous systems, gives:

$$\lambda = \frac{p'_f}{p'} = \frac{p_f - p_w}{p - p_w} = \frac{p_f - p_w}{\frac{\sigma_1+\sigma_3}{2} - p_w} \tag{B.10}$$

Equation (B.9) can then be rewritten as

$$\sigma'_1 - \sigma'_3 = (\sigma'_1 + \sigma'_3)\,\sin\varphi_e \qquad \text{with} \tag{B.11}$$

$$\sin\varphi_e = (1-\lambda)\sin\varphi_0 \quad \text{and} \tag{B.12}$$

$$\sigma' = \sigma - p_w. \tag{B.13}$$

In the example of the continental margin system, the maximum stress in the extensional setting is the vertical stress σ_{zz}, the minimum stress is the horizontal stress σ_{xx}. In the compressive setting, minimum and maximum stresses are oriented in the opposite way. The following relations for σ'_{xx} and σ'_{zz} are then obtained from equation (B.11)

$$\sigma'_{xx} = \sigma'_{zz}\,k_a \qquad (extension) \tag{B.14}$$

$$\sigma'_{xx} = \sigma'_{zz}\,k_p \qquad (shortening) \tag{B.15}$$

$$k_a = \frac{1-\sin\varphi_e}{1+\sin\varphi_e} \tag{B.16}$$

$$k_p = \frac{1}{k_a} = \frac{1+\sin\varphi_e}{1-\sin\varphi_e}, \tag{B.17}$$

with σ'_{zz} being the weight of the overburden excluding the water load p_w.

$$\sigma_{zz} = \sigma'_{zz} + p_w = \rho_s\,g\,h(x) + \rho_w\,g\,h_w(x) \tag{B.18}$$

To calculate the total horizontal force for either tensile or compressive failure in the overburden, we need to integrate the horizontal stresses vertically throughout the

overburden:

$$F_1 = \int_0^{h_1} \sigma_{xx,\,extension}\, dh = \int_{h_1}^{0} (k_a\, \rho_s\, g\, h(x) + \rho_w\, g\, h_{w1})\, dh$$

$$\boxed{F_1 = \frac{1}{2}\, k_a\, g\, \rho_s\, h_1^2 + \rho_w\, g\, h_{w1}\, h_1} \qquad \text{(B.19)}$$

with h_{w1} given in equation (B.6).

For the case of compressive failure

$$F_2 = \int_0^{h_2} \sigma_{xx,\,shortening}\, dh = -\int_{h_2}^{0} (k_p\, \rho_s\, g\, h(x) + \rho_w\, g\, h_{w2})\, dh$$

$$\boxed{F_2 = -\frac{1}{2}\, k_p\, g\, \rho_s\, h_2^2 - \rho_w\, g\, h_{w2}\, h_2} \qquad \text{(B.20)}$$

with h_{w2} given in equation (B.7).

ρ_s is the overburden density and h_1 and h_2 are the sediment thicknesses at tensile and compressive failure, respectively. In Chapter 2 (*Gradmann et al.*, 2009) it was considered that h_{w1}=0 and hence $F_1 = \frac{1}{2}\, \rho_s\, g\, k_a\, h_1^2$.

Poiseuille-Flow Force F_p

A Poiseuille (or channel) flow is induced in a viscous layer by the pressure difference of the overburden and by the slope of the viscous layer itself. The shear stress exerted on the boundary of the viscous layer integrated over the entire failing section gives the total horizontal force. The flow is driven by the pressure difference across the viscous layer. Because this does not depend on the water load itself but on its difference across the failing region, the Poiseuille-flow force is as calculated in Chapter 2 (*Gradmann et al.*, 2009):

$$\boxed{F_p = \frac{1}{2}\, g\, R\, (\rho_s - \rho_w)\, h_c\, (h_1 - h_2)}. \qquad \text{(B.21)}$$

Downslope (Gliding) Force Owing to Isostasy F_{iso}

The tilt of the base of the system adds an extra gravity-induced downslope (gliding) force to the system. This force is simply calculated by

$$F_{iso} = \int_{x_1}^{x_2} F_G \, \sin\alpha_2(x) \, dx \tag{B.22}$$

where

$$F_G = \rho_s \, g \, h(x) + \rho_w \, g \, h_w(x) \text{ and} \tag{B.23}$$

$$\sin\alpha_2 \approx \tan\alpha_2 = \frac{d\,h_m(x)}{d\,x} = (R-1)\frac{d\,h(x)}{d\,x} \tag{B.24}$$

according to equation (B.8). It follows that

$$F_{iso} = \int_{h_1}^{h_2} \rho_s \, g \, h(x) \cdot (1-R) \, dh(x) + \int_{h_{w1}}^{h_{w2}} \rho_w \, g \, h_w(x) \cdot \frac{1-R}{R} \, dh_w(x)$$

$$\boxed{F_{iso} = -\frac{1}{2}\,\rho_s \, g \, (1-R)(h_1^2 - h_2^2) - \frac{1-R}{R}\,\frac{1}{2}\,\rho_w \, g \, (h_{w2}^2 - h_{w1}^2)}. \tag{B.25}$$

This result is again slightly different than in Chapter 2 (*Gradmann et al.*, 2009), where h_{w1}=0 and $h_{w2} = R\,(h_1 - h_2)$.

Force of Water Load F_w

The water exerts a buttress force against the seaward movement of the overburden. This force is the integrated pressure of the water column that acts on the overburden.

$$F_w = \int_{h_w(x_1)}^{h_w(x_2)} \rho_w \, g \, h_w(x) \, dh_w(x)$$

$$\boxed{F_w = -\frac{1}{2}\,\rho_w \, g \;\, (h_{w2}^2 - h_{w1}^2)} \tag{B.26}$$

As in Chapter 2 (*Gradmann et al.*, 2009), this equation is again simplified to

$$F_w = -\frac{1}{2}\,\rho_w \, g \;\, R^2 (h_1 - h_2)^2. \tag{B.27}$$

Force Balance

At the point of failure the horizontal forces balance states

$$\begin{aligned}
0 &= F_1 + F_2 + F_p + F_{iso} + F_w \\
&= \frac{1}{2}\,k_a\,g\,\rho_s\,h_1^2 + \rho_w\,g\,h_{w1}\,h_1 - \frac{1}{2}\,k_p\,g\,\rho_s\,h_2^2 - \rho_w\,g\,h_{w2}\,h_2 \\
&\quad + \frac{1}{2}\,g\,R\,(\rho_s - \rho_w)\,h_c\,(h_1 - h_2) \\
&\quad - \frac{1}{2}\,\rho_s\,g\,(h_1^2 - h_2^2)\,(1-R) - \frac{1-R}{R}\,\frac{1}{2}\,\rho_w\,g\,(h_{w2}^2 - h_{w1}^2) \\
&\quad - \frac{1}{2}\,\rho_w\,g\;(h_{w2}^2 - h_{w1}^2) \\
&= \frac{1}{2}\,\rho_s\,g\,h_1^2\,(k_a - (1-R)) - \frac{1}{2}\,\rho_s\,g\,h_2^2\,(k_p - (1-R)) \\
&\quad - \frac{1}{2}\,\rho_w\,g\,(h_{w2}^2 - h_{w1}^2)\left(\frac{1-R}{R} - 1\right) \\
&\quad - \frac{1}{2}\,R\,(\rho_s - \rho_w)\,g\,(h_1 - h_2)\;h_c + \rho_w\,g(h_{w1}\,h_1 - h_{w2}\,h_2)
\end{aligned} \tag{B.28}$$

By substituting h_{w2} with $h_{w1}+R(h_1-h_2)$, dividing by $\frac{1}{2}\,\rho_s\,g\,h_c^2$ (non-dimensionalizing), and introducing the non-dimensional parameters $h^* = h/h_c$, $\rho_w^* = \rho_w/\rho_s$, the following relations are obtained

$$\begin{aligned}
0 &= h_1^{*2}\,(k_a - 1 + R) - h_2^{*2}\,(k_p - 1 + R) + (h_1^* - h_2^*)\,R\,(1 - \rho_w^*) \\
&\quad - \rho_w^*\frac{1}{R}\;\left(2\,R\,h_{w1}^*\,(h_1^* - h_2^*) + R^2\,(h_1^* - h_2^*)^2\right) \\
&\quad + 2\,\rho_w^*(h_{w1}^*\,h_1^* - h_{w1}^*\,h_2^* + R\,(h_1^* - h_2^*)\,h_2^*) \\
&= h_1^{*2}\,(k_a - 1 + R) - h_2^{*2}\,(k_p - 1 + R) \\
&\quad + (h_1^* - h_2^*)\,R\,(1 - \rho_w^*) - \rho_w^*\,R\;\left((h_1^* - h_2^*)^2 - 2\,(h_1^* - h_2^*)\,h_2^*\right) \\
&= h_1^{*2}\,(k_a - 1 + R) - h_2^{*2}\,(k_p - 1 + R) \\
&\quad + (h_1^* - h_2^*)\,R\,(1 - \rho_w^*) - \rho_w^*\,R\,(h_1^{*2} - h_2^{*2}) \\
&= h_1^{*2}\,(k_a - 1 + R - \rho_w^*\,R) - h_2^{*2}\,(k_p - 1 + R - \rho_w^*\,R) + (h_1^* - h_2^*)\,R\,(1 - \rho_w^*).
\end{aligned} \tag{B.29}$$

From the relation of these parameters, a yield criterium can be defined for a given set of properties of a continental margin setting. If the densities, the internal angle of

friction, the salt layer thickness, and the sediment thickness at the shelf are given, the horizontal force balance allows prediction of the maximum basinward thickness for which the system would be unstable. For example, for given values of ρ_s=2300 kg/m^3, ρ_m=3300 kg/m^3, φ_e=10°, h_c=1000 m, h_1=2300 m, the limiting basinward thickness of h_2 is 600 m. This means that a sediment pile thicker than 600 m in the basin would prevent the entire system from failing and the overburden from sliding, a system with a sediment layer thinner than 600 m in the basin would fail. This relationship is plotted in Figure B.4, here with the limiting basinward sediment thickness h_2 as a function of the effective internal angle of friction φ_e. The relationships are calculated for different values of the shelf sediment thickness h_1. The domain of small h_2 and φ_e represents unstable systems. For greater values of h_2 and φ_e the system is stable. The graphs for different values of h_1 intersect, which only occurs for isostatically balanced systems. This circumstance allows certain models to develop an extensional zone along the slope, not at the shelf edge. This behavior is further analyzed and discussed in section B.5.

In order to get an impression of the order of magnitude of the forces contributing to the force balance, Figure B.5 shows the values of the forces F_1, F_2, F_p, F_{iso} and F_w as a function of the internal angle of friction. The graph shows that F_1 and F_{iso} contribute most to the force balance.

B.3 Comparison of Analytical and Numerical Calculations of System Including Water load

The theory derived above should predict the behavior of finite element models. Several models with same values for h_1, h_c, ρ_s and ρ_m but different input parameters for h_2 and φ_e were run using the software SOPALE, described in Chapter 2. In plots of strain rates and displacement velocities (Figure B.6) it can be seen that models behave either stable or unstable, depending on values of h_2 and φ_e. Figure B.7 shows the comparison of analytic theory and finite element models. They match very well except for regions of extremely low effective angles of friction.

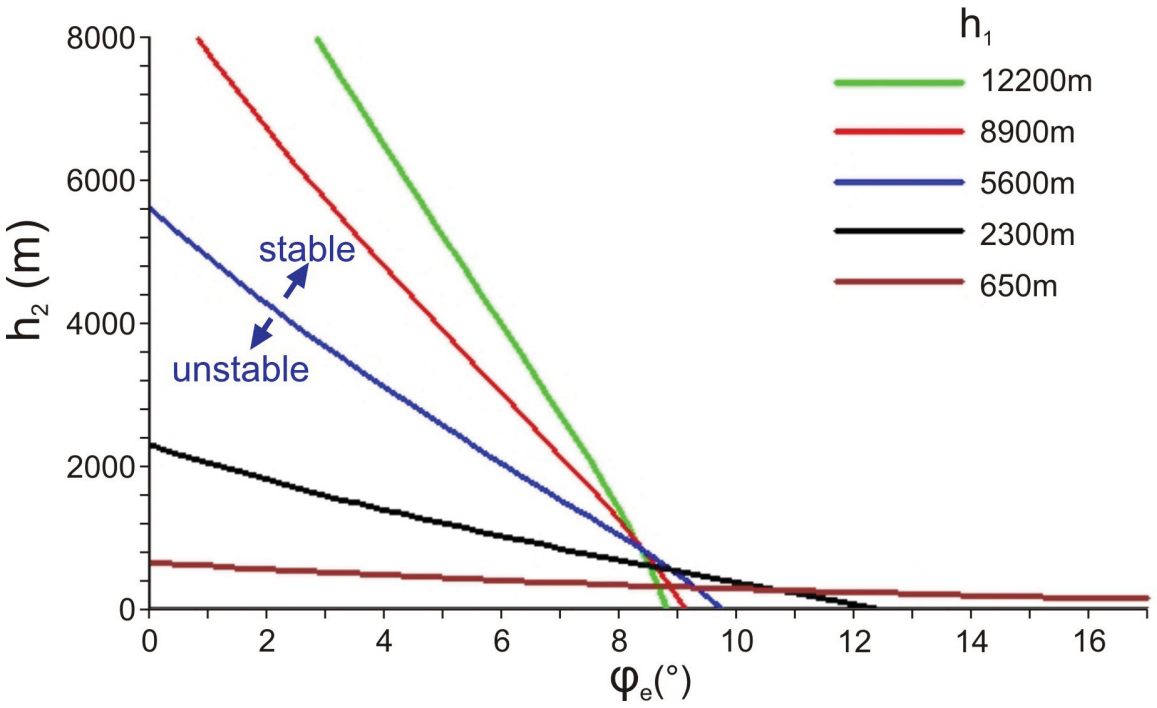

Figure B.4: Dependance of seaward sediment thickness h_2 on the effective internal angle of friction φ_e for a seaward sliding frictional overburden at failure submerged under water and underlain by a viscous substratum. For all curves, salt and sediment density ρ_s is 2300 kg/m^3, mantle density ρ_m is 3300 kg/m^3, water density ρ_w is 1000 kg/m^3, salt layer thickness h_c is 1000 m and the landward sediment thickness h_1 varies as shown in the plot. The graphs show that systems become unstable for weaker sediments (lower φ_e), smaller seaward sediment thickness h_2, or larger landward sediment thickness h_1.

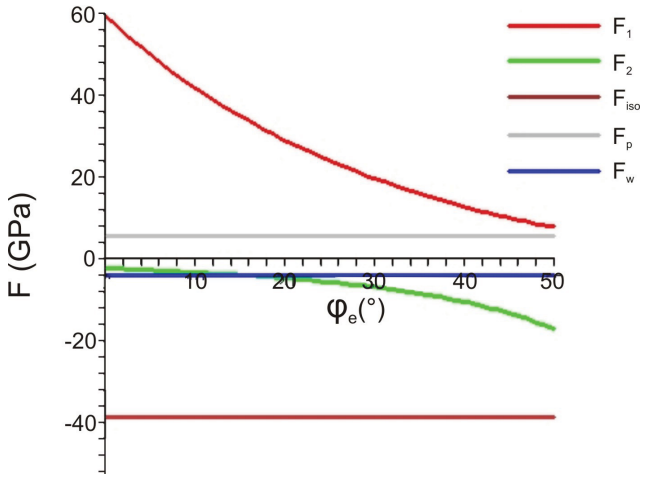

Figure B.5: Plot of the forces contributing to the horizontal force balance as a function of the internal angle of friction. Parameters are as for Figure B.4 with h_2=200 m and h_1=2300 m.

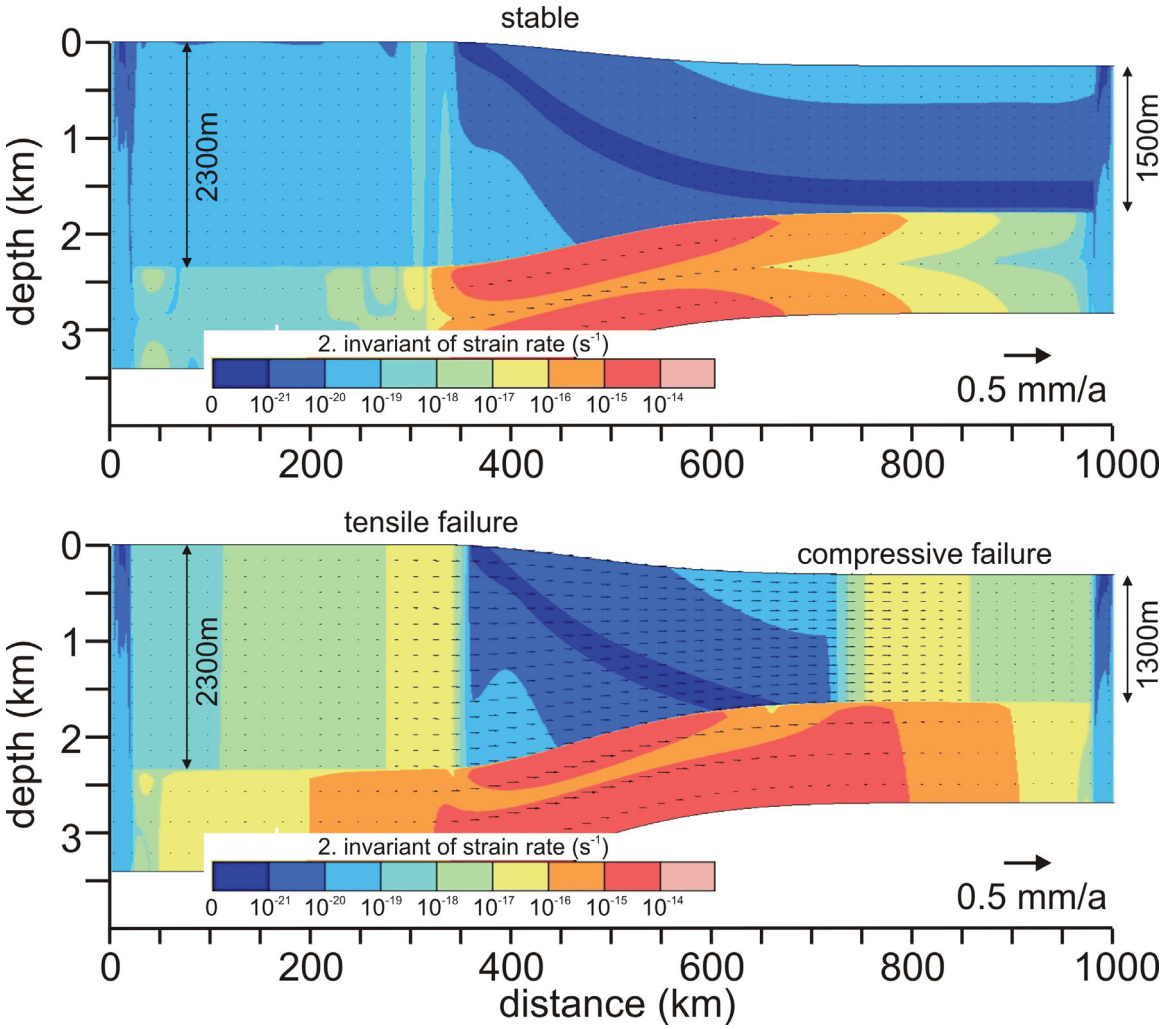

Figure B.6: Two finite element models of an isostatically balanced, wedge-shaped frictional-plastic overburden overlying a 1000 m thick, viscous salt layer. The plots show strain rates and displacement velocities. The two models differ in the seaward sediment thickness (h_2=1500 m and h_2=1300 m) but have the same landward sediment thickness (h_1=2300 m), same salt, sediment and mantle densities (ρ_s=2300 kg/m^3, ρ_m=3300 kg/m^3) and same overburden strength ($\varphi_e = 5°$). The first model, which is considered stable, shows very small strain rates in the overburden and a Poiseuille-type velocity distribution in the salt layer. The second model, which is considered unstable, shows high strain rates and displacement velocities at the shelf edge (zone of extension) and at the toe of the slope (zone of shortening).

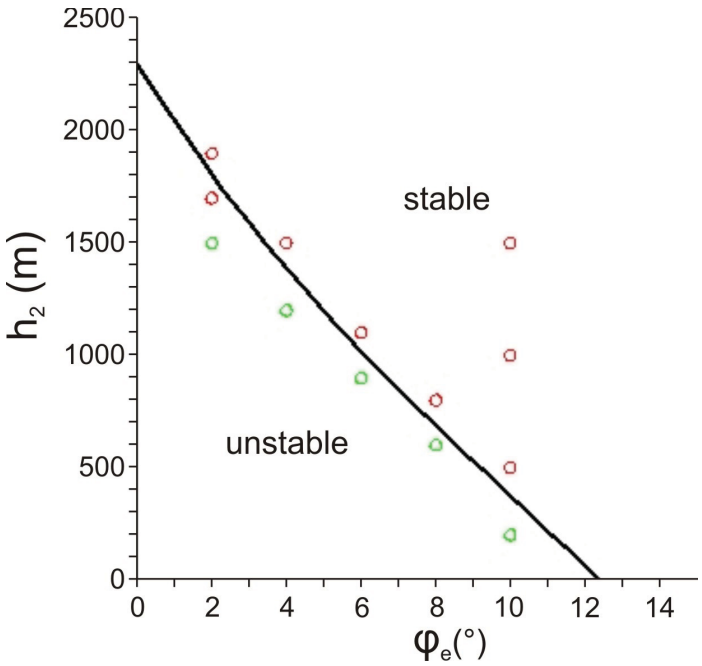

Figure B.7: Comparison of theoretical and numerical results of stability analysis. The graph shows the stability criteria for a frictional overburden submerged under water above a viscous substratum as a function of h_2 and φ_e with h_1=2300 m and all other parameters as for Figure B.4. The numerical model results are plotted as red and green dots (stable and unstable models, respectively). The numerical results fit very well the theoretical results except for domains of very low effective angles of friction.

B.4 Additional, Simplified Cases of the Stability Analysis

The above derived equations can easily be simplified for the case of a non-submerged continental margin and for the non-isostatically balanced case already considered by *Gradmann et al.* (2005). For completion, the respective force balance equations are presented here and the comparison to the numerical solutions is shown.

B.4.1 Stability Analysis for a Continental Margin System Without Water Load

The case of a non-submerged continental margin can be derived from the equations of the previous section by setting ρ_w=0 and p_w=0. Without waterload, pore-fluid pressure will be absent (λ=0 and $\sin\varphi_e = \sin\varphi_0$).

A Few Geometric Relations Without Water Load

Airy isostasy and geometric considerations yield

$$(h(x) + h_c)\,\rho_s = \overline{h}_m(x)\,\rho_m \tag{B.30}$$

$$h_w(x) + h(x) + h_c = h_0 + \overline{h}_m(x) \tag{B.31}$$

Combining equations (B.30) and (B.31) yields

$$\overline{h}_m(x) = (h(x) + h_c)\,\frac{\rho_s}{\rho_m} \tag{B.32}$$

$$\frac{d\overline{h}_m(x)}{dx} = \frac{\rho_s}{\rho_m}\frac{dh(x)}{dx} \tag{B.33}$$

Individual Forces

By omitting the integration over the waterload for F_1, F_2 and F_{iso} (equations B.19, B.20 and B.25, respectively) it follows that

$$F_1 = \frac{1}{2}\,\rho_s\,g\,k_a\,h_1^2 \tag{B.34}$$

$$F_2 = -\frac{1}{2}\,\rho_s\,g\,k_p\,h_2^2 \tag{B.35}$$

$$F_{iso} = \int_{x_1}^{x_2} \rho_s\,g\,h(x)\,\sin\alpha_2(x)\,dx = -\frac{1}{2}\,\frac{\rho_s^2}{\rho_m}\,g\,(h_1^2 - h_2^2) \tag{B.36}$$

By substituting ρ_w=0 in equation (B.21), the Poiseuille-flow force becomes

$$F_p = \frac{1}{2}\,\rho_s\,g\,(1 - \frac{\rho_s}{\rho_m})\,h_c\,(h_1 - h_2). \tag{B.37}$$

The water loading force is zero.

Sum of Forces

Substituting the above values in the force balance yields

$$\begin{aligned} 0 &= F_1 + F_2 + F_{iso} + F_p \\ &= \frac{1}{2}\,\rho_s\,g\left(h_1^2\,(k_a - \frac{\rho_s}{\rho_m}) - h_2^2\,(k_p - \frac{\rho_s}{\rho_m}) + (h_1 - h_2)\,h_c\,(1 - \frac{\rho_s}{\rho_m})\right). \end{aligned} \tag{B.38}$$

Non-dimensionalization of thicknesses and densities leads to

$$h_1^{*2}\,(k_a - \frac{\rho_s}{\rho_m}) - h_2^{*2}\,(k_p - \frac{\rho_s}{\rho_m}) + (h_1^* - h_2^*)\,(1 - \frac{\rho_s}{\rho_m}) = 0. \tag{B.39}$$

The resulting relations of h_2 and φ_0 are again plotted for different values of h_1 in Figure B.8. As in the case of the submerged margin, F_1 and F_{iso} contribute most to the force balance (Figure B.9). The numerical models again show very similar behavior as predicted by the analytical calculations (Figure B.10).

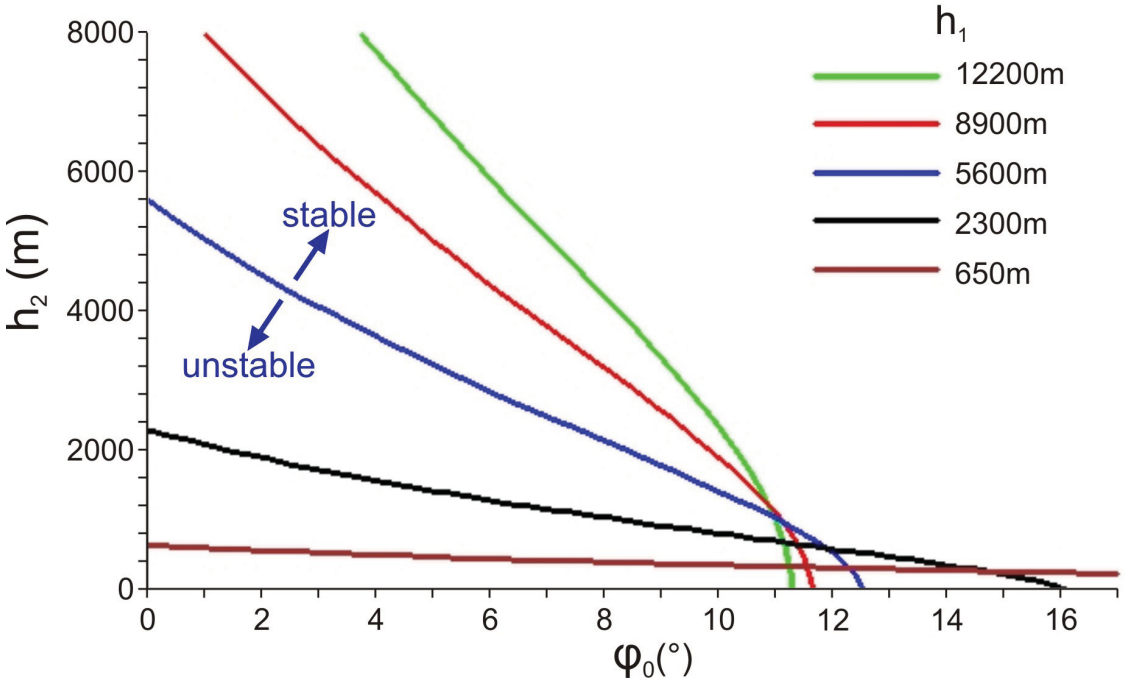

Figure B.8: Conditions for gravity spreading of a non-submerged continental margin system. The plots show the dependance of distal sediment thickness h_2 on the internal angle of friction φ_0 for a seaward sliding frictional overburden at failure above a viscous substratum. The landward sediment thickness h_1 varies as shown in the plot, all other parameters are as for Figure B.4. The graphs show that systems become unstable for weaker sediments (lower φ_0), smaller seaward sediment thickness h_2, or larger landward sediment thickness h_1.

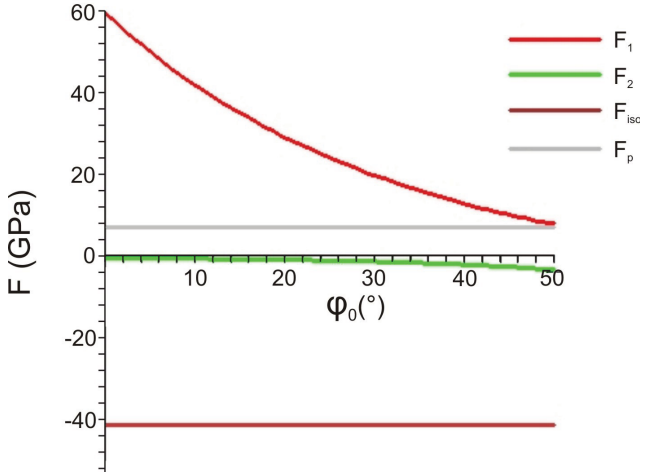

Figure B.9: Plot of the forces contributing to the horizontal force balance without water load as a function of the internal angle of friction. Parameters are as for Figure B.8 with h_2=200 m and h_1=2300 m.

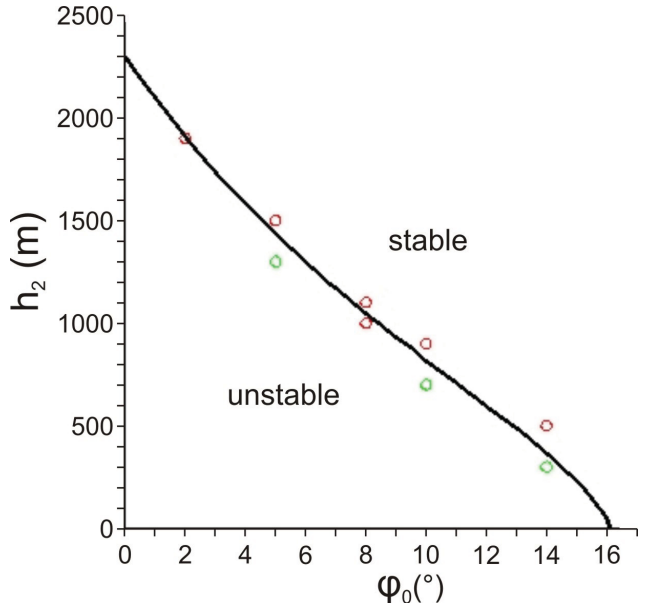

Figure B.10: Comparison of analytical and numerical results of stability analysis of a non-submerged continental margin system. The graph shows the stability criteria for a frictional overburden above a viscous substratum as a function of h_2 and φ_0 with h_1=2300 m and all other parameters as for Figure B.8. The numerical model results are plotted as red and green dots (stable and unstable models, respectively).

B.4.2 Stability Analysis for a Non-Isostatically Balanced Continental Margin System

The equations for the non-isostatically balanced case can be easily obtained from the above calculation by setting $\rho_m \to \infty$. They have also been derived and discussed by *Gemmer et al.* (2005).

Non-Isostatically Balanced System With Water Load

$$
\begin{aligned}
F_1 &= \frac{1}{2}\, k_a\, g\, \rho_s\, h_1^2 + \rho_w\, g\, h_{w1}\, h_1 \\
F_2 &= -\frac{1}{2}\, k_p\, g\, \rho_s\, h_2^2 - \rho_w\, g\, h_{w2}\, h_2 \\
F_p &= \frac{1}{2}\, g\, R\, (\rho_s - \rho_w)\, h_c\, (h_1 - h_2) \\
F_w &= -\frac{1}{2}\, \rho_w\, g\ (h_{w2}^2 - h_{w1}^2) \\
F_{iso} &= 0
\end{aligned}
$$

with $h_{w2} = h_{w1} + (h_1 - h_2)$ follows:

$$
\begin{aligned}
F_1 &= \frac{1}{2}\, \rho_s\, g\, k_a\, h_1^2 + \rho_w\, g\, h_{w1}\, h_1 \\
F_2 &= -k_p\, g\, \frac{1}{2}\, \rho_s\, h_2^2 - \rho_w\, g\, (h_{w1} + h_1 - h_2)\, h_2 \\
F_p &= \frac{1}{2}\, (\rho_s - \rho_w)\, g\, h_c\, (h_1 - h_2) \\
F_w &= -\frac{1}{2}\, \rho_w\, g\ (h_{w1}^2 + 2\, h_{w1}\, (h_1 - h_2) + (h_1 - h_2)^2 - h_{w1}^2)
\end{aligned}
$$

Substituting the above values in the force balance yields

$$
\begin{aligned}
0 &= F_1 + F_2 + F_p + F_w \\
&= \frac{1}{2}\,\rho_s\, g\,\left(h_1^2\, k_a - h_2^2\, k_p + (h_1 - h_2)\, h_c\right) \\
&\quad + \rho_w\, g\,\left(h_{w1}\, h_1 - h_{w1}\, h_2 - (h_1 - h_2)\, h_2 - h_{w1}\,(h_1 - h_2) - \frac{1}{2}(h_1 - h_2)^2\right) \\
&\quad - \frac{1}{2}\,\rho_w\, g\,(h_1 - h_2)\, h_c \\
&= \frac{1}{2}\,\rho_s\, g\,\left(h_1^2\, k_a - h_2^2\, k_p + (h_1 - h_2)\, h_c\right) \\
&\quad - \frac{1}{2}\,\rho_w\, g(h_1^2 - h_2^2 + (h_1 - h_2)\, h_c)
\end{aligned}
\tag{B.40}
$$

Non-dimensionalization of thicknesses and densities leads to

$$
h_1^{*2}\,(k_a - \rho_w^*) - h_2^{*2}\,(k_p - \rho_w^*) + (h_1^* - h_2^*)\,(1 - \rho_w^*) = 0. \tag{B.41}
$$

The predictions of analytical and numerical calculations are shown in Figure B.11 as the relation of h_2 to φ_e. Numerical and analytical results agree very well.

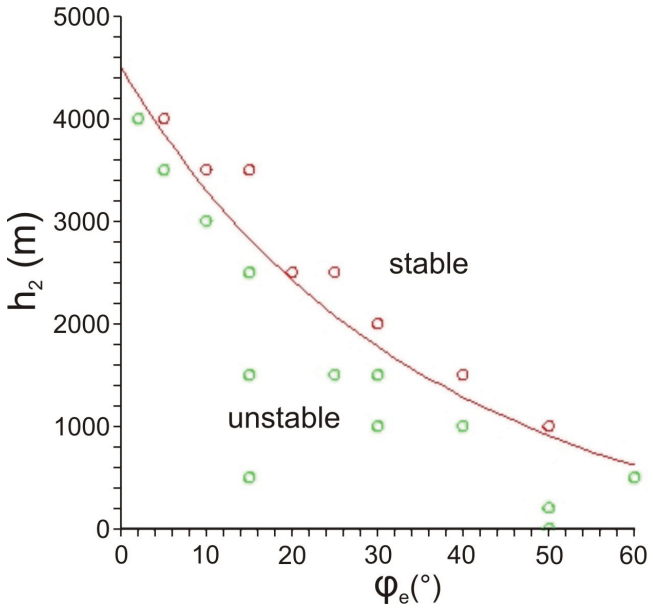

Figure B.11: Comparison of theoretical and numerical results of stability analysis of a non-isostatically balanced continental margin system. The curve shows the analytically calculated dependance of seaward sediment thickness h_2 on the internal angle of friction φ_e. The landward sediment thickness h_1 is 4500 m and all other parameters are as for Figure B.4. The graphs show that systems become unstable for weaker sediments (lower φ_e), smaller seaward sediment thickness h_2 or larger landward sediment thickness h_1. The numerical model results are plotted as red and green dots (stable and unstable models). The numerical results agree very well with the analytical calculations.

B.5 Failure at Shelf Edge vs. Failure along Slope

As mentioned in section B.2 and again shown in Figure B.12, the graphs of the internal angle of friction φ_e versus the seaward sediment thickness h_2 for an isostatically balanced continental margin system at failure intersect for different landward sediment thickness h_1. This means that a system that is unstable for a given h_1 is not necessarily unstable (let alone more unstable) for a larger h_1 as one would expect at first. For example, the continental margin system marked in Figure B.12 (left blue dot) with h_2=1000 m, $\varphi_e = 15°$ and h_1=5600 m is in the unstable region. For the same landward sediment thickness, a system with, for example, $\varphi_e = 25°$ and h_2=100 m is in the stable region (right blue dot). However, with respect to smaller landward thicknesses of 2300 m or 650 m, the system is in the unstable region. For such a system with a landward thickness of h_1=5600 m this implies that it will not fail at the maximum sediment thickness located beneath the shelf edge but at smaller sediment thickness located along the slope. This result is confirmed and illustrated by a numerical model in Figure B.13.

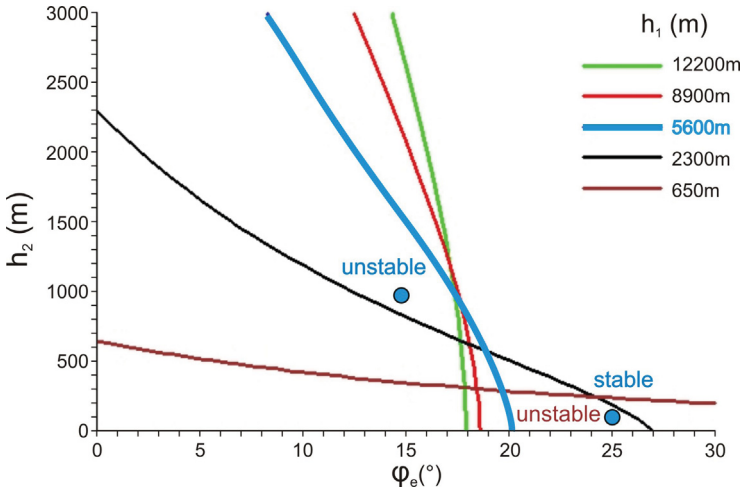

Figure B.12: Graphs of seaward sediment thickness h_2 as a function of the internal angle of friction φ_e for different landward sediment thicknesses h_1. Other parameters are as given in Figure B.4. Two models are marked with blue dots, which represent an unstable and stable model with respect to a h_1 of 5600 m. However, the model with the higher internal angle of friction is unstable with respect to smaller landward thicknesses of 2300 m or 650 m.

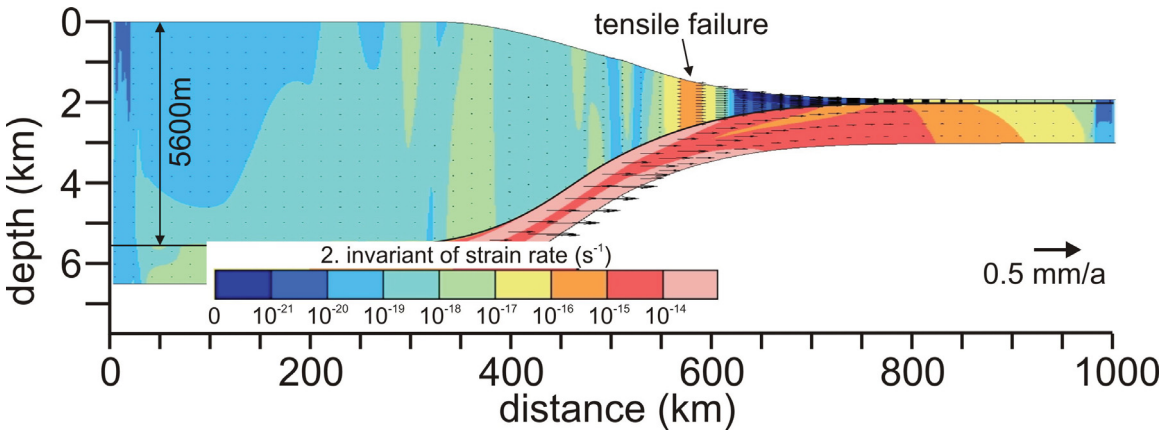

Figure B.13: Finite element models of an isostatically balanced, wedge-shaped frictional-plastic overburden overlying a 1000 m thick, viscous salt-layer. The plot shows strain rates and displacement velocities. The models has landward and seaward sediment thicknesses of h_1=5600 m and h_2=100 m, salt and sediment density of ρ_s=2300 kg/m^3, mantle density of ρ_m=3300 kg/m^3, water density of ρ_w=1000 kg/m^3, and an effective internal angle of friction of $\varphi_e = 17°$. The model shows very small strain rates at the shelf edge but high strain rates and displacement velocities at a zone of extension along the slope and at the toe of the slope (zone of shortening). The additional vertical stripes of higher strain rates along the slope up to the shelf edge are the result of the evolution of the system. Once failure and extension occurs at one point of the slope, the new space created here allows the more landward overburden to follow, fail and slide basinward into the space created by the first failure.

The reason behind this behavior is the dependence of the individual forces on h_1. Both the tensile force F_1 and the downhill force F_{iso} depend on h_1^2, the first one facilitating failure, the second one inhibiting it. The Poiseuille flow force F_p depends linearly on h_1. The sum of forces, plotted in dependence of the landward sediment thickness h_1, follows a hyperbola, which crosses the abscissa twice (Figure B.14). This illustrates that there are two candidates for failure localization on a continental margin system. If the conditions for failure are met during the gradual built-up of the sedimentary wedge, the system will fail once the lower critical h_1 is reached. If the conditions of failure are only met after the sedimentary wedge is emplaced (e.g by delayed development of fluid overpressure), tensile failure may occur in more than one location.

The calculations presented here, which do not assume a fixed location of tensile failure on the margin, are an expansion of those presented in Chapter 2 (*Gradmann et al.*, 2009), but do not invalidate the results obtained there. In the case of the Perdido Fold Belt gravity-spreading system, the location of tensile failure (the Corsair fault system) is known and hence the landward sediment thickness h_1 can be estimated from seismic sections. Thus, it does not represent an unknown in the stability analysis equations. Furthermore, localization of extension along the slope would only be observed at the very onset of gravity spreading. During the following evolution, tensile failure would propagate upslope as seen in Figure B.12. Thus, the Oligocene extensional structures of northwestern GoM that are seen in seismic data are likely representing the upslope region of tensile failure.

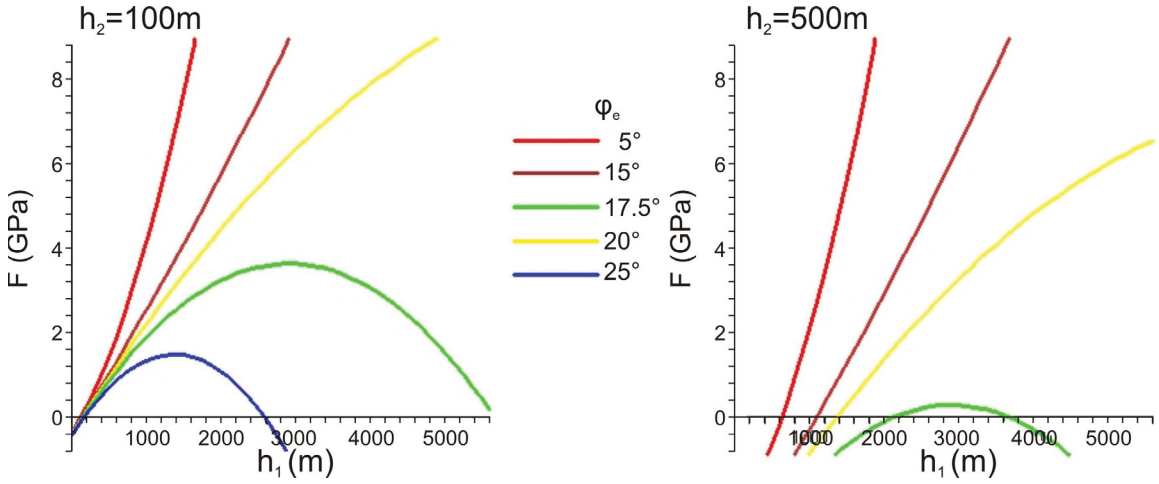

Figure B.14: Plots of landward thickness h_1 versus sum of forces $F_1+F_2+F_p+F_{iso}+F_w$ for different internal angles of friction φ_e and h_2=100 m (left graph) and h_2=500 m (right graph). Other parameters are as for Figure B.13.

Appendix C

Addendum to Chapters 3 and 4

Chapters 3 and 4 investigate the complex feedback effects between compaction-induced fluid-pressure generation and mechanical deformation. A number of technical issues could not be addressed in the two chapters in order to keep the focus on the salt-sediment interaction. In this Addendum two of these issues are addressed: First, different strategies to eliminate non-physical behavior of the numerical models (super-lithostatic fluid pressure and strong decompaction) are presented. Second, I discuss how to separate the different modes of shortening occurring during fold-belt evolution (folding, pure-shear thickening and horizontal compaction).

C.1 Elimination of Non-Physical Model Behavior

The software SOPALEff yields calculations of compaction and fluid-pressure generation that are physically reasonable and in agreement with observations, provided that the values of the control parameters are chosen appropriately (Chapters 3 and 4). In a few cases, unphysical processes occurred in the models such as evolution of super-lithostatic fluid pressure (i.e. fluid pressure that is larger than the lithostatic pressure, models ML-1 and ML-Q30) and decompaction (models SL-Sh1 and ML-Q20 to ML-Q35). I made several efforts to eliminate these behaviors with more or less success. In this chapter the different changes to the software that I tested are described, together with the corresponding impact on the numerical experiments. The issues of too high fluid pressure and of decompaction are addressed separately.

C.1.1 Super-Lithostatic Fluid Pressure and Fault-Valving

Super-lithostatic fluid pressure develops in the numerical experiments in very rapidly compacting model material (model ML-1). In the natural case, extreme fluid pressure would lead to fracturing of the surrounding rock, to the flow of fluid into these fractures, and to a consequent decrease in the fluid pressure. I implemented this kind of

'fault-valving' behavior in the models by locally increasing the hydraulic conductivity if the pore-fluid pressure ratio λ was exceeding a certain threshold value.

The hydraulic conductivity is normally calculated as

$$k = k_0 \left(\frac{n}{n_0} \right)^m$$

where k_0 and n_0 are the hydraulic conductivity and porosity at the surface, respectively, n is the material porosity, and the exponent m is an empirical, material-dependent constant. The

hydraulic conductivity k was substituted by a modified value k_{new}, which increases exponentially towards a value $F \cdot k$ over a pre-defined range of pore-fluid pressure ratios (λ_1 to λ_2)

$$k_{new} = \begin{cases} k & \lambda \leq \lambda_1 \\ k \cdot F^{\frac{\lambda - \lambda_1}{\lambda_2 - \lambda_1}} & \lambda_1 < \lambda < \lambda_2 \\ F \cdot k & \lambda \geq \lambda_2 \end{cases} \tag{C.1}$$

Figure C.1 shows the comparison of a model with and without the fault-valving mechanism. The model is similar to model ML-Q35 of Chapter 4. In the model of Figure C.1 only one shale layer was deposited during the aggradation phase and the pore compressibility of both sandstone-type and shale-type material is slightly higher than in model ML-Q35 ($3 \cdot 10^{-7}\,\mathrm{Pa}^{-1}$ instead of $10^{-7}\,\mathrm{Pa}^{-1}$). The values used for fault-valving were $F = 10^5, \lambda_1 = 0.85$, and $\lambda_2 = 0.95$. In the model without fault-valving, extremely high pore-fluid pressure develops in the sediments below the toe of the slope (black region in Figure C.1a). In the model with fault-valving, this extreme pore-fluid pressure is reduced to moderate values (Figure C.1b). However, in the sediments above the distal part of the salt basin, the pore-fluid pressure is slightly higher than in the model without fault valving. Here, supra-lithostatic pore-fluid pressure also develops after additional 10 Ma of model time (Figure C.1c). The fault-valving mechanism now no longer succeeds in discharging this overpressure, indicating that the relation between overpressure and hydraulic conductivity is not appropriately captured. The local modification of the hydraulic conductivity is not consistent with the solution of the calculations. A more thorough coupling between overpressure and hydraulic conductivity would be required.

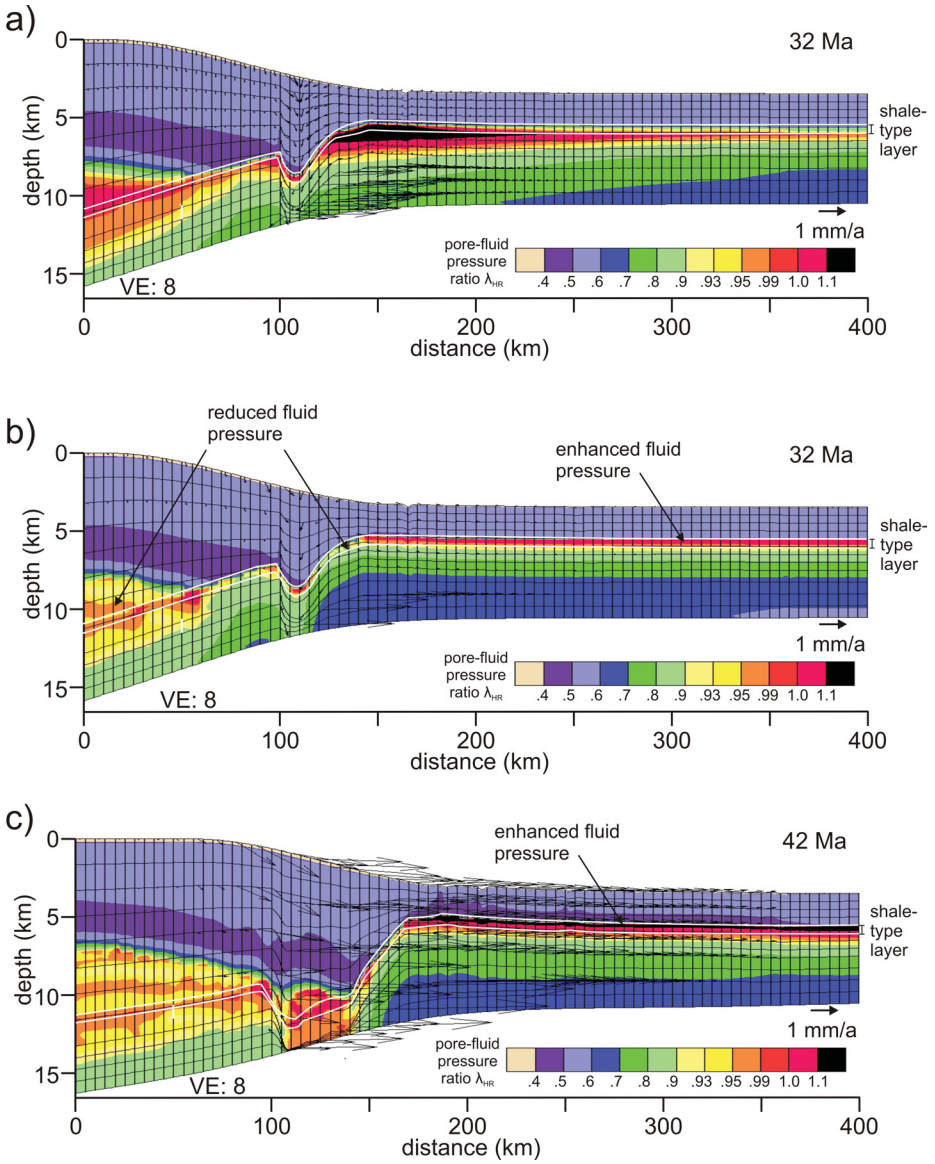

Figure C.1: Model results demonstrating fault-valving mechanism. (a) Model without fault-valving mechanism developing ultra-high overpressure in the center of the model domain. (b) Same model as above with fault-valving mechanism activated. Fluid pressure is strongly reduced in the landward and central part of the model domain. (c) Same model as to the left after additional 10 Ma of model time. Super-lithostatic fluid pressure has developed in the seaward part of the model domain and is not discharged by the fault-valving mechanism. This indicates that the imposed relation between pore-fluid pressure ratio and hydraulic conductivity is not consistent with the overall coupling of fluid flow and mechanical calculations.

In an alternative implementation, the deviatoric strain rate $\dot{\varepsilon}'$ is used instead of the pore-fluid pressure ratio λ to provide a range over which the hydraulic conductivity increases. This approach approximates the conductivity increase expected in active faults owing to brecciation under high fluid pressure. Although it aims to closely simulate the natural processes, it fails to reduce artificially developing fluid pressure such as that in Figure C.1a, because the high fluid pressure not necessarily develops in regions with strong deformation.

To avoid the problem of artificially high pore-fluid pressure, the compaction efficiency of the shale-type material was reduced in the models of Chapters 3 and 4 by using a lower pore compressibility.

C.1.2 Decompaction

As discussed in Chapter 3, reversed mechanical compaction (i.e. decompaction) occurs where the effective pressure P_{eff} decreases.

$$\frac{1}{1-n}\frac{Dn}{Dt} = -\beta_b(n)\frac{DP_{eff}}{Dt} - \frac{P_{eff}}{\xi(n)} \tag{C.2}$$

Mechanical compaction is here controlled through the bulk compressibility $\beta_b(n)$=$(n-n_c)\beta_p$ (β_p and n_c are the pore compressibility and cut-off porosity, respectively), and viscous compaction is controlled through the compactional shear viscosity $\xi(n)$.

The first attempt to eliminate decompaction was undertaken by artificially setting $DP_{eff}/Dt = 0$, if this parameter would have otherwise taken a negative value. This approach did indeed prevent porosity from increasing, but at the same time the fluid pressure increased dramatically, reaching pore-fluid pressure ratios much larger than 1 (Figure C.2). The model shown is similar to the model shown in Figure C.1 and to model ML-Q35 of Chapter 4. A single shale layer is deposited during the aggradation phase, the pore compressibility of both sandstone-type and shale-type material is $10^{-7}\,\mathrm{Pa}^{-1}$, the compactional shear viscosity is 35 kJ/mole. Decompaction occurs in the shale-type layer during gravity-induced fold-belt evolution (Figure C.2b). In the model with suppressed decompaction (Figure C.2d) ultra-high pore-fluid pressure develops. The suppression of porosity changes is apparently too rigorous, it corresponds to the use of a bulk compressibility of β_p=0. It needs to be considered that the bulk

compressibility β_b is not only affecting the porosity change, but is also included in two numerical parameters that enter the calculations for the deformation velocities (*bulkv*2 and *srcecompac*, *Morency*, 2006). *bulkv*2 is an effective compressibility that is included in the force-balance equation of quasi-incompressible material. It represents the so-called penalty method for the purely mechanical calculations, used to avoid an ill-conditioned stiffness matrix (*Fullsack*, 1995). A third occurrence of the parameter β_b takes place in the calculations of the fluid pressure (*Morency*, 2006).

A more comprehensive approach was to modify the parameter β_b in every element in which decompaction was about to occur and to use this new value wherever the parameter occurs: in the calculations for porosity changes, the ones for displacement velocities and the ones for fluid-pressure generation. Modification of β_b was achieved through a new input parameter $\beta_{p_{min}}$, which is used locally to recalculate the bulk compressibility if $DP_{eff}/Dt < 0$. Although this approach provided consistent treatment of the bulk compressibility everywhere, it led to similar effects observed previously, namely extremely high pore-fluid pressure (Figure C.2b). A change of one parameter in such a complex system can only be effective, if it is in accordance with the key mechanisms, which control fluid pressure generation and deformational velocities.

A new approach that was to avoid changes of porosity or compressibility that were inconsistent with previous timesteps or adjacent elements. A record was kept of the minimum porosity achieved during the model evolution and accordingly of the minimum bulk compressibility $\beta_{b_{min}}$. These values were used throughout the following model time steps to calculate porosity changes, deformation velocities and fluid-pressure generation. This approach is not able to fully eliminate decompaction, but it reduces it in a way that is consistent with the other calculations (velocities, fluid pressure, previous timesteps, adjacent elements). This way of controlling decompaction has been used in the models of Chapter 3 and 4.

Figure C.3 shows an example of this control mechanism on decompaction. The model is again similar to the model shown in Figure C.2, only is the compactional shear viscosity slightly higher (40 kJ/mole instead of 35 kJ/mole). Decompaction occurs in the shale during gravity-induced fold-belt evolution (Figure C.3a). The model with the activated control mechanism (Figure C.3c) greatly reduces this process. The

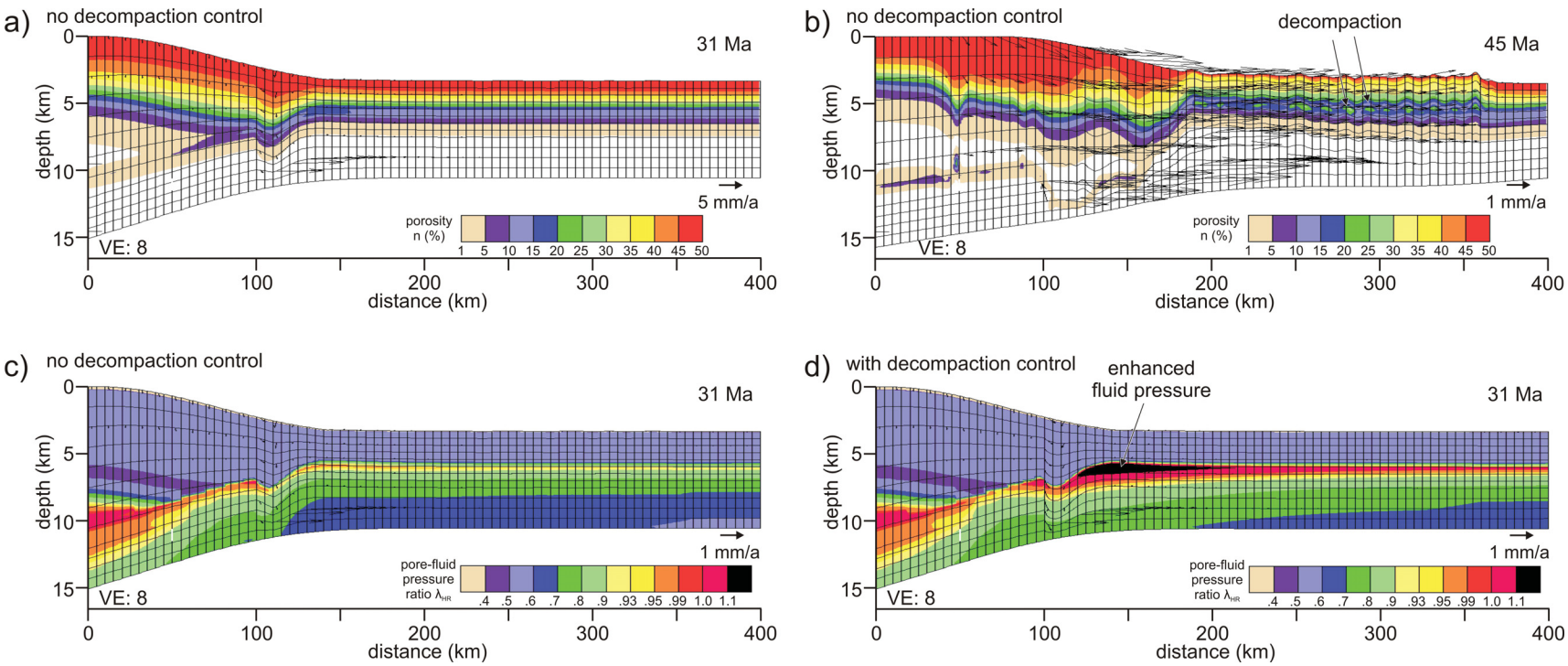

Figure C.2: Model result demonstrating the occurrence of decompaction and an attempt of suppressing it. (a), (b) Porosity plot of model without control mechanism at 31 and 45 Ma of model time, respectively. Porosity in the sedimentary overburden decrease to below 15% (a), later increase again to up to 25%. (c), (d) Plots of pore-fluid pressure ratio in model without and with mechanism intended to control decompaction, respectively. Even before significant decompaction occurs, the new mechanism leads to unrealistically high pore-fluid pressure.

fluid pressure is not strongly affected by the control mechanism (Figure C.3b,d).

C.2 Strain Rates During Horizontal Compaction

In Chapter 4 (*Gradmann and Beaumont*, 2012), the fold belt evolution in a system with dynamically calculated pore-fluid pressure is investigated. This study addresses the effects of both vertical and horizontal stress on sediment compaction. It is noted that the term 'horizontal compaction' does not accurately describe the processes occurring in the models, because compaction is modeled as a purely volumetric process, driven by the mean stress and fluid pressure, and is independent of direction. It is furthermore concluded that the porosity loss resulting from a horizontal, compressive stress regime must therefore occur as a superposition of volumetric compaction and pure-shear deformation.

This superposition of processes is only qualitatively addressed in Chapter 4 but their respective contributions to total shortening are not separated or quantified. An attempt of a quantitative analysis of the model strain rates is discussed in this section. Additionally, observations from laboratory experiments and natural settings are presented that indicate a similar superposition of different modes of strain during compaction.

The considerations presented here demonstrate that the stresses involved in the compaction process are still not thoroughly investigated and understood. It furthermore reveals possible limitations of the compaction mechanisms that are implemented in the numerical models.

Strain Rates of Mechanical Deformation

The 2D strain-rate tensor $\dot{\varepsilon}_{ij}$ includes all components of the rate of deformation of a plastic material: isotropic (volumetric) and deviatoric (pure-shear and simple-shear).

$$\dot{\varepsilon} = \begin{bmatrix} \dot{\varepsilon}_{xx} & \dot{\varepsilon}_{xy} \\ \dot{\varepsilon}_{yx} & \dot{\varepsilon}_{yy} \end{bmatrix}$$

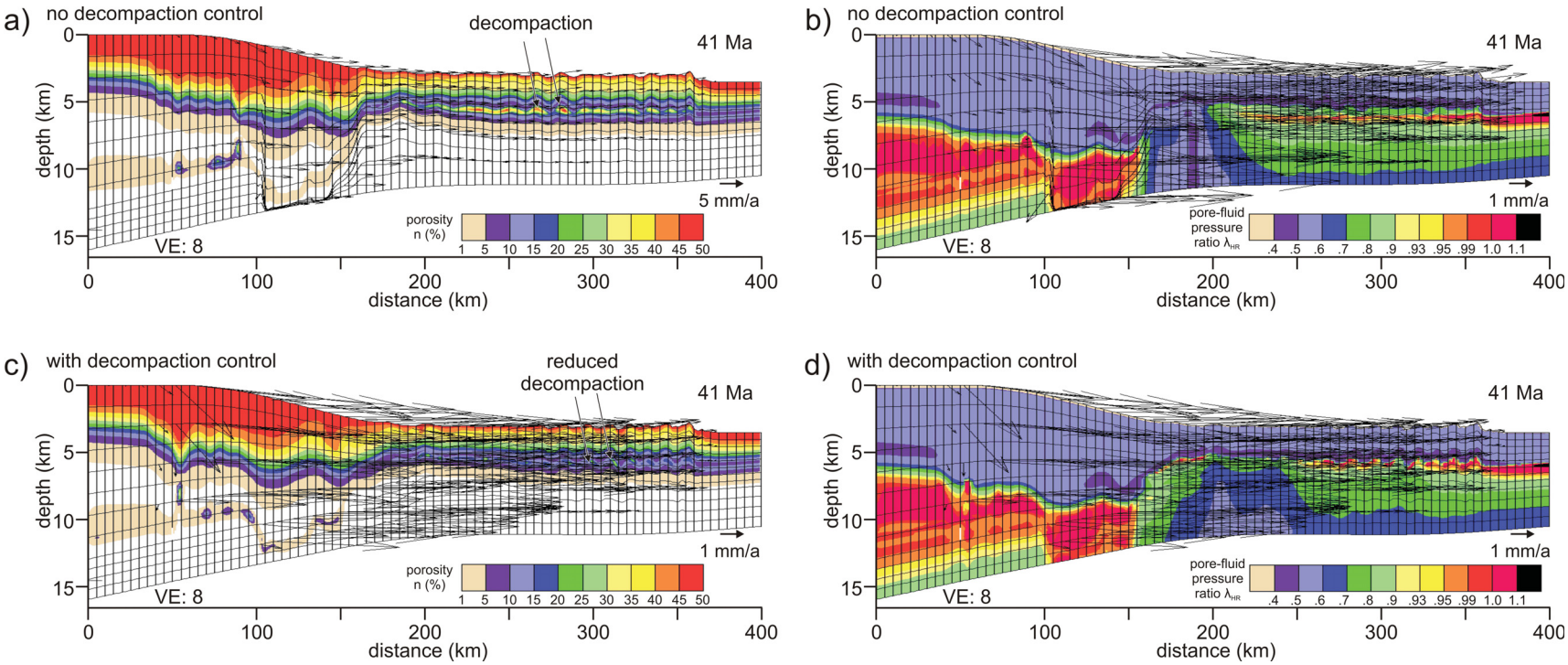

Figure C.3: Model result demonstrating the control mechanism on decompaction. (a) In the model without control mechanism, porosities increase to values of 40% in the evolving fold belt after they had decreased to less than 15% during compaction. (b) Fluid pressure is high but not super-lithostatic. (c) Model with control mechanism on decompaction. Here, porosities increase only to 20% during fold belt evolution. (d) Fluid pressure evolve similarly as in the model without control mechanism.

The isotropic strain rate $\dot{\varepsilon}_V$ is given by

$$\dot{\varepsilon}_V = (\dot{\varepsilon}_{xx} + \dot{\varepsilon}_{yy})/2. \tag{C.3}$$

The deviatoric strain rate tensor $\dot{\varepsilon}'$ then becomes

$$\dot{\varepsilon}' = \begin{bmatrix} \dot{\varepsilon}'_{xx} & \dot{\varepsilon}'_{xy} \\ \dot{\varepsilon}'_{yx} & \dot{\varepsilon}'_{yy} \end{bmatrix} = \begin{bmatrix} \dot{\varepsilon}_{xx} - \dot{\varepsilon}_V & \dot{\varepsilon}_{xy} \\ \dot{\varepsilon}_{yx} & \dot{\varepsilon}_{yy} - \dot{\varepsilon}_V \end{bmatrix}$$

The off-diagonal elements ($\dot{\varepsilon}_{xy}$ and $\dot{\varepsilon}_{yx}$) describe the simple-shear deformation, the diagonal elements ($\dot{\varepsilon}'_{xx}$ and $\dot{\varepsilon}'_{yy}$) the pure-shear deformation with

$$\dot{\varepsilon}'_{xx} = -\dot{\varepsilon}'_{yy}. \tag{C.4}$$

The Case of 'Vertical Compaction'

In Chapter 4 we attempted to analyze how shortening in a fold belt is distributed between the different modes of deformation, namely simple-shear deformation (primarily folding), pure-shear deformation (primarily thickening), and volumetric deformation (primarily horizontal compaction). Here the more simple and more common case of pure vertical compaction is considered: a sandbox is laterally confined and subject only to vertical (e.g. gravity-driven) compaction. All strain rates associated with this case are marked by an asterisk and the following equations apply

$$\dot{\varepsilon}^*_{xx} = 0 \tag{C.5}$$

$$\dot{\varepsilon}^*_{yy} = 2 \cdot \dot{\varepsilon}^*_V \tag{C.6}$$

$$\dot{\varepsilon}^*_{xy} = \dot{\varepsilon}^*_{yx} = 0 \tag{C.7}$$

$$\dot{\varepsilon}^{*'}_{yy} = \dot{\varepsilon}^*_{yy} - \dot{\varepsilon}^*_V = \dot{\varepsilon}^*_V \tag{C.8}$$

$$\dot{\varepsilon}^{*'}_{xx} = \dot{\varepsilon}^*_{xx} - \dot{\varepsilon}^*_V = -\dot{\varepsilon}^*_V. \tag{C.9}$$

These simple relations show that the volumetric deformation ($\dot{\varepsilon}^*_V$) is only half the total observed deformation ($\dot{\varepsilon}^*_{yy} = 2 \cdot \dot{\varepsilon}^*_V$), but that this is augmented by vertical thinning owing to pure-shear flattening ($\dot{\varepsilon}^{*'}_{yy} = \dot{\varepsilon}^*_V$). In the horizontal direction, no net deformation occurs. Volumetric compaction occurs at a rate $\dot{\varepsilon}^*_V$ but is compensated by

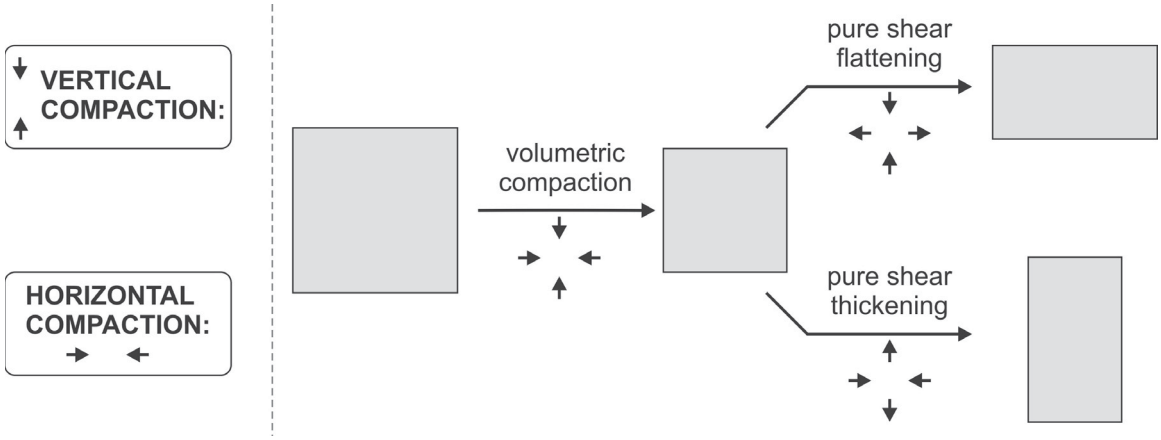

Figure C.4: Schematic of vertical compaction, representing the superposition of volumetric compaction and pure-shear flattening.

pure-shear flattening with equal and opposite strain rate ($\dot{\varepsilon}^{*'}_{xx} = -\dot{\varepsilon}^{*}_{V}$). Because porosity loss during 'vertical compaction' does not occur as a volumetric process, this term must notionally be understood as the superposition of volume loss by compaction, which leads to contraction both horizontally and vertically, plus superimposed pure-shear flattening which increases the vertical contraction of the matrix and expands it laterally to its original width (Figure C.4). Thus a part of volumetric compaction is converted to pure-shear flattening. Equivalently, 'horizontal compaction', which is expected to occur during fold belt formation in the models of Chapter 4, is the product of volume loss by compaction plus superimposed pure-shear shortening and thickening in response to a horizontal stresses. This new interpretation of 'directed compaction' has already been proposed in Chapter 4. Here we attempt to quantify the amount of 'directed compaction' in a more general setting.

General Case of Compaction

Whenever net compaction is not volumetric (as in the case of any confined sedimentary basin, any non-uniformly compacting layered sediments), a component of directed compaction exists with a pure-shear part equal to the compaction part in the prevailing shortening direction ($\dot{\varepsilon}^{*'}_{yy} = \dot{\varepsilon}^{*}_{V}$), and equal but opposite in the perpendicular direction ($\dot{\varepsilon}^{*'}_{xx} = -\dot{\varepsilon}^{*}_{V}$). Instead of dividing the strain rate into isotropic and deviatoric parts, we can divide it into volumetric compaction (sub-index $_V$), directed compaction (sub-index $_C$) and a net thinning or thickening component (sub-index $_D$).

It follows that

$$\dot{\varepsilon}_{xx} = \overbrace{\dot{\varepsilon}_V}^{\text{isotropic}} + \overbrace{\dot{\varepsilon}'_{xx}}^{\text{deviatoric}} \tag{C.10}$$

$$= \dot{\varepsilon}_{V_V} + \dot{\varepsilon}_{V_C} + \dot{\varepsilon}'_{xx_C} + \dot{\varepsilon}'_{xx_D} \tag{C.11}$$

$$= \underbrace{\dot{\varepsilon}_{V_V}}_{\text{volumetric compaction}} + \underbrace{\dot{\varepsilon}_{V_C} + \dot{\varepsilon}'_{xx_C}}_{\text{directed compaction}} + \underbrace{\dot{\varepsilon}'_{xx_D}}_{\text{volume preserving deformation}} . \tag{C.12}$$

$\dot{\varepsilon}_{V_C}$ corresponds to $\dot{\varepsilon}^*_V$ of equation (C.8) and (C.9), where it also represented the volumetric component of the directed compaction. In order to separate this value one would have to isolate either this or the compaction-induced pure-shear deformation.

The 2D strain-rate tensor $\dot{\varepsilon}_{ij}$ and its invariants are part of the equations of large-scale incompressible flow, which the software SOPALE uses. The different modes of volumetric or pure-shear deformation (the part associated with directed compaction) do not occur as separate variables in the governing equations and can therefore not be isolated. Only if additional constraints on the volumetric or pure-shear deformation are known (e.g. no net vertical or net horizontal deformation) is it possible to separate out the compaction-induced pure-shear component from the calculations. Additional insight can also be obtained by comparison of two regions of the model that are known to behave differently (this has been done in Chapter 4). But a full, quantitative separation of the different strain rates is not possible with the current numerical implementation of mechanical deformation and compaction.

Conditions for the Different Modes of Deformation

In the modeled sediments, mechanical deformation can only occur if the yield criterion is fulfilled, i.e. if the differential stress reaches the yield stress. Compaction, however, occurs without a threshold, as a viscous process. This is certainly correct for pressure solution (viscous compaction). It is also assumed for grain re-arrangement during mechanical compaction, which may or may not be correct. Nevertheless, the above analysis shows that directed compaction is always accompanied by pure-shear deformation in the models, and hence that frictional failure must take place, because this is a pre-requisite for deviatoric deformation. This is indeed the case in the modeled

sediments. The Drucker-Prager yield condition is met in the models wherever compaction occurs - even in the very shallow sediments during pure vertical compaction. This observation raises the question whether similar behavior is to be expected in nature and whether evidence for it has been found.

Stress Measurements in Analogue Settings

Evidence of vertical volume loss coupled with failure of the sediment during vertical compaction comes from shear failure experiments of the sediments. *Shin et al.* (2008) describe and model numerically as well as physically the state of stress in a problem closely related to the simple case of sediments undergoing vertical gravity-driven compaction. Here, sediments in a laterally confined container are subject to dissolution and loss of some of the sediment particles, which results in vertical compaction. In their models, which are hence subject to small amounts of volumetric compaction strain, the ratio of internal principle stresses σ_{xx}/σ_{zz} is measured and progressively decreases until it reaches the Rankine active failure state. These results demonstrate that compaction reduces the horizontal stress exerted by the sediment to the point that the sediment fails under deviatoric tension. This is exactly the first stage notional behavior described above, which is in our numerical models followed by shear deformation of the sediment that results in the pure-shear vertical flattening accompanying the volumetric compaction.

Katahara (2009) discusses the presence of elastic strain during vertical compaction. He analyzes uniaxial loading/unloading experiments with zero lateral strain by *Karig and Hou* (1992), which demonstrated that induced horizontal plastic strain is compensated by equal and opposite elastic strain so that the net strain remains zero. *Katahara* (2009) notes that the assumption of zero lateral elastic strain therefore fails in many common geological settings and furthermore that the magnitude of the elastic strain is controlled by material properties for plastic behavior.

Stress measurements in a section of layered limestone and argillite reveal that minor horizontal stresses (σ_h) in the weaker argillite layer are much higher than in the stiffer limestone layer, while the major horizontal stress (σ_H) is nearly equal and in direction of the last tectonic shortening event (*Gunzburger*, 2010). The author suggests

an ultra-slow viscous pressure-solution creep of the limestone layer, which operates on different timescales and magnitudes in the different major stress directions.

Despite the limited number of experiments that investigate horizontal stress and strain during vertical compaction, it becomes clear that horizontal components nevertheless play a role in otherwise vertical deformation. An improved understanding of the stress and strain regimes can yield better insight into the time- and stress-dependent compaction process. The superposition of volumetric and pure-shear deformation during compaction, as seen in our numerical models, is not directly confirmed by observations from laboratory experiments or nature, which are sparse and not necessarily consistent. Mechanical failure during compaction, as it is implied by pure-shear deformation and required by our numerical models, is to a certain degree also observed in the experiments of *Shin et al.* (2008). The other experiments listed here, however, reveal possible shortcomings of the compaction formulation. Elastic deformation is not included in the model materials' rheology but may be an alternative mechanism to plastic pure-shear deformation for accommodating lateral stresses. It may especially be of relevance to compaction in shallow areas, where yield stresses have not been reached. Nevertheless, the laboratory experiments agree with the numerical ones with respect to the equal but opposite deviatoric strain (elastic vs. pure-shear) occurring during directed compaction and thus a coupling between different modes and control parameters of deformation. The observations of *Gunzburger* (2010), which suggest that pressure-solution can operate differently in the different directions of principle stress, has implications for our current formulation of viscous compaction. It is easy to comprehend that solution at the grain boundaries depends on the local stress, and that grain contacts perpendicular to the major stress direction would dissolve fastest. As long as diffusion is the overall rate-limiting process during viscous compaction, differences in dissolution rate should not become relevant. If, however, dissolution rates are the limiting factor (*Revil*, 2001), viscous compaction is expected to be direction dependent.

Summary

It was shown that the current implementation of compaction requires equal and opposite pure-shear deformation, where compaction occurs in a preferred direction. The

magnitude of this induced pure-shear deformation cannot be extracted from the model result without additional constraints (e.g no volumetric, only directed compaction), because it is not part of the underlying governing equations of the software. The induced pure-shear deformation implies failure of the frictional-plastic material. This result is in agreement with certain laboratory compaction experiments, which also suggest tensile failure of sediments during vertical compaction (*Shin et al.*, 2008). Other studies suggest that elastic material behavior and viscous compaction operating in preferred directions are important factors, that are not included in the numerical models presented here. We therefore conclude that the special compaction behavior observed in the models (plastic failure, induced pure-shear deformation) cannot be directly transferred to compaction processes occurring in natural settings. Improved numerical descriptions of compaction (including direction-dependent viscous compaction), augmented by more stress measurements in analogue experiments and natural settings, need to be investigated and tested for.

Appendix D

Description of Electronic Supplements

For Chapters 2-5, animations of selected model are provided, which have also been added as supplementary, electronic material in the published version of the chapters. These animations can also be found on Dalspace (http://libraries.dal.ca/collections/dalspace.html). The folder 'Animations' contains the following files:

- Animations_Chapter2-readme.txt - description of the three animations belonging to Chapter 2
- Animation_modelR0.mp4 - first animation of Chapter 2
- Animation_modelRM1.mp4 - second animation of Chapter 2
- Animation_modelRM2.mp4 - third animation of Chapter 2
- Animations_Chapter3-readme.txt - description of the animation belonging to Chapter 3
- Animation_SL-Sh1.mov - animation of Chapter 3
- Animations_Chapter4-readme.txt - description of the animation belonging to Chapter 4
- Animation_ML-Q30.mov - animation belonging to Chapter 4
- Animations_Chapter5-readme.txt - description of the animations belonging to Chapter 5
- Animation_SD1.wmv - first animation of Chapter 5
- Animation_BA1.wmv - second animation of Chapter 5

Appendix E

Copyright Release for Thesis Chapters Published as Journal Articles

WebMail :: Inbox: RE: permission to include manuscripts in phd thesis https://wm4.dal.ca/horde/imp/message.php?mailbox=INBOX&index=32031

Open Folder | Inbox

Inbox | Empty Trash | New Message | Folders | Search | Fetch Mail | Address Book | Options | Help | Log out

Quota status: 430.89 MB / 488.28 MB (88.25%)

Inbox: RE: permission to include manuscripts in phd thesis (1 of 3344)

Mark as: | Move | Copy | This message to | Back to Inbox

Delete | Reply | Forward | Redirect | View Thread | Block | Accept | Message Source | Save as | Print | Headers

Date: Tue, 25 Sep 2012 13:17:10 +0000 [10:17:10 AM ADT]
From: Michael Connolly <MConnolly@agu.org>
To: Sofie Gradmann <s.gradmann@dal.ca>
Subject: RE: permission to include manuscripts in phd thesis

We are pleased to grant permission for the use of the material requested for inclusion in your thesis. The following non-exclusive rights are granted to AGU authors:

* All proprietary rights other than copyright (such as patent rights).
* The right to present the material orally.
* The right to reproduce figures, tables, and extracts, appropriately cited.
* The right to make hard paper copies of all or part of the paper for classroom use.
* The right to deny subsequent commercial use of the paper.

Further reproduction or distribution is not permitted beyond that stipulated. The copyright credit line should appear on the first page of the article or book chapter. The following must also be included, "Reproduced by permission of American Geophysical Union." To ensure that credit is given to the original source(s) and that authors receive full credit through appropriate citation to their papers, we recommend that the full bibliographic reference be cited in the reference list. The standard credit line for journal articles is: "Author(s), title of work, publication title, volume number, issue number, citation number (or page number(s) prior to 2002), year. Copyright [year] American Geophysical Union."

If an article was placed in the public domain, in which case the words "Not subject to U.S. copyright" appear on the bottom of the first page or screen of the article, please substitute "published" for the word "copyright" in the credit line mentioned above.

Copyright information is provided on the inside cover of our journals. For permission for any other use, please contact the AGU Publications Office at AGU, 2000 Florida Ave., N.W., Washington, DC 20009.

Michael Connolly
Program Manager, Journals
American Geophysical Union
+1.202.777.7365
MConnolly@agu.org
www.agu.org

AGU galvanizes a community of Earth and space scientists that collaboratively advances and communicates
science and its power to ensure a sustainable future.

2012 AGU Fall Meeting Essentials:
3-7 December * San Francisco, California, USA
Visit us at http://fallmeeting.agu.org
Get the latest information on Twitter and Facebook and follow us at #AGU2012!

Support the American Geophysical Union!
Visit the AGU Blogosphere

Get the latest information on Facebook and tweet us at @TheAGU!

Bibliography

Adam, J., and C. Krezsek (2012), Basin-scale salt tectonic processes of the Laurentian Basin, Eastern Canada: Insights from integrated regional 2D seismic interpretation and 4D physical experiments, in *Salt tectonics, sediments and prospectivity*, *Geological Society Special Publications*, vol. 363, edited by I. Alsop, pp. 331–360, Geological Society of London.

Albertz, M., and C. Beaumont (2010), An investigation of salt tectonic structural styles in the Scotian Basin, offshore Atlantic Canada, Part 2: Comparison of observations with geometrically complex numerical models, *Tectonics*, *29*, doi: 10.1029/2009TC002540.

Angevine, C. L., and D. L. Turcotte (1983), Porosity reduction by pressure solution: A theoretical model for quartz arenites, *Geological Society of America Bulletin*, *94*(10), 1129–1134.

Athy, L. F. (1930), Density, porosity, and compaction of sedimentary rocks, *Bulletin of the American Association of Petroleum Geologists*, *14*(1), 1–24.

Audet, D. M., and A. C. Fowler (1992), A mathematical model for compaction in sedimentary basins, *Geophysical Journal International*, *110*(3), 577–590.

Behrmann, J. H., P. B. Flemings, C. M. John, and the IODP Expedition 308 Scientists (2006), Rapid sedimentation, overpressure, and focused fluid flow, Gulf of Mexico continental margin, *Scientific Drilling*, *3*, 12–17.

Berry, F. A. F. (1973), High fluid potentials in California Coast Ranges and their tectonic significance, *AAPG Bulletin*, *57*(7), 1219–1249.

Biot, M. A. (1941), General theory of three-dimensional consolidation, *Journal of Applied Physics*, *12*(2), 155–164.

Birchwood, R. A., and D. L. Turcotte (1994), A unified approach to geopressuring, seal formation and secondary porosity generation in sedimentary basins, *EOS, Transactions, American Geophysical Union*, *73*(14), 279.

Bird, D. E., K. Burke, S. A. Hall, and J. F. Casey (2005), Gulf of Mexico tectonic history; hotspot tracks, crustal boundaries, and early salt distribution, *AAPG Bulletin*, *89*(3), 311–328.

Bjørlykke, K. (1997), An overview of factors controlling rates of compaction, fluid generation and flow in sedimentary basins, in *Growth, dissolution and pattern formation in geosystems*, edited by B. Jamtveit and P. Meakin, pp. 381–404, Kluwer Academic Publishers, Dordrecht, Netherlands, Netherlands.

Bradley, J. S., and D. E. Powley (1994), Pressure compartments in sedimentary basins: A review, in *Basin compartments and seals*, *AAPG Memoir*, vol. 61, edited by P. J. Ortoleva, pp. 3–26, AAPG, Tulsa, Oklahoma.

Bredehoeft, J. D., and B. B. Hanshaw (1968), On the maintenance of anomalous fluid pressures: Part 1, Thick sedimentary sequences, *Geological Society of America Bulletin*, *79*(9), 1097–1106.

Butler, R. W. H., and D. A. Patron (2010), Evaluating lateral compaction in deep-water fold and thrust belts: How much are we missing from "nature's sandbox" ?, *GSA Today*, *20*(3), 4–10.

Camerlo, R., D. Meyer, and R. Meltz (2004), Shale tectonism in the northern Port Isabel Fold Belt, in *Salt Sediment Interactions and Hydrocarbon Prospectivity: Concepts, Applications, and Case Studies for the 21st Century. GCSSEPM Conference Proceedings*, pp. 817–839.

Camerlo, R. H., and E. F. Benson (2006), Geometric and seismic interpretation of the Perdido fold belt: Northwestern deep-water Gulf of Mexico, *AAPG Bulletin*, *90*(3), 363–386.

Carter, N. L., S. T. Horseman, J. E. Russell, and J. Handin (1993), Rheology of rocksalt, *Journal of Structural Geology*, *15*(9-10), 1257–1271.

Casas, E., and T. K. Lowenstein (1989), Diagenesis of saline pan halite: Comparison of petrographic features of modern, Quaternary and Permian halites, *Journal of Sedimentary Petrology*, *59*(5), 724–739.

Cathles, L. M. (1975), *The viscosity of the Earth's mantle*, Princeton Univ. Press, Princeton, N.J., USA.

Chemia, Z., H. Koyi, and H. Schmeling (2008), Numerical modelling of rise and fall of a dense layer in salt diapirs, *Geophysical Journal International*, *172*(2), 798–816.

Cinar, Y., G. Pusch, and V. Reitenbach (2006), Petrophysical and capillary properties of compacted salt, *Transport in Porous Media*, *64*(2), 199–228.

Cobbold, P., E. Rossello, and B. Vendeville (1989), Some experiments on interacting sedimentation and deformation above salt horizons, *Bulletin de la Societé Géologique de France*, *8*(3), 453–460.

Cobbold, P. R., P. Szamarti, L. S. Demercian, D. Coelho, and E. A. Rossello (1995), Seismic and experimental evidence for thin-skinned horizontal shortening by convergent radial gliding on evaporites, deep-water Santos Basin, Brazil, in *Salt Tectonics, A Global Perspective*, *AAPG Memoir*, vol. 65, edited by M. P. A. Jackson, D. G. Roberts, and S. Snelson, pp. 305–321, AAPG, Tulsa, Oklahoma.

Colten-Bradley, V. A. (1987), Role of pressure in smectite dehydration: Effects on geopressure and smectite-to-illite transformation, *AAPG Bulletin*, *71*(11), 1414–1427.

Connolly, J. A. D., and Y. Y. Podladchikov (1998), Compaction-driven fluid flow in viscoelastic rocks, *Geodin. Acta*, *11*, 55–84.

Connolly, J. A. D., and Y. Y. Podladchikov (2000), Temperature-dependent viscoelastic compaction and compartmentalization in sedimentary basins, *Tectonophysics*, *324*(3), 137–168.

Corbet, T. F., and C. M. Bethke (1992), Disequilibrium fluid pressures and groundwater flow in the Western Canada sedimentary basin, *Journal of Geophysical Research*, *97*(B5), 7203–7217.

Costa, E., and B. C. Vendeville (2002), Experimental insights on the geometry and kinematics of fold-and-thrust belts above weak, viscous evaporitic décollement, *Journal of Structural Geology*, *24*(11), 1729–1739.

Couzens-Schultz, B. A., C. A. Hedlund, and C. Guzman (2007), Integrating geology and velocity data to constrain pressure prediction in foldbelts, *Abstracts: Annual Meeting - American Association of Petroleum Geologists*, *2007*, 28.

Coward, M., and S. Stewart (1995), Salt-influenced structures in the Mesozoic-Tertiary cover of the southern North Sea, U.K, in *Salt Tectonics, A Global Perspective*, *AAPG Memoir*, vol. 65, edited by M. P. A. Jackson, D. G. Roberts, and S. Snelson, pp. 229–250, AAPG, Tulsa, Oklahoma.

Cramez, C., and M. P. A. Jackson (2000), Superposed deformation straddling the continental-oceanic transition in deep-water Angola, *Marine and Petroleum Geology*, *17*(10), 1095–1109.

Daudre, B., and S. Cloetingh (1994), Numerical modelling of salt diapirism: Influence of the tectonic regime, *Tectonophysics*, *240*(1-4), 59–79.

David, C., T.-F. Wong, W. Zhu, and J. Zhang (1994), Laboratory measurement of compaction-induced permeability change in porous rocks: Implications for the generation and maintenance of pore pressure excess in the crust, *Pure and Applied Geophysics*, *143*(1-3), 425–456.

Davis, D., J. Suppe, and F. A. Dahlen (1983), Mechanics of fold-and-thrust belts and accretionary wedges, *Journal of Geophysical Research*, *88*(B2), 1153–1172.

Davison, I. (2007), Geology and tectonics of the South Atlantic Brazilian salt basins, in *Deformation of the continental crust; the legacy of Mike Coward*, *Geological Society Special Publications*, vol. 272, edited by A. Ries, R. Butler, and R. Graham, pp. 345–359, Geological Society of London.

Davison, I. (2009), Faulting and fluid flow through salt, *Journal of the Geological Society of London*, *166*(2), 205–216.

Decalf, C., S. Lock-Williams, N. Weber, M. Cubanski, C. Yough, M. Etemadi, and L. Liro (2004), Emplacement and evolution of salt in the Alaminos Canyon protraction area, Gulf of Mexico, in *Salt Sediment Interactions and Hydrocarbon Prospectivity: Concepts, Applications, and Case Studies for the 21st Century. GCSSEPM Conference Proceedings*, pp. 636–651.

Demercian, S., P. Szatmari, and P. R. Cobbold (1993), Style and pattern of salt diapirs due to thin-skinned gravitational gliding, Campos and Santos basins, offshore Brazil, *Tectonophysics*, *228*(3-4), 393–433.

Deptuck, M. E., D. J. W. Piper, B. Savoye, and A. Gervais (2008), Dimensions and architecture of late Pleistocene submarine lobes off the northern margin of east Corsica, *Sedimentology*, *55*(4), 869–898.

Dewers, T., and P. J. Ortoleva (1990), Interaction of reaction, mass transport, and rock deformation during diagenesis: Mathematical modeling of intergranular pressure solution, stylolites, and differential compaction/cementation, in *Prediction of reservoir quality through chemical modeling*, vol. 49, edited by I. D. Meshri and P. J. Ortoleva, pp. 147–160, AAPG, Tulsa, Oklahoma.

Diegel, F. A., J. F. Karlo, D. C. Schuster, R. C. Shoup, and P. R. Tauvers (1995), Cenozoic structural evolution and tectono-stratigraphic framework of the northern Gulf Coast continental margin, in *Salt Tectonics, A Global Perspective*, *AAPG Memoir*, vol. 65, edited by M. P. A. Jackson, D. G. Roberts, and S. Snelson, pp. 109–151, AAPG, Tulsa, Oklahoma.

Downey, M. W. (1984), Evaluating seals for hydrocarbon accumulations, *AAPG Bulletin*, *68*(11), 1752–1763.

Fiduk, J. C., B. D. Trudgill, M. G. Rowan, P. Weimer, P. E. Gale, B. E. Korn, R. L. Phair, W. T. Gafford, G. R. Roberts, S. W. Dobbs, and C. K. Guu (1996), Allochthonous salt surrounding Alaminos Canyon, northwestern deep Gulf of Mexico, *Transactions - Gulf Coast Association of Geological Societies*, *46*, 27–38.

Fiduk, J. C., P. Weimer, B. D. Trudgill, M. G. Rowan, P. E. Gale, R. L. Phair, B. E. Korn, G. R. Roberts, W. T. Gafford, R. S. Lowe, and T. A. Queffelec (1999), The Perdido fold belt, Northwestern deep Gulf of Mexico, Part 2; Seismic stratigraphy and petroleum systems, *AAPG Bulletin*, *83*(4), 578–612.

Flemings, P. B., H. Long, B. Dugan, J. Germaine, C. M. John, J. H. Behrmann, D. Sawyer, and the IODP Expedition 308 Scientists (2008), Pore pressure penetrometers document high overpressure near the seafloor where multiple submarine landslides have occurred on the continental slope, offshore Louisiana, Gulf of Mexico, *Earth and Planetary Science Letters*, *269*(3-4), 309–324.

Fletcher, R. C., M. R. Hudec, and I. A. Watson (1995), Salt glacier and composite sediment-salt glacier models for the emplacement and early burial of allochthonous salt sheets, in *Salt Tectonics, A Global Perspective*, *AAPG Memoir*, vol. 65, edited by M. P. A. Jackson, D. G. Roberts, and S. Snelson, pp. 77–107, AAPG, Tulsa, Oklahoma.

Fort, X., J. P. Brun, and F. Chauvel (2004), Contraction induced by block rotation above salt (Angolan margin), *Marine and Petroleum Geology*, *21*(10), 1281–1294.

Fowler, A. C., and X. Yang (1999), Pressure solution and viscous compaction in sedimentary basins, *Journal of Geophysical Research*, *104*(B6), 12,989–12,998.

Freed, R. L., and D. R. Peacor (1989), Geopressured shale and sealing effect of smectite to illite transition, *AAPG Bulletin*, *73*(10), 1223–1232.

Fullsack, P. (1995), An arbitrary Lagrangian-Eulerian formulation for creeping flows and its applications in tectonic models, *Geophysical Journal International*, *120*(1), 1–23.

Fuqua, D. A. (1990), Seismic structural analysis of the Perdido fold belt, Alaminos Canyon area, northwestern Gulf of Mexico, Master's thesis.

Galloway, W. E., P. E. Ganey-Curry, X. Li, and R. Buffler (2000), Cenozoic depositional history of the Gulf of Mexico basin, *AAPG Bulletin*, *84*(11), 1743–1774.

Garven, G. (1986), The role of regional fluid flow in the genesis of the Pine Point Deposit, Western Canada sedimentary basin; reply, *Economic Geology and the Bulletin of the Society of Economic Geologists*, *81*(4), 1015–1020.

Ge, H., M. P. A. Jackson, and B. C. Vendeville (1997), Kinematics and dynamics of salt tectonics driven by progradation, *AAPG Bulletin*, *81*, 398–423.

Gemmer, L., S. J. Ings, S. Medvedev, and C. Beaumont (2004), Salt tectonics driven by differential sediment loading: Stability analysis and finite element experiments, *Basin Research*, *16*, 199–219.

Gemmer, L., C. Beaumont, and S. J. Ings (2005), Dynamic modeling of passive margin salt tectonics: Effects of water loading, sediment properties, and sedimentation patterns, *Basin Research*, *17*, 383–402.

Giles, K. A., and T. F. Lawton (2002), Halokinetic sequence stratigraphy adjacent to the El Papalote Diapir, northeastern Mexico, *AAPG Bulletin*, *86*(5), 823–840.

Goldhammer, R. K., and C. A. Johnson (2001), Middle Jurassic-Upper Cretaceous paleogeographic evolution and sequence-stratigraphic framework of the Northwest Gulf of Mexico rim, in *The western Gulf of Mexico basin; tectonics, sedimentary basins, and petroleum systems*, *AAPG Memoir*, vol. 75, edited by C. Bartolini, R. T. Buffler, and A. Cantu-Chapa, pp. 45–81, AAPG, Tulsa, Oklahoma.

Gordon, D. S., and P. B. Flemings (1998), Generation of overpressure and compaction-driven fluid flow in a Plio-Pleistocene growth-faulted basin, Eugene Island 330, offshore Louisiana, *Basin Research*, *10*(2), 177–196.

Goteti, R., S. Ings, and C. Beaumont (2012), Development of salt mini basins initiated by sedimentary topographic relief, *Earth and Planetary Science Letters*, *339-340*, 103–116.

Gradmann, S., and C. Beaumont (2012), Coupled fluid flow and sediment deformation in margin-scale salt-tectonic systems: 2. Layered sediment models and application to the northwestern Gulf of Mexico, *Tectonics*, *31*(4), doi: 10.1029/2011TC003035.

Gradmann, S., C. Hübscher, Z. Ben-Avraham, D. Gajewski, and G. Netzeband (2005), Salt tectonics off northern Israel, *Marine and Petroleum Geology*, *22*(5), 597–611.

Gradmann, S., C. Beaumont, and M. Albertz (2009), Factors controlling the evolution of the Perdido Fold Belt, northwestern Gulf of Mexico, determined from numerical models, *Tectonics*, *28*(2).

Gradmann, S., C. Beaumont, and S. Ings (2012), Coupled fluid flow and sediment deformation in margin-scale salt-tectonic systems: 1. Development and application of simple, single-lithology models, *Tectonics*, *31*(4), doi: 10.1029/2011TC003033.

Grando, G., and K. R. McClay (2004), Structural evolution of the Frampton growth fold system, Atwater Valley-southern Green Canyon area, deep water Gulf of Mexico; Oil and gas in compressional belts, *Marine and Petroleum Geology*, *21*(7), 889–910.

Gratz, A. J. (1991), Solution-transfer compaction of quartzites: Progress toward a rate law, *Geology*, *19*(9), 901–904.

Guerin, G., Y. Philippe, and J.-A. Dal (2006), Impact of amount of gravity-driven compression and intermediate décollement levels on the Sigsbee Salt Canopy formation, Gulf of Mexico, *Abstracts, CD-ROM, AAPG Annual Convention*.

Gunzburger, Y. (2010), Stress state interpretation in light of pressure-solution creep: Numerical modelling of limestone in the Eastern Paris Basin, France, *Tectonophysics*, *483*(3-4), 377 – 389.

Hall, S. H. (2002), The role of autochthonous salt inflation and deflation in the northern Gulf of Mexico, *Marine and Petroleum Geology*, *19*(6), 649–682.

Hart, B., P. Flemings, and A. Deshpande (1995), Porosity and pressure: Role of compaction disequilibrium in the development of geopressures in a Gulf Coast Pleistocene basin, *Geology*, *23*(1), 45–48.

Heaton, R. C., M. P. A. Jackson, M. Barmahmoud, and S. O. Nani (1995), Superposed Neogene extension, contraction and salt canopy emplacement in the Yemeni Red Sea, in *Salt Tectonics, A Global Perspective*, *AAPG Memoir*, vol. 65, edited by M. P. A. Jackson, D. G. Roberts, and S. Snelson, pp. 333–352, AAPG, Tulsa, Oklahoma.

Heiniö, P., and R. Davies (2006), Degradation of compressional fold belts: Deep-water Niger Delta, *AAPG Bulletin*, *90*(5), 753–770, doi: 10.1306/11210505090.

Helle, H., K. Easterling, and M. Ashby (1985), Hot-isostatic pressing diagrams: New developments, *Acta Metallurgica*, *33*, 2163–2174.

Hubbert, M. K., and W. W. Rubey (1959), Role of fluid pressure in mechanics of overthrust faulting: Part 1, Mechanics of fluid-filled porous solids and its application to overthrust faulting, *Geological Society of America Bulletin*, *70*(2), 115–166.

Hudec, M. R. (2004), Salt intrusion: Time for a comeback?, in *Salt Sediment Interactions and Hydrocarbon Prospectivity: Concepts, Applications, and Case Studies for the 21st Century. GCSSEPM Conference Proceedings*, pp. 119–132, (CD-ROM - ISSN: 1544-2462).

Hudec, M. R., and M. P. A. Jackson (2004), Regional restoration across the Kwanza Basin, Angola; salt tectonics triggered by repeated uplift of a metastable passive margin, *AAPG Bulletin*, *88*(7), 971–990.

Hudec, M. R., and M. P. A. Jackson (2006), Advance of allochthonous salt sheets in passive margins and orogens, *AAPG Bulletin*, *90*(10), 1535–1564.

Hudec, M. R., M. P. A. Jackson, and D. D. Schultz-Ela (2009), The paradox of minibasin subsidence into salt; clues to the evolution of crustal basins, *Geological Society of America Bulletin*, *121*(1-2), 201–221.

Huffman, A. R., and G. L. Bowers (Eds.) (2002), *Pressure regimes in sedimentary basins and their prediction*, *AAPG Memoir*, vol. 76, AAPG, Tulsa, Oklahoma.

Husson, L., P. Henry, and X. L. Pichon (2008), Thermal regime of the NW shelf of the Gulf of Mexico: Part A, Thermal and pressure fields, *Bulletin de la Societe Geologique de France*, *179*(2), 129–137.

Ings, S. J. (2006), Passive continental margin salt tectonics: Numerical modelling, analytical stability analysis, and applications to the Scotian Margin, offshore Eastern Canada, Ph.D. thesis, Dalhousie University.

Ings, S. J., and C. Beaumont (2010a), Continental margin shale tectonics: Preliminary results from coupled fluid-mechanical models of large-scale delta instability, *Journal of the Geological Society of London*, *167*(3), 571–582.

Ings, S. J., and C. Beaumont (2010b), Shortening viscous pressure ridges, a solution to the enigma of initiating salt "withdrawal" minibasins, *Geology*, *38*(4), 339–342.

Jackson, M. P. A. (1995), Retrospective salt tectonics, in *Salt Tectonics, A Global Perspective*, *AAPG Memoir*, vol. 65, edited by M. P. A. Jackson, D. G. Roberts, and S. Snelson, pp. 1–28, AAPG, Tulsa, Oklahoma.

Jackson, M. P. A., and C. J. Talbot (1986), External shapes, strain rates, and dynamics of salt structures, *GSA Bulletin*, *97*(3), 305–323.

Jackson, M. P. A., and C. J. Talbot (1991), A glossary of salt tectonics, *Tech. Rep. 91-94*, University of Texas at Austin, Bureau of Economic Geology, Austin, TX, United States (USA).

Jackson, M. P. A., and B. C. Vendeville (1994), Regional extension as a geologic trigger for diapirism, *GSA Bulletin*, *106*, 57–73.

Karig, D., and G. Hou (1992), High-stress consolidation experiments and their geologic implications, *Journal of Geophysical Research*, *97*(B1), 289–300.

Katahara, K. (2009), Lateral earth stress and strain, *SEG Technical Program Expanded Abstracts*, *28*(1), 2165–2169.

Kawabata, K., H. Tanaka, Y. Kitamura, and K.-F. Ma (2009), Apparent activation energy and rate-limiting process estimation from natural shale deformed by pressure solution in shallow subduction zone, *Earth and Planetary Science Letters*, *287*(1-2), 57–63.

Korvin, G. (1984), Shale compaction and statistical physics, *Geophysical Journal of the Royal Astronomical Society*, *78*, 35–50.

Koyi, H. (1996), Salt flow by aggrading and prograding overburdens, in *Salt Tectonics*, *Geological Society Special Publications*, vol. 100, edited by G. Alsop, D. Blundell, and I. Davison, pp. 243–258, Geological Society of London.

Krezsek, C., J. Adam, and D. Grujic (2007), Mechanics of fault/rollover systems developed on passive margins detached on salt: Insights from analogue modelling and optical strain monitoring, in *Structurally Complex Reservoirs*, *Geological Society Special Publications*, vol. 292, edited by S. J. Jolley, D. Barr, J. J. Walsh, and R. J. Knipe, pp. 103–121, Geological Society of London.

Kulenkampff, J. M., and U. Yaramanci (1993), Frequency-dependent complex resistivity of rock-salt samples and related petrophysical parameters, *Geophysical Prospecting*, *41*(8), 995–1008.

Leftwich, J. T., and T. Engelder (1994), The characteristics of geopressure profiles in the Gulf of Mexico Basin, in *Basin compartments and seals*, *AAPG Memoir*, vol. 61, edited by P. J. Ortoleva, pp. 119–129, AAPG, Tulsa, Oklahoma.

Letouzey, J., B. Colletta, R. Vially, and J. C. Chermette (1995), Evolution of salt-related structures in compressional settings, in *Salt Tectonics, A Global Perspective*, *AAPG Memoir*, vol. 65, edited by M. P. A. Jackson, D. G. Roberts, and S. Snelson, pp. 41–60, AAPG, Tulsa, Oklahoma.

Lobkovsky, L., and V. Kerchman (1991), A two-level concept of plate tectonics; application to geodynamics, *Tectonophysics*, *199*(2-4), 343–374.

Luo, X., and G. Vasseur (1996), Geopressuring mechanism of organic matter cracking: numerical modeling, *AAPG Bulletin*, *80*(6), 856–874.

Marton, L. G., G. C. Tari, and C. T. Lehmann (2000), Evolution of the Angolan passive margin, West Africa, with emphasis on post-salt structural styles, in *Atlantic Rifts and Continental Margins*, *Geophysical Monograph*, vol. 115, edited by W. Mohriak and M. Talwani, pp. 129–149, AGU, Washington, D.C.

Maxwell, S. A. (2009), Deformation styles of allochthonous salt sheets during differential loading conditions: Insights from discrete element models, Master's thesis, Rice University, Houston, Texas.

McBride, B. C., M. G. Rowan, P. Weimer, N. Hurley, and P. Weimer (1998), The evolution of allochthonous salt systems, northern Green Canyon and Ewing Bank (offshore Louisiana), northern Gulf of Mexico, *AAPG Bulletin*, *82*(5B), 1013–1036.

McDonnell, A., R. G. Loucks, and W. E. Galloway (2008), Paleocene to Eocene deep-water slope canyons, western Gulf of Mexico: Further insights for the provenance of deep-water offshore Wilcox Group plays, *AAPG Bulletin*, *92*(9), 1169–1189.

McDonnell, A., M. R. Hudec, and M. P. Jackson (2009), Distinguishing salt welds from shale detachments on the inner texas shelf, western gulf of mexico, *Basin Research*, *21*, doi: 10.1111/j.1365-2117.2008.00375.x.

Mello, U. T., G. D. Karner, and R. N. Anderson (1994), A physical explanation for the positioning of the depth to the top of overpressure in shale-dominated sequences in the Gulf Coast basin, United States, *Journal of Geophysical Research*, *99*(B2), 2775–2789.

Meyer, D., L. Zarra, D. Rains, B. Meltz, and T. Hall (2005), Emergence of the Lower Tertiary Wilcox trend in the deepwater Gulf of Mexico, *WorldOil Magazine*, *226*(5).

Meyer, D., L. Zarra, and J. Yun (2007), From BAHA to Jack, evolution of the Lower Tertiary Wilcox trend in the deepwater Gulf of Mexico, *The Sedimentary Record*, *5*(3), 4–9.

Mohriak, W. U., J. M. Macedo, R. T. Castellani, H. D. Rangel, A. Z. N. Barros, M. A. L. Latgé, A. M. P. Mizusaki, P. Szamarti, L. S. Demercian, J. G. Rizzo, and J. R. Aires (1995), Salt tectonics and structural styles in the deep-water province of the Cabo Frio region, Rio de Janeiro, Brazil, in *Salt Tectonics, A Global Perspective*, *AAPG Memoir*, vol. 65, edited by M. P. A. Jackson, D. G. Roberts, and S. Snelson, pp. 273–304, AAPG, Tulsa, Oklahoma.

Morency, C. (2006), *Coupled pore fluid flow / skeleton matrix deformation: SOPALEff modifications*, Dalhousie Geodynamics Group.

Morency, C., R. S. Huismans, C. Beaumont, and P. Fullsack (2007), A numerical model for coupled fluid flow and matrix deformation with applications to disequilibrium compaction and delta stability, *Journal of Geophysical Research*, *112*(B10), 407.

Morley, C. K., and G. Guerin (1996), Comparison of gravity-driven deformation styles and behavior associated with mobile shales and salt, *Tectonics*, *15*(6), 1154–1170.

Mourgues, R., and P. R. Cobbold (2003), Some tectonic consequences of fluid overpressures and seepage forces as demonstrated by sandbox modelling, *Tectonophysics*, *376*(1-2), 75–97.

Mourgues, R., E. Lecomte, B. Vendeville, and S. Raillard (2009), An experimental investigation of gravity-driven shale tectonics in progradational delta, *Tectonophysics*, *474*(3-4), 643 – 656.

Nelson, T. H., and L. Fairchild (1989), Emplacement and evolution of salt sills in the northern gulf of mexico, *The Bulletin of the Houston Geological Society*, *32*(1), 6–7.

Nettleton, L. L. (1934), Fluid mechanics of salt domes, *AAPG Bulletin*, *27*(1), 51–63.

Nettleton, L. L., and T. A. Elkins (1947), Geologic models made from granular materials, *American Geophysical Union Transactions*, *28*, 451–466.

Neuzil, C. E. (1994), How permeable are clays and shales?, *Water Resources Research*, *30*(2), 145–150.

Obert, L., and W. I. Duvall (1967), *Rock mechanics and the design of structures in rock*, John Wiley and Sons, New York.

Osborne, M. J., and R. E. Swarbrick (1997), Mechanisms for generating overpressure in sedimentary basins: A reevaluation, *AAPG Bulletin*, *81*(6), 1023–1041.

Palciauskas, V. V., and P. A. Domenico (1989), Fluid pressures in deforming porous rocks, *Water Resources Research*, *25*(2), 203–213.

Paterson, M. S. (1973), Nonhydrostatic thermodynamics and its geologic applications, *Reviews of Geophysics and Space Physics*, *11*(2), 355–389.

Peach, C. J., C. J. Spiers, and P. W. Trimby (2001), Effect of confining pressure on dilatation, recrystallization, and flow of rock salt at 150 degrees C, *Journal of Geophysical Research*, *106*(B7), 13,315–13,328.

Peel, F. J., C. J. Travis, and J. R. Hossack (1995), Genetic structural provinces and salt tectonics of the Cenozoic offshore U.S. Gulf of Mexico: A preliminary analysis, in *Salt Tectonics, A Global Perspective*, *AAPG Memoir*, vol. 65, edited by M. P. A. Jackson, D. G. Roberts, and S. Snelson, pp. 153–175, AAPG, Tulsa, Oklahoma.

Pettingill, H., and P. Weimer (2002), Worldwide deepwater exploration and production: Past, present, and future, *The Leading Edge*, *21*(4), 371–376.

Philippe, Y., and G. Guerin (2006), Development of turtle-back anticlines in gravity-driven compressional domains: Evidences from the deepwater Gulf of Mexico, *Abstracts, CD-ROM, AAPG Annual Convention*.

Philippe, Y., D. Wittoesch, and G. Guerin (2005), Importance of gravity-driven compressional tectonics in northern offshore and deep-offshore Gulf of Mexico: New observations and implications for subsalt interpretation, *Abstracts, CD-ROM, AAPG Annual Convention*.

Pindell, J., and J. F. Dewey (1982), Permo-Triassic reconstruction of western Pangea and the evolution of the Gulf of Mexico/Caribbean region, *Tectonics*, *1*(2), 179–211.

Pindell, J., and L. Kennan (2007), Rift models and the salt-cored marginal wedge in the northern Gulf of Mexico: Implications for deep water Paleogene Wilcox deposition and basinwide maturation, in *Transactions of GCSSEPM 27th Annual Bob F. Perkins Research Conference*, pp. 146–186, (CD Rom).

Pindell, J. L. (1985), Alleghenian reconstruction and subsequent evolution of the Gulf of Mexico, Bahamas, and proto-Caribbean, *Tectonics*, *4*(1), 1–39.

Poliakov, A., Y. Podladchikov, and C. Talbot (1993a), Initiation of salt diapirs with frictional overburdens: Numerical experiments, *Tectonophysics*, *228*(3-4), 199–210.

Poliakov, A., R. van Balen, Y. Podladchikov, B. Daudre, S. Cloetingh, and C. Talbot (1993b), Numerical analysis of how sedimentation and redistribution of surficial sediments affects salt diapirism, *Tectonophysics*, *226*(1-4), 199–216.

Poliakov, A. N. B., Y. Y. Podladchikov, E. C. Dawson, and C. J. Talbot (1996), Salt diapirism with simultaneous brittle faulting and viscous flow, in *Salt Tectonics*, *Geological Society Special Publications*, vol. 100, edited by G. I. Alsop, D. J. Blundell, and I. Davison, pp. 291–302, Geological Society of London.

Popp, T., H. Kern, and O. Schulze (2001), Evolution of dilatancy and permeability in rock salt during hydrostatic compaction and triaxial deformation, *Journal of Geophysical Research*, *106*(B3), 4061–4078.

Prelat, A., J. Covault, D. Hodgson, A. Fildani, and S. Flint (2010), Intrinsic controls on the range of volumes, morphologies, and dimensions of submarine lobes, *Sedimentary Geology*, *232*(1-2), 66 – 76.

Radovich, B., J. Moon, C. Connors, and D. Bird (2007a), Insights into structure and stratigraphy of the northern Gulf of Mexico from 2D pre-stack depth migration imaging of mega-regional onshore to deep water, long-offset seismic data, *Transactions - Gulf Coast Association of Geological Societies*, *57*, 633–637.

Radovich, B., C. Connors, and J. Moon (2007b), Deep imaging of the Paleogene, Miocene structure and stratigraphy of the western Gulf of Mexico using 2D pre-stack depth migration of mega-regional onshore to deep water, long-offset seismic data, in *The Paleogene of the Gulf of Mexico and Caribbean Basins: Processes, Events, and Petroleum Systems. GCSSEPM Conference Proceedings*, pp. 307–322, (CD Rom).

Reilly, M. J., and P. B. Flemings (2010), Deep pore pressures and seafloor venting in the Auger Basin, Gulf of Mexico, *Basin Research*, *22*(4), 380–397.

Revil, A. (2001), Pervasive pressure solution transfer in a quartz sand, *Journal of Geophysical Research*, *106*(B5), 8665–8686.

Revil, A., and L. M. Cathles (1999), Permeability of shaly sands, *Water Resources Research*, *35*(3), 651–662.

Revil, A., D. Grauls, and O. Brevart (2002), Mechanical compaction of sand/clay mixtures, *Journal of Geophysical Research*, *107*(B11), 15.

Rowan, M. G., and K. F. Inman (2005), Counterregional-style deformation in the deep shelf of the northern Gulf of Mexico, *Transactions - Gulf Coast Association of Geological Societies*, *55*, 716–724.

Rowan, M. G., B. D. Trudgill, and J. C. Fiduk (2000), Deep-water, salt-cored foldbelts: Lessons from the Mississippi Fan and Perdido Foldbelts, northern Gulf of Mexico, in *Atlantic Rifts and Continental Margins*, *Geophysical Monograph*, vol. 115, edited by W. Mohriak and M. Talwani, pp. 173–191, AGU, Washington, D.C.

Rowan, M. G., F. J. Peel, and B. C. Vendeville (2004), Gravity-driven fold belts on passive margins, in *Thrust tectonics and hydrocarbon systems*, *AAPG Memoir*, vol. 82, edited by K. R. McClay, pp. 157–182, AAPG, Tulsa, Oklahoma.

Rowan, M. G., K. F. Inman, and J. C. Fiduk (2005), Oligo-Miocene extension at the Louann level in the northern Gulf of Mexico: Kinematic models and examples, *Transactions - Gulf Coast Association of Geological Societies*, *55*, 725–732.

Rutter, E. H. (1976), The kinetics of rock deformation by pressure solution, *Philosophical Transactions of the Royal Society of London, Series A: Mathematical and Physical Sciences*, *283*(1312), 203–219.

Rutter, E. H., and D. H. Mainprice (1978), The effect of water on stress relaxation of faulted and unfaulted sandstone, in *Rock friction and earthquake prediction*, vol. 116, edited by J. D. Byerlee and M. Wyss, pp. 634–654, Birkhäuser Verlag.

Salvador, A. (1991), Origin and development of the Gulf of Mexico Basin, in *The Gulf of Mexico Basin*, *The geology of North America*, vol. J, edited by A. Salvador, pp. 389–444, GSA, USA.

Schleder, Z., J. L. Urai, S. Nollet, and C. Hilgers (2008), Solution-precipitation creep and fluid flow in halite: A case study of Zechstein (Z1) rocksalt from Neuhof salt mine (Germany), *International Journal of Earth Sciences*, *97*(5), 1045–1056.

Schmeling, H. (1987), On the relation between initial conditions and late stages of Rayleigh-Taylor instabilities, *Tectonophysics*, *133*, 16–31.

Schmoker, J., and R. Halley (1982), Carbonate porosity versus depth: A predictabler-Relation for South Florida, *AAPG Bulletin*, *66*(12), 2561–2570.

Schneider, F., J. L. Potdevin, S. Wolf, and I. Faille (1996), Mechanical and chemical compaction model for sedimentary basin simulators, *Tectonophysics*, *263*(1-4), 307–317.

Schoenherr, J., J. L. Urai, P. A. Kukla, R. Littke, Z. Schleder, J.-M. Larroque, M. J. Newall, N. Al-Abry, H. Al-Siyabi, and Z. Rawahi (2007), Limits to the sealing capacity of rock salt: A case study of the infra-Cambrian Ara Salt from the South Oman salt basin, *AAPG Bulletin*, *91*(11), 1541–1557.

Schultz-Ela, D. D. (2001), Excursus on gravity gliding and gravity spreading, *Journal of Structural Geology*, *23*(5), 725–731.

Schultz-Ela, D. D., M. P. A. Jackson, and B. C. Vendeville (1993), Mechanics of active diapirism, *Tectonophysics*, *228*(3-4), 275–312.

Sclater, J., and P. Christie (1980), Continental stretching: an explanation of the post-mid-Cretaceous subsidence of the Central North Sea Basin, *Journal of Geophysical Research*, *85*, 37113739, doi: 10.1029/JB085iB07p03711.

Scott, D. R., and D. J. Stevenson (1984), Magma solitons, *Geophysical Research Letters*, *11*(11), 1161–1164.

Shin, H., J. C. Santamarina, and J. A. Cartwright (2008), Contraction-driven shear failure in compacting uncemented sediments, *Geology*, *36*(12), 931–934.

Simmons, G. R. (1992), The regional distribution of salt in the northwestern Gulf of Mexico; styles of emplacement and implications for early tectonic history, *Bulletin - Houston Geological Society*, *35*(4), 7.

Skene, K. I., D. J. W. Piper, and P. S. Hill (2002), Quantitative analysis of variations in depositional sequence thickness from submarine channel levees, *Sedimentology*, *49*(6), 1411–1430.

Smith, J. E. (1971), The dynamics of shale compaction and evolution of pore-fluid pressures, *Journal of the International Association for Mathematical Geology*, *3*(3), 239–263.

Spathopoulos, F. (1996), An insight on salt tectonics in the Angola Basin, South Atlantic, in *Salt tectonics*, *Geological Society Special Publications*, vol. 100, edited by G. Alsop, D. Blundell, and I. Davison, pp. 153–174, Geological Society of London.

Stephenson, L. P., W. J. Plumley, and V. V. Palciauskas (1992), A model for sandstone compaction by grain interpenetration, *Journal of Sedimentary Research*, *62*(1), 11–22.

Stern, R. J., and W. R. Dickinson (2010), The Gulf of Mexico is a Jurassic backarc basin, *Geosphere*, *6*(6), 739–754.

Suetnova, E., and G. Vasseur (2000), 1-D modelling rock compaction in sedimentary basins using a visco-elastic rheology, *Earth and Planetary Science Letters*, *178*(3-4), 373–383.

Swarbrick, R. E., and M. J. Osborne (1998), Mechanisms that generate abnormal pressures: an overview, in *Abnormal pressures in hydrocarbon environments*, *AAPG Memoir*, vol. 70, edited by B. Law and C. Spencer, pp. 13–34, AAPG, Tulsa, Oklahoma.

Talbot, C. (1979), Fold trains in a glacier of salt in southern Iran, *Journal of Structural Geology*, *1*(1), 5–18.

Talbot, C. J. (1998), Extrusions of Hormuz salt in Iran, *Geological Society Special Publications*, *143*, 315–334.

Talbot, C. J., and P. Aftabi (2004), Geology and models of salt extrusion at Qum Kuh, central Iran, *Journal of the Geological Society*, *161*(2), 321–334.

Talbot, C. J., and E. A. Rogers (1980), Seasonal movements in a salt glacier in Iran, *Science*, *208*(4442), 395–397.

Tari, G., J. Molnar, and P. Ashton (2003), Examples of salt tectonics from West Africa: a comparative approach, in *Petroleum Geology of Africa: New Themes and Developing Technologies*, *Geological Society of London Special Publication*, vol. 207, edited by T. J. Arthur, D. S. MacGregor, and N. R. Cameron, pp. 85–104, Geological Society of London, London,UK.

Ter Heege, J. H., J. H. P. de Bresser, and C. J. Spiers (2005), Rheological behaviour of synthetic rocksalt; the interplay between water, dynamic recrystallization and deformation mechanisms, *Journal of Structural Geology*, *27*(6), 948–963.

Terzaghi, K. (1936), The shearing resistance of saturated soil and the angle between the planes of shear, *Proc. 1st Int. Conf. Soil Mech*, *1*, 54–56.

Terzaghi, K. (1943), *Theoretical soil Mechanics*, John Wiley and Sons, New York.

Trudgill, B. D., M. G. Rowan, J. C. Fiduk, P. Weimer, P. E. Gale, B. E. Korn, R. L. Phair, W. T. Gafford, G. R. Roberts, and S. W. Dobbs (1999), The Perdido fold belt, northwestern deep Gulf of Mexico: Part 1, Structural geometry, evolution and regional implications, *AAPG Bulletin*, *83*(1), 88–113.

Trusheim, F. (1957), Über Halokinese und ihre Bedeutung für die strukturelle Entwicklung Norddeutschlands, *Zeitschrift der Deutschen Geologischen Gesellschaft*, *109*, 111–151.

Trusheim, F. (1960), Mechanism of salt migration in northern Germany, *AAPG Bulletin*, *44*, 1519–1540.

Urai, J. L., C. J. Spiers, H. J. Zwart, and G. S. Lister (1986), Weakening of rock salt by water during long-term creep, *Nature*, *324*, 554–557.

van Keken, P. E., C. J. Spiers, A. P. van den Berg, and E. J. Muyzert (1993), The effective viscosity of rocksalt: Implementation of steady-state creep laws in numerical models of salt diapirism, *Tectonophysics*, *225*(4), 457–476.

van Ruth, P., R. Hillis, P. Tingate, and R. Swarbrick (2003), The origin of overpressure in 'old' sedimentary basins: An example from the Cooper Basin, Australia, *Geofluids*, *3*(2), 125–131.

Vendeville, B., and V. Gaullier (2005), Salt diapirism generated by shortening and buckle folding, *Abstracts, CDROM, AAPG Annual Convention*.

Vendeville, B. C. (2005), Salt tectonics driven by sediment progradation: Part 1, Mechanics and kinematics, *AAPG Bulletin*, *89*(8), 1071–1079.

Vendeville, B. C., and M. P. A. Jackson (1992), The rise of diapirs during thin-skinned extension, *Marine and Petroleum Geology*, *9*(4), 331–353.

Waller, T. D. (2007), Structural Analysis of the Perdido Fold Belt: Timing, Evolution and Structural Cycle, Master's thesis, Texas A&M University.

Warsitzka, M., J. Kley, F. Jahne, and N. Kukowski (2011), Salt diapirism driven by differential loading some insights from analogue modelling, *Tectonophysics*, doi: 10.1016/j.tecto.2011.11.018.

Watts, A. B. (2001), *Isostasy and flexure of the lithosphere*, University of Cambridge, Cambridge, United Kingdom.

Weijermars, R., M. P. A. Jackson, and B. C. Vendeville (1993), Rheological and tectonic modeling of salt provinces, *Tectonophysics*, *217*, 143–174.

Weimer, P., and R. T. Buffler (1992), Structural geology and evolution of the Mississippi Fan fold belt, deep Gulf of Mexico, *AAPG Bulletin*, *76*(2), 225–251.

Whaley, J. (2006), Huge Potential Still Waiting in the Gulf of Mexico, *GEO ExPro*, *3*(4), 14–24.

Willett, S. D. (1999), Rheological dependence of extension in wedge models of convergent orogens, *Tectonophysics*, *305*(4), 419–435.

Wilson, H. H. (2003), Extensional evolution of the Gulf of Mexico Basin and the deposition of Tertiary evaporites, *Journal of Petroleum Geology*, *26*, 403–428.

Winker, C. D. (2004), Stratigraphy and structural timing of the Perdido Foldbelt, an emerging toe-of-slope play in the northwestern deep-water Gulf of Mexico, *Transactions - Gulf Coast Association of Geological Societies*, *54*, 765.

Winker, C. D., and R. Buffler (1988), Paleogeographic evolution of early deep-water Gulf of Mexico and margins, Jurassic to Middle Cretaceous (Comanchean), *AAPG Bulletin*, *72*(3), 318–346.

Worral, D. M., and S. Snelson (1989), Evolution of the northern Gulf of Mexico, with emphasis on Cenozoic growth faulting and the role of salt, in *The Geology of North America - an overview*, vol. A, edited by A. W. Bally and A. R. Palmer, pp. 97–138, GSA, Boulder, Colorado.

Wu, S., and A. W. Bally (2000), Slope tectonics; comparisons and contrasts of structural styles of salt and shale tectonics of the northern Gulf of Mexico with shale tectonics of offshore Nigeria in Gulf of Guinea, in *Atlantic Rifts and Continental Margins*, *Geophysical Monograph*, vol. 115, edited by W. Mohriak and M. Talwani, pp. 151–172, AGU, Washington, D.C.

Yang, X. S. (2001), A unified approach to mechanical compaction, pressure solution, mineral reactions and the temperature distribution in hydrocarbon basins, *Tectonophysics*, *330*(1-2), 141–151.

Yassir, N. A., and J. S. Bell (1996), Abnormally high fluid pressures and associated porosities and stress regimes in sedimentary basins, *SPE Formation Evaluation*, *11*(1), 5–10.

Zaleski, S., and P. Julien (1992), Numerical simulation of Rayleigh-Taylor instability for single and multiple salt diapirs, *Tectonophysics*, *206*(1-2), 55–69.